The Research and Development of *in situ* non-intrusive Optical and Temperature diagnostics in an Internal Combustion Engine

Trevor Stewart Wilson
BEng (Hons)

Thesis submitted in partial fulfilment of the requirements for the degree of Doctor of Philosophy

University of Warwick, School of Engineering
September 2002

To Wendy and our kids…

(should we be so blessed)

ABSTRACT

Novel instrumentation has been developed and evaluated in a low-cost, purpose built, single-cylinder internal combustion engine test facility designed to simulate many of the combustion features that are common between an internal combustion engine, a gas turbine combustor and a steel rolling furnace. High bandwidth in-cylinder surface temperature measurements are demonstrated with a new application of platinum thin film resistance thermometers. These gauges are exposed to the combustion gases and are mounted to both the cylinder head and piston. It is shown that calculation of flame speed, determination of heat flux levels and flame structure observation are possible. Fibre optic probes capable of high frequency spectral measurements of the combustion emission are presented. The spectral measurements are shown to complement the temperature measurement by being able to differentiate the flame front from the general combustion emission and hot by-products. Beyond this, other optical techniques have been explored in order to gain an understanding of the flame front and flow within the combustion chamber. The novel spark plug described is capable of combustion imaging and its application to in-cylinder PIV and flow visualisation is demonstrated. Combustion modelling has been undertaken using published engine models and a comparison between measured and predicted values of pressure and heat flux is provided as a validation of the in-cylinder heat flux measurements.

TABLE OF CONTENTS

INDEX OF FIGURES

ACKNOWLEDGEMENTS

I have many to thank for their support, encouragement and patience whilst undertaking the mammoth task of writing this thesis.

Who else can I start with other than my beautiful assistant – Wendy, my wife, who has only ever known me neck deep in a PhD! Thank you for enduring all those lonely evenings and weekends, for loving me, caring for me and feeding me…

Roy and Irene, my parents, who have never stopped believing I could pull this off.

My supervisor, Pete, and Brenda who have gone way beyond the call of duty in their unending support, help, proof reading and advice, throughout my many years at The University of Warwick.

To Paul, Phil and the other great guys in the OEL who have made every year at Warwick unforgettable.

To Huw and the others in micro engineering who can make the most incredible masterpieces from the off cuts.

To God who created me, gave me life and enabled me to perform this miracle. "I can do all things through Christ who strengthens me" (Philippians 4:13)

To Jubilee Church Coventry, my family, who have held me together and prayed for me 'without ceasing'.

LIST OF ABBREVIATIONS

2D	Two-Dimensional
3D	Three-Dimensional
a	Gauge thickness
AFR	Air Fuel Ratio
α	Temperature coefficient of resistance
ATDC	After Top Dead Centre (Degrees crank angle)
b	Engine bore
BDC	Bottom Dead Centre
BMEP	Brake Mean Effective Pressure
c	Specific heat
CAD	Crank Angle Degrees
CAI	Controlled Auto Ignition
CARS	Coherent Anti-Stokes Raman Scattering
Cblowby	Piston blowby constant
CCD	Charge Coupled Device
CFD	Computational Fluid Dynamics
CH_4	Methane
CO	Carbon monoxide
CO_2	Carbon dioxide
CRDS	Cavity Ring-Down Spectroscopy
DGV	Doppler Global Velocimetry
ε (eps)	Half stroke to rod ratio
EB	Energy Balance
ECP	Equilibrium Combustion Products
EGR	Exhaust Gas Recirculation
f	Frequency, focal length or residual fraction
FARG	Fuel Air Residual Gas
FTIR	Fourier Transform InfraRed spectroscopy
GDI	Gasoline Direct Injection
GMcB	Gordon and McBride airscheme
GRIN	GRaded INdex
h	Heat transfer coefficient
H(s)	Transfer function
h(t)	Impulse response function
H_2	Hydrogen
H_2O	Water
HC	Hydrocarbons
hcb	Burned region heat transfer coefficient
HCCI	Homogeneous Charge Compression Ignition
hcu	Unburned region heat transfer coefficient
HWA	Hot Wire Anemometry
I	Characteristic length

IC	Internal Combustion
iCCD	Intensified Charge Coupled Device
ICLAS	IntraCavity Laser Absorption Spectroscopy
IMEP	Indicated Mean Effective Pressure
IR	InfraRed
K	Kelvin
k	Thermal conductivity
$\mathscr{L}$	Laplace function
L2F	Laser two focus
LDA	Laser Doppler Anemometry
LHI	Laser Holography Interferometry
LIF	Laser Induced Fluorescence
m	mass
mfb	Mass Fraction Burned
N	Number of samples
N_2	Nitrogen
N_2O	Nitrogen dioxide
NGV	Nozzle Guide Vance
nm	Nanometer
NO_x	Oxides of Nitrogen
O_2	Oxygen
OH	Hydroxyl
p	Pressure
ρ	Density
ϕ (phi)	Equivalence ratio
p1	Initial pressure
PIV	Particle Image Velocimetry
pLIF	Planar Laser Induced Fluorescence
PTV	Particle Tracking
q	Heat flux
r	Compression ratio
RPM	Revolutions Per Minute
s	Engine Stroke
SI	Spark Ignition
SPIV	Stereoscopic Particle Image Velocimetry
T	Temperature
t	time
T1	Initial temperature
TDC	Top Dead Centre
θ_s (theatas)	Start of burn
θ_b (thetab)	Burn duration
T_w	Surface temperature
UPI	Environmental Prognosis Institute
US	United States
UV	UltraViolet
V	Volume
v	Velocity
v_n	Mole fraction of given species
x_b	Mass Fraction Burned

RELATED PUBLICATIONS

T. S. Wilson, P. Bryanston-Cross, K. S. Chana, P. Dunkley, T. V. Jones & P. Hannah (2002) Combustion & Flow Diagnostics (Part A&B). "**High Bandwidth Heat Transfer and Optical Measurements in an instrumented Spark Ignition Internal Combustion Engine**". SAE paper 2002-01-0747, Presented at SAE 2002 World Congress, SAE, Detroit. (Appendix B)

K.S. Chana, **T. S. Wilson**, M. Burnett, P.J. Bryanston-Cross & T.V. Jones (2001) "**High-bandwidth heat-transfer measurements in an internal combustion engine under low load and motored conditions**". Presented at the Applied Vehicle Technology Panel: Symposium on Advanced Flow Management, Leon, Norway. (Appendix C)

PART I

THE REQUIREMENT

CHAPTER 1

INTRODUCTION

1.1 Background

The need exists to more fully understand the combustion process, be that in a Gas Turbine or Internal Combustion engine. The project began with the formation of the INTErSECT Faraday project, "The Application of Data Fusion to a Multi-Sensored Intelligent Engine" [1], that sought to develop novel instrumentation for application to the internal combustion and gas turbine engines in order to assist engine designers and developers gain a more complete understanding of the behaviour of the combustion.

An important aspect of the project was the ability to test and evaluate new instrumentation for studying combustion. For this, the internal combustion engine was chosen over the gas turbine due to the similar combustion temperatures and pressures, yet the internal combustion engine affords more convenient access to the combustion zone and may be easily bench tested, unlike gas turbines that are only available in industry and are therefore unsuitable for lengthy development work.

A small, fully contained, bench-top, low-cost, single-cylinder test facility was built for this purpose. It is illustrated in Figure 1.1 and described in Appendix A.

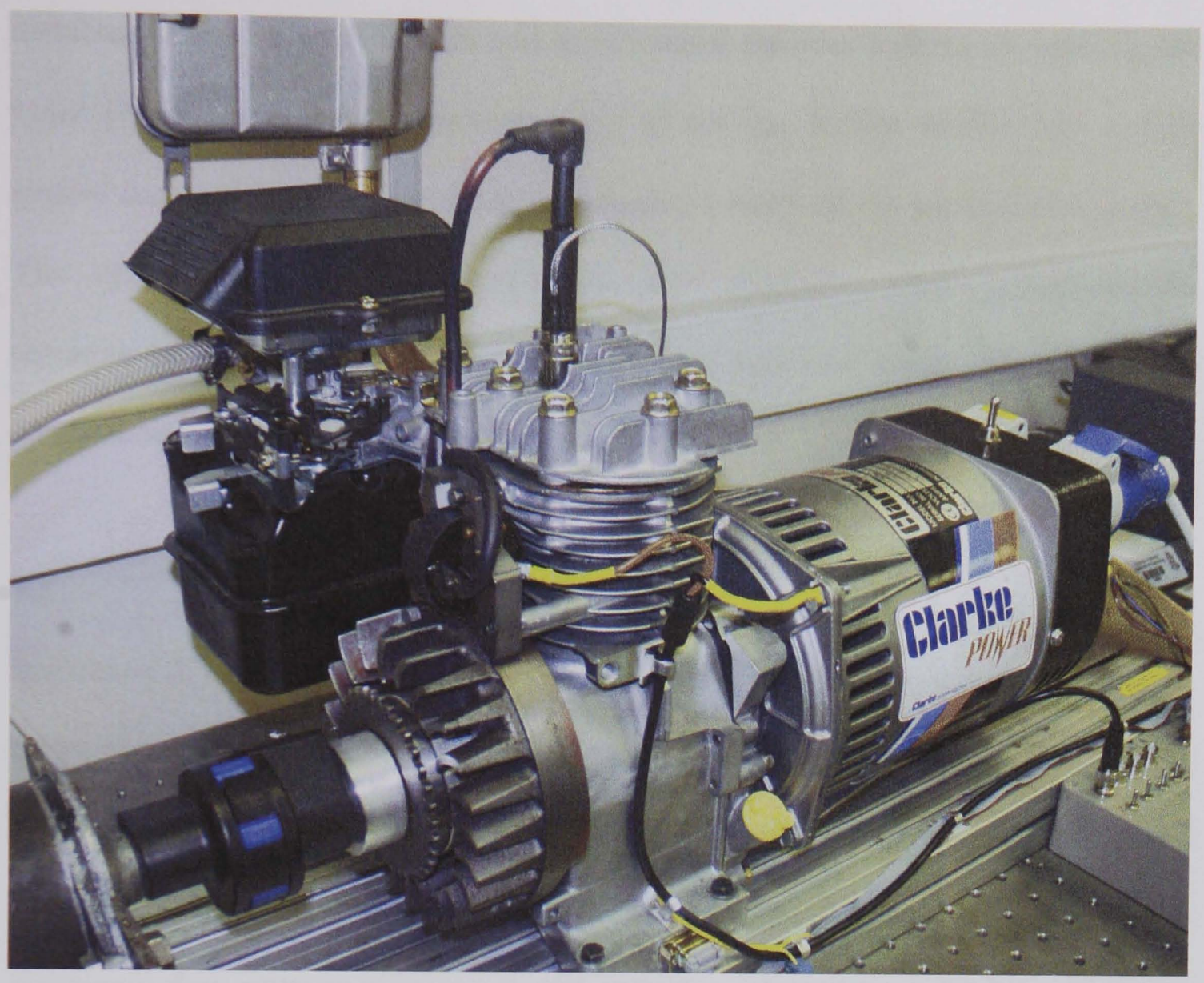

Figure 1.1, Photo of 'bench-top' internal combustion engine test rig.

This thesis concentrates on the novel application of two experimental techniques to the Internal Combustion Engine, namely fast response thin film gauges and optical sensors.

1.2 Aims and Objectives

The aim of this work is to provide improved experimental techniques that will assist in gaining an understanding of the processes at work within the internal combustion engine. These techniques will be useful not only for designers of the internal combustion engine, but also for validation of computational models of internal combustion engine combustion and flows. At the same time the work demonstrates the relevance and usefulness of the techniques themselves to areas they have not been applied before. The heat flux measurements show how thin film gauges, previously

restricted in use to wind tunnels and experimental facilities looking at nozzle guide vanes (NGVs) and the compression stage of the gas turbine engine, can also be applied successfully to the harsh and hostile environment of the combustion chamber. The optical measurements demonstrate how relatively simple measurements, requiring very little modification to the engine can yield useful information on engine combustion.

1.3 Thesis Outline

In Chapter 2, the processes involved in combustion are described showing that surface temperature and species presence must be measured. Chapter 3 then gives a discussion of literature on relevant measurement techniques that are currently in use in both the internal combustion and gas turbine engines. It covers optical and other techniques that measure flow speed and velocities, chemical composition of flames and pressure measurements. The following chapter (Chapter 4, Review of heat flux instrumentation) continues to describe in greater depth the techniques that are currently in use for heat flux determination in combustion. Many of these techniques are still in the research and development stage, and not yet recognised as established experimental techniques. The literature survey provided in these chapters identifies not only the difficulties and pitfalls experienced in combustion measurement, but also identifies a current gap in instrumentation. It was decided to address this gap with both high bandwidth temperature measurements and the optical flame measurements, while learning from published experiences.

Experimentally, the thesis concentrates on two measurement techniques, surface temperature measurement and optical measurements. An understanding of heat

transfer from the combustion to the piston and chamber walls is essential for piston design, coolant jacket design and combustion modelling. Furthermore it is also crucial for emission control as combustion temperature and heat transfer rates define wall temperatures that in turn have a significant effect on emissions, e.g. a few degrees change in wall temperature gives a large percentage change in oxides of Nitrogen (NO_x) and un-burnt hydrocarbons (HC) [2]. However, existing techniques can only measure heat fluxes at low frequency. The new techniques presented enable localised high bandwidth heat flux measurements that help give a combustion understanding by recording the turbulent temperature fluctuations. A discussion of the thin film gauge construction and the heat flux processing are presented in Chapter 5, Heat flux theory.

Attention shifts in Chapter 6 to the optical aspects of the project where the development of an optical spark plug for flow and combustion imaging is described. Experience from industrial partners has demonstrated the reality that large modifications are required to engines in order to gain useable optical data. The optical measurement techniques described therefore hold the potential to be a simple bolt on conversion for an existing engine, either for research and development work, fault finding or even a permanently installed dialogistic tool. Following in Chapter 7, the development of other non-imaging optical probes are described. Such probes are used to extract flame speed and spectral information from the combustion event.

Results are contained in the four chapters starting from Chapter 8. First results from the optical probes are presented, including flow visualisation, PIV and spectral measurements. Next, in Chapter 9 (Temperature and heat flux results), typical in-cylinder temperature and heat flux results are presented and discussed. Following

these individual results chapters, the information gathered from the optical and temperature measurements is combined in Chapter 10 to illustrate some possible data processing routes available from such measurements. Finally in Chapter 11 the heat fluxes measured within the cylinder are compared to those calculated using a two-zone computer model.

The conclusions and further work chapter completes the thesis by summarising the knowledge obtained with the new techniques and proposes the direction of further investigation.

In summary, the thesis divides into five parts. Part One presents the context and is followed with a review of existing combustion measurements in Part Two. In Part Three, the development of novel instrumentation is described. The results are presented in Part Four, and finally in Part Five, the effectiveness and benefits of these new techniques are summarised and suggestions for further development are set forward.

1.4 Novel Contribution

Simultaneous temperature and optical measurements have been performed in an internal combustion engine. It has been shown that the temperature gauges are spectrally insensitive and the optical measurements only qualitative; therefore although both techniques are valuable individually, the use of both techniques together leads to a more complete understanding of the combustion event.

1.4.1 High Bandwidth Heat Flux Measurements

The temperature measurements and heat flux determination in the internal combustion engine form a new application of existing thin film temperature gauges. Through this novel application a new route for the study of flame structure within the internal combustion engine is provided. The use of thin film gauges has enabled simultaneous high frequency heat flux measurements to be made at several localised points within the cylinder combustion zone. This is a step forward from existing techniques since the high frequency temperature measurements follow more accurately the surface temperatures. In addition, several gauges instrumented in a ray from the spark plug permit flame and structure tracking.

1.4.2 Optical Measurements

The use of multiple optical probe positions, the post-processing of the data, the flame speed information and the determination of the spectral content of the flame are all novel techniques. In addition, the development of a spark plug for combustion imaging provides a simple, bolt on, new optical accessory for any internal combustion engine.

Additionally it has been shown that both the temperature and optical measurements indicate similar flame speeds and structures.

PART II

REVIEW OF CURRENT TECHNOLOGY

CHAPTER 2

REVIEW OF COMBUSTION

2.1 Overview

An Internal Combustion Engine is defined as an engine in which the chemical energy of the fuel is released inside the engine and used directly for mechanical work, as opposed to an external combustion engine in which a separate combustor is used to burn the fuel. [3]

This chapter looks at the basics of combustion; first discussing the processes involved in the release of energy from the fuel, then both the ideal and real cycles within the Internal Combustion Engine.

2.2 Combustion

Combustion and its control are very important for our existence on this planet, and is essential for our current standard of living. In the United States (US) in 1996, approximately 85% of the energy used came from combustion sources [4]. Generation of electricity is primarily from combustion: again in the US in 1996, only 10.8% of electricity was generated from hydroelectric and 21.9% from nuclear sources, while the balance was obtained from oil, gas and coal combustion [4]. It is doubtless that we are and will be dependent for some time on combustion as our primary energy source.

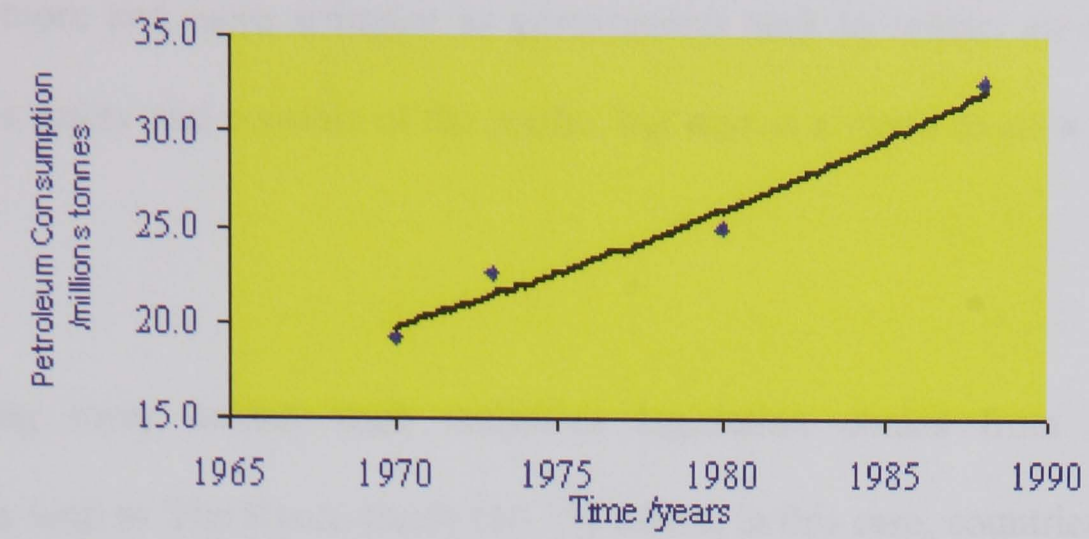

Figure 2.1, Increase in UK Petrol Consumption 1970-1988, (Reproduced from [5])

Traffic consumes 60% of worldwide oil consumption. The total petroleum demand for Europe has quadrupled since 1960, doubled in the USA and increased sixfold in the Pacific, Figure 2.1 shows how petrol consumption for traffic use in the UK alone has increased in the 20 years from 1980. The Environmental-Prognoses-Institute (UPI) in Heidelberg, Germany, estimates that under a 'business-as-usual' scenario the worldwide fuel consumption will double within the next thirty years [6]. It is obvious therefore not only that we are very dependent upon fossil fuel combustion as an energy source, but also our consumption of that fuel is increasing at a high rate.

Apart from the fuel sources being limited, another problem with using combustion is that by-products of combustion cause environmental problems. Emission controls started to be introduced in the mid-60's following the smog problems that began to affect large urban areas such as Los Angles or Tokyo in the 1940's. This was due to sunlight driven reactions involving NOx and HCs from automotive exhaust emissions [7]. As a result emission standards were introduced which forced the installation of emission control devices [8]. There have been various studies performed into

identifying and reducing exhaust emissions [9]. However, emission legislation is still becoming more and more stringent as governments seek to reduce air pollution not only for the safety and comfort of the public, but also in a move to slow down global warming.

The driving force behind such emissions legislation comes from international agreements such as The Kyoto treaty [10,11] where, in this case, countries responsible for more than 55% of the world's carbon emissions set an "ultimate objective" of stabilising "greenhouse gas (carbon dioxide CO_2, methane CH_4, and nitrous oxide N_2O) concentrations in the atmosphere to a level that would prevent dangerous anthropogenic (human-induced) interference with the climate system." The practical outworking of the treaty is that governments will encourage, through taxation or legislation, the redesign of products such as refrigerators, automobiles, cement mixes, and fertilisers so that they produce lower greenhouse gas emissions.

Therefore, minimising fuel consumption and emission of greenhouse gasses is essential as long as we remain dependent upon carbon based energy sources, such as fossil fuels, for our lifestyle. The work of this thesis concentrates on the development of new techniques that will enable designers of internal combustion engines to improve and develop new engines using new combustion strategies at higher efficiency and/or causing less environmental damage.

2.3 Mechanisms of Combustion

Webster's Dictionary defines combustion as "*rapid oxidation generating heat, or both light and heat; also, slow oxidation accompanied by rather little heat and no light.*" In

this description however we will only consider the rapid oxidation as in reality this is the more common process, and the process present in the internal combustion engine.

There are two basic modes of combustion: flame and non-flame modes. Flames in turn, are categorised as being either premixed flames or nonpremixed (diffusion) flames [12,13]. Stephen Turns provides a good explanation of each mode and flame type in his book, "An Introduction to Combustion" [4]. It is summarised here.

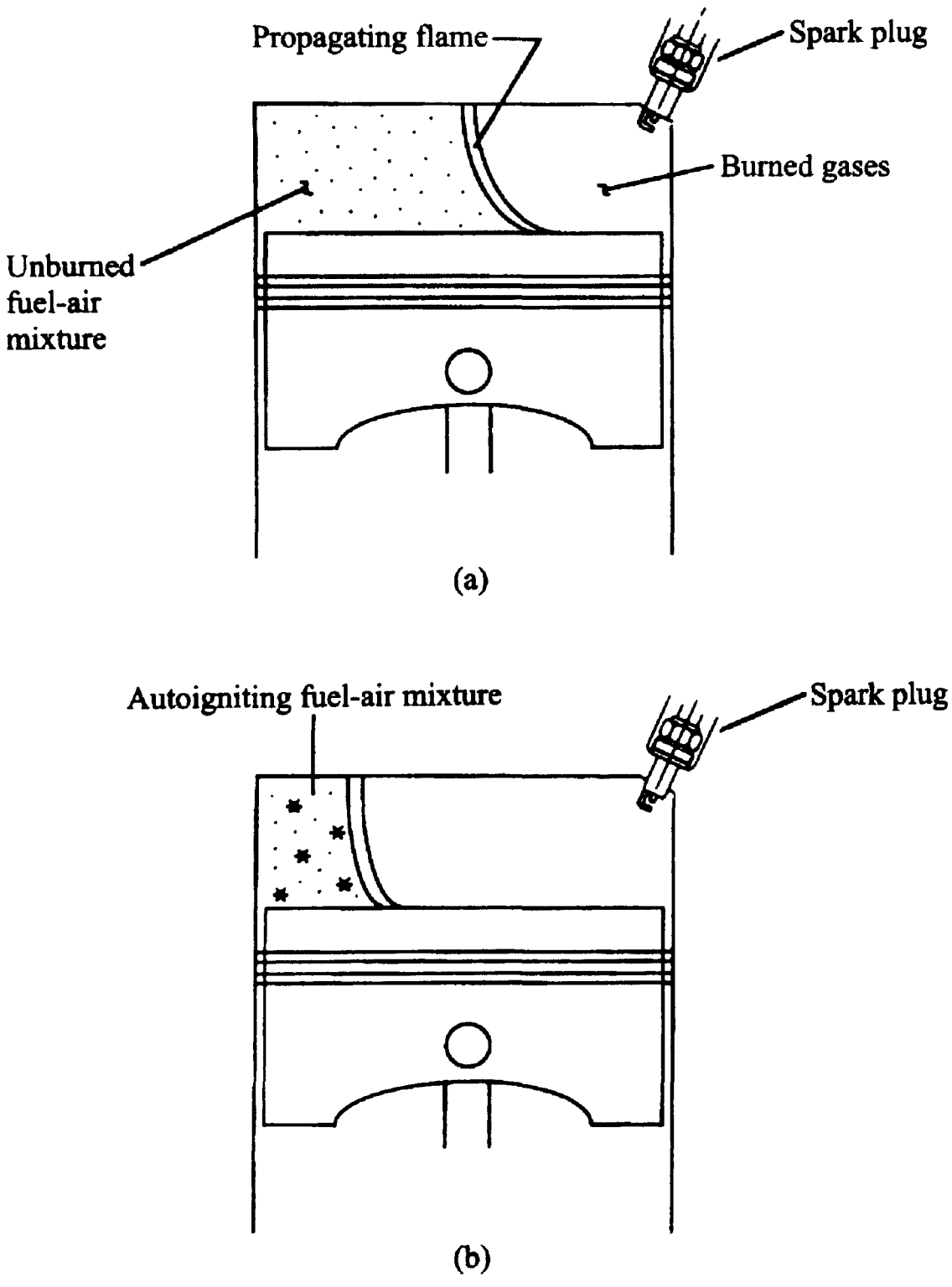

Figure 2.2, (a) flame and (b) nonflame modes of combustion in a spark ignition engine. (Reproduced from [4])

The difference between flame and nonflame modes of combustion can be illustrated by considering a knocking spark-ignition engine, Figure 2.2. In Figure 2.2a, we see a thin zone of intense chemical reaction (the flame) propagating across the unburned fuel-air mixture. Behind the flame, the hot gasses are the by-products of combustion. As this flame propagates across the cylinder, it causes the temperature and pressure to rise in the unburned mixture. If the temperatures and pressures rise too much for the particular fuel and mixture ratio, rapid oxidation reactions (nonflame combustion) occur at many locations within the unburned gas, leading to very rapid combustion throughout the volume, Figure 2.2b. This essentially volumetric heat release is called autoignition, and the very rapid pressure rise leads to the characteristic sound of engine knock.

Note that the flame itself is not causing combustion, rather if it occurs, is a product of combustion. Even within an internal combustion engine, given certain conditions, combustion can occur with no flame. This is called autoignition and unless carefully controlled will cause high emissions and rapidly destroy an engine due to the high rates of pressure rise. Typically an internal combustion engine will be fuelled and ignited in such a way to avoid autoignition or knock. Current research is on going into what is commonly called Controlled Auto Ignition (CAI) or Homogeneous Charge Compression Ignition (HCCI) where this autoignition is carefully controlled in a manner that improves efficiency and reduces emissions. The improved efficiency is a result of the rapid combustion resulting in an engine cycle much closer to that of the ideal Otto cycle. CAI or HCCI can only occur in premixed fuel and when combustion starts, it begins at multiple points within the chamber and all the fuel burns over approximately 10° crank angle (CA), therefore there is no flame boundary or edge,

which in turn is the cause of the reduced emissions as the in-cylinder temperatures are lower.

The flame class, premixed or nonpremixed (diffusion), is related to the state of mixedness of the reactants. Historically spark-ignition engines operate on fuel that is premixed at molecular level (that is the fuel is mixed as a vapour, not as droplets) before entering the combustion chamber, resulting in the premixed flame mode. In a nonpremixed flame, the reactants are initially separated, and the reaction occurs only at the interface between the fuel and oxidiser, where mixing and oxidisation both take place. An example of a diffusion flame is a simple candle.

Typically premixed and diffusion flames may both be present in various degrees. Diesel engine combustion for example is generally considered to have significant amounts of both premixed and diffusion burning.

For understanding combustion and improving the environmental effects of IC engines, it is essential to gain a better understanding of the chemical mechanisms of combustion. There have been various attempts to detail the chemical mechanisms, for example [14-16]. The GRI-mechanism is particular [15] considers 53 species and 325 mechanisms, including NOx chemistry during methane combustion and is available for download through the internet. Each attempt at detailing the chemical reactions of combustion seeks to follow the reactions starting with the fuel and working through to the by-products of the combustion. For an example of the chemical reactions of natural gas combustion in Oxygen see Figure 2.3.

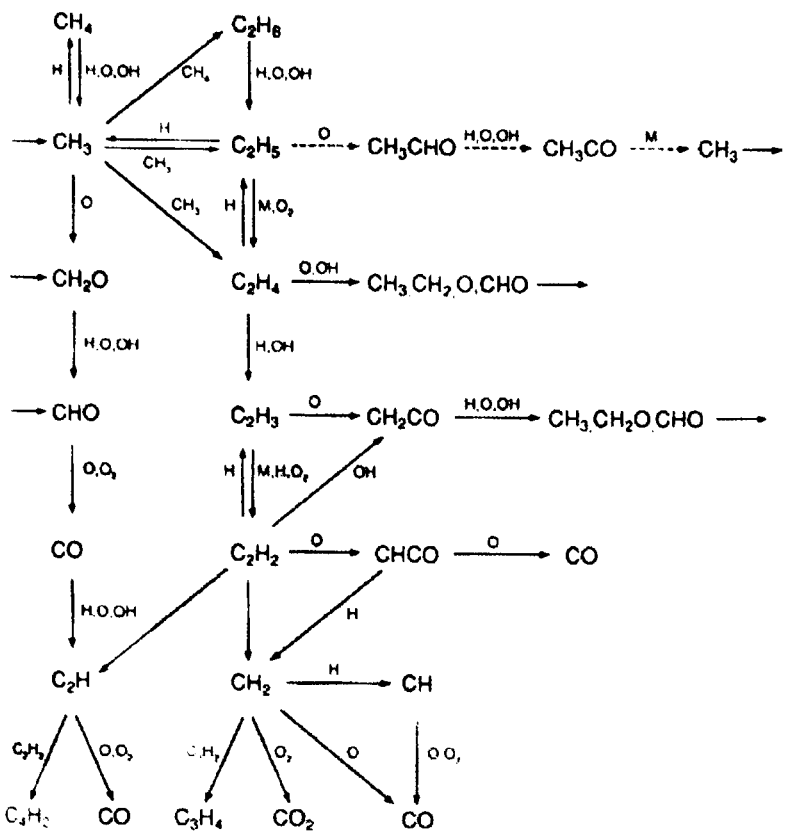

Figure 2.3, Chemical reactions of CH_4 combustion in O_2.

2.4 Light Emission During Combustion

A striking feature of most combustion processes is the emission of light that occurs with both flame and non-flame combustion. Early investigations of the type and quantity of light emitted by flames identified that each fuel and each burning condition have their own characteristic spectrum, and that these may be distinguished purely based on the emitted light spectrum [12,13].

Although the emitted light (visible and ultraviolet) is only a small proportion of the energy released by the flame, and this radiation in turn comes from the very small fraction of the molecules that are electronically excited, the emission of light is probably the most distinctive single property of a flame. Studies of the light emission of flames have supported theories, based on chemical kinetics, that there exist chain reactions within a flame [13]. These are initiated by the formation and breakdown of peroxides and are propagated by reactions of radicals such as Hydroxide (OH) with

fuel and oxygen. It is from theories such as these that it is possible to use radicals such as OH to identify the reaction zone and 'flame front' in the combustion of an IC engine.

For more information, a fair summary of the reaction processes within flames is given by Gaydon in his book, "Spectroscopy of Flames" in Chapter 10 [12].

2.5 Internal Combustion Engines

Internal combustion engines were conceived and developed in the late 1800's and now have been developed to a high level of refinement and efficiency. They can deliver power from 0.01 kW to 20 $x10^3$ kW, however, in the majority they are produced for vehicular applications (where power is of the order of 10^2 kW)

In the automotive sector, they are the primary power source due to the relatively low cost, favourable power to weight ratio, sufficiently high efficiency and relatively simple and robust operating characteristics.

2.5.1 Principles of Operation

A spark ignition, internal combustion, 4-stroke engine operates in a cycle consisting of 4 phases: induction/intake, compression, power and exhaust. The four phases require two complete revolutions of the engine. Most measurements are relative to crank angle; this is because crank angle is a useful independent variable since engine processes occupy almost constant crank angle intervals over a wide range of engine speeds [17]. 0° CA is said to occur at top dead centre (TDC) before the power stroke, 180° CA is therefore bottom dead centre (BDC) before the exhaust stroke, 360° CA is

TDC before intake, 540° CA is BDC before compression and 720° CA, being the same as 0° CA, is TDC after compression and before power, as is shown in Figure 2.4.

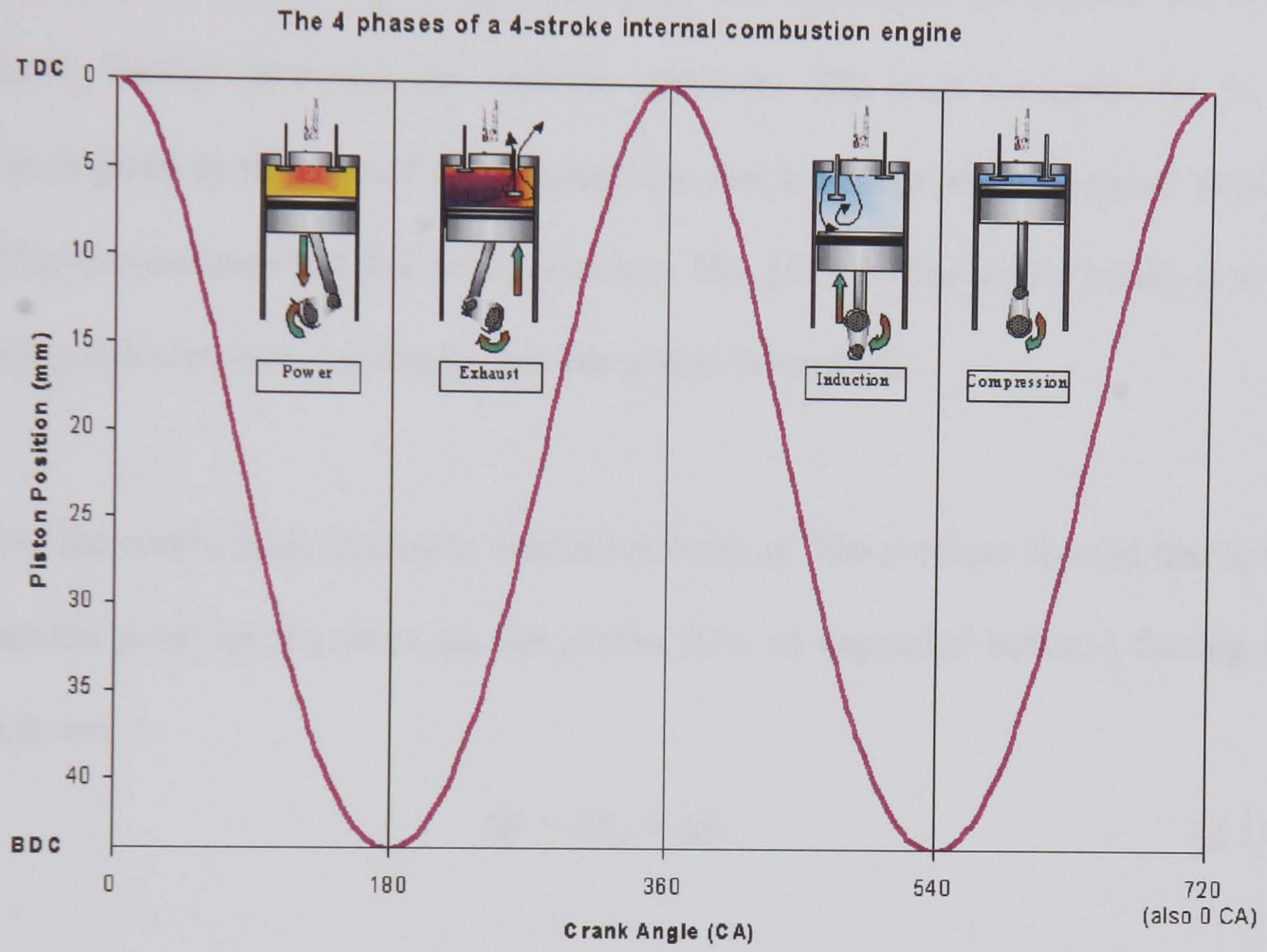

Figure 2.4, The four phases of a four-stroke internal combustion engine.

During intake, the inducted fuel and air mix in the cylinder with the residual burned gasses remaining from the previous cycle. After the intake valve closes, the cylinder contents are compressed to above atmospheric pressure and temperature as the piston moves upwards reducing the cylinder volume. Some heat transfer to the piston, cylinder head, and cylinder walls occurs but the effect on unburned gas properties is modest [17].

Just before the compression stroke is completed, a discharge from the spark plug generates a turbulent flame that propagates across the mixture of air, fuel and residual burnt gas in the cylinder, and extinguishes at the combustion chamber wall. The duration of this burning process varies with the engine design and operation, but is typically 40 to 60 crank angle degrees (CAD). The burning of the fuel-air mixture in the flame, further increases the cylinder pressure. The total pressure rise in the cylinder is given as the sum of the pressure rise due to compression by piston motion, ΔP_v, plus the pressure rise due to combustion, ΔP_c, [18]. In this power phase, it is the increasing cylinder pressure that pushes the piston downward.

In effect the combustion process is controlled burning. The pressure created due to the combustion provides the force on the piston (like an expanded balloon) forcing the piston down.

$$\Delta P = \Delta P_c + \Delta P_v \tag{2.1}$$

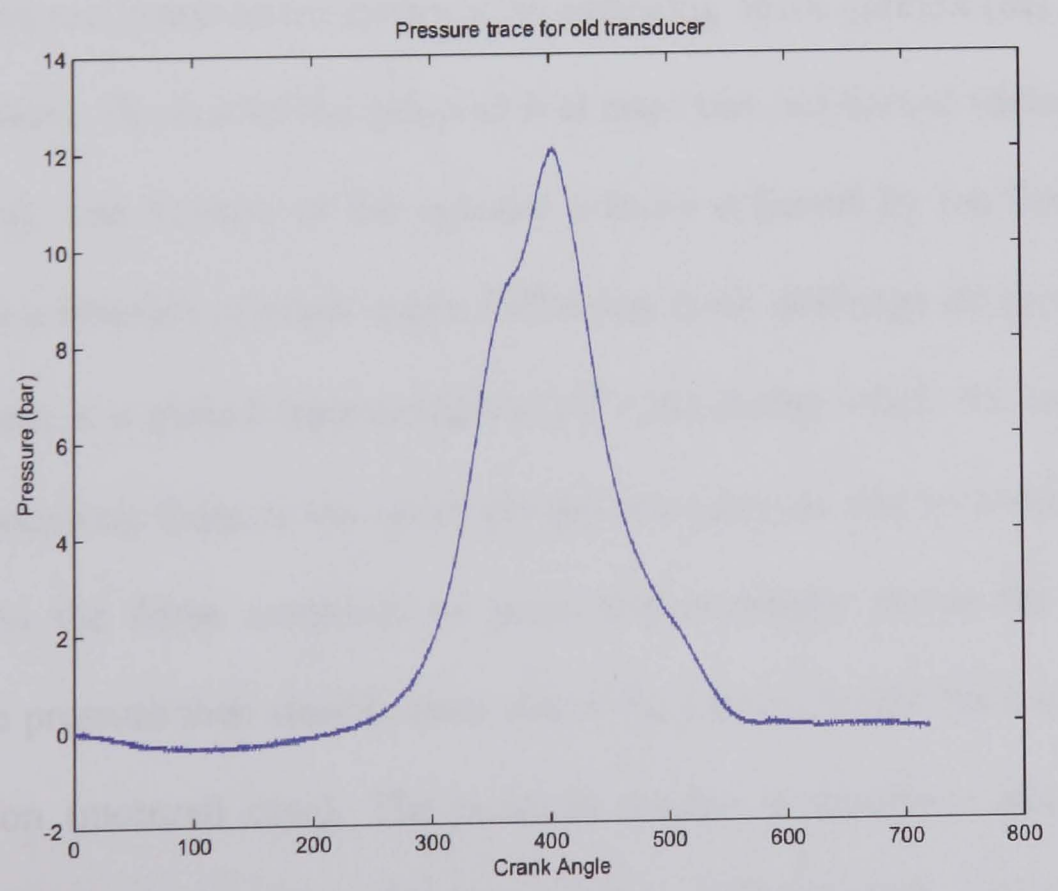

Figure 2.5, Pressure trace as recorded during experiments.

Note that due to differences in the flow pattern and mixture composition between cylinders, and within each cylinder cycle-by-cycle, the development of each combustion process differs somewhat. As a result, the shape of the pressure versus crank angle curve in each cylinder is not exactly the same, Figure 2.6. [17]

The pressure in the cylinder initially increases during the expansion stroke due to the heat addition from the fuel, and then decreases due to the volume increase. The indicated mean effective pressure (IMEP) is the net work per unit displacement volume done by the gas during compression and expansion and can be calculated from integrating the pressure trace [3]. The brake mean effective pressure (BMEP) is the external shaft work per unit volume done by the engine and is measured with a dynometer or similar attached to the engine.

Additional features of the combustion process are evident from the data in Figure 2.6, taken from several consecutive cycles of an operating spark ignition (SI) engine. The cylinder pressure, fraction of the inducted fuel mass that has burned (determined from pressure data), and fraction of the cylinder volume enflamed by the flame front are shown, all as a function of crank angle. Following spark discharge (at approximately -30° CA), there is a period (approximately 20° CA) during which the energy release from the developing flame is too small for the pressure rise due to combustion to be discerned. As the flame continues to grow and propagate across the combustion chamber, the pressure then steadily rises above the value it would have in the absence of combustion (motored case). The pressure reaches a maximum after Top Dead Centre (TDC) but before the cylinder charge is fully burned, and then steadily

decreases as the cylinder volume continues to increase during the remainder of the expansion stroke.

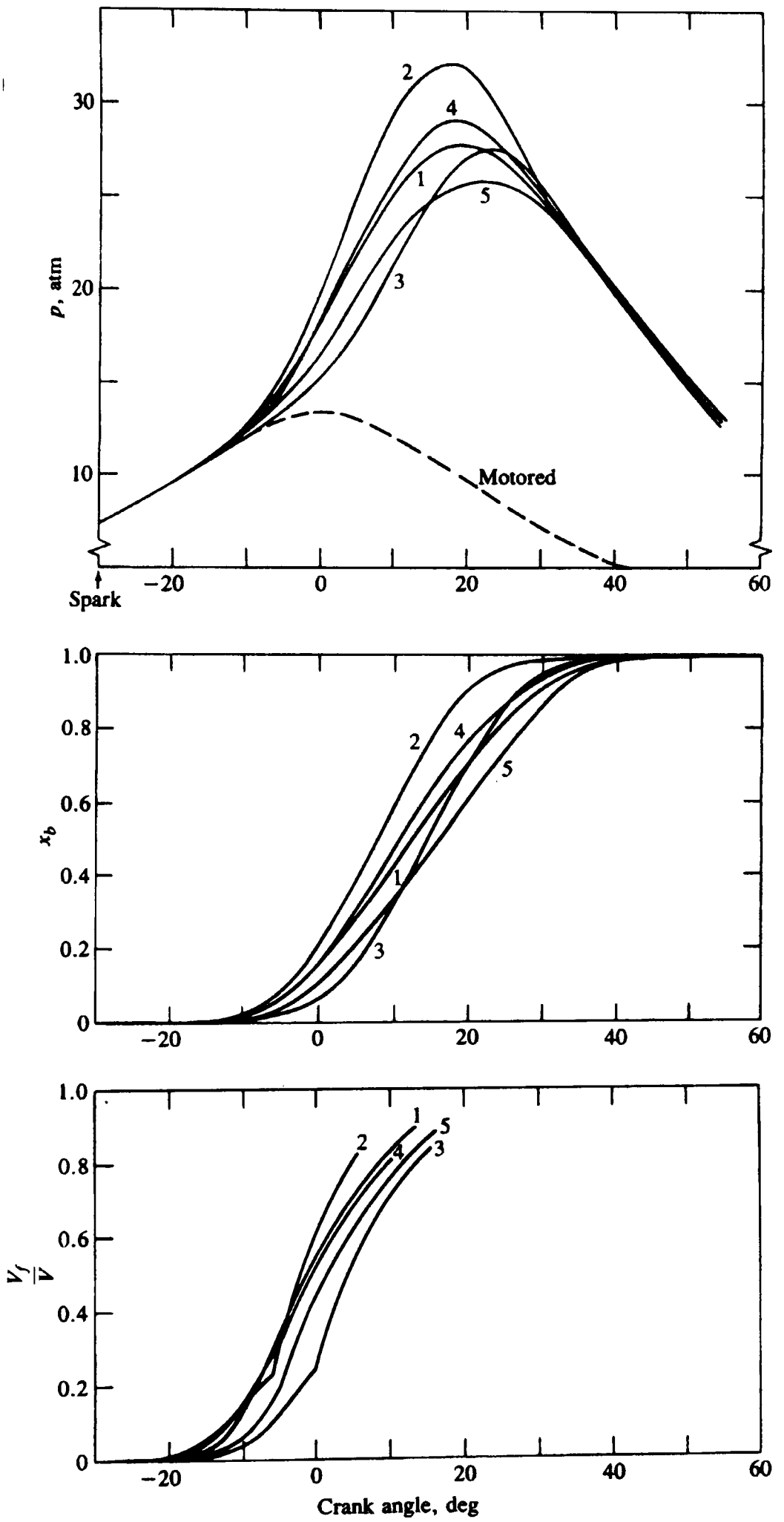

Figure 2.6, Variations in pressure (p), mass fraction burned (x_b) and fraction of cylinder enflamed (V_f/V) by flame front over several consecutive cycles: 1,2,3,4 and 5. (Reproduced from [17])

The flame development and the subsequent propagation vary considerably cycle-to-cycle, as can be seen from the significant variation in the shape of the pressure, volume fraction enflamed, and mass fraction burned curves between each cycle. This is because flame growth depends on local mixture motion and composition. These quantities vary in successive cycles in any given cylinder. Especially significant are the mixture motion and composition in the vicinity of the spark plug at the time of spark discharge since these govern the early stages of flame development.

Note that the fraction of the enflamed volume rises more quickly than the fraction of the burned mass. In large part, this is because the density of the unburned mixture ahead of the flame is about 4 times the density of the burned gasses behind the flame: even when the entire combustion chamber is almost fully enflamed, some 25% of the fuel mass is still unburned.

Based on this description, the combustion process is divided into 4 distinct phases [17]: (1) spark ignition; (2) early flame development; (3) flame propagation; and (4) flame termination.

2.5.2 Ideal Cycles

The Otto cycle is the ideal internal combustion engine cycle and considers the special case of an engine where the addition of heat is so rapid that the piston is assumed not to have moved during the burning of fuel and therefore is at constant volume. The working fluid in the Otto cycle is assumed to be an ideal gas and so the four basic processes are isentropic compression (1 to 2), constant volume heat addition (2 to 3),

isentropic expansion (3 to 4), and constant volume heat rejection (4 back to 1), Figure 2.7.

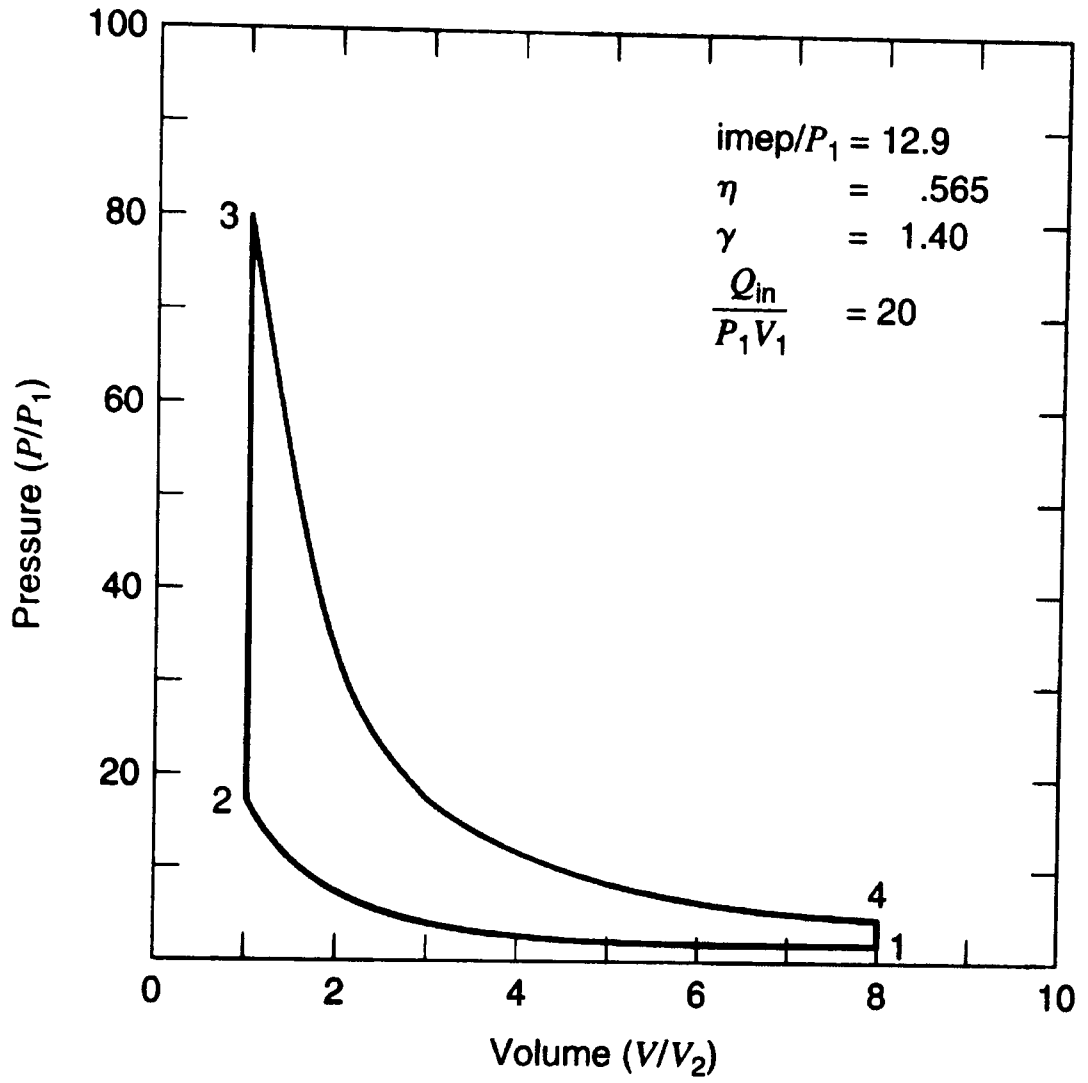

Figure 2.7, The Otto cycle. (Reproduced from [3]), showing compression (1 to 2), heat addition (2 to 3), expansion (3 to 4) and heat rejection (4 back to 1).

The Otto cycle assumes that [2]:

1. air behaves as a perfect gas with constant specific heat capacity, and all processes are fully reversible
2. there is no induction or exhaust process, but a fixed quantity of air and no leakage
3. heat addition is from an external source, in contrast to internal combustion
4. to complete the cycle heat rejection is transferred to the environment, as opposed to an exhaust stroke

However, in reality internal combustion engines operate on a non-optimised thermodynamic cycle with additional strokes to facilitate the gas exchange. It is necessary therefore to use idealised Figure 2.8 and stylised Figure 2.9 indicator diagrams for a four-stroke engine. An idealised indicator diagram takes the ideal Otto cycle and includes the induction and exhaust cycles, however, induction (0 to 1) is assumed to occur with no pressure drop, the compression and expansion (1 to 2 and 3 to 4) are not adiabatic and so neither are they isentropic, and combustion is assumed to occur instantaneously at constant volume (2 to 3). Finally, when the exhaust valve opens, the exhaust is assumed to instantly pass into the exhaust manifold (4 to 1) and the exhaust stroke occurs with no pressure drop (1 to 0). This idealised 4-stroke cycle is used for the simplest of computer models.

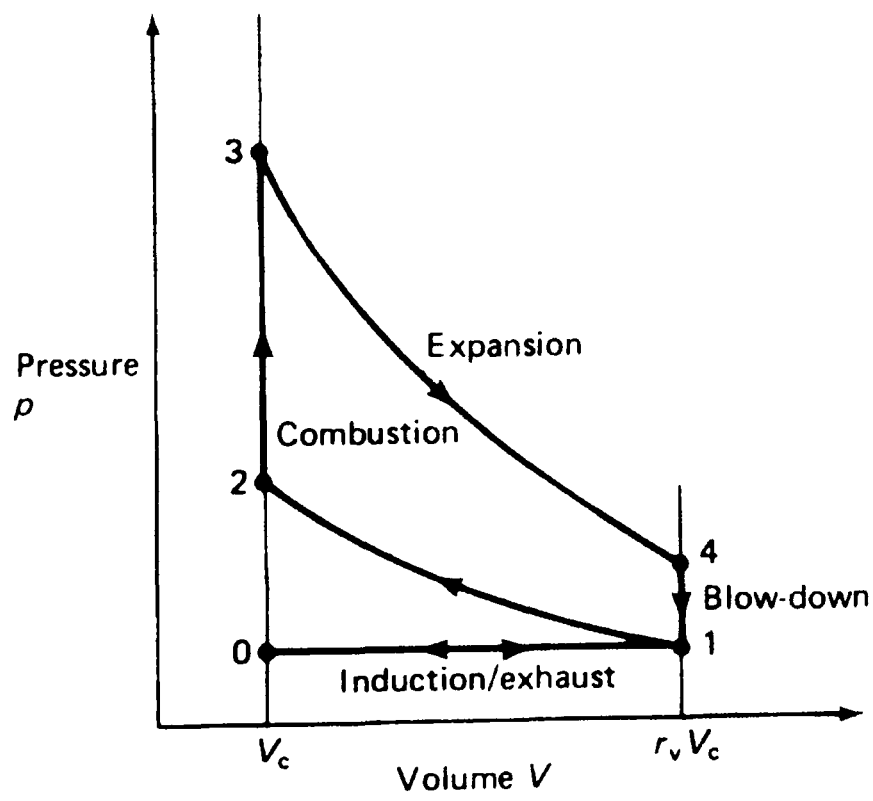

Figure 2.8, Idealised indicator diagram. (Reproduced from [2])

The stylised indicator diagram is generated from real pressure measurements and is shown Figure 2.9 with an exaggerated pressure difference between induction and exhaust strokes. The area enclosed between these two gas exchange strokes (A_2)

represents negative work done, termed pumping losses, and must be subtracted from the positive work done given by the area enclosed between the other two strokes (A_1).

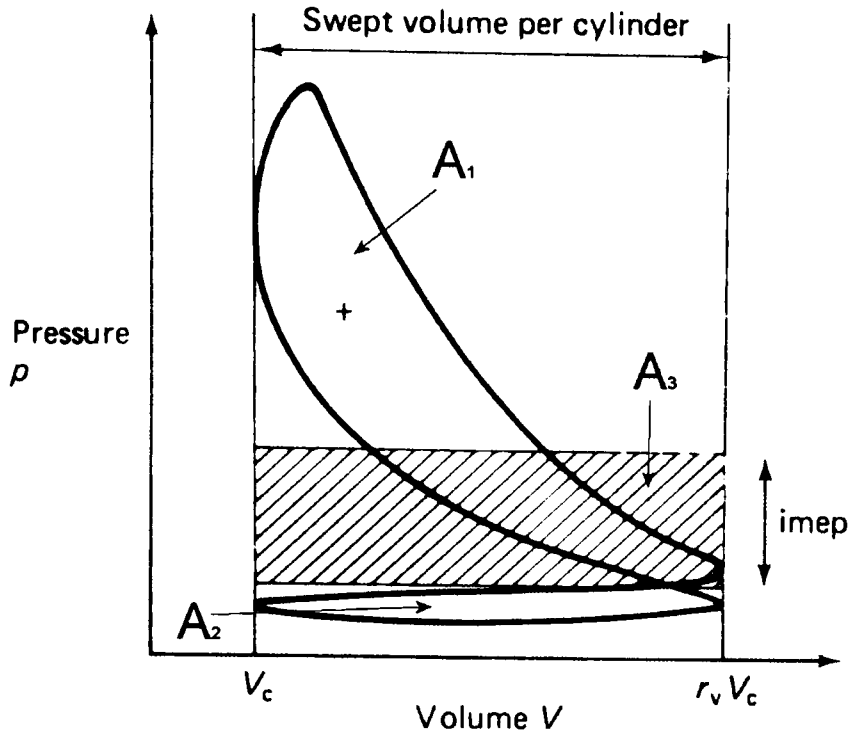

Figure 2.9, Stylised indicator diagram. (Reproduced from [2])

The indicated work output for a given swept volume in a cycle is called the indicated mean effective pressure (IMEP). This is the work done on the piston due to the pressure rise, however all of this work is not removed from the engine as useful energy due to losses. The shaded area (A_3) in Figure 2.9 is equal to the net area enclosed by the pressure trace $(A_1 - A_2)$, and therefore the height of this shaded area represents the IMEP since it has the same volume scale as the indicator diagram $\left[IMEP = \left(\frac{A_1 - A_2}{\text{Displaced Volume}}\right)\right]$.

2.5.3 Real Cycles

The Otto cycle is highly idealised. In real engines combustion cannot be conducted at constant volume, i.e. instantaneously at TDC. In reality, the burning process takes time since the period of heat release exists over a burn duration; after the spark plug

ignites the mixture no pressure rise is seen for a delay period of about 10° crank angle. The resulting mass fraction burned curve has an exponential profile, and all the while the piston keeps moving and the cylinder volume is changing. It is accepted that if the piston could be held stationary at TDC while combustion takes place and then moving it down the power stoke when all is burned (closer to ideal cycle), the IMEP and power would increase. Some suggest by as much as 50% [19].

Attempts have been made to reduce NO_x levels and improve fuel consumption by running engines with lean combustion; however, one disadvantage of lean operation is the reduced burning rate over stoichiometric combustion. (Stoichiometric air fuel ratio (AFR) is the AFR where all the fuel burns completely using all the cylinder air.) This burning rate reduction results in an increase in the overall combustion duration, which in turn leads to increase heat transfer losses to the cylinder walls and a decrease in the overall thermal efficiency [20].

One factor that is known to affect burning rate is the in-cylinder turbulence. Turbulence causes a distortion or wrinkling of the flame front that increases the flame front area and thus the burning rate. Various methods of controlling the turbulence are used; including swirl induced by the inlet port shape and piston squish during compression. Flame imaging is a useful tool for observations on the effect of turbulence and swirl on burning rate. The challenge to any measurement technique is meeting the spatial-temporal envelope within the combustion event; in other words, the flows and processes within the combustion chamber are varying significantly over a very large area both locally and regionally, plus are changing at a very high frequency. If one sought to image the entire chamber at a resolution that enabled

determination of the small-scale turbulence, this is nearly impossible with today's technology, and that is before one considers the frame rate that would be required which in itself is nearly impossible given today's technology. Hence the need for complex data and statistical analysis, commonly termed Data Fusion.

Heat transfer calculations within internal combustion engines have become increasingly important with the drive towards higher efficiencies and cleaner exhaust emissions. Although internal combustion engines have been studied for many years, combustion chamber temperature and heat transfer rates have been investigated to a lesser extent.

As an example of the importance of an understanding of in-cylinder heat transfer, consider that during a combustion cycle the peak gas temperature can reach levels around 2500 Kelvin (K). Metal components of the combustion chamber can withstand approximately 600 K for cast iron and 500 K for aluminium alloys [21]. Hence, cooling of the cylinder head, block and piston is required. Heat flux levels experienced in a combustion chamber vary both spatially and periodically and reach levels as high as several MW/m^2. Indeed this can lead to local regions with high thermal stresses resulting in cracking of the components. Furthermore, lubrication of the cylinder walls is achieved with a film of oil that will deteriorate above approximately 450 K.

2.5.4 Advances in Technology

Engine pumping losses are the work done during the intake and exhaust strokes in an engine cycle and are increased by the pressure drop across the throttle. Since they

account for significant losses in an internal combustion engine, the ability to operate an engine without a throttle holds potential for reducing fuel consumption. To achieve this unthrottled operation, air and fuel flow must be controlled through varying the valve events rather than restricting the airflow with a throttle. Recently, the concept of variable valve timing for load control in an unthrottled internal combustion engine has shown a reduction in fuel consumption by 15% in the New European Driving Cycle, while simultaneously offering optimisation of cold start, warm up and transient operation. In particular a modified valve timing strategy during start-up, provides a reduction in start-up HC emissions of approximately 60% [22].

Homogeneous Charge Compression Ignition (HCCI) is currently under widespread investigation because of its potentially reduced levels of NOx and particulate emissions, while maintaining a high thermal efficiency. Engine types have included not only two- and four-stoke designs, but also fuels such as diesel, petrol, methanol, natural gas and hydrogen. The process basically involves inducting premixed fuel and air, between lean and stoichiometric, and compressing until ignition commences. Cyclic variability is reduced, and the very rapid combustion phase releases all the heat in approximately 10°CA. [23-29]

2.6 Conclusions

The combustion present within the internal combustion engine is highly turbulent, highly chaotic, of short duration and exhibits wide cycle-to-cycle variations. High bandwidth measurements of in-cylinder heat fluxes and species development would therefore be useful in the understanding of IC engine combustion.

CHAPTER 3

REVIEW OF CURRENT EXPERIMENTAL TECHNIQUES

3.1 Overview

This chapter gives an overview of sensors used on flow and combustion within the internal combustion engine. It will be shown the need exists for new and more accurate high-speed sensors to be applied to the internal combustion engine.

3.2 Sensors

Sensors are critical elements for combustion control and combustion monitoring [8]. Most measurements are relative to crank angle; this is because crank angle is a useful independent variable since engine processes occupy almost constant crank angle intervals over a wide range of engine speeds [17].

3.2.1 Sensors - Optical Techniques

All optical techniques for combustion, not only for measurements of flow, but also of species and temperature, require optical access to the combustion chamber. It is essential that the method of optical access is non-intrusive; otherwise measured values are not representative of real values. Various methods of optical access have been proposed to obtain optical access with minimum changes to an engine, ranging from windows in the cylinder head or piston [30] to even an endoscope based system [31]

or fully transparent optical engine with a 'glass' bore. Each technique has associated advantages and disadvantages.

3.2.1.1 Laser Two Focus (L2F)

Laser Two Focus is a technique that measures the time interval for a particle to travel between two previously chosen locations in a fluid, which are defined by the focus points of two parallel laser beams [32-34]. The light scattered by a particle that traverses each of the focus points is recorded onto a separate photo-detector. The difference in time of recording between the two detectors and the known distance between the two signals are used to determine the velocity of the particle.

A large laser energy density allows small (0.1 micron) particles to be detected, and the upper velocity limit is in the hypersonic region (700 m/s). The minimum velocity measurable is limited to about 50 m/s, and is determined by the maximum obtainable distance between the two focus points that still permits the identification of individual particles. L2F typically is used in turbomachinery flows with low turbulence levels since higher turbulence levels result in the particles not passing both beams.

L2F in summary is an intrusive measurement since it requires seeding of the flow and special optical windows, but more importantly is unsuitable for use in a turbulent environment. Therefore this technique will not be further pursued.

3.2.1.2 Laser Doppler Anemometry (LDA)

Yeh and Cummins invented the LDA experimental technique in 1964. It is based on the frequency shift between the incident and the scattered light caused by moving

particles seeded into the flow (Doppler effect) [35,36], see Figure 3.1. Interference fringes are produced within a small volume created by the intersection of two laser beams within the flow field. When a particle passes through this volume, it scatters light with a frequency shift proportional to the particle velocity. The shift is measured using a spectrometer and converted into intensity using an absorption line filter.

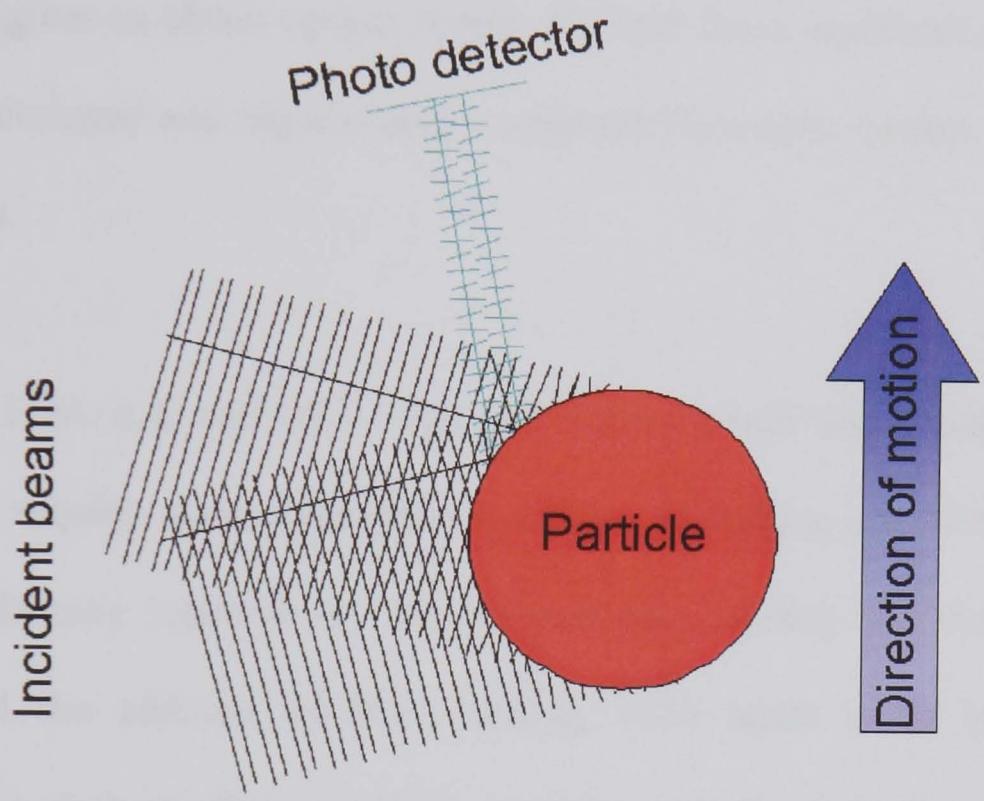

Figure 3.1, Principle of operation of LDA, [37].

Typically LDA has a 180° ambiguity in flow direction; however, if two laser sources with different wavelengths are used, a beat frequency of a lower value is obtained. The beat frequency is dependent on the velocity component perpendicular to the direction resulting from the vector addition of the two beam directions and is independent of the observation direction [32-38].

Cairns and Sheppard discovered that although previous LDA measurements implied a homogeneous and isentropic mixture, flow visualisation clearly demonstrated this was not the case. This error was due to the way the LDA measurement averaged out the

cyclic variability over the many cycles required to generate the LDA data at each point [39]. It is important that with LDA measurements homogeneous seeding is required and consideration must be given to flow averaging from building up a flow image from many point measurements.

Historically, the use of LDA generally requires significant modifications to internal combustion engines to obtain optical access. To limit these modifications, Obokata et al. [40] have designed and implemented a coherent fibre-optic system to transmit the incident beams.

To conclude, LDA is a well researched and relatively well understood experimental technique that requires special consideration given to seeding and averaging. Due to the optical windows required for the measurement altering the chamber thermal properties and the addition of flow seeding, LDA again is an intrusive, point measurement technique that requires complex set-up and due to the small interrogation region is unsuitable for turbulent flows.

3.2.1.3 Doppler Global Velocimetry (DGV)

DGV, like LDA is based on the Doppler shifted light scattered by particles [33,34]. The shift is measured simultaneously for a whole 2D plane, via an absorption line filter, typically an iodine cell (whereas LDA is a point measurement). The iodine cell converts the frequency shift across the field into a modulation of intensity, higher intensity corresponding to positive shifts, lower intensity corresponding to negative shifts. Thus, DGV provides a full-field measurement of the velocity without

directional ambiguity. However, it requires a complex experimental set-up and calibration procedure.

In summary DGV is the 2-D application of LDA and although shortcomings with LDA such as being a point measurement have obviously been addressed, the disadvantages of complex calibration, set-up and being unsuitable for turbulent flow still hinder its application to the internal combustion engine.

3.2.1.4 Particle Image Velocimetry (PIV)

PIV is based on the optical detection of the position of particles in a flow field at two well-defined moments in time [32-34,36,41-47]. The flow is seeded and a thin light sheet is produced which defines a two-dimensional plane in the flow field, Figure 3.2. The two-dimensional (2D) velocity component of the flow in the light sheet plane can be measured with a one-camera arrangement and the out of plane component is typically measured with a stereo arrangement. This is a well-established, relatively robust technique that performs well provided seeding and light source are carefully selected.

In 2D PIV, 2 laser pulses capture the locations of the particles within the light sheet at precisely defined moments in time. Depending on the system in use, either the both pulses will be imaged on one camera frame, or each pulse will correspond to a different camera frame. If the one frame is used significant cost savings can be made, however there is a directional ambiguity in the measurement and particularly in particle tracking errors can result due to incorrect particle pairing.

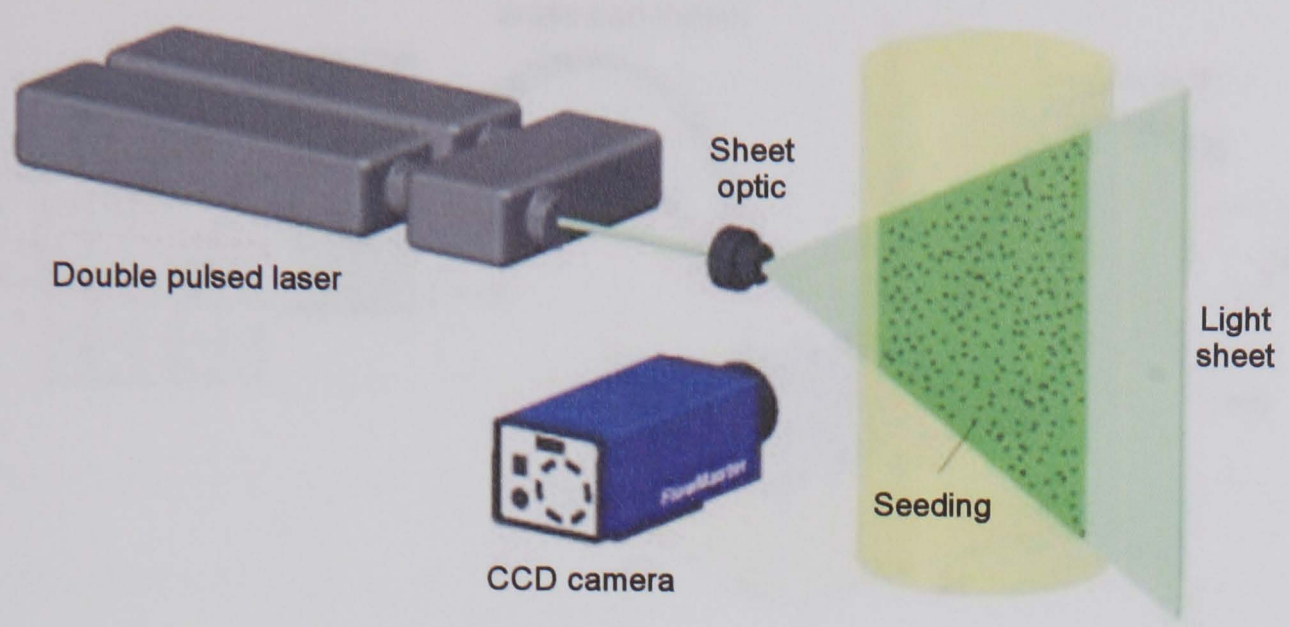

Figure 3.2, PIV schematic, [48].

For the PIV processing, one of two methods is used depending upon the seeding density. For sparsely seeded flows, each particle is 'paired' by interrogating a small area of the image. By knowing the pixel shift in x and y, Figure 3.3, the distance in meters moved by the particle is known; similarly the time taken is known from the laser pulse separation and thus the velocity can be determined. For densely seeded flows the velocity is calculated in a similar manner, however a correlation technique is used on a small interrogation area of the flow to determine the average particle displacement, as shown in Figure 3.4.

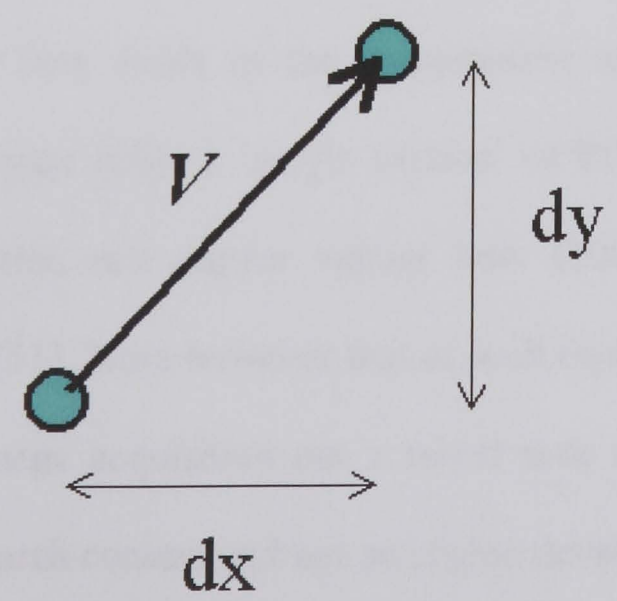

Figure 3.3, Processing by particle tracking.

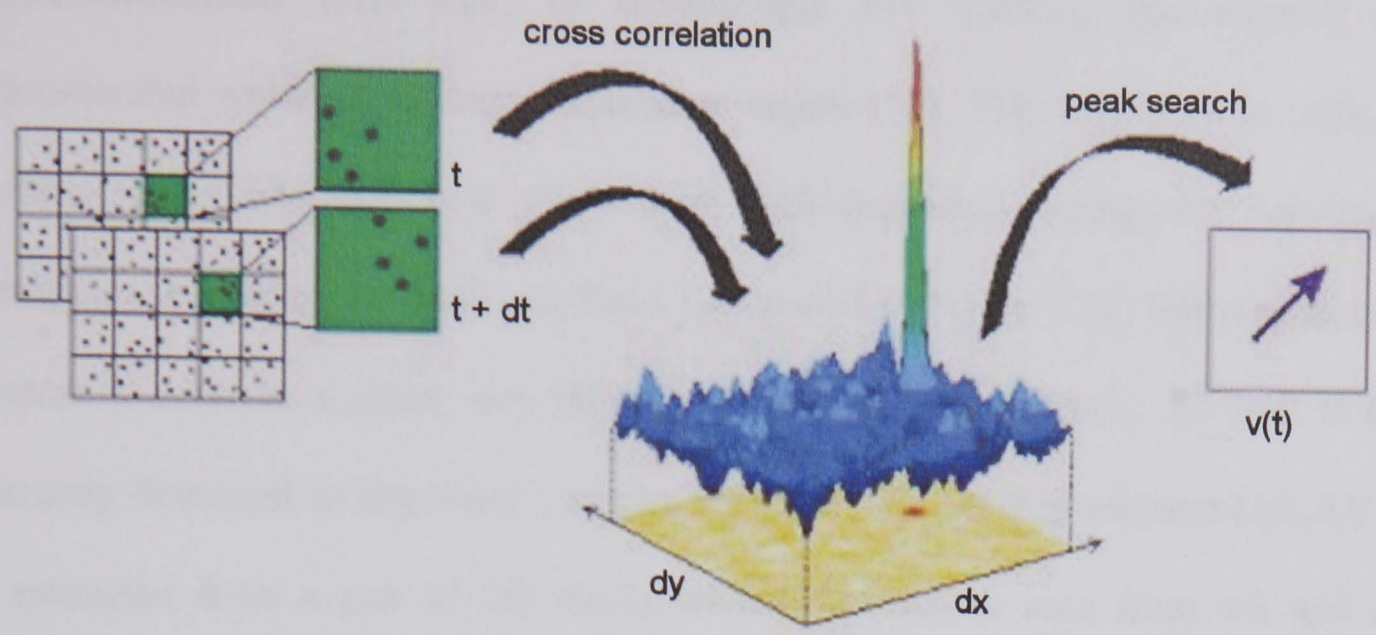

Figure 3.4, Example of PIV cross correlation, [48].

Inherent assumptions with both PIV methods are that the tracer particles follow the fluid motion, that the tracer particles are distributed homogeneously, that the two laser pulses are capturing the same particles (they are not passing through the light sheet) and that there is a uniform displacement (velocity) within the interrogation region, [37].

PIV has been applied to both motoring and firing internal combustion engines [49,50], and through careful choice of instrumentation the flow development within one engine cycle can be measured. For example Hartmann *et al.* performed an investigation into the flow fields in the compression stroke of a square cylinder internal combustion engine using a 'movie version' of PIV. The experimental set-up included a high repetition rate copper vapour laser (100 pulses at 30 kHz) and a rotating drum camera [51]. Note however that at such repetition rates the laser power is very low making image acquisition not a trivial task and firmly positioning such experiments into a research context and not an engine development one.

Three-dimensional (3D) PIV, or stereoscopic PIV (SPIV), has recently been demonstrated within an internal combustion engine [52]. This is performed using two cameras that view the flow plane from different angles using the Scheimpflug arrangement to keep the planes in focus (illustrated in Figure 3.5). The resultant flow vectors are 3D in a plane, not 3D in a volume, in other words, 3D PIV is more correctly described as improved accuracy 2D PIV. The 3D displacement ($\Delta X, \Delta Y, \Delta Z$) is estimated from a pair of 2D displacements ($\Delta x, \Delta y$) as seen from left and right camera respectively, also shown in Figure 3.5. Obviously like all 3D data, clearly displaying the results is not a trivial task. The results from the above investigation were similar to that of a concurrent 2D PIV experiment, picking up similar flow structures and again illustrating that ensemble averaged flow velocities are not representative of individual cycles [52]. This is an important proof as many point measurement techniques build up a 2D image from ensemble averaging; here it is shown that the application of any ensemble averaging must be carefully considered.

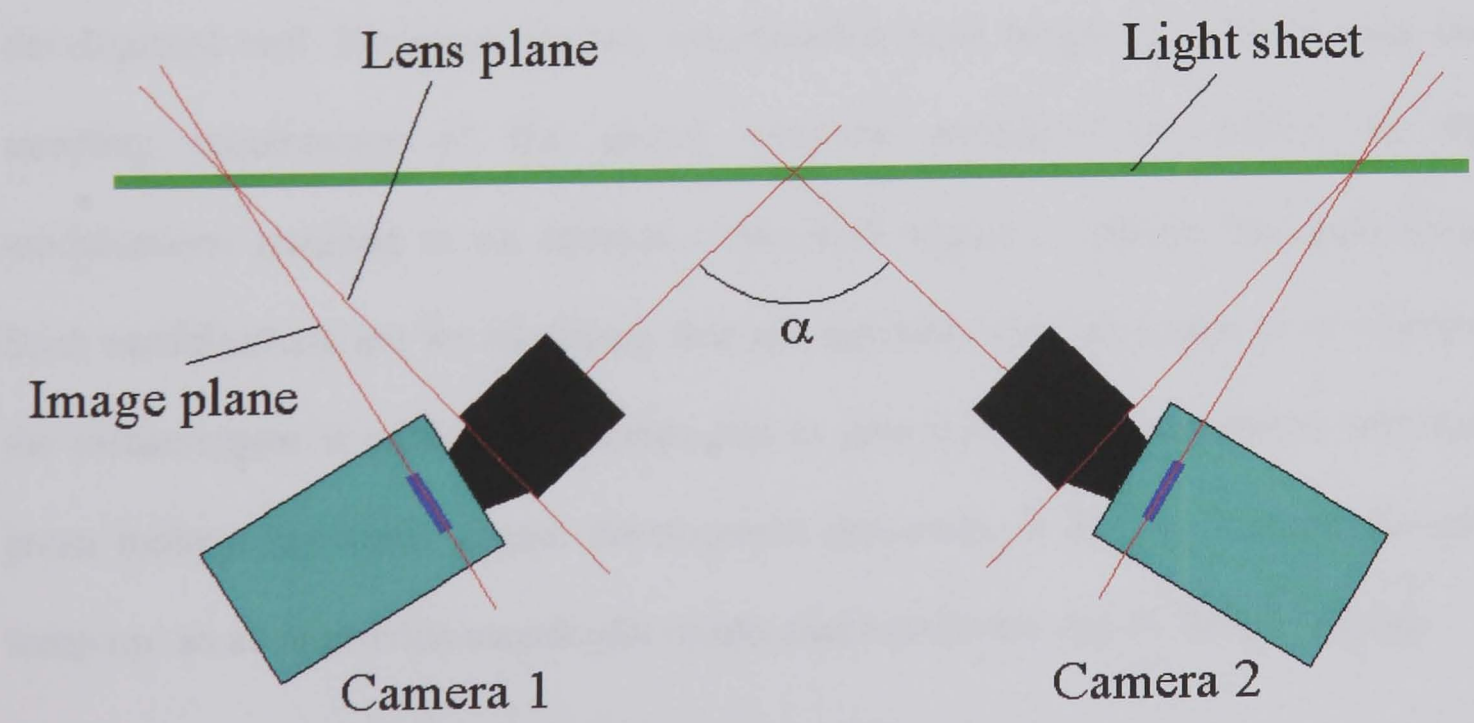

Figure 3.5, Schematic of stereo PIV set-up.

Similarly, Choi and Guezennec [53] have demonstrated 2D PIV and 3D Particle Tracking Velocimetry (PTV) measurements in a water-analogue engine-rig. The use of a water analogue rig has many associated limitations, such as the inability to replicate the compression stroke, however advantages include simpler implementation of image based measurement techniques and operation at a much reduced piston speed allowing reduced cost engine development. Their investigation provides a useful comparison of 2D PIV and 3D PTV optical techniques.

Reeves *et al.* [54] provide a comprehensive review of PIV and describe a 'turnkey', high-speed digital imaging system that provides combined real-time flow visualisation and processed PIV data in an optical research engine facility.

So in summary, PIV may be described as a capable technique that has had much development in recent years to the extent that turnkey systems are now available truly removing PIV from the academic or research stage and permitting it to be used as a development tool. However, serious consideration must be given to the meeting the sampling requirement of the spatial temporal envelope, in addition to the modifications required to an internal combustion engine to permit the application. Such modifications are so significant that the question must be raised as to whether the measurement is sufficiently unobtrusive to give accurate measurements and that given today's fast track engine development processes, if PIV as a technique can 'keep up' so as to provide meaningful results that benefit the engine design process.

3.2.1.5 MIE Scattering

For MIE scattering, small particles (that are either introduced or already present in the flow) that burn or change scattering characteristics within the flame are illuminated with laser light and photographed [39]. The reduced laser power required with this technique (over PLIF, *below*) has allowed rapid repetition rate lasers to be used, permitting multiple images to be resolved within a single combustion event. This alternative MIE scattering technique has the advantage that the same particles may be used to provide flow visualisation information prior to combustion. Recently the combination of direct flame photography, flow visualisation and MIE scattering has been demonstrated.

The problem is that the capture of a complete description of the flame front is non-trivial since it is three dimensional, highly turbulent and requires a high bandwidth technique.

3.2.1.6 Shadowgraphy

Shadowgraphy is a non-intrusive optical technique that provides a qualitative visualisation of density gradients in a flow. It operates on the principle that light refracts when passing through strong density gradients. A collimated beam of light is projected through the flow field onto a screen. Dark areas will appear on the screen where the light has been deflected away. Shadowgraphy visualises the displacement of a disturbed ray that has passes through an inhomogeneous field. Shadowgraphy is sensitive to changes in the second derivative of the gas density, and is therefore well suited for visualising shock waves and turbulent flow fields [33,35]. Figure 3.6 shows the experimental layout for shadowgraphy where a screen is replaced with a camera.

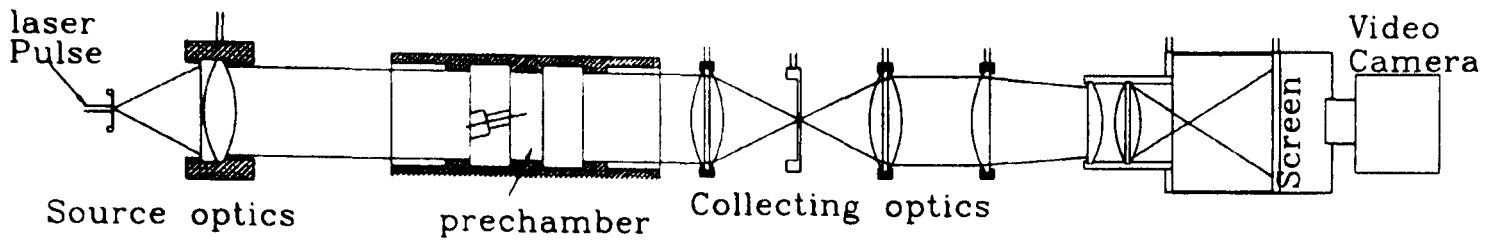

Figure 3.6, Schematic layout of shadowgraph optics. (Reproduced from [55])

In summary, shadowgraphy is a technique that provides pretty pictures useful for visualisation of density gradients, however quantification and interpretation is difficult. Application to the internal combustion engine is so far limited to analysis of fuel sprays, [55].

3.2.1.7 High Speed Schlieren

This technique, similarly to shadowgraphy, is based on the deflection of light due to density gradients in the flow [33,35]. A collimated light beam is sent through a flow, after which it is focused by passing through a lens or concave mirror. In this focal plane an image is formed of the light source. When the collimated beam is deflected, the deflected light is imaged slightly displaced in the focal plane. By placing a knife edge or 'schlieren filter' in the focal plane, these deflections become visible in the image plane. A lens is used to form an image of the flow section, which eliminates the shadow effects. In general, the intensity change is proportional to the component of the density gradient normal to the knife-edge.

Schlieren techniques may be used to define both laminar and turbulent burning velocity relevant to internal combustion engines such as performed at the University of Leeds. Precise burning velocity definitions are important as they are used in mathematical models of spark-ignition engine combustion. The study identified

considerable differences in reported values and explains these due to previously neglected effects of flame stretch rate and instabilities on burning velocities [56].

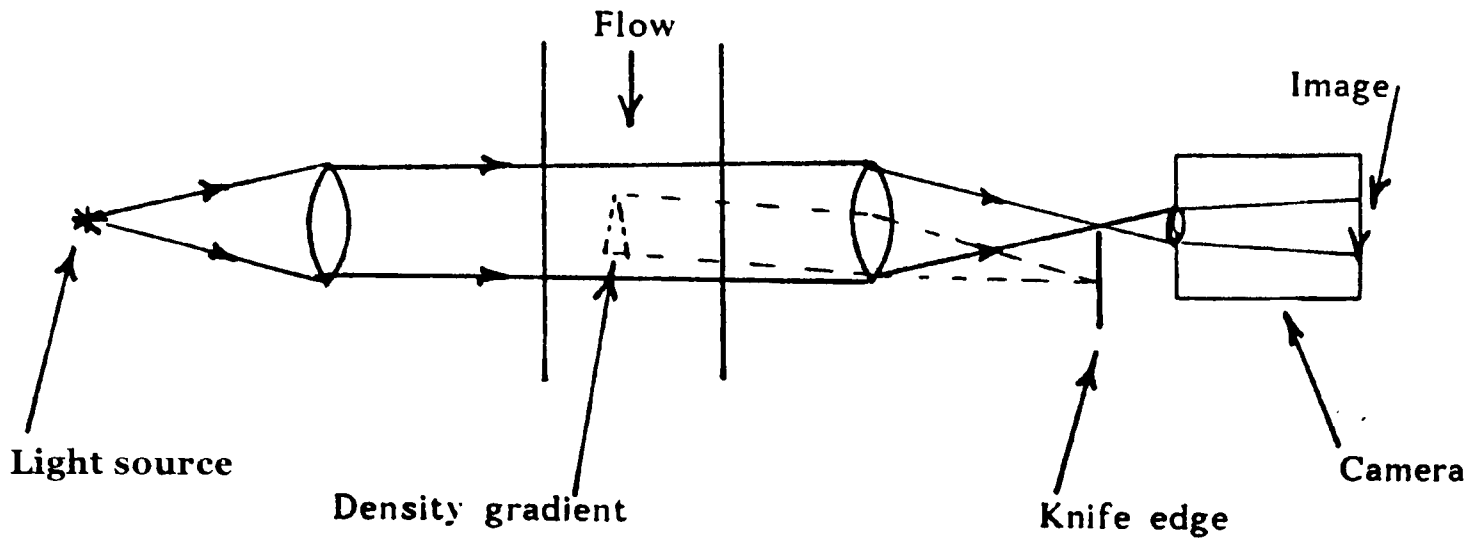

Figure 3.7, Schlieren experimental set-up. (Reproduced from [35])

Schlieren may also be applied to a motored engine. Reitz and Rutland [57] describe gas temperature measurements using an acousto-optical schlieren photography technique, where a laser was focused to break down the gas at a hot spot within the combustion chamber. Schlieren visualisation of the resulting shockwave propagation was used to determine the gas temperature. The temperature measurements were shown to have good agreement to CFD predictions of the in-cylinder gas temperature variation during the compression stroke.

In summary, schlieren photography is very similar to shadowgraphy both in operation and value of results. However, the application of Schlieren to the internal combustion engine is more extensive than shadowgraphy with it being used to research flame kernel development and growth, [58,59], although significant modifications to the combustion chamber are required.

3.2.1.8 Speckle Photography

Speckle photography (digitally or photographically) of transparent media can be used for quantitative measurements of the instantaneous temperature fields in 3D unsteady flows. The recorded Young's fringes in the specklegram are analysed as they hold the information on the deflection angle of the light beam passing through the flow. This deflection angle is directly related to the density gradient integrated along the optical path, this in turn is related to the temperature gradient. For 2D flows in air the maps of the deflection angles obtained can easily be transformed to 2D temperature maps with simple calculations and no calibration. Thus the laser speckle technique enables the finding of a temperature gradient via measuring deflection angles of the light passing through the medium under study. See Figure 3.8.

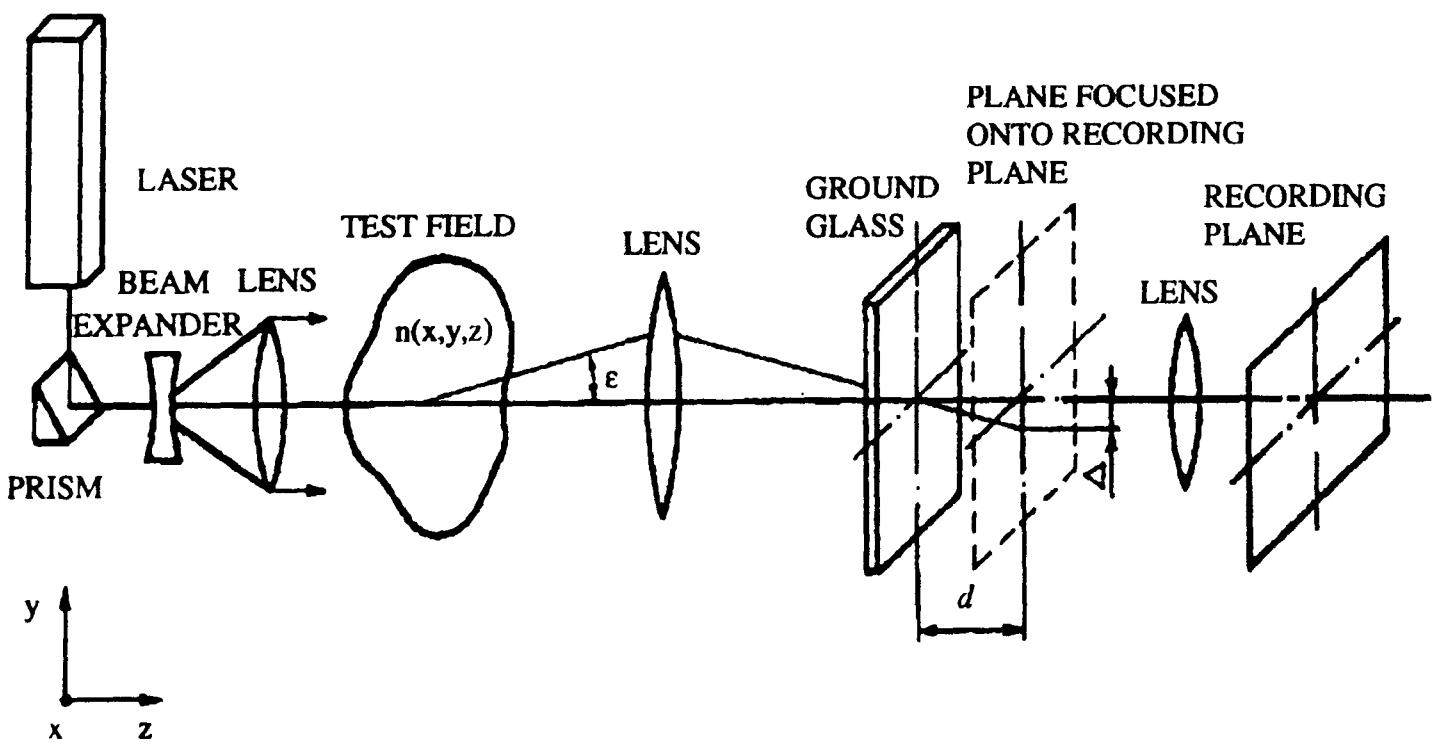

Figure 3.8, Optical set-up for speckle photography of an extended transparent object and the definition of the co-ordinates and the deflection angle. (Reproduced from [60])

Speckle photography allows direct measurements of temperature gradients in flow and at the wall surface; this provides access to determining the local heat transfer coefficients with high accuracy [60]. However for the reconstructing of a 3D

temperature field, a computerised tomography technique must be used which due to optical access restrictions, is not possible within the internal combustion engine.

In summary, the complex process involved with speckle photography has meant that it remains a research tool.

3.2.1.9 Spectroscopy

Spectroscopy is the term given to the examination of spectra for determination, from the position of the spectral lines, the composition of the substance. In practice, for flames this means examining the emission spectra (where the light is broken down into its component wavelengths) to determine the existence of individual wavelengths that are related to known chemical species, Figure 3.9. This means that if the spatial and time resolved spectra for a particular flame was known, the timing and position of each chemical species would be know.

There are various methods of collecting emission spectra. Typically light from the combustion event is incident onto a grating that diffracts each wavelength through different angles. This 'spread out' spectrum is now sampled typically with a row CCD or row of photodiodes, Figure 3.10. To add spatial resolution the light emitted from a line across the flame can be collected and passed through an imaging spectrometer that acts like many individual spectrometers stacked on top of each other. The diffracted light is sampled with a normal two-dimensional CCD chip. To increase the temporal resolution faster framing cameras can be used and if coupled with image intensifiers short integration times and low light emissions can be accommodated.

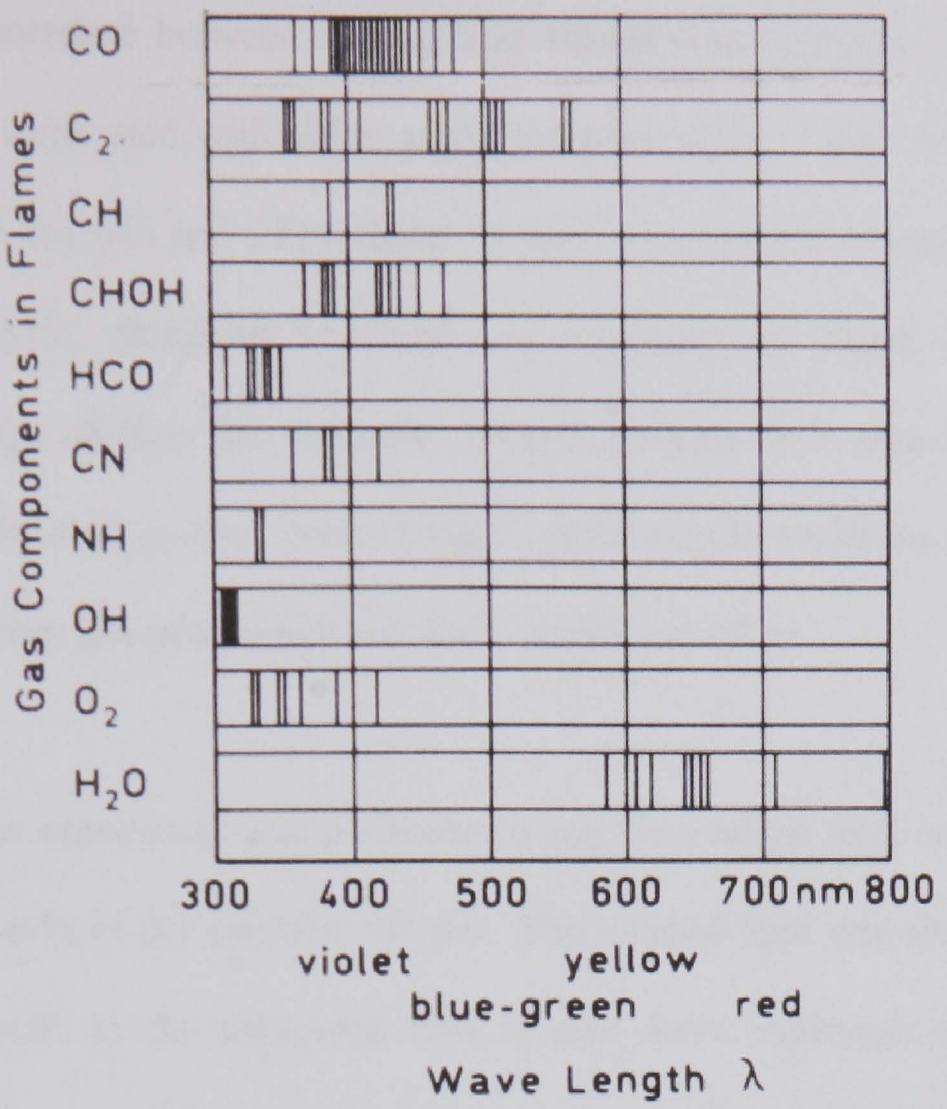

Figure 3.9, Wavelengths of known species emission in flames.

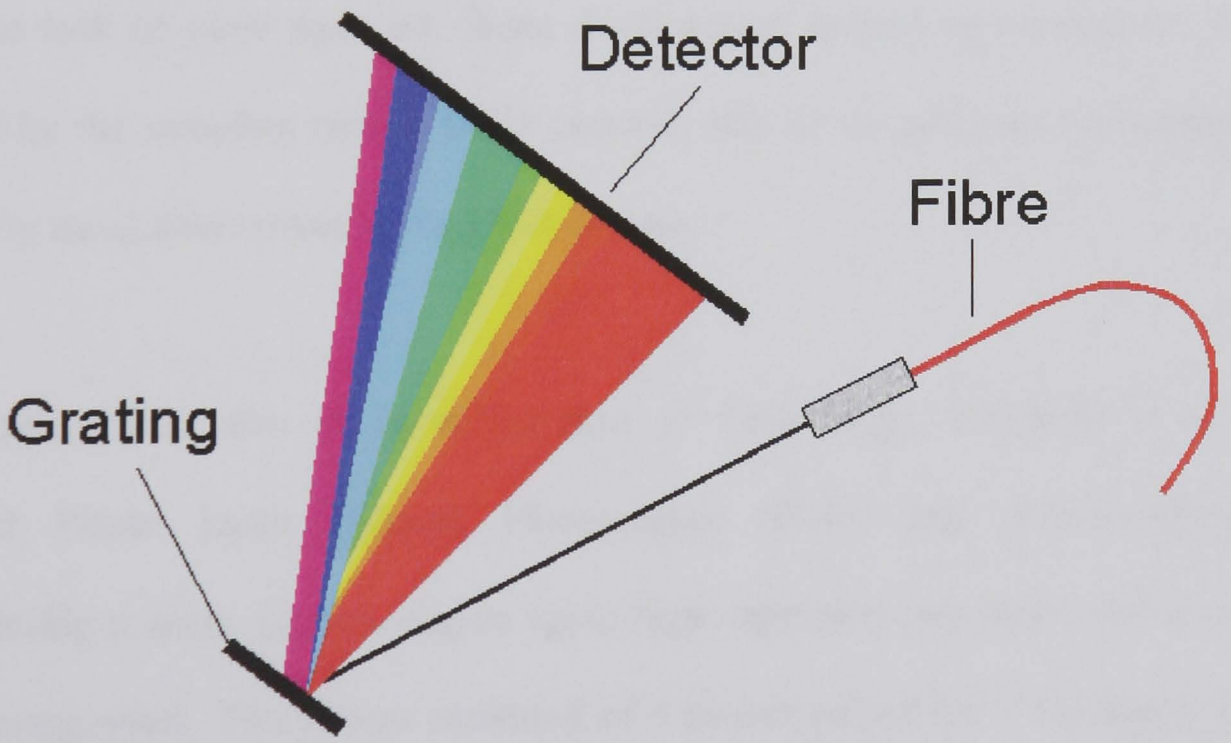

Figure 3.10, Schematic illustrating operation of a spectrometer.

Hultqvist performed an investigation applying spectrometry and chemi-luminescence imaging to combustion in an optically accessible compression ignition engine, [61]. It was possible to determine the major active species, flame development, cycle-to-cycle

variation and correlate between rate of heat release and intensity. Image intensified CCD cameras were used with either a spectrometer or band pass filters to view the development of the OH and CH radicals. It was only possible to sample over 1° CA during each cycle, therefore to obtain an indication of flame development an ensemble-average of how the emission spectra changed with time was constructed from many individual cycles. Even though cycle-to-cycle variation was low in this engine design, they describe how it still had a significant effect.

The heat release correlation was performed using the average total emitted light from approximately 40% of the chamber volume. This emitted light was shown to correlate "surprisingly well" to the calculated heat release curve. Although a valuable study into the main species emitted and in particular the work correlating heat release with light emission is very useful, the main drawbacks associated with this method are simply the lack of cycle resolved, flame development species measurements. This is restricted by the sampling rate of CCD cameras; this thesis offers an improvement in this area by using alternatives to the CCD camera.

The following year also at Lund Institute of Technology, Kaminski et al. [62] performed Planar Laser Induced Fluorescence (PLIF) and chemiluminescence imaging inside a spark ignition engine using high repetition rate lasers and a custom camera arrangement. The system consisted of 4 double pulsed Nd:YAG lasers, Figure 3.11, as a pumping source for a conventional dye laser system, whereas the image acquisition was performed using eight independently intensified 8 bit, 378x576 pixel CCD detectors viewing the source through a prism beam splitter, Figure 3.12. An additional 3-stage intensifier module was also attached to the input, increasing gain

and making the system UV sensitive. The authors claim image acquisition rates of up to 1MHz which is sufficient to meet the spatial temporal envelope.

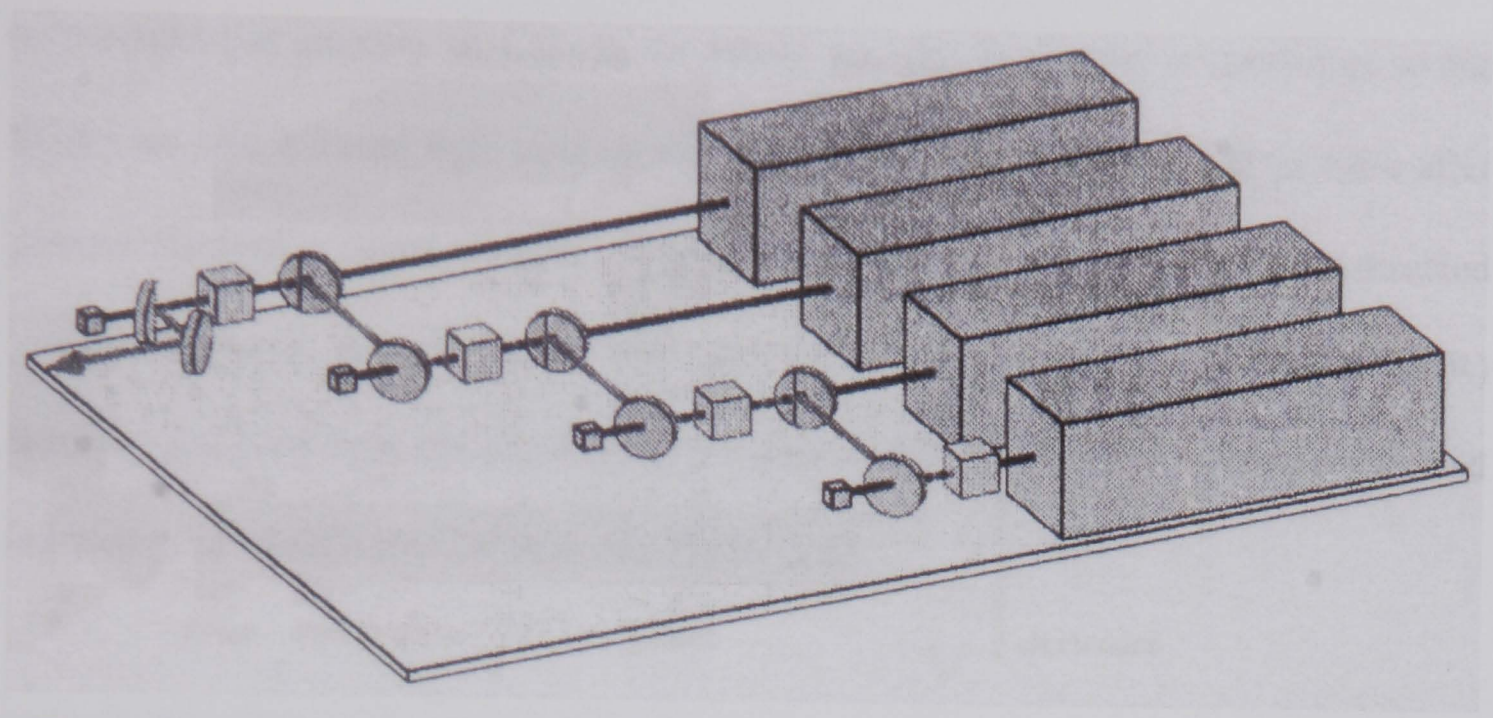

Figure 3.11, Multiple YAG cluster. Round elements are dichroic beam splitters that are transmissive for 1064nm and reflective for 532nm. Large cubes: Frequency doubling crystals. Small cubes: beam dumps. (Reproduced from [62])

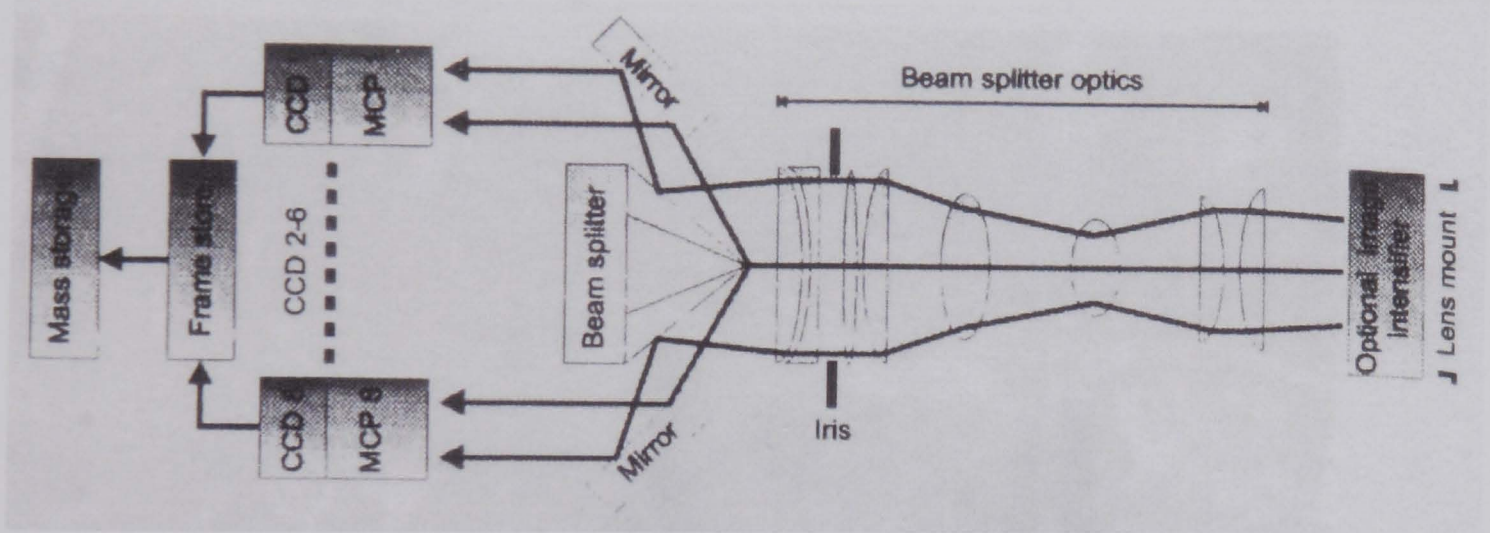

Figure 3.12, Operating principle of fast framing camera. MCP: Multi channel plate image intensifier. Light enters from right, passes internal optics and an iris before impringing on a prism image-splitter. The latter directs individual images onto the MCPs that are sequentially gated. (Reproduced from [62])

The system although very impressive and capable of imaging species formation and flame development within an engine cycle is limited by its sheer expense and non-user friendliness to the research laboratory context and is not a viable experimental technique.

An alternative application of spectroscopy has recently been proven for measuring exhaust gas recirculation rates (EGR) in an internal combustion engine. In the investigation by Hall and Zuzek in 2000 [63], IR absorption spectroscopy was utilised to measure the quantity of CO_2 in the intake air, this is directly proportional to the EGR rate. An infrared light source was focused onto a 500 μm diameter fibre after passing through a signal chopper. The fibre exit was in the airflow and was directed towards a mirror. A similar fibre that returned to a band-pass filter and infrared (IR) detector received light reflected from the mirror. Use of the signal chopper allowed correction of background IR emission Figure 3.13.

The system detects the transmission of the strongest C-O vibrational-rotational absorption band of CO_2, centred on a wavelength of 4.3μm. The radiation transmitted is related to the spatially averaged concentration of CO_2 through the Beer-Lambert law.

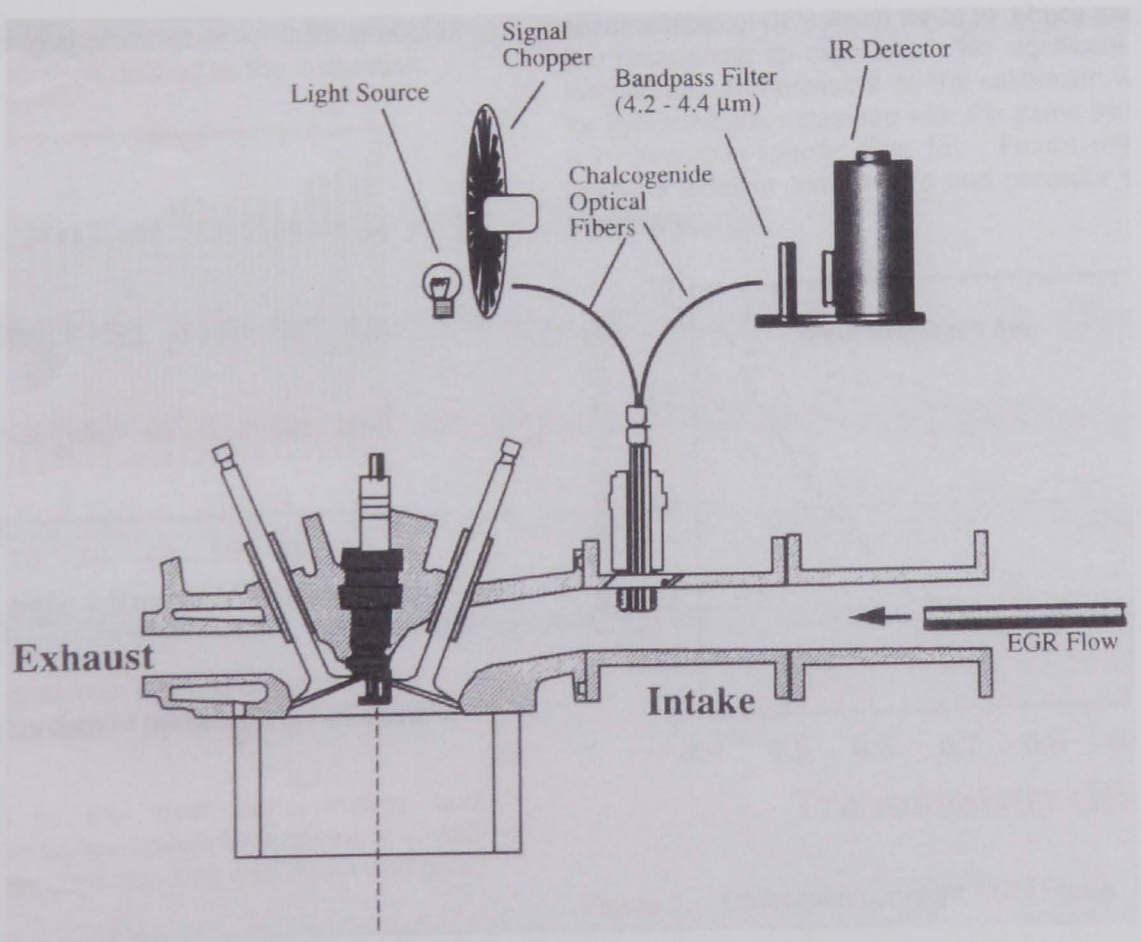

Figure 3.13, Schematic of experimental set-up. (Reproduced from [63])

In addition, Cheskis discusses two new spectroscopic techniques, intracavity laser absorption spectroscopy (ICLAS) and cavity ring-down spectroscopy (CRDS). Both of these techniques are reviewed and discussed along side laser induced fluorescence (LIF) in relation to quantitative absolute concentration measurements in flames [14]. He concludes that the two new techniques complement each other in terms of signal-to-noise ratio, frequency range and ability to cope with a sooty flame; however, both techniques require complex set-up and calibration and for the time being remain firmly within a research context.

In conclusion, spectroscopy is an important tool for the analysis of the chemical mechanisms of combustion. Not only are these techniques useful but also they can be applied with several methods varying in complexity yielding increasing amounts of information. Depending upon the technique applied, spectroscopy can meet the requirements of the spatial temporal window and in addition is a technique that can easily be taken out of the research stage and be used as a genuine development tool.

3.2.1.10 Fourier Transform Infra-Red Spectroscopy

Fourier transform infra-red spectroscopy (FTIR) is similar to IR absorption for emission analysis of species and temperature. Hilton and Lettington provide a good description of this technique, which is typically used within the gas turbine engine for combustion measurements, [64]. Measurements taken with FTIR typically look at the larger particulate burning products.

3.2.1.11 Emission-Absorption Spectroscopy

Emission and absorption spectroscopy has been used in engines, since the late 1920's [65]. The method is based on the simultaneous measurement of both the spectral radiance $L_\lambda(T)$ and spectral absorption $a_\lambda(T)$ along a line of sight [66]. Here T is the true gas temperature, and the subscript λ denotes the wavelength dependency of L and a, respectively. While the spectral radiance of a blackbody radiator $L^b_\lambda(T)$ depends solely on its temperature following Plank's law or Wien's approximation, the spectral radiance emitted from the combustion chamber depends not only on temperature but also on the species present. Therefore measuring spectral radiance alone is usually not sufficient to determine gas temperature, except for cases in which the absorption approaches blackbody condition, i.e. $a_\lambda \rightarrow 1$.

Combustion chamber temperatures are derived from the measured L_λ, and a_λ data using Kirchoff's Law, equation (3.1).

$$L_\lambda(T) = a_\lambda(T).L^b_\lambda(T) \tag{3.1}$$

It is important however to carefully select the emission lines and fuel additives as for non-equilibrium conditions, the measured data can yield an excitation temperature which may lie above the true gas temperature [12,66].

The technique of absorption-emission spectroscopy has also been combined with tomography within an internal combustion engine to give a 2D cross-sectional representation of engine soot concentration [67]. However, since Natural Gas is the fuel required for this investigation, techniques based on black body emission of soot

are unsuitable since a negligible quantity of soot is formed, in addition this is a complex experimental method that operates in a research environment.

3.2.1.12 Absorption / Radiation Pyrometer

The radiation from a perfectly radiating solid body can also be related to its temperature by Plank's law. However, this is complicated and an approximation is possible using Wien's Radiation law that is less cumbersome and introduces a relatively small error when used with an Infrared pyrometer. Kirchoff's law gives an exact relation between emission and absorption for monochromatic radiation at a constant temperature. So with correct use of each law, it is possible to determine the gas temperature of a given volume. It should be noted that an infrared pyrometer measures a temperature weighted towards the peak gas temperature. See [68] for an in-depth discussion. As for each of the other techniques utilising the black body emission from soot, this technique is not applicable to Natural Gas combustion and so will not be pursued.

3.2.1.13 Coherent Anti-Stokes Raman Scattering (CARS)

CARS is a research technique that in recent years has received much publicity for its claimed ability to measure flame temperature. For a description of the method see [69-72], in particular Grandin *et al.* [71] provide a very comprehensive description. One must remember that not only does CARS require complex set-up, calibration and expensive equipment but this technique is also still in the development phase and has yet to be proven accurate, [38].

3.2.1.14 Laser Induced Fluorescence (LIF)

Laser Induced Fluorescence is used to determine the concentration of a species of interest over a region [14,73-75]. Essentially, a laser pulse of a carefully chosen wavelength is used to excite a particular species to an artificially high energy level. The chosen chemical species can either be naturally present, such as OH* or CH* radicals, or artificially added, such as acetone added to the fuel for fuel spray distribution measurement. This raised energy level cannot be sustained and so as the electrons return to the ground state the extra energy is emitted as fluorescent light. The fluorescent light level is collected and quantified, and is known to have an approximate linear relation to species concentration. Planar LIF (pLIF) utilises an image intensified charge coupled device (iCCD) camera to record the spatial distribution of the species concentration.

The linear relationship between light emission and species concentration is important for ease of calibration and use, however, unfortunately some species exhibit a fluorescence emission that is dependent on temperature and pressure. Complex relationships between light emission and concentration in many cases make the techniques essentially qualitative. [73]

In summary, LIF is a useful technique for species concentration measurement in a plane. The technique requires optical access for both a pulsed ultraviolet (UV) laser and light collection optics, and due to complex calibration often yields a qualitative species concentration. The application of LIF or pLIF measurement techniques to an essentially unmodified internal combustion engine will not be developed, however it

is acknowledged that a probe capable of PIV measurements would require minimal modification in order to provide a pLIF measurement.

3.2.1.15 Optical (and 2 or 3 Colour) Pyrometry

Optical in-cylinder soot temperature measurements are based on the property that soot particles emit radiation in a continuous spectrum, similar to that of a black body. By definition, a black body is a perfect emitter of radiation in a continuous spectrum with an emissivity of 1, however the radiation spectrum of soot is different to that of a black body by a factor ε_λ, the spectral emissivity.

By measuring the light intensity of two narrow bands, $I_{\lambda 1}$ and $I_{\lambda 2}$, and knowing the soot concentration factor, as well as calibrating against the radiation from a light source of known emissivity and temperature, it is possible to convert from intensity to apparent temperature. This is the temperature a black body would have if it had the same spectral intensity as the emitting soot. When this method of in-cylinder temperature determination is used, it is recognised that the temperature measured is in fact the soot temperature and the assumption is made that this closely follows the flame temperature. For a description of the technique, along with mathematical equations used, see [31,33].

Since Natural Gas is the fuel required for this investigation, techniques based on black body emission of soot are unsuitable since a negligible quantity of soot is formed.

3.2.1.16 Flame Imaging

There are many experimental techniques that have been applied and are available to detect and either quantify or qualify flow conditions before combustion, such as flow visualisation [32,46,47,51,54,76], PIV [32,41-47,50,76], particle tracking velocimetry (PTV) [49,53,77], as well as many techniques that can detect combustion phenomena, such as ionisation probe sensor [20] and LDA [32,35,38-40], however these results are not always adequate to sufficiently describe the combustion process. Observation of flame propagation is one of the most capable methods to visualise and understand the in-cylinder combustion process [20]. The investigation of flame propagation allows investigation of the effects of swirl and piston cavity shape on the combustion characteristics, such as flame front shape and flame speed [20].

Optical access through the piston is a common method of optical access, although a lower surface temperature on the quartz surface leads to inaccuracies in observed combustion [30].

There are alternatives to using an optical engine; for example the University of Wisconsin-Madison have presented results using an endoscope based imaging system where they de-activated an exhaust port and inserted a 10mm endoscope which was used for flame imaging and flame temperature measurement [31,57]. Though successful in capturing images, by using exhaust valve deactivation, they were unsuccessful in making unobtrusive measurements and were limited by high levels of light loss due to the endoscope, requiring image intensifiers and long integration times.

Sandia National Laboratories, in collaboration with the University of Toronto, developed in 1988 a fibre-optic instrumented spark plug for measuring early flame development in spark ignition engines [78]. This idea has recently been commercialised by AVL with little modification and is now available as a bolt-on diagnostic for engine development [79]. The probe consists of a standard spark plug, with a ring of optical fibres positioned around it that may be inserted into any engine. Processing of the light levels seen by each fibre yields the arrival time of the early flame kernel in each direction. Unfortunately, this technique allows only a comparison of the early flame development between different running conditions and spark timing and therefore provides minimal information; however, its ability to be bolted onto an engine within its development cycle raises much interest in the automotive sector.

Nwagboso and Pendlebury recently conducted an investigation into the use of a fibre optic based combustion intensity detection sensor developed for monitoring and controlling combustion in a natural gas internal combustion engine. The sensor was placed on the top of the engine block and measures intensity of light emission from combustion with a photodiode. The study includes modelling of the probe to identify optimum position, as well as comparisons between light emission and heat release and mass fraction burned calculated from the in-cylinder pressure. The authors claim their model provides the ability to monitor completely the stages of combustion within the cycle-to-cycle operation of the engine and use the output signal for management and control of the engine [80]. However, it was found that probe position hand a significant effect on the light signal profile and intensity. Since it is noted the authors make no attempt to identify species development or track flame speed, one wonders if

such information would be more beneficial for engine control. Results of such investigations are included in Chapter 8, Optical Probe Results.

3.2.2 Sensors – Non-Optical Techniques

3.2.2.1 Hot Wire Anemometry (HWA)

Hot-wire anemometry is a common single point technique used for monitoring the air velocities inside motored internal combustion engines, providing measurements of in-cylinder air flow rates and turbulence levels. Thermal anemometry consists of a short 'active' length of wire having many times the resistance of the support prongs and probe cables. Passed through this wire is an electric current which has a heating effect, the supply apparatus (bridge) is set in such a way as to keep the temperature of this wire constant. As air flows past the wire, it has a cooling effect and so the bridge must compensate to keep the temperature constant. The electrical energy supplied by the bridge is proportional to the flow speed past the 'hot-wire'. After calibration, hot-wire anemometry provides measurements of the velocity of the flow field. The most significant problem with hot-wire measurements in internal combustion engines is caused by the large temperature variation through the engine cycle due to compression of the cylinder gases. This is overcome by corrections during processing, however uncertainty still exists in the region around TDC [33,35,36]. HWA can only be used in a motored engine since the wire temperature must be higher than the fluid temperature to permit the 'cooling' effect.

In summary, HWA is not a non-intrusive measurement since the flow is disrupted by the insertion of the probe, and is further restricted by only providing a point

measurement. In addition uncertainty exists due to the change in temperature of the cylinder gases. For these reasons HWA will not be further considered.

3.2.2.2 Air Mass Flow Rate Sensor

Air mass flow is an important and necessary measurement during engine development within the internal combustion engine as it permits the calculation of equivalence ratio. Air mass flow is not a trivial measurement to make; however, significant research has opened many possible methods of measuring air flow from hotwire anemometry, positive displacement flow meters through to optical techniques.

For example, utilisation of diode laser absorption sensors allows the possibility to determine the velocity of a ducted flow. The velocity of the flow can be deduced from the Doppler frequency shift. In addition, the absorption measurement itself may be used to obtain the density of the gas. When combined with the velocity deduced from the Doppler shift, a direct estimation of the mass flow rate may be gained. Alternative methods such as these for determination of air mass flow rate are particularly useful for regulation of the equivalence ratio since the fuel mass flow rate is often accurately known from the injectors [8].

Although not measured during the tests shown in this thesis since the primary emphasis is upon the development of instrumentation, it is acknowledged that air mass flow is an important measurement in engine research.

3.2.2.3 Pressure Sensors

The analysis of combustion pressure diagrams plays an important role in diagnosing spark ignition engines as has been shown previously in Chapter 2, [18]. A brief discussion of the more common methods of pressure measurement is now provided.

Currently most in-cylinder pressure transducers operate utilizing the piezoelectric effect. Piezoelectricity is a property of certain crystalline materials where the crystalline structure produces a voltage proportional to a pressure applied to it. This voltage or charge is amplified and recorded. From a calibration it is possible to determine the pressure. There is great flexibility in the mounting position; transducers can be located in the cylinder head, spark plug, or anywhere with direct contact with the combustion, recently in a variable compression engine, location in a secondary piston has been used [81].

Currently pressure transducers are used only in research engines or large marine diesels, however work is ongoing as low cost, non-intrusive pressure sensors are developed to allow *in situ* monitoring of in-cylinder pressure for condition monitoring and control [82].

A major problem with making accurate cylinder pressure measurements using piezoelectric pressure transducers in internal combustion engines is thermal shock. Cyclic exposure of a piezoelectric transducer to the combustion event in internal combustion engines results in the contraction and expansion due to the large temperature variation during each cycle of the diaphragm that separates and protects the crystal from the combustion gases. This causes the force on the quartz to be

different to that applied by the cylinder pressure alone for part of the cycle. This phenomenon is called thermal shock, and can cause inaccuracies in measured and derived parameters, particularly IMEP where an error of up to 10% may be experienced [83].

Rai *et al.* [83] have published findings where correlations between thermal shock and peak pressure have been established, and a numerical thermal shock correction routine was developed to improve the accuracy of the calculated IMEP. The IMEP errors were reduced from between –7% and –20% to between –1.5% and +1.4%.

An alternative approach is to use a water-cooled pressure transducer where the effects of temperature variation are limited, such as those commercially available from AVL [79].

3.2.2.4 Semi-Conductors and Electronic Nose

The use of a platinum-insulator-silicon carbide (MISiC) fast gas sensors has been proven for exhaust emissions monitoring with an internal combustion engine [84]. The sensors respond within milliseconds to changes, and as such can distinguish between exhaust pulses from different cylinders. Cylinder specific engine monitoring therefore becomes possible with only one sensor.

3.3 Conclusions

A discussion of temperature and heat flux instrumentation is sufficiently important to merit a separate chapter; therefore this discussion will follow in Chapter 4, Review of Heat Flux Instrumentation.

CHAPTER 4

REVIEW OF HEAT FLUX INSTRUMENTATION

4.1 Overview

Alkidas *et al.* [85] observed in 1990 that the application of sophisticated analytical techniques for the design of spark-ignition engines had brought about the need for detailed information of the heat transfer processes in these engines. However in the 12 years since that statement, progress in the determination of heat transfer and the measurement of heat flux within the IC engine has been limited. Similarly Ball *et al.*, [18] in 1998, when reviewing computational models of combustion, still attributed inaccuracies in prediction models to heat transfer from the product gasses to the combustion chamber walls. As recently as 2000, Stone *et al.* [69] report how comparisons between experimental surface heat flux measurements and established heat transfer models show large discrepancies. To improve predictions, a greater understanding of the heat transfer process is required, and this will only be possible when instrumentation is available that can measure the heat flux rates accurately.

Catania *et al.* [86], recently have given a good review of the limitations of computational models applied to combustion. In particular, their survey of heat release combustion models has given specific attention to the bulk gas-wall heat transfer correlations used. Their conclusion, backed by experiments, was that most of

the heat transfer correlations are incapable of predicting the time lag that occurs between the gas-wall temperature rise due to the hot combustion gas or the heat transfer rates during engine compression and expansion strokes. This was contributed to the transient properties of the fluid directly in contact with the wall. Their investigation proves yet again the need for more accurate, faster response, heat flux measurements within the internal combustion engine [86]. See Chapter 11 for a more in-depth look at the computational models used and some basic predictions alongside experimental results.

Franco and Martorano [87] in 1999, proposed that the engine heat transfer is among the most complicated of engineering heat transfer problems for the reason that it involves rapid changes of temperature and velocity, and the distributions of velocity and temperature of the gas contained in the cylinder are far from uniform. Moreover, the heat transfer from the hot combustion gases includes forced convection through the hot gas boundary layer, conduction through the cylinder wall, and forced convection into the fluid coolant in the head, engine block, and piston. There is also, for a gasoline engine, a small radiant component of heat transfer (about 5%), generally ignored in calculations. Their investigation looks not only critically at the computational models used in engine prediction, but also provides a good background into the theory of internal combustion engine heat transfer analysis.

Further, Grandin and Denbratt [72], in an investigation into knocking in spark ignition engines, discuss that since light emission during knocking combustion varies by only a few percent it may be concluded that autoignition and subsequent engine knock is most likely to be studied in changes in convective heat transfer. In simultaneous

experiments, they performed an investigation through temperature measurement by Dual-broadband rotational Coherent Anti-Stokes Raman Spectroscopy, and through measurement of pressure and heat flux in an optically accessible single cylinder engine. They used a thin film resistance temperature transducer (platinum of 0.3μm thickness on an aluminium oxide rod) that appears from their results to have a slow response; taking approximately 10° CA to indicate a temperature rise of less than 10 K and in general recording in-cylinder wall temperature traces that contain only low frequency data.

This chapter looks at the methods of heat flux measurement in use and provides a discussion of the drawbacks associated with each. Thermocouples in particular are used for the vast majority of experimental procedures that determine heat transfer rates and so appropriate space has been given to their evaluation.

4.2 History of Heat Transfer in IC Engines

Investigation into the variation of in-cylinder wall temperatures started as early as 1894, when Donkin inserted small mercury thermometers through the wall of a slow speed internal combustion engine. He observed a periodic rise and fall in the mercury level, [88]. Since those first investigations by Donkin, many others have sought to characterise these varying temperatures, including Coker using a thermometer and galvanometer in 1913 [89], Nusselt in 1914 with a bomb who performed fundamental investigations into heat transfer coefficients [90], Eichelberg who in 1938 used thermocouples embedded below the chamber surface to develop heat transfer coefficient correlations [91] through to Woschni who repeated and improved Nusselt's original experiments and in 1967 presented the Woschni heat transfer

coefficient correlation that even today is still widely used [92]. These, and many more, have all investigated these varying in-cylinder wall temperatures with novel, increasingly accurate techniques, as technology advanced, [93].

4.3 Frequency Response

The temperature fluctuations of the gas within an engine are turbulent. Therefore, to determine the heat transfer rates correctly, the temperature measurements should be fast enough to follow the rapid changes. Typically thermocouples have been used for this measurement. Thermocouple advantages include low cost, reliability and simplicity since no optical access or elaborate support electronics are required. However, the design of a thermocouple represents a compromise between accuracy, ruggedness and response rate: Larger thermocouples can generally withstand higher temperature extremes, however have slower response times and therefore cannot accurately follow a rapidly varying temperature. Smaller probes on the other hand have higher response rates, yet lack ruggedness and will fail at high temperatures [94,95]. See Table 4-1 where the response times of various K-type thermocouples are given, note that in this instance, response time is defined as the time taken for the thermocouple to read 63.2% of the instantaneous step change in temperature from 20° C (air) to 100° C (boiling water).

Overall Sheath Diameter						
mm	0.25	1.0	2.0	4.5	6.0	10.8
Response time (s)	0.015	0.15	0.4	1.4	3.0	9.0

Table 4-1, Response times for thermocouples of different diameters. Reproduced from [94].

Although thermocouples are suitable for the measurement of temperature fluctuations up to around 1 kHz in a flowing gas or liquid, their use is limited in engines as the frequency of the time-dependent fluid temperature is normally much higher. In addition, even at frequencies lower than 1 kHz, the measured signal must be compensated since the frequency of the time-dependent fluid temperature is normally much higher than the corner frequency of the thermocouple probe [96].

Often when a thermocouple is evaluated, it is the time before a response to a change in temperature that is measured, not the time it takes the sensor to read the new steady temperature of the gas or liquid. It is not sufficient to immerse the sensor in a container of water to determine its response time. The resultant "response time" is masked by the laminar layers adjacent to the probe, the speed with which the probe is immersed into the water, the heat transfer coefficient of the water, etc. In fact, such a test gives a 'Rise Time', which for a sensor with a fast response time, simply changes directly with the velocity with which the probe is travelling through the water [97]. It would appear that authors and manufacturers that claim response times in the region of microseconds are in fact discussing the short delay before the thermocouple responds to a temperature difference, not the time taken for the sensor to reach a steady temperature.

4.4 Heat Transfer Determination from Pressure

It is possible from cylinder pressure analysis to make estimations of the heat transfer coefficient. Huber and Woschni [98] performed an investigation into this technique, this section is complied from that material.

The heat transfer coefficient can be calculated using the first law of thermodynamics, (4.1), and the thermal equation of state, (4.2).

$$\frac{dE}{d\vartheta} = \frac{dQ_B}{d\vartheta} + \frac{dQ_W}{d\vartheta} + \frac{dW}{d\vartheta} + \frac{dH}{d\vartheta} \tag{4.1}$$

$$p \cdot V = m \cdot R \cdot T \tag{4.2}$$

These equations are applied between the intake valve closing and the exhaust valve opening, i.e. during compression and the combustion/power stroke. During this phase of the engine cycle the masses flowing out of the system (fuel mass & leakage) are very small and their integral values are measurable.

From the knowledge of known variables such as pressure (p), mass (m) and volume (V) within the cylinder, it is possible to determine the gas temperature (T) from (4.2).

The first law of thermodynamics yields the heat release in the cylinder, the integral of which over this range of crank angles can be related to the energy of the fuel and is designated in percentage terms as the energy balance (EB), (4.3).

$$EB = \frac{\int_0^{720} \frac{dQ_B}{d\vartheta} \cdot d\vartheta}{m_B \cdot Hu} \cdot 100\% \tag{4.3}$$

In a motored engine, no energy release occurs within the cylinder, therefore the first law of thermodynamics can be solved for the heat losses and if the wall and gas temperatures are known then h can be computed.

It is therefore possible from cylinder pressure analysis between intake closure and exhaust opening, to determine the heat transfer coefficient. In a fired case only the integral of the transferred wall heat, and in a motored case the curve of h over time can be found.

It should be noted however that the heat transfer coefficients obtained using cylinder pressure analysis represent only averages over the entire combustion chamber surface, and are limited in their assumptions. Also, in order to obtain a reasonable accuracy, it is necessary to measure each of the required variables, e.g. air mass, compression ratio, mean wall temperature, pressure and crank angle, to a high accuracy. None the less, this technique provides a useful tool for indicating an averaged heat transfer rate [98].

The First Law analysis method is very sensitive to heat release and gas property calculations, as found by Shayler, May and Ma in 1993 [99]. The alternative computational approach they favoured equates cycle-averaged chamber heat transfer to the difference between heat rejected to the coolant and gas heat transfer to the exhaust port and was used as a basis for calibrating the Woschni correlation [92].

4.5 Laser-Holographic Interferometry (LHI)

Laser-holographic interferometry can provide both flow visualisation and local heat transfer distribution, however, until now usually has only been applied to the study of flow visualisation, thermal diffusion and forced and free convection phenomena. There are no recorded applications of LHI to the internal combustion engine, probably because of the practicalities involved with optical access. Figure 4.1 shows the

arrangement of a laser-holographic interferometer applied to forced convection applications.

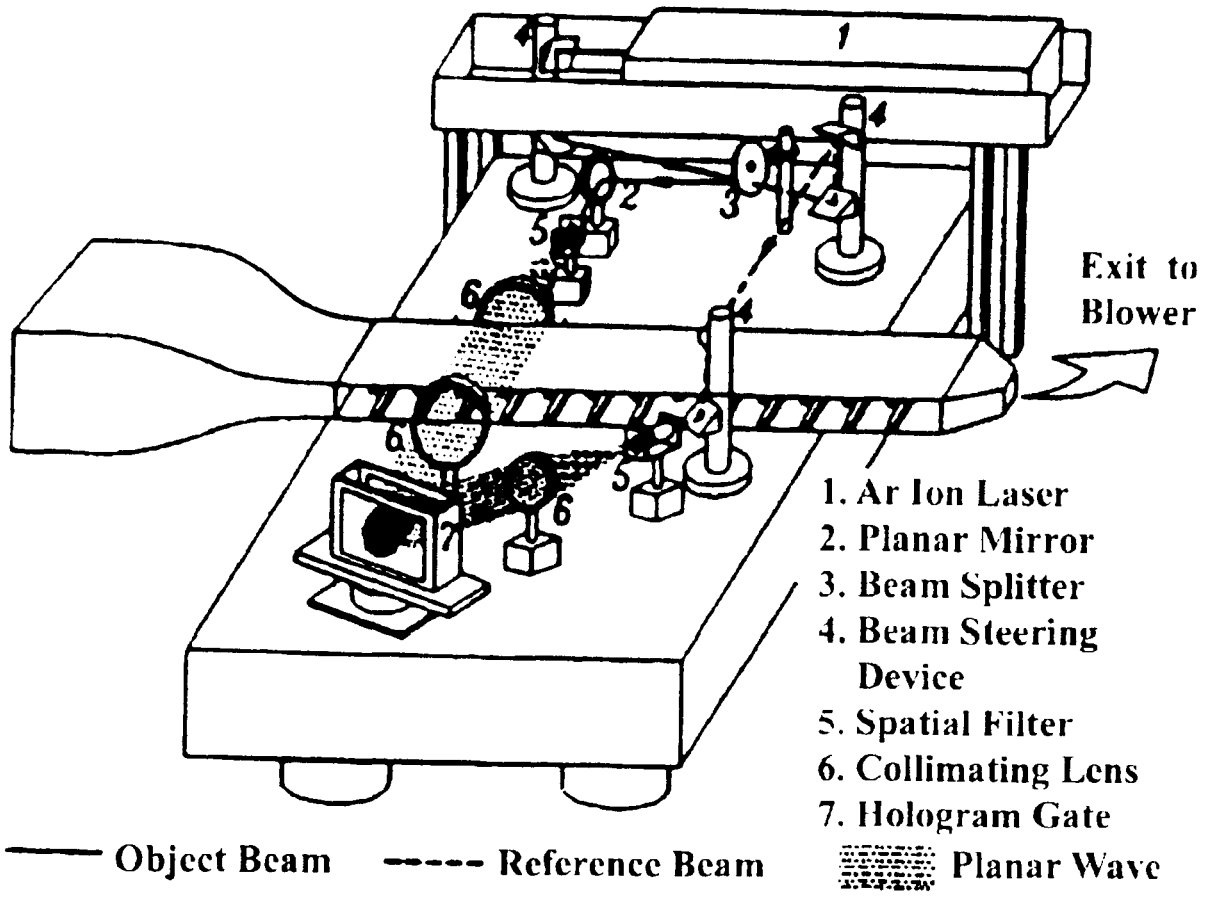

Figure 4.1, Schematic drawing of overall experimental set-up for laser holographic interferometry. (Reproduced from [77])

In Figure 4.1, before the ribbed walls are heated, the hologram is exposed so a comparison wave is recorded. When the planar object wave passes through the heated test section, it is distorted as a result of the refractive index field generated by local temperature variation in the test section. The distorted object wave passes through the hologram, where it interferes continuously with the comparison wave, reconstructed by the reference wave. Thus, an instantaneous interference field forms behind the hologram plate [77].

The LHI measurement can provide an instantaneous temperature distribution as well as local Nusselt number ratio. An application to flames is described in [77].

4.6 Temperature Measurement

In order to determine heat transfer rates, it is necessary to measure the transient surface temperature of the surface of interest. In order to measure this local transient temperature accurately in an engine, it is necessary to use a probe that is rugged enough to withstand the combustion. Also, the sensing element needs to be as small as possible, and should have a minimal heat capacity in order to follow the temperature of the flow as accurately as possible. Although heat transfer determination is well documented within the internal combustion engine, it is the stage of surface temperature measurement where most information is lost due to slow responses.

4.6.1 Eroding Thermocouple

The "Eroding" thermocouple [100-102] is designed for accurate wall-surface temperature measurements and as such is used in many experimental investigations into heat flux rates. The sensing elements in this thermocouple are in thin (≈ 25 μm), flat ribbon form at the sensing tip. This allows use of extremely thin (≈ 5 μm), flat sheets of mica for insulation purposes reducing the thermocouple size and therefore the heat capacity and permits the formation of the thermocouple junction as shown in Figure 4.2.

The thermal junction is formed by a simple abrasive action across the sensing surface with a medium grit size abrasive paper. This sanding and polishing action causes thousands of microscopic hot junctions, which join one ribbon to the other ribbon. Since the thermal junction is formed by an abrasive action, any additional erosion through usage simply removes the old junctions while simultaneously forming new

junctions. Thus this thermal sensor design has a self-renewing feature that is useful in applications where the wall is subject to wear [97].

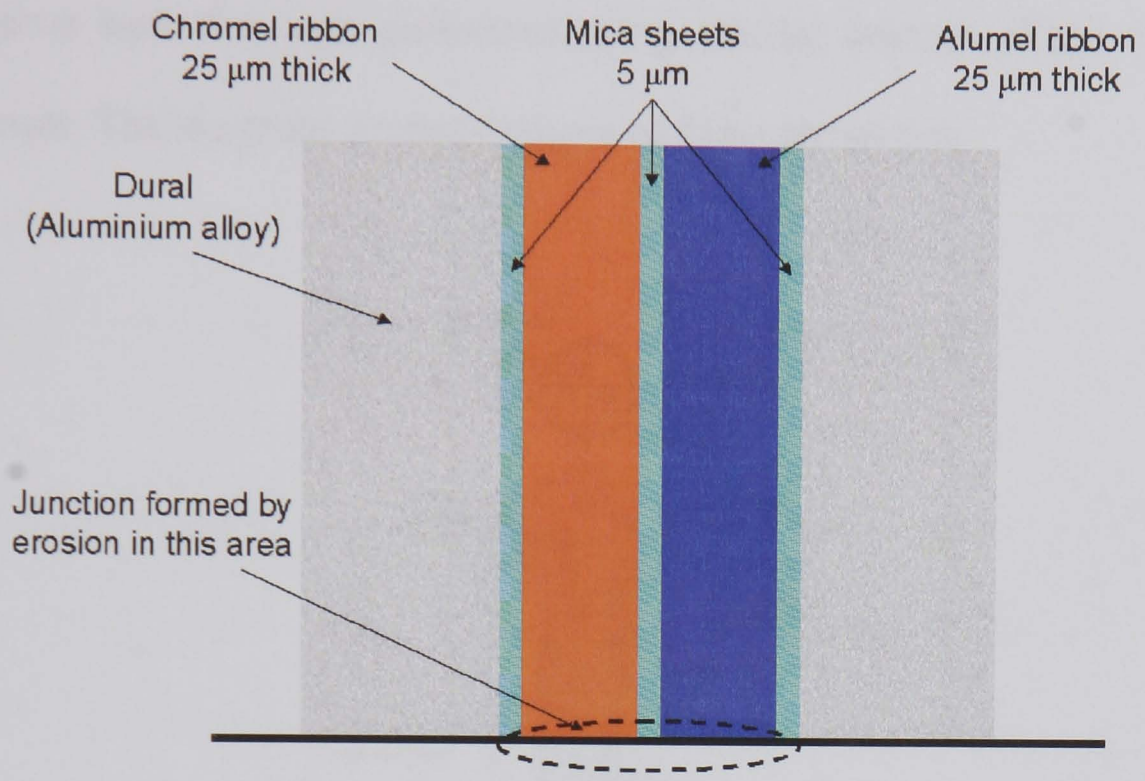

Figure 4.2, Schematic of eroding thermocouple heat flux gauge as used by Buttsworth [101].

One drawback of such thermocouples that receives little attention is the resulting 3D heat conduction through the thermocouple [101]. This is an important consideration since the application of Fourier's heat conduction equation requires 1D heat flow, which if not present requires consideration in processing which to-date has never been performed. This can be avoided by the use of thin film temperature sensors.

4.6.2 Thin Film Type Thermocouple

Harigaya & Toda [103], developed a surface temperature, wall heat flux sensor and ion probe in one convenient package, Figure 4.3. The surface temperature was measured using a thin film thermocouple composed of copper and constantan with a hot junction covered with copper plating. A second thermocouple was installed inside the sensor at a known distance, x_c (0.6 – 0.8 mm) from the surface junction. This

secondary thermocouple measures the steady state component of the heat flux. The sensor was fixed at the measuring position of the combustion chamber wall with a thermal insulating paste to encourage one-dimensional heat flow. Calculation of the instantaneous heat flux was performed using Fourier analysis of the temperature measurement. The ion probe permits analysis of flame arrival time.

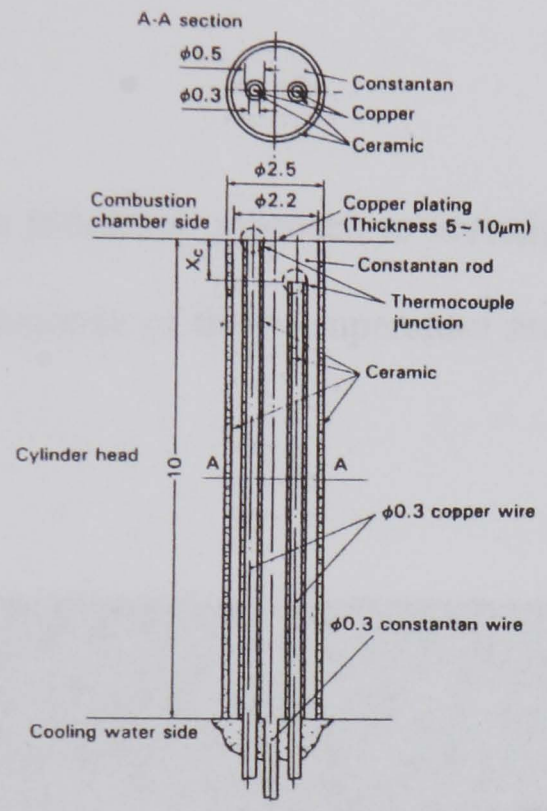

Figure 4.3, Surface temperature and heat flux sensor as used by Harigaya and Toda. [103]

The study permitted validation of previous claims by Alkidas [104,105] that the initial high rate of increase of heat flux at the measurement position coincides with the arrival of the flame front, and continues with the observation that the maximum heat flux decreases as the flame arrival time increases.

Harigaya and Toda also looked at the spatial variance of the local heat flux by taking measurements at 24 separate positions. Predictions of heat flux are derived on the hypothesis that the Nusselt number can be expressed as a function of the Reynolds and Prandtl numbers, and these equations are also assumed uniform over the

combustion chamber. Therefore, while the area-averaged heat transfer coefficient may be predicted from such equations, the localised heat transfer coefficient may not. Nonetheless, it is still required that local heat transfer is studied in order to analyse thermal problems, cycle simulation and develop more accurate models for combustion simulation; unfortunately it is generally observed that reports of local heat flux measurements on piston and cylinder head of the combustion zone are few due to difficulties in measurement.

Harigaya and Toda show a promising approach to investigating local heat flux levels. However, the frequency response of their temperature measurement may be too low for meaningful results.

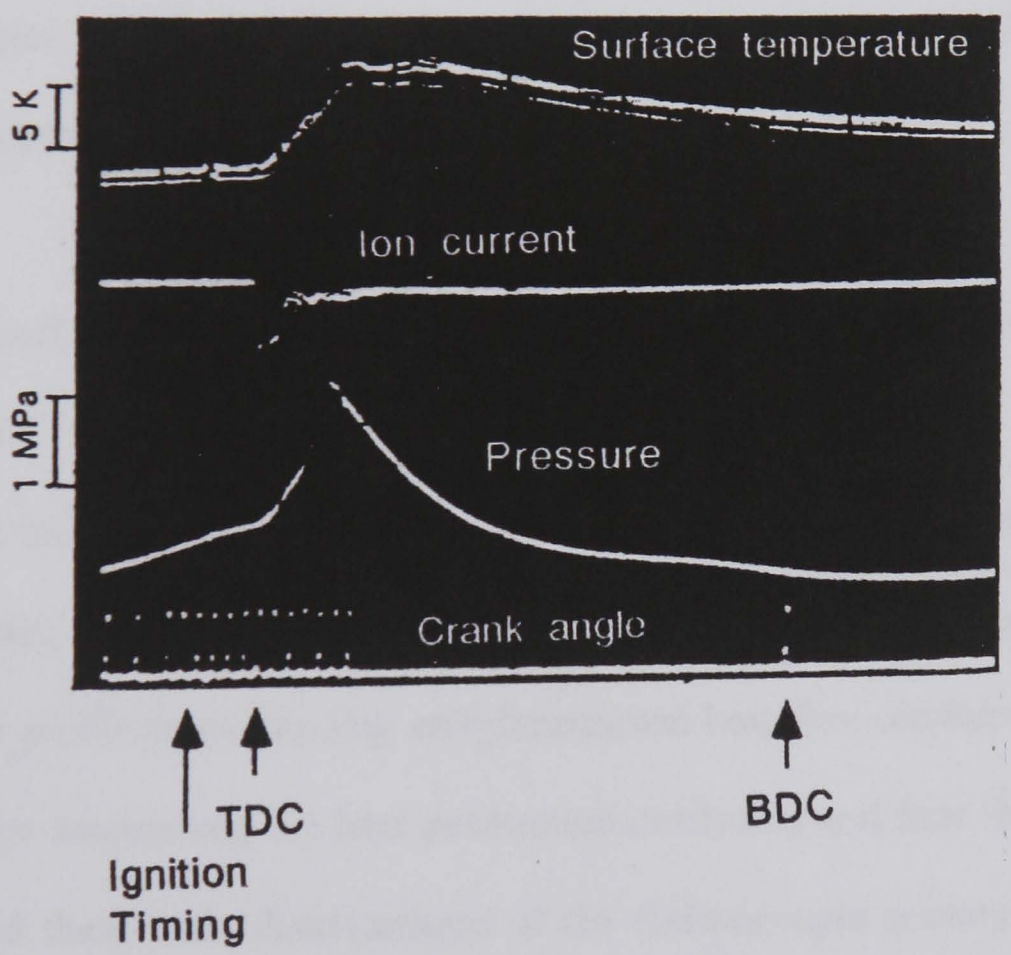

Figure 4.4, Typical trace of surface temperature and ion current. (Reproduced from [103])

Similarly, Ishii et al [106] undertook an in-depth analysis of the measurement of heat transfer in combustion chamber walls, in their case using coaxial thin film

thermocouples. Much of the work presented concentrates on computational modelling of the temperature profile through coaxial thin film thermocouples, attempting to find optimum core and insulation diameters. In this type of thermocouple, the response to temperature is non-linear and thus they need to be calibrated to extract the true temperature. Furthermore, they require the measurement of the cold junction temperature, making the use this type of thermocouple for surface temperature measurement quite complicated.

Yet again, the authors offer no discussion on the frequency response on the designs of thin film thermocouple used, and although they appear to offer an improved response over that of the design by Harigaya & Toda [103], the long time period before reading the peak gas temperature and the lack of high frequency content in the surface temperature plot of Figure 4.4 indicate a slow response. Unfortunately the authors offer no explanation.

In summary, surface thermocouples offer ease of manufacture, small packages, simple calibration and comprehensive documentation. However, they also hold certain disadvantages including the large thermal mass resulting in slow responses. Probably more significant, the different materials to be found at the hot junction of these sensors cause problems maintaining one-dimensional heat flux conditions, which is a prerequisite for determining the heat penetration coefficient and heat fluxes [107]. In order to avoid these basic disadvantages of the thermocouple sensors, the platinum resistance surface temperature sensor was developed.

4.6.3 Thin Film Resistance Thermometer

Generally these use a thin layer of a conductor deposited on an insulating layer. As the temperature of the conductor varies, it's resistance changes, which if measured can be related back to temperature. Such sensors have been successfully applied to the measurement of temperatures within the internal combustion engine [107-109] and are the sensors used in the work of this thesis. A more complete description of the manufacturing process, properties and the calculations will follow in Chapter 5, Heat Flux Theory.

In 2000, Wimmer *et al.* [107] reported on the development of a thin film resistance temperature sensor to be used in an internal combustion engine, Figure 4.5. Their conclusion was that this sensor type allows for very precise heat flux measurements, yet presents associated disadvantages, being mainly the relatively large exterior dimensions making fitting into the combustion chamber impractical, limited durability and high production costs, due to the complexity of the manufacturing process.

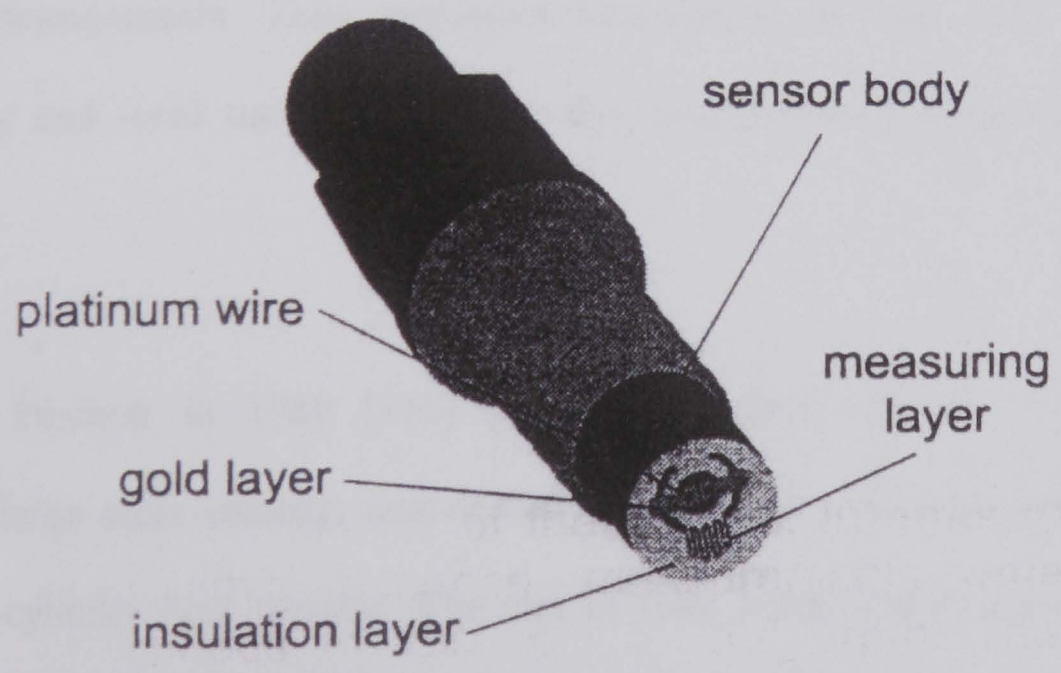

Figure 4.5, Thin film resistance temperature sensor, as used by Wimmer. (Reproduced from [107])

4.7 Previous Studies of Heat Flux

Overbye *et al.* [93] performed one of the first studies into unsteady heat transfer in engines. Their exhaustive investigation includes the design of a thermocouple and comparison to numerical predictions. The thermocouple design in particular is clever in that it uses the iron cylinder wall as a common terminal in each of the two hot junctions making installation simple Figure 4.6.

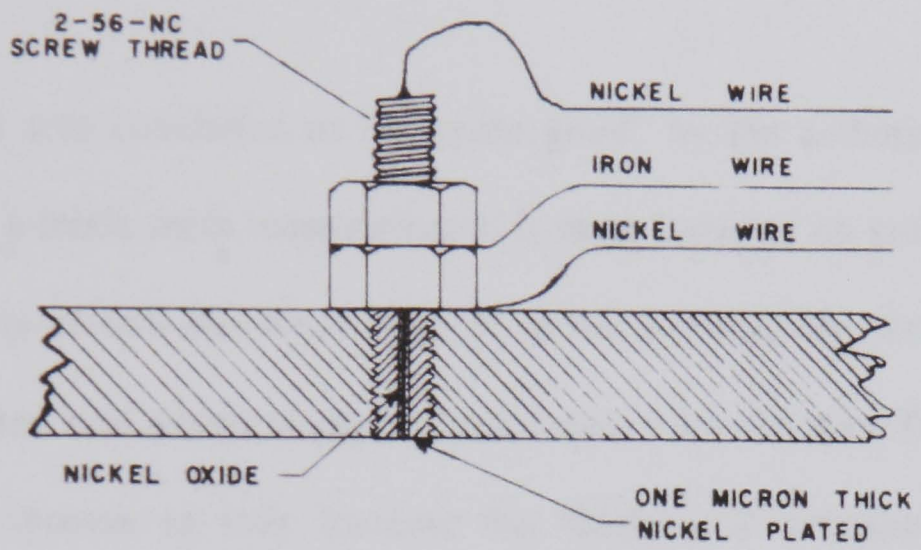

Figure 4.6, Installation and construction of thermocouples. (Reproduced from [93])

In 1990, Alkidas *et al.* looked at effects of intake-flow configuration on optical and heat flux measurements. They performed heat-release analysis, high speed flame photography and local time-resolved heat-flux measurements using thermocouples [85].

Gilaber & Pinchon in 1988 [110] performed surface heat-flux measurements, turbulence, large scale velocity, heat-release analysis and multidimensional modelling to study in-cylinder heat transfer. The aim of their work was to validate a multi-dimensional gas-wall heat transfer model applied to the case of spark-ignition engines. The investigation attempted correlating measurements of heat flux at various

locations within the engine with measurements of velocity and turbulence data obtained by LDA.

The intention was to validate a gas-wall heat-transfer model; however, due to the relative cost computationally to compute the boundary layer using a small mesh size the model was required to calculate the heat flux across the boundary layer, thus heat flux is approximated using a wall function.

The final model was concluded to be "quite good" by the authors, with predicted values showing a misfit from measurements. It must however be considered whether the measurements of heat-flux were accurate in the first instance, since the design of thermocouple used is of slower response to that claimed in the text. This inaccuracy in measured value proves to only increase the discrepancy between calculated and measured. Further investigation suggests that from observations of the measured heat flux, a much averaged and dampened heat flux is recorded.

Bauer and Heywood [111], from MIT, performed in 1988 some interesting investigations into the heat transfer of a steady and a pulsating entry flow intake manifold of a spark-ignition engine. They provide an excellent discussion on error analysis and calculation difficulties encountered determining heat transfer coefficients when faced with insulation difficulties and varying axial conduction rates.

Buttsworth and Wright [112] recently identified a 'flame structure' progressing away from the spark plug location. They used small k-type thermocouples to measure transient heat flux, instrumented in a ray from the spark plug location. Thee describe

the structure as the identification of a region of cold gas behind the flame front and propose a 5 mm structure length.

A combined investigation between the University of Twente and the University of Oxford in 2001 [102], investigate experimentally and computationally unsteady in-cylinder heat-transfer in a spark ignition engine. They found experimentally that in the expansion stroke, heat could flow from the wall into the combustion chamber, even though the bulk gas temperature is higher than the wall temperature.

This somewhat unexpected result, never previously reported, is attributed to unsteady flows and heat conduction within the gas side boundary layer of the cylinder. Modelling of the chamber showed that these unsteady effects change the phasing of the heat flux, compared to that predicted by a simple convection correlation based on the bulk gas property.

The combustion chamber was modelled with computational fluid dynamics (CFD), however measured values were not in good agreement with prediction. As a result of these findings, the authors conducted a review of boundary layer assumptions and attributed discrepancies to assumptions in the law of the wall and the Reynolds analogy.

However, this is the only investigation to make such conclusions, and the question must be raised whether such measured values are a function of the instrumentation and processing, or indeed present in the engine. Buttsworth [101] proposes, backed with probe modelling, the findings of Nijeweme *et al.* are in fact due to inaccurate

modelling of the heat flux probes in use. Buttsworth shows 3D heat conduction exists in the probes that must be taken into account, instead of the 1D conduction that is generally assumed in most processing. This assumption alone could inaccurately indicate reverse direction heat flux. Buttsworth continues and concludes that the use of thin film heat flux sensors as used for the experimental temperature measurement presented in Chapter 9, Temperature and Heat Flux results, ensure true 1D heat flow and therefore more accurate heat flux determination.

In 2000, Rakopoulos et al. [113,114] performed two studies into instantaneous wall heat fluxes in a direct injection air cooled diesel engine. Their analysis of the results revealed many interesting effects of transient engine heat transfer. In particular, simultaneous presentation of heat fluxes on the cylinder head and exhaust manifold, together with the engine indicator diagram, sheds light into the mechanisms governing the transient heat transfer [113].

4.8 Conclusions

In summary, there are many experimental techniques available for the study of combustion. These techniques vary in three regards; first the ease of application to the internal combustion engine including the degree of modification from the standard geometry required to permit the measurement. For example, PIV typically has required significant modification to the engine geometry in the way of optical pistons and optical liners; these significant modifications not only result in changes to the thermal properties, but also place the techniques outside the rapid prototyping timescales important for engine design.

Secondly, the techniques vary in their ease of use. For example, Coherent Anti-Stokes Raman Scattering (CARS) is still very much an experimental technique requiring complex equipment and significant operator skill. Conversely, pressure sensors are low cost (typically £2000) items of instrumentation used for the calculation of burn rates and effective pressure and are widely accepted as necessary in any engine test cell and that require minimal operator ability.

Thirdly, the value of information yielded by each of the techniques varies significantly. This is a difficult variable to quantify; however, by looking into industry and observing the standard practices used in engine development, conclusions may be drawn on the perceived worth of each technique. Typically it is noted that computer models are extensively used in the initial design stages of an internal combustion engine. The designers past experiences and 'feel' significantly influence this stage. Once complete, single cylinder testing (as it is the quickest technique to implement) is used considerably to fine tune and optimise the design (typically for 6 months to 1 year). Once sufficient progress is complete, multi-cylinder testing begins, followed shortly with the optical testing (PIV and flow visualisation).

The long delay before optical testing is a result of the difficulties in modifying a typical optical engine. Initial optical testing is usually not 'on-line' until thermal testing has proved a design works. Optical testing effectively is later initiated to see why. As design changes are made, they are first introduced to the single cylinders, secondly the multi-cylinders and finally the optical engines. Unfortunately, as the design stage has usually progressed a step or two from the design tested optically, conclusions drawn from the testing are therefore usually too late to be of use.

Observations of industry therefore imply that many experimental techniques are perceived to hold no value for engine development. It may therefore be concluded that for a technique to be useful in industry for engine development, it must require little operator skill, be easily applied to a standard thermal engine and provide information that assists engine designers.

It must be remembered that the other side of the coin is that computer models are extensively used for engine development. Techniques that may be used for model validation and more significantly for model development therefore have a knock on effect resulting in benefits in the engine development process. Industrial observations show that the use of computer models is increasing with engine design moving from being evolutionary, towards computational fluid dynamics (CFD) being used as a design tool.

Discussions with a premier car manufacturer have shown that until recently their computer models did not contain combustion models, and were used simply for port and chamber flow design. Engine performance prediction utilised simple two-zone engine models. With the transition towards gasoline direct injection (GDI), substantial design groundwork is covered using complex multi-dimensional flow models calculating velocity, turbulence and spray distribution and thus fuel distribution within hypothetical engine designs before testing begins. Initial engine testing concentrates on model validation, and typically many (≈ 8) iterative cycles are required before the models are representative of real flow.

Engine performance predictions are now based on flame propagation models that in turn use the velocity and turbulence distributions found with the flow models. These models are very much in their early stages of development and are requiring significant validation in the early stages of engine design. It is clear that experimental techniques useful either for model development or model validation are essential for reducing engine development time.

Finally, it has been shown that many experimental techniques are available for the study of combustion. From this background, it is decided to investigate the development of two techniques in a low cost single-cylinder engine test facility (described in Appendix A1), firstly to determine applicability to real-time engine design and secondly for application to computer model development.

The first technique is the use of optical probes. It is noted that currently there are few optical probes that may be applied to the study of combustion within an internal combustion engine, and none that are used within the real-time engine development process.

The second technique is the measurement of surface temperature and the determination of heat flux within an internal combustion engine. This technique will be evaluated for relevance to computer model development and for applicability to the engine development process.

PART III

DEVELOPMENT OF NOVEL INSTRUMENTATION

CHAPTER 5

HEAT FLUX THEORY

5.1 Overview

Of the energy available within the cylinder from the air/fuel mixture, only about 25% is converted into useful work. The remaining 75% must be transferred as heat out of the engine.

In this chapter the basic mechanisms of heat transfer are investigated and summarised, followed by the background and theory of the gauges used to measure the temperature and determine the heat flux rates within the engine. The method of gauge analysis is discussed before the mathematical theory behind the processing is given appropriate space. Finally a brief discussion of sampling rates and measurement bandwidth is included.

5.2 Heat Transfer Mechanisms

The three heat transfer mechanisms are Conduction, Convection and Radiation.

Radiation heat transfer is energy transport due to the emission of Electro magnetic waves or photons from a surface or volume. Heat transfer through radiation may be

estimated from the Stefan-Boltzmann law [115] that states that the energy flux, Φ, emitted from a blackbody at temperature T, is given by Equation 5.1.

$$\Phi = \sigma T^4 \tag{5.1}$$

where σ is the Stefan-Boltzmann constant (5.670e-8 J K^{-4} m^{-2} s^{-1})

Therefore for cylinder gas and wall temperatures of 1400K and 700K respectively (as expected at approximately 45° CA i.e. end of burn), the Energy flux emitted if the gas was a black body would be 2.04 e5 W/m^2.

Since a natural gas flame does not emit as a perfect black body, this may be corrected by multiplying the energy flux by the emissivity of the flame [116]. A Natural gas flame has an emissivity of approximately 0.25 [117], therefore, the instantaneous energy flux emitted due to radiation at 45° CA is approximately 2.04e5 x 0.25 = 0.51e5 W/m^2.

At this same instant of the combustion cycle, typical measured values of heat flux due to conduction are approximately 10e5 W/m^2. Heat flux due to radiation is therefore shown to account for approximately 5% of the total in-cylinder heat transfer. Heat transfer due to radiation within the engine may therefore be assumed negligible [87].

<u>Conduction</u> heat transfer is energy transport due to molecular motion and interaction. Conduction heat transfer through solids is due to molecular vibration. Fourier determined, Equation 5.2, that Q/A (Heat transfer per unit Area, W/m^2) is

proportional to the temperature gradient ($^{dT}/_{dx}$). The constant of proportionality is called the material thermal conductivity, k.

$$\frac{Q}{A} = -k\frac{dT}{dx} \tag{5.2}$$

Convection heat transfer is energy transport due to bulk fluid motion. Convection heat transfer through gases and liquids from a solid boundary results from the fluid motion along the surface.

Newton determined, Equation 5.3, that the heat transfer per unit area, Q/A, is proportional to the fluid solid temperature difference $T_s - T_f$. The temperature difference usually occurs across a thin layer of fluid adjacent to the solid surface. This thin fluid layer is called a boundary layer. The constant of proportionality is called the heat transfer coefficient, *h*.

$$\frac{Q}{A} = h(T_s - T_f) \tag{5.3}$$

The heat transfer coefficient depends on the type of fluid and the fluid velocity.

It may therefore be assumed that the heat transfer from the hot combustion gasses includes forced convection through the hot gas boundary layer, conduction through the cylinder wall and convection for cooling.

Heat transfer is periodic due to piston motion; when the combustion flame impacts the cylinder wall the heat flux begins rising and reaches a maximum when the cylinder temperature and pressure peaks. The penetration depth of a step pulse after a set time

may be calculated [118]. For example, in the case of Aluminium, the pulse travels 1mm in about 1 ms, whereas it takes about 160 ms to travel through a 100 μm layer of upliex and glue. As the spark in an internal combustion engine occurs significantly quicker than every 160 ms (typically every 40 ms), it is therefore known that the pulse could travel approximately 6 mm into the Aluminium over this period, but where covered by the upliex and glue, the pulse will not penetrate the Aluminium. One may now conclude that the heat flux penetration into the Aluminium will not effect the heat flux measurement, provided the temperature is measured on both sides of a layer such as upliex and glue.

As seen in Chapter 4, Review of Heat Flux instrumentation, it is impossible to measure this heat flux using thermocouples embedded in the cylinder walls. This is partly because thermocouple measurements require a wall temperature profile that is constant in order to apply Fourier's conduction equation and the constant heat conduction equation; however, by applying thin film gauges to the cylinder surface, the resulting conduction is 1D [101], permitting the measurement of both steady and transient components of heat flux.

5.3 Theory

It is known that the resistance of a conductor is affected by temperature. By monitoring the resistance of a thin film metal layer placed on a substrate of known thermal properties, the surface temperature history and the surface heat flux history can be calculated from the appropriate analytical model.

The use of such gauges is well documented [119-122], however this chapter demonstrate the application of this technique to the internal combustion engine.

Generally thin film gauges fall into three categories [121]; first when the gauge is mounted directly onto a semi-infinite layer, e.g. a platinum resistance thermometer fired onto a quartz substrate. Secondly when the surface is coated with a thin insulating layer onto which the gauges are mounted, and thirdly, as in this case, two layered gauges where the temperature difference across a layer of known thermal properties is known.

The gauges used for this experiment are accurately manufactured and glued to the surface required. A 0.5 μm thick Platinum film, sits on a 50μm insulating layer of Upliex that is bonded to the Aluminium by a premanufactured 20μm layer of adhesive.

Previously heat transfer gauges had a complex manufacturing process and a time consuming calibration process, these problems have been overcome for the thin film gauges presented here. Due to the simple manufacturing process it is possible to manufacture these gauges in a uniform and predictable way, and the calibration is only for the temperature coefficient of resistance, not for thickness or geometry.

For a detailed description of the manufacturing process, see the laboratory reports by Hofeldt [123] and Guo [124], or the paper by Piccini [122]. A brief summary is provided in Appendix A.

5.4 Analysis

When the upilex sheet is mounted onto the piston surface, the system must be analysed as a layered gauge, since the piston material has different thermal properties to the gauge. The system is calibrated in order to establish the thickness of the upilex / glue insulating layer. Even considering these different thermal properties of the gauges and piston, it is known that the gauges are non-intrusive in nature since the temperature difference across the gauge (typically 150 K) is small compared to the temperature difference between the combustion gases and the piston.

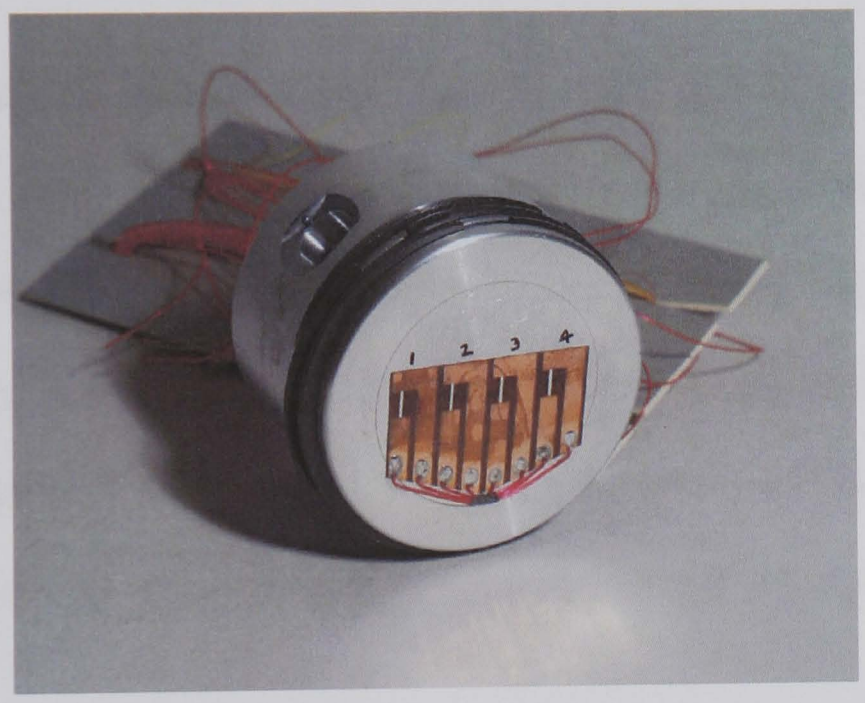

Figure 5.1, Gauges attached to the piston surface.

Figure 5.1 is a photo of the first generation of heat flux gauges; it is shown how the gauges are mounted onto the piston surface. In this example, there are four gauges mounted on the firing surface, with two thermocouples mounted on the underside of the piston. Similarly, Figure 5.2 illustrates the second-generation temperature gauges. Note that a second layer of upliex has been positioned over the soldered joints to protect them from the high temperature combustion. Gauge numbering, as used throughout this thesis, is marked for the head in Figure 5.2; whereas for the piston, gauge 1 is furthest from the spark plug and gauge 7 is closest to the spark plug.

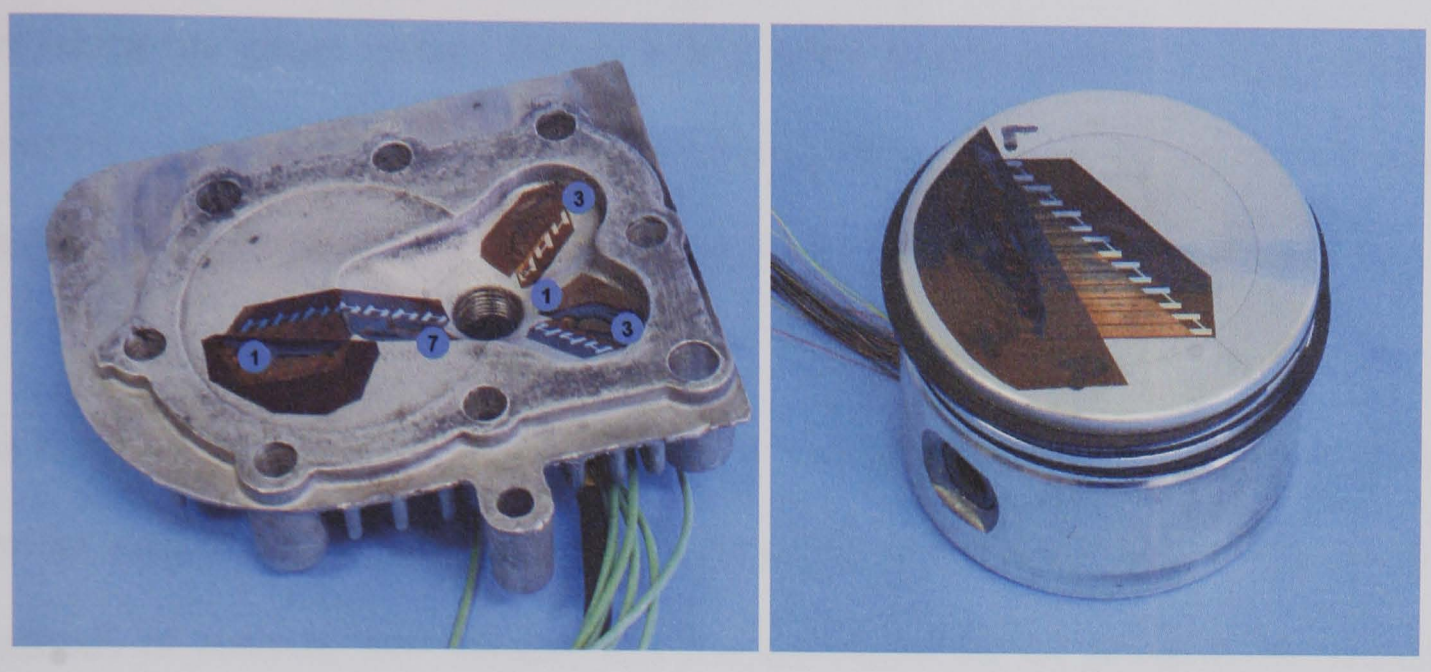

Figure 5.2, Second generation gauges shown instrumented on the cylinder head and piston.

The gauges are used in constant current analysis mode. In order to calculate the heat flux a small (less than 1mA) constant sensing current is passed through the gauge. This supply comes from a HTA1 unit. The HTA1 constantly varies the voltage in order to keep the current constant, it is this varying voltage that is amplified and measured. The change in voltage is known to be proportional to the change in the thin film resistance, and the resistance proportional to the change in temperature.

The relationship between the surface temperature (T) and the gauge resistance is given by Equation 5.4.

$$R = R_0\left(1 + \alpha(T - 20)\right) \tag{5.4}$$

where R_0 is the resistance at 20°C and α is the temperature coefficient of resistance.

Due to the nature of the gauges, they all have the same thermal properties. This simplifies the calibration, leaving α the only variable that needs calibrated for.

By taking the gauge voltage history it is possible to calculate the change in gauge resistance with respect to time and by combining this with the temperature / resistance calibration it is possible to calculate the time history of the surface temperature.

As the construction of the gauge is known, it is possible to now use a layered analysis on the surface temperature history; this yields the heat transfer rate. There are two methods of analysis, one assumes that the appearance of the piston to the thermal waves hitting the surface to be infinitely thick (semi-infinite analysis); the second finitely thick.

5.4.1 Semi-Infinite

When the back wall is assumed semi-infinite, the system is assumed to consist of two elements. A thermally insulating layer, $(i = 1, 0 < x < a)$, and the metal, $(i = 2, a < x < \infty)$, where a is the thickness of the upilex and the glue. The governing equation is,

$$\frac{\partial^2 T_i}{\partial x^2} = \frac{1}{\beta_i}\frac{\partial T_i}{\partial t}, i = 1,2 \qquad (5.5)$$

where $\beta_i = k/\rho c$. β_i is the thermal diffusivity of the layer i, defined in terms of the thermal conductivity, k, density, ρ, and specific heat, c.

With the four boundary conditions $\dot{q} = -k\frac{\partial T_1}{\partial x}$ at x=0, T_1=T_2 at x=a, $-k_1\frac{\partial T_1}{\partial x} = -k_2\frac{\partial T_2}{\partial x}$ at x=a, and $\frac{\partial T_2}{\partial x} = 0$ at x=∞. These equations have been solved for $\overline{T_1}$ and $\overline{T_2}$ using Laplace transforms, for the solution see [121].

5.4.2 Finite Depth

If the metal is assumed to have a finite dimension, the model has a thermally insulating layer, $(i = 1, 0 < x < a)$ of upilex and glue, and a metal substrate $(i = 2, a < x < b)$ of finite dimension *b-a*. In this case Equation 5.5 is solved as above, except the boundary condition $\frac{\partial T_2}{\partial x} = 0$ now occurs at x=b, not at x=∞. Solutions for this case have been obtained, however this is only required when the back wall is thin and is therefore not used in this application.

From these calculations it is possible to plot the surface temperature history and the surface heat flux history.

5.5 Processing

The writing of this section was greatly assisted by [122,125,126], see these references for further information.

Given a linear, time-invariant system, we can define a function called the impulse response function, *h(t)*, (the Laplace transform of which is called the transfer function, *H(s)*), that describes how the system responds to a impulse function, *δ(t)*. It can also be shown that the response of a system, *y(t)*, with zero initial conditions to any input

function, *f(t)*, is given by the convolution of *f(t)* with the system's impulse response, Equation 5.6.

$$y(t) = \mathscr{L}^{-1}\{H(s)F(s)\} = \int_0^t h(\tau)f(t-\tau)d\tau = h(t) * f(t) \quad (5.6)$$

where $\mathscr{L}$ is the Laplace transform

From this result two problems can be solved. First, given a known output, *y(t)*, and a known input, *f(t)*, it is possible to determine the impulse response, *h(t)*, by finding *F(s)* and *Y(s)*, where *F(s)* = $\mathscr{L}\{f(t)\}$ and *Y(s)* = $\mathscr{L}\{y(t)\}$. *H(s)* is then given by *H(s)* = *Y(s)* / *F(s)* and so the impulse response can be found from *h(t)* = $\mathscr{L}^{-1}\{H(s)\}$. This is how the impulse response is determined for the heat flux gauges.

Second, if the impulse response, *h(t)*, is known, then with any given input, *f(t)*, it is possible to determine the system output, *y(t)*. This can be done by convolving in the time domain, $y(t) = f(t) * h(t)$, or by using Laplace transforms. Now it is easy to find the Laplace of the output function, *Y(s)*, since it is given by $Y(s) = H(s)F(s)$ and by taking the inverse Laplace we get the system output in the time domain, $y(t) = \mathscr{L}^{-1}\{Y(s)\}$. This second method is how the temperature signal is processed once the impulse response is known.

The impulse response method is used to process the heat flux gauge signals. Filter impulse responses of the same length as the data are derived using deconvolution. The surface heat flux rate, *q(t)*, can be seen as the convolution of an impulse response, *h(t)*, with the measured surface temperature history, *T(t)*, see Equation 5.7.

$$q(t) = h(t) * T(t) = \int_{-\infty}^{\infty} h(\tau)T(t-\tau)d\tau \tag{5.7}$$

Since this integral can be difficult to evaluate in the continuous time domain, and as the measurements are discrete, we switch to the discrete time domain. The measured signal is sampled at intervals of T_s, so we can solve in the discrete time domain where the continuous signals $T(t)$ and $q(t)$ are replaced with discrete sequences $T[n] = T(nT_s)$ for n = … -3,-2,-1,0,1,2,3 … Now the convolution integral of Equation 5.7 is replaced by the discrete convolution sum of Equation 5.8.

$$q[n] = h[n] * T[n] = \sum_{k=-\infty}^{\infty} h[k]T[n-k] = \sum_{k=-\infty}^{\infty} h[n-k]T[k] \tag{5.8}$$

Since we are sampling for a finite number of samples (N), we are not interested in samples before $n = 0$, or after n = N. Therefore all signals are assumed zero for $n < 0$ and are not calculated for $n >$ N. These zero initial conditions meet the requirements for the convolution property of Laplace transforms. The discrete convolution now becomes Equation 5.9.

$$q[n] = h[n] * T[n] = \sum_{k=0}^{N} h[k]T[n-k] = \sum_{k=0}^{N} h[n-k]T[k] \tag{5.9}$$

for k = 0,1,2,3 … N-1

Now with a given surface temperature sample sequence, $T[n]$, and a known impulse response, $h[n]$, it is possible to calculate the heat flux through convolution.

All that remains is the determination of the impulse response, $h[n]$, for a given surface temperature sample length. $h[n]$ can be determined if a non-singular solution for $q[n]$ ($q_1[n]$) is known for a given $T[n]$ ($T_1[n]$), as in Equation 5.10. These known solutions are called the basis functions and are calculated from the known heat transfer characteristics of the gauge material.

$$q_1[n] = h[n] * T_1[n] \tag{5.10}$$

For a semi-infinite gauge, the basis functions used are a step function in q and the resulting parabolic function in T. A step function is an idealised 'switch' that switches on at time $t = 0$, and if multiplied with another function will serve to switch it on also at $t = 0$. It is determined as:

$$u(t) = \begin{cases} 1 & t \geq 0 \\ 0 & t < 0 \end{cases}$$

and graphed as:

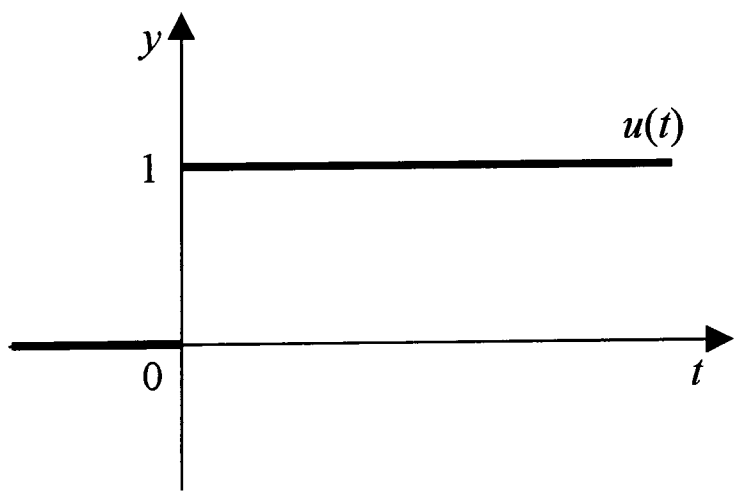

What must be determined is the parabolic function in T, Figure 5.3, that results from this step function in q; this is solved from the 1D heat conduction Equation 5.11.

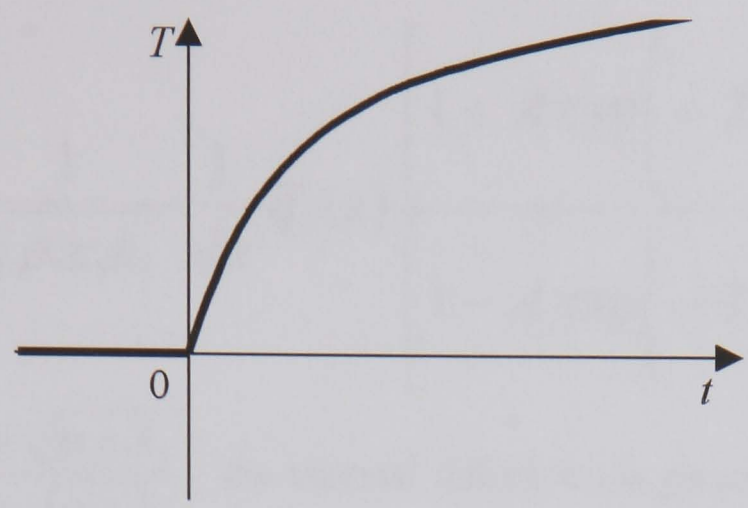

Figure 5.3, Parabolic function in *T* resulting from step function in *q*.

$$\frac{\partial^2 T}{\partial x^2} = \frac{1}{\alpha}\frac{\partial T}{\partial t} \tag{5.11}$$

where α is the thermal diffusivity, given by $\alpha = \frac{k}{\rho c}$ (k is the thermal conductivity, ρ is the density and c is the specific heat)

When Equation 5.11 is solved in Laplace space for a two layer heat flux gauge as illustrated in Figure 5.4, the solution is given by Equation 5.12, [125,127]. (Note that this solution for a two layer gauge will be used later in the solution of a double sided gauge.)

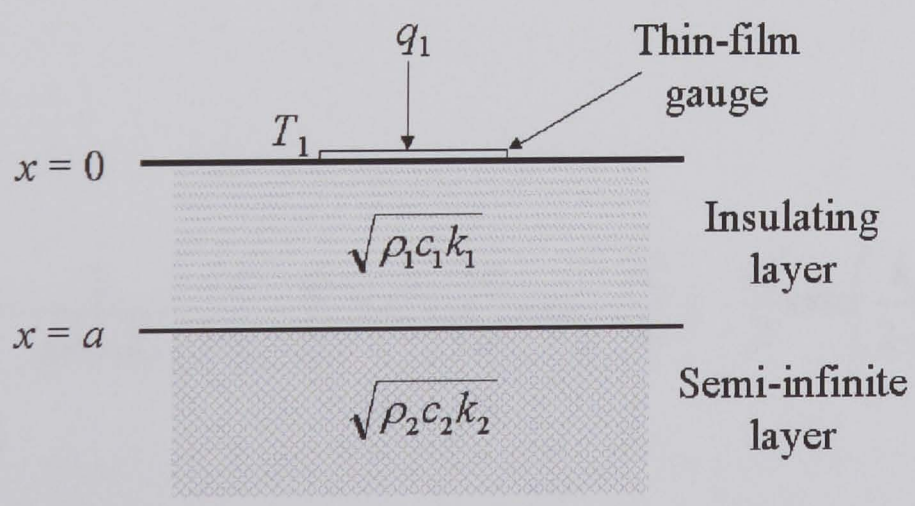

Figure 5.4, Two layer heat flux gauge.

$$\overline{T}_1(s) = \frac{1}{\sqrt{\rho_1 c_1 k_1}} \frac{1}{\sqrt{s}} \overline{q}_1(s) \frac{\left[1 + A\exp\left(-2a\sqrt{\frac{s}{\alpha_1}}\right)\right]}{\left[1 - A\exp\left(-2a\sqrt{\frac{s}{\alpha_1}}\right)\right]} \quad (5.12)$$

where $A = \frac{\sqrt{\rho_1 c_1 k_1} - \sqrt{\rho_2 c_2 k_2}}{\sqrt{\rho_1 c_1 k_1} + \sqrt{\rho_2 c_2 k_2}}$, the thermal diffusivity is given by $\alpha_1 = \frac{k_1}{c_1}$, a = the insulating layer thickness and s is the Laplace variable.

The step change in the heat flux leaves $q_1(t) = u(t)$, so taking Laplace transforms we can substitute $\overline{q}_1(s) = \frac{1}{s}$ into Equation 5.12 giving:

$$\overline{T}_1(s) = \frac{1}{\sqrt{\rho_1 c_1 k_1}} \frac{1}{\sqrt{s^3}} \frac{\left[1 + A\exp\left(-2a\sqrt{\frac{s}{\alpha_1}}\right)\right]}{\left[1 - A\exp\left(-2a\sqrt{\frac{s}{\alpha_1}}\right)\right]} \quad (5.13)$$

By taking the inverse Laplace transform of $\overline{T}_1(s)$ we get $T_1(t)$ and so return to the time domain:

$$T_1(t) = \frac{2}{\sqrt{\rho_1 c_1 k_1}} \left[\sqrt{\frac{t}{\pi}} + \sum_{n=1}^{\infty} 2A^n \left\{\sqrt{\frac{t}{\pi}} \exp\left(-\frac{k_s^2}{4t}\right) - \frac{k_s}{2} \operatorname{erfc}\left(\frac{k_s}{2\sqrt{t}}\right)\right\}\right] \quad (5.14)$$

where $k_s = \frac{2an}{\sqrt{\alpha_1}}$

Equation 5.14 is the solution in time of the response in temperature to a step change of heat flux for a two-layer heat flux gauge as illustrated in Figure 5.4.

By sampling $q_1(t)$ and $T_1(t)$, now $q_1[n]$ and $T_1[n]$ in Equation 5.10 are approximately known, making it possible to calculate $h[n]$. However, since the gauges used in this investigation, Figure 5.5, can measure the temperature both sides of the insulating layer it is necessary to re-evaluate Equation 5.10.

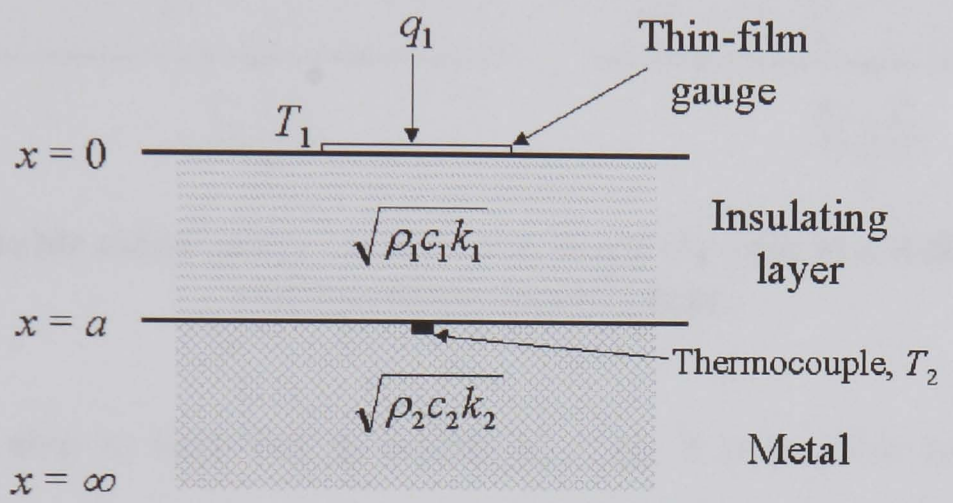

Figure 5.5, Double sided gauge as used for this investigation.

In order to determine the impulse response of this gauge, it is necessary to break it down into parts [125]. The double sided gauge of Figure 5.5 can be considered the sum of a differential gauge with temperatures $\frac{T_1 - T_2}{2}$ and $-\frac{T_1 - T_2}{2}$ top and bottom, together with a common mode gauge with temperatures $\frac{T_1 + T_2}{2}$ both top and bottom, Figure 5.6.

Each of these individual parts can now be solved using the solution previously determined for a two-layer gauge. For the differential gauge, the temperature at mid depth ($x = a/2$) is $T = 0$ and corresponds to an infinitely conducting lower substrate

giving A = -1. For the common mode gauge, at the mid depth ($x = a/2$), q = 0 and corresponds to an insulating lower substrate giving A = +1.

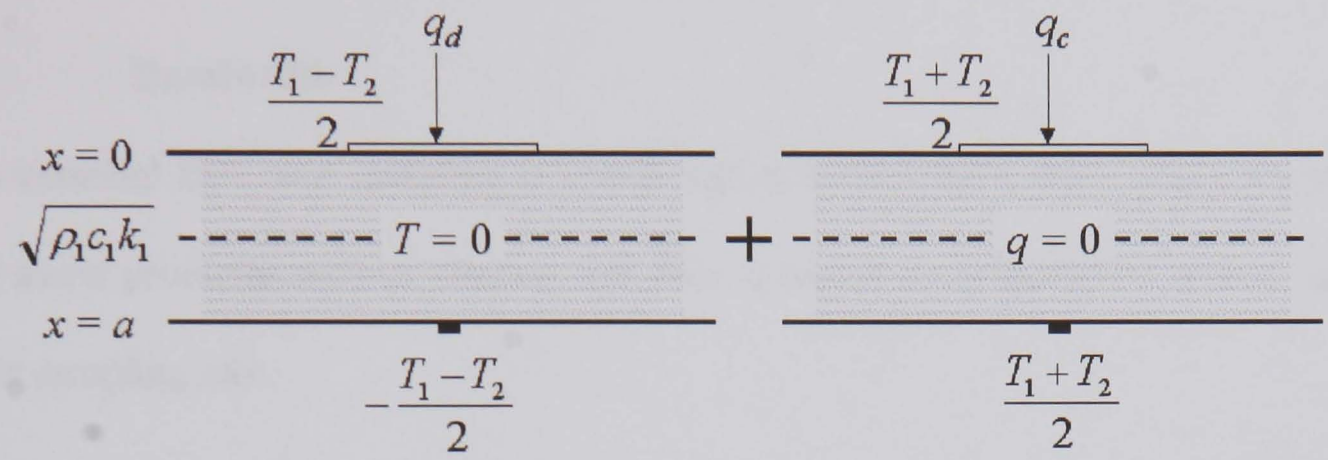

Figure 5.6, Double sided gauge can be considered the sum of a differential gauge and a common mode gauge.

Since the unit step in heat flux q_1 equals $q_c + q_d$, it is possible to determine the common and differential mode impulse responses, $h_c[n]$ and $h_d[n]$, from these solutions and unit steps in the heat flux, q_d and q_c, by summing the solutions from convolution theory, Equation 5.15.

$$q_1 = q_c + q_d = h_c * \frac{T_1 + T_2}{2} + h_d * \frac{T_1 - T_2}{2} = T_1 * \frac{h_c + h_d}{2} + T_2 * \frac{h_c - h_d}{2} \quad (5.15)$$

so, if we define h_1 and h_2 as, $h_1 = \frac{h_c + h_d}{2}$ and $h_2 = \frac{h_c - h_d}{2}$, from Equation 5.15, Equation 5.10 becomes:

$$q_1 = T_1 * h_1 + T_2 * h_2 \quad (5.16)$$

It is now possible from Equation 5.14 and the definitions of a common mode gauge and differential mode gauge to determine T_1 and T_2 resulting from a step change in q.

So finally the impulse responses h_1 and h_2 may be found and used to process the measured temperatures each side of the insulating layer that yield the heat flux from Equation 5.16.

5.6 Bandwidth

It is essential that data sampling is conducted at a sufficiently high frequency to not only avoid problems such as aliasing, but also to ensure no information is 'lost' due to a low sampling rate.

The combustion that occurs within an internal combustion engine is unsteady. An unsteady flow is one that by definition varies with time. Making measurements of such a flow requires that sufficient measurements be taken at a high enough frequency rate or bandwidth. The characteristic frequency of the flow, f, is given by,

$$f = \frac{v}{I} \tag{5.17}$$

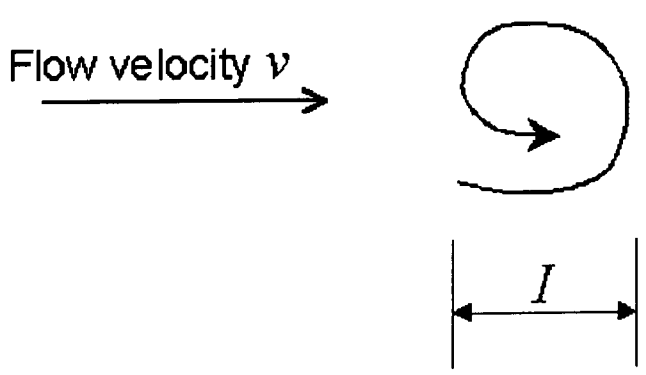

Figure 5.7, Determination of the characteristic frequency. (Modified from [35])

Where v is the characteristic velocity of the disturbance being measured (usually the convection velocity) and I is the characteristic length of either the disturbance or the transducer size making the measurement, [35].

For the heat flux measurements the characteristic length is taken as the transducer length (2 mm) since this is assumed smaller than the turbulent structure size, estimated at about 5 mm. The flow velocity can be calculated from either the measurements from the heat flux gauges or from the optical measurements, and is found to be less than 70 m/s at an engine speed of 3000 revolutions per minute (RPM).

The characteristic frequency is therefore calculated at 70/0.002 = 35 kHz. Since no measurement was taken with a sampling rate of less than 100 kHz, and the anti-aliasing filter was set at 50 kHz, it may be assumed that a sufficiently high sampling rate was chosen.

However, the characteristic frequency, f, of a turbulent boundary layer of thickness, t, and characteristic velocity, v, is given by,

$$f \approx \frac{v}{t} \tag{5.18}$$

The characteristic velocity is known to have a maximum of 70 m/s, and if the boundary layer thickness is assumed to be 1.5 mm, the characteristic frequency is shown to be ≈ 50 kHz. This is at the limit of the current data acquisition system.

The dimensions of the thin film gauge affect the maximum frequency response of the gauge as follows [35]. As the thickness of the thin metal resistance layer increases, the response to higher frequencies reduces. Oldfield, University of Oxford, proposes that

a 100 kHz response requires a gauge thickness no larger than 0.5 μm, [35]. The gauge thickness in this case (0.04 μm) is therefore known to permit a 100 kHz bandwidth.

Similarly both the gauge width and the flow velocity limit the gauge rise time, Equation 5.19.

$$\tau = \frac{w}{v} \tag{5.19}$$

For example, to achieve a bandwidth of 100 kHz a rise time of less than 1.6 μs is required. In order to achieve this 100 kHz bandwidth with a flow speed of 70 m/s, the gauge width must be no greater than 1.6E-6 x 70 = 1.12E-4 m, or 112 μm. As the gauges used in this investigation are 100 μm by 2 mm, it is obvious that orientated in one direction a bandwidth of greater than 100 kHz is achievable, whereas in the other direction the bandwidth is reduced to 35 kHz (which is approximately the predicted characteristic frequency of the flow).

5.7 Conclusions

It may be concluded that from basic calculations, the heat flux gauges as used in this series of experiments are capable of a bandwidth of at least 100 kHz. Reducing the width and thickness of the gauges could increase this figure, although gauge robustness should be considered before such modifications. It must be noted, however, that the gauges used (each gauge measuring 100 μm by 2 mm), may be positioned in one of two orientations, i.e. with the 2 mm edge parallel or perpendicular to the direction of flame travel. Although in this instance the gauges are parallel to the flow and therefore are less sensitive to turbulent structures within the

flow, it may be assumed that they are capable of a sufficiently high frequency measurement. It is recommended that during further work the effect of alternative gauge orientations be investigated. Note however that the bandwidth of the gauges is sufficiently high to provide an accurate measurement of surface temperature and heat flux; it is the small-scale turbulence that the gauges will be less sensitive to, making structure tracking more challenging.

Similarly, it has been shown that the frequency of the predicted turbulent structures is below Nyquist's criterion for avoiding aliasing when the sampling rate of 100 kHz is used.

CHAPTER 6

DEVELOPMENT OF OPTICAL SPARK PLUG

6.1 Summary

Described is the research and design of an optical probe for viewing non-intrusively the combustion phenomena through a modified spark plug. Also described is the design and testing of optical combustion probes, capable of providing images of not only combustion, but also qualitative and quantitative descriptions of the flows occurring within the internal combustion engine, in a manner that does not disturb the processes within the engine. Flame imaging, flow visualisation and PIV are described using a novel spark plug optical probe. Field curvature, aberrations and image quality are considered and where appropriate measures have either been taken to improve quality or to correct for undesired effects.

The work of this chapter was carried out with Richard Marsh as part of his MRes research project [76].

6.2 Current Techniques

From literature there are three main methods for providing non-intrusive optical access to study the combustion phenomena within an internal combustion engine: optical/transparent engine, 'small' windows or optical probes placed in the wall.

6.2.1 Optical Engine / 'Small' Windows

The most common method of providing optical access to the combustion chamber is to construct an optical engine or to fit optical windows to the combustion chamber. Such engines are widely used for engine research and provide much useful information. They are effective in providing easy optical access; however they suffer drawbacks such as significantly altered heat transfer rates, large financial outlay and significant preparation time. Therefore, not only are the results from such engines now intrusive measurements since the engine characteristics have significantly changed, but the large preparation time results in optical engines lagging behind the engine development process, being one or two stages or generations behind as they do not meet the manufacturing speed required for rapid prototyping.

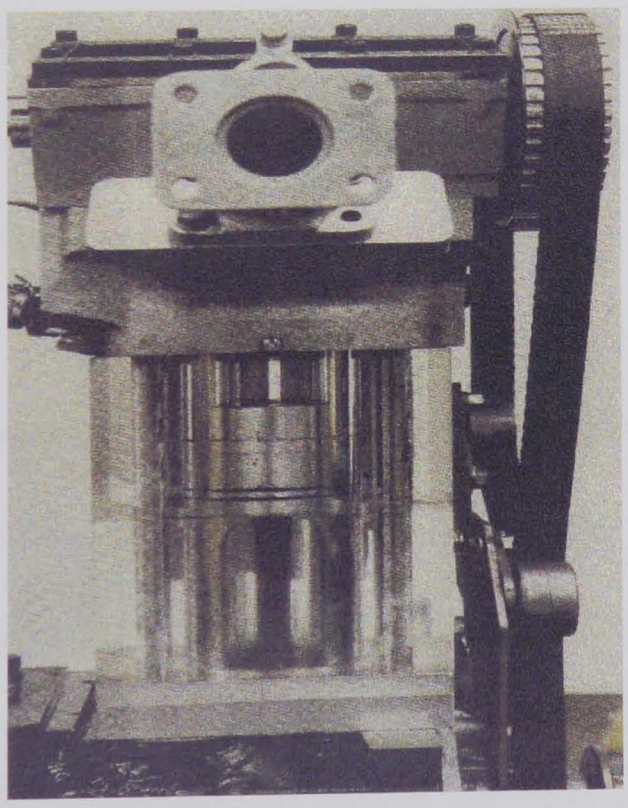

Figure 6.1, Optical engine as used by Rover Group.

There have been various attempts at combating the drawbacks of optical internal combustion engines, such as optical windows inserted into a conventional engine, or using only an optical piston instead of a complete optical head or bore, but such

designs have not been overly successful, still requiring a substantial cost investment, being difficult to alter and still having significant flat optical surfaces resulting in different heat transfer rates and altered flows instead of the profiled metal surfaces.

6.2.2 Colour Tune Spark Plug

An alternative to obtain optical access is to use an optical spark plug. A commercially available product has been in use for a number of years by automotive enthusiasts to study combustion chamber luminosity. The 'Colortune window' is a fully functioning spark plug that includes a semi-transparent high temperature epoxy-based insulator. Using the spark plug, the user can view the 'colour' of the flame and from a supplied colour chart, perform crude spectral diagnostics by tuning the engine to deliver a blue flame, which is indicative of cleaner combustion as apposed to a yellow flame that implies a broadband soot content to the combustion process. The plug is used to improve engine efficiency and reduce emissions. Due to the transmission properties of the epoxy resin it is not possible to obtain any kind of flame image, instead just a general indication of the flame colour.

The device is readily available, retailing for less than £20. It is capable of safely withstanding the combustion chamber idle conditions for run times of 10 to 15 minutes, however will fail under load or driving conditions. Such a product proves the application of a spark plug for optical access, but in its current form the lack of durability yields it unsuitable for engine development application.

6.2.3 Optical Probes

Several institutes and manufacturers, (e.g. The Rover Group, DERA (now QinetiQ) and Rolls Royce Aerospace), have designed optical probes for the spectral analysis of combustion. Prof. J. Jones of Heriot-Watt University designed the probe used by Rover Group. It views combustion through a special access point in the chamber directed towards the spark plug region, and captures light of the combustion process with a 2 mm diameter fibre optic cable bonded with an epoxy resin into the probe. This fibre is not focused in any manner, and simply collects light from its cone of vision defined by the numerical aperture of the fibre, Figure 6.2. In order to use such a probe the additional access point is required, leaving it unsuitable for some engines, and light from large portions of the cylinder is not collected.

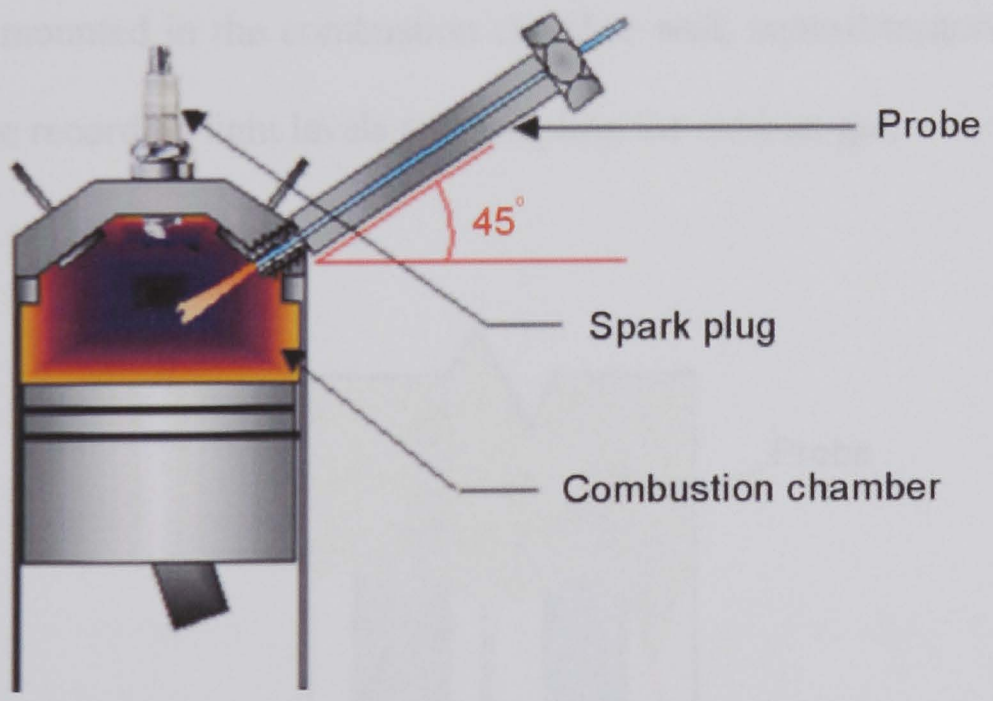

Figure 6.2, Schematic representation of Rover optical probe in-situ.

The light collected with the optical probe is filtered with a monochromator to allow sampling of one particular wavelength with resolution of 0.5 nm at ¼° CA intervals. It was designed to withstand 2000 K and 50 bar pressure, and is therefore a rather durable probe that may be used in a modified engine to view spectral content of the combustion flame. Soot deposits on the fibre give the disadvantage of reduced light

intensity the longer the engine is operated, requiring the probe to be removed and cleaned before additional data is captured. This restricts ability to make quantitative light intensity measurements as the light intensity recorded varies with engine run duration due to soot build up.

QinetiQ designed and manufactured an optical probe that is purged using Argon gas, at a pressure slightly higher than the combustion pressure, past the fibre optic to reduce the soot deposits. The probe simultaneously samples the combustion gas at its point of insertion. It is successful in capturing optical data in the combustor of a modified gas turbine engine, however has limited application to the combustion zone of an internal combustion engine since the purging of an inert gas is not feasible in a chamber of varying high pressures. The probe design is shown in Figure 6.3. The probe is not mounted in the combustion chamber wall; instead transverses across the exhaust plume recording light levels and sampling the exhaust gas.

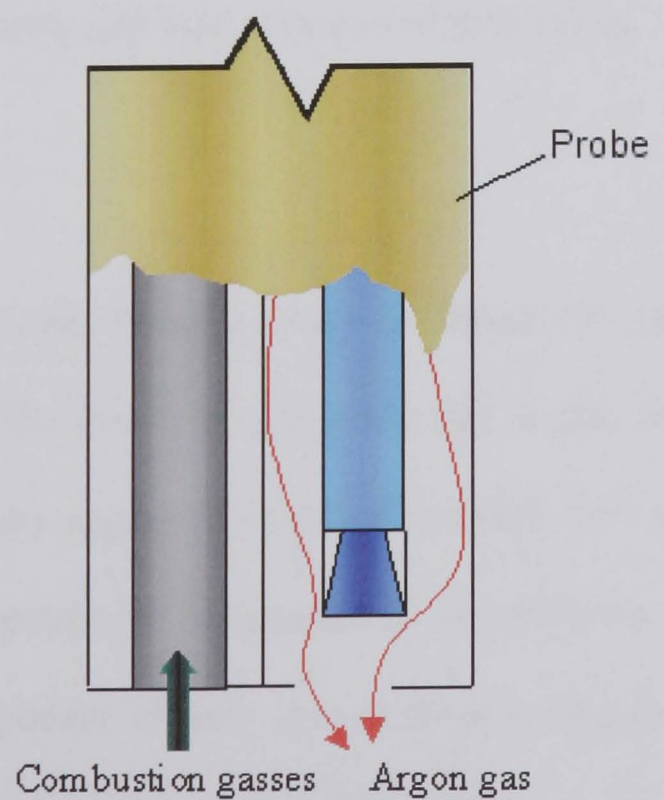

Figure 6.3, Schematic of QinetiQ probe.

In addition Rolls Royce aerospace designed a probe similar to the Rover probe that collected light directly from a fibre with no associated light collection optics. The probe was not again not mounted in the combustion chamber, instead was mounted downstream viewing the exhaust plume of the gas turbine. It is not described due to the similarities between it and the above designs.

6.3 Probe Specification

Consultation with industrial automotive partners led towards an agreement of specification. The automotive partners were keen to have a system that could provide in-cylinder engine diagnostics without modification to the test engine, since optical engines were proving to not be suitable in terms of development time. It was decided that the probe must allow a view of the entire cylinder, without any modification to the engine block or cylinder head, and the system must be capable of providing flow, velocity and spectroscopic data at around 1° CA resolution. In addition to this, it was important to develop a system that was durable and easy to use.

6.4 Spark Plug

The preferential access point through which to image the combustion chamber is through the spark plug. The principal reason for this is that the use of a spark plug would enable practically any engine to be quickly modified for optical access, without requiring special access points to be machined, or stripping and rebuilding of the engine. Simply one component already standardised in dimensions can be screwed into place and used for non-intrusive optical diagnostics.

However, in order to make the 'optical spark plug' non-intrusive and generally applicable, it is necessary to construct a device that stays close to the design of an existing spark plug, yet simultaneously offers sufficient optical access. A modern spark plug has many components, each performing a specific task as described below in Figure 6.4. It is a basic requirement that the components of the designed spark plug perform each of these functions.

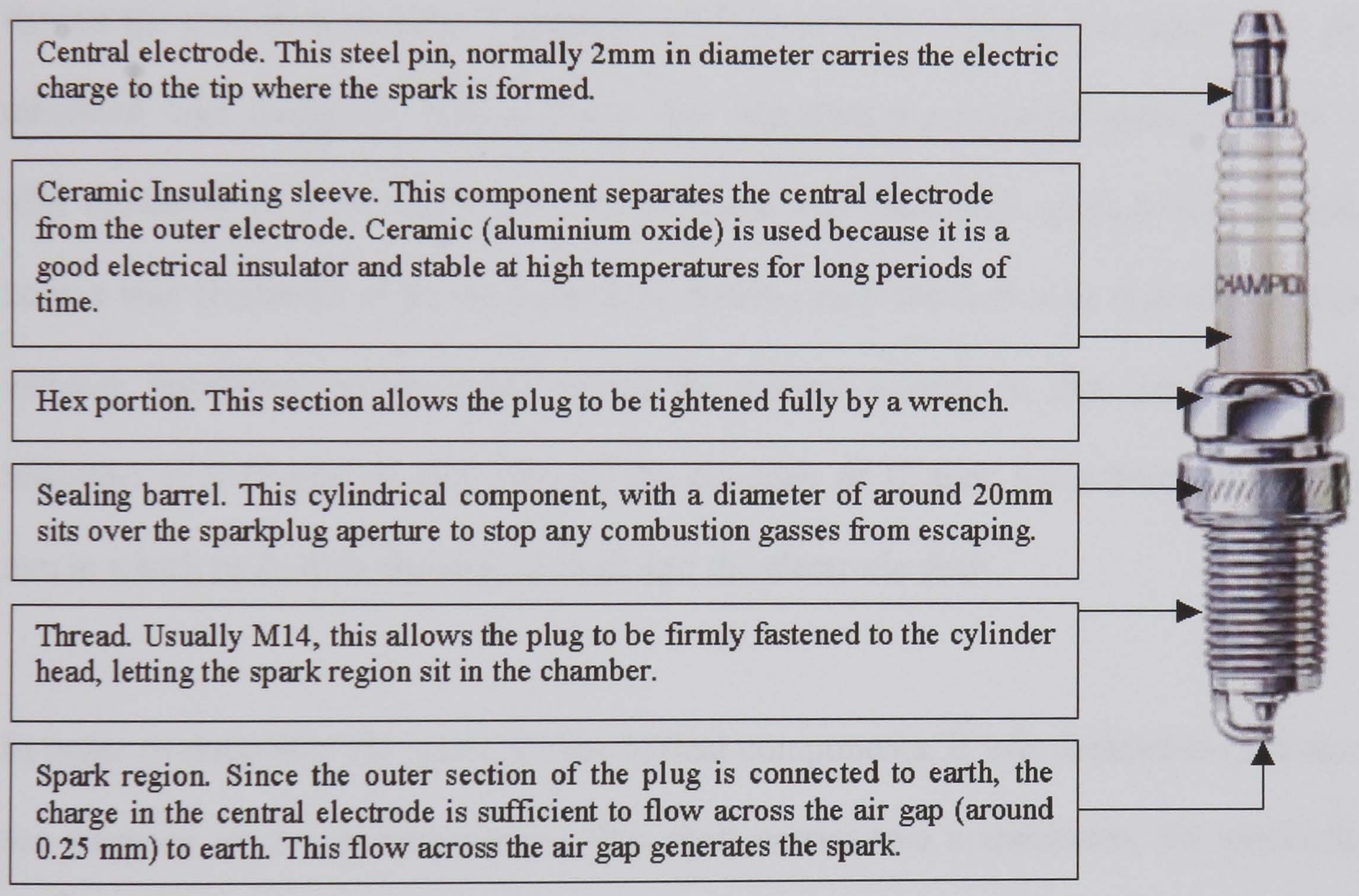

Figure 6.4, Schematic of a typical spark plug. (Reproduced from [76])

It may therefore be summarised that the minimum requirements that the spark plug must fulfil are,

- Ability to screw into a M14 thread and seal with the cylinder head
- Electrode should easily connect to flying high voltage lead
- Electrode must also be sufficiently insulated from other metal components
- A similar spark should be produced compared to conventional spark plugs
- Must provide optical access to the combustion chamber

The design falls into two parts, first the spark plug body must be designed that allows maximum room for the electrode and optics, and second the electrode and optics must be designed to fit the body.

The body of the spark plug is required to withstand the forces that will be applied to it, both from the pressure due to combustion and the torque required initially to tighten the plug into position. Calculations of these forces were performed to find the minimum wall thickness. It was found that including a substantial safety margin, a wall thickness of 0.75 mm would be sufficient. As traditional spark plugs typically have a wall thickness of about 2 mm it is obvious they are well over manufactured to increase durability. As durability is not the highest priority in this context, a wall thickness of 0.75 mm on each side off the diameter of 12 mm, left a diameter of 10.5 mm in which to fit both the optical shaft and the electrode shaft.

In order to maximise the space for the optical components, it was decided to minimise the diameter of the electrode shaft. This shaft carries two components, the electrode itself and the insulator. Experimentally it was shown that an electrode diameter of greater than 0.5 mm did not affect the spark discharge; considering a typical electrode potential of 15 kV with an aluminium oxide insulator with dielectric breakdown strength of around 40 $\times 10^6$ V/m, an insulator thickness of around 0.375 mm is shown to be sufficient.

An extruded, commercially available, cylindrical cross section aluminium oxide insulator with wall thickness 0.375 mm, interior diameter 0.55 mm, exterior diameter 1.3 mm and length of 50 mm was therefore chosen, Figure 6.5.

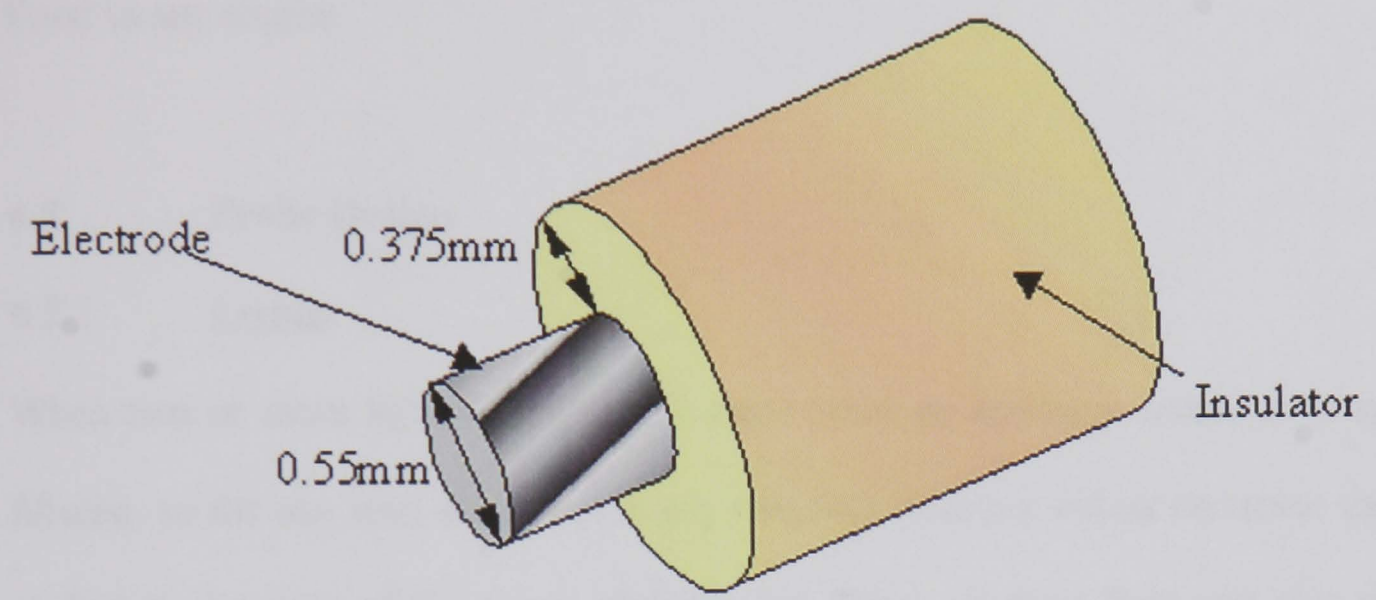

Figure 6.5, Schematic of electrode and insulator.

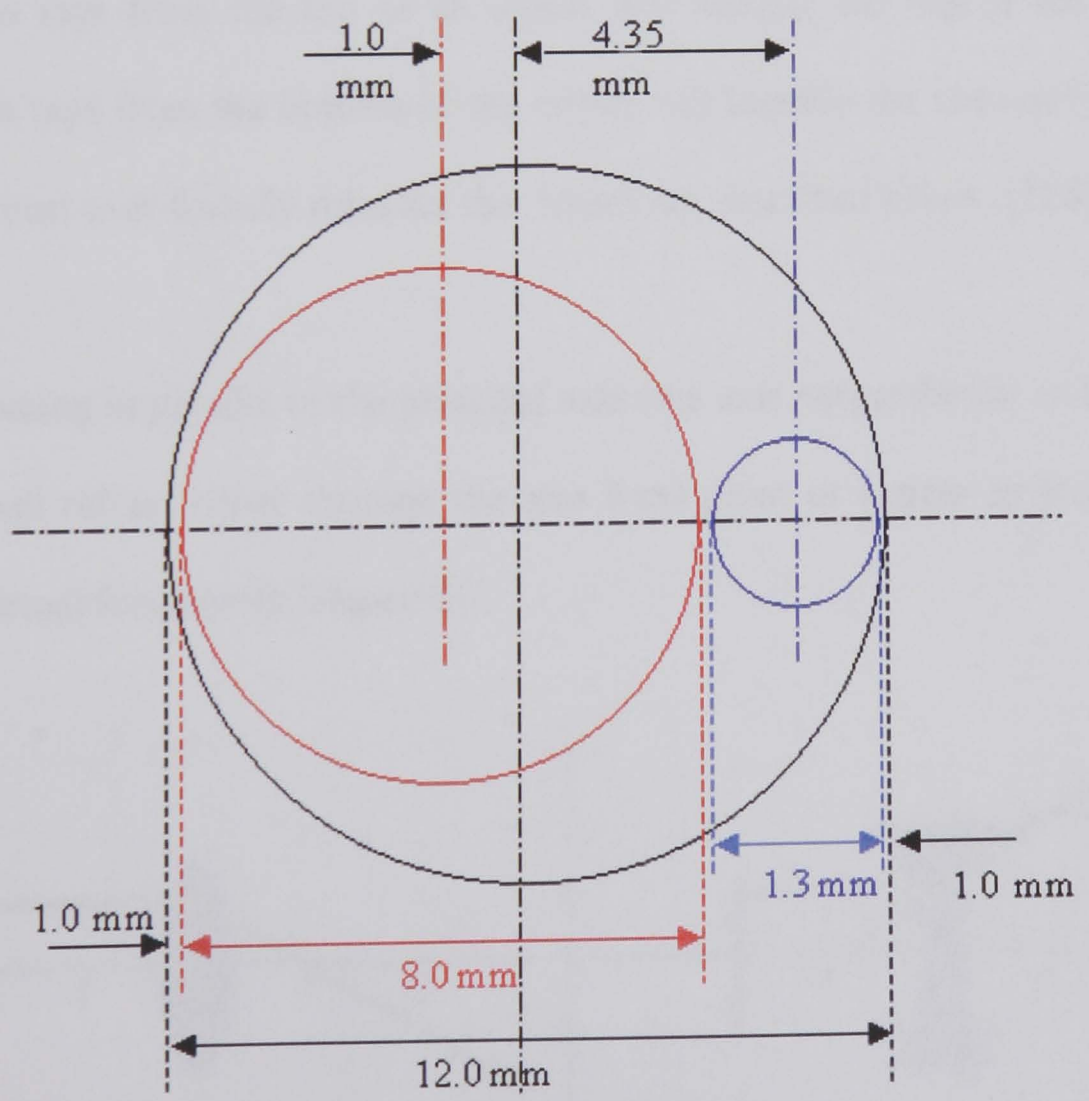

Figure 6.6, Plan view of optical and electrode shafts.

Now given the external dimensions of the electrode and insulator, it may be calculated the diameter available for the optics is approximately 8 mm, see Figure 6.6. The optics must be designed to fit within an 8 mm diameter to achieve an optical probe that can image the entire combustion chamber and be in a package that can be easily fitted to any engine.

6.5 Probe Design

6.5.1 Lenses

When two or more light rays from the same point on an image cross, an image gets formed, so for any lens, we can pick any two rays from our object and trace them out to find the location of the image of that point. There are three light rays that are easy to trace, using any two of them will identify where the location of the image is. So, tracing two rays from the top of an object will identify the top of the image, and tracing two rays from the bottom of the object will identify the bottom of the image. The three most user friendly rules for thin lenses are described below, [128].

Any ray coming in parallel to the principal axis (the axis perpendicular to the centre of the lens) will refract either through the lens focal point or appear as though it came from the virtual focus point, Figure 6.7.

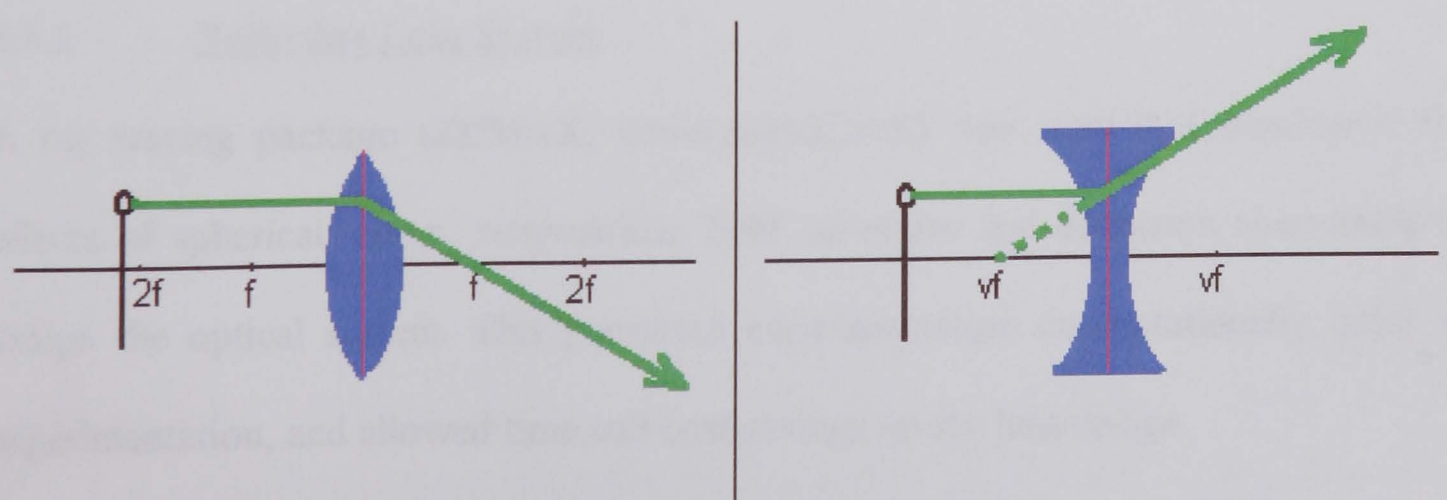

Figure 6.7, Rule 1: In parallel, out through focal point. [128]

Any ray coming through the focal point (or seeming to pass through the virtual focus) will refract parallel to the principal axis, Figure 6.8.

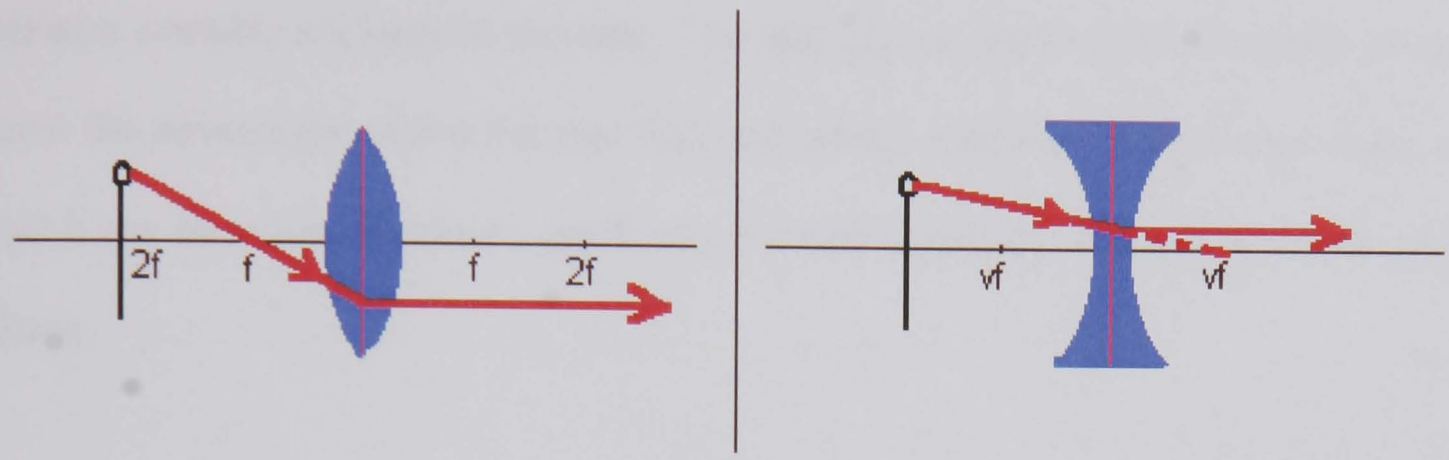

Figure 6.8, Rule 2: In through focal point, out parallel. [128]

Any ray passing through the centre of a lens will pass straight through without changing direction, Figure 6.9.

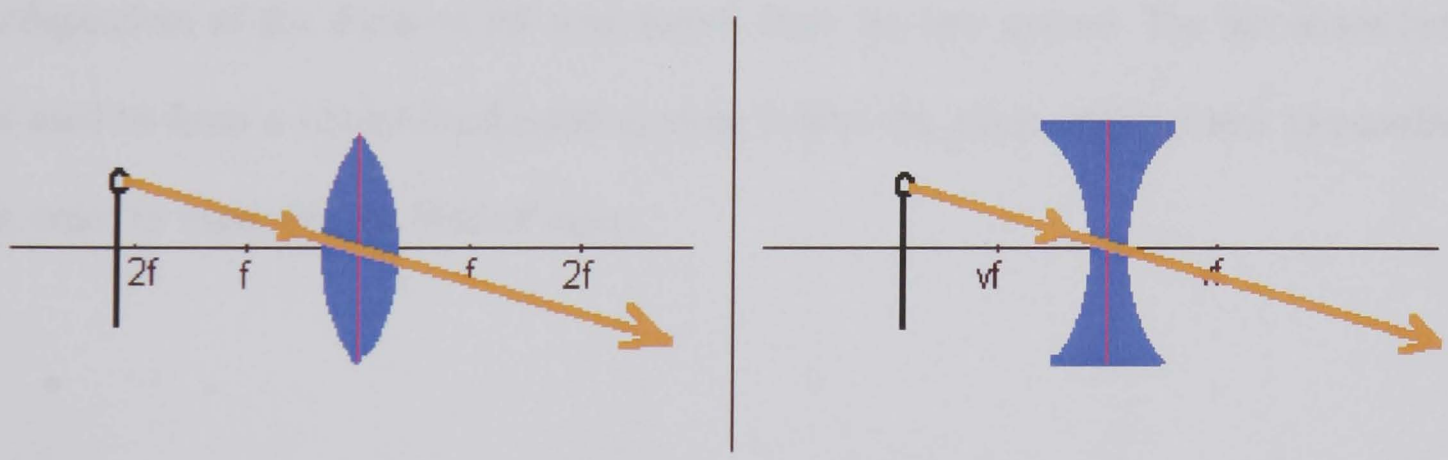

Figure 6.9, Rule 3: In the centre, out the centre. [128]

6.5.2 Collecting Lens System

A ray tracing package (ZEMAX, www.zemax.com) was used that considered the effects of spherical, coma, astigmatism, field curvature and distortion aberrations to design the optical system. This permitted experimentation computationally, prior to experimentation, and allowed time and cost savings on the lens design.

In order to image the maximum proportion of the engine cylinder, a very wide-angle lens must be used. Such a lens system available today is a 'fisheye lens'. A fisheye lens system consists of many lenses arranged in a manner that provides a very wide field of view and an increased depth of field; however all commercial fisheye lens systems available are large in diameter. The lens system required for the probe should have the advantages of the fish eye lens, but with a maximum diameter of 6mm, so that it can be mounted within a spark plug for non-intrusively imaging the combustion flame.

Figure 6.10 shows the ray trace diagram of the lens system used in the spark plug. It may be observed that the focal point is an imaginary focal point. The observer is positioned to the left of the diagram, where the rays are exiting parallel. These parallel rays result in a very large depth of field where the object is always in focus, independent of the distance the user stands from the lens system. The biconcave lens is used to form a virtual focal point as close behind the plano-concave lens as possible in order to maximise the field of view.

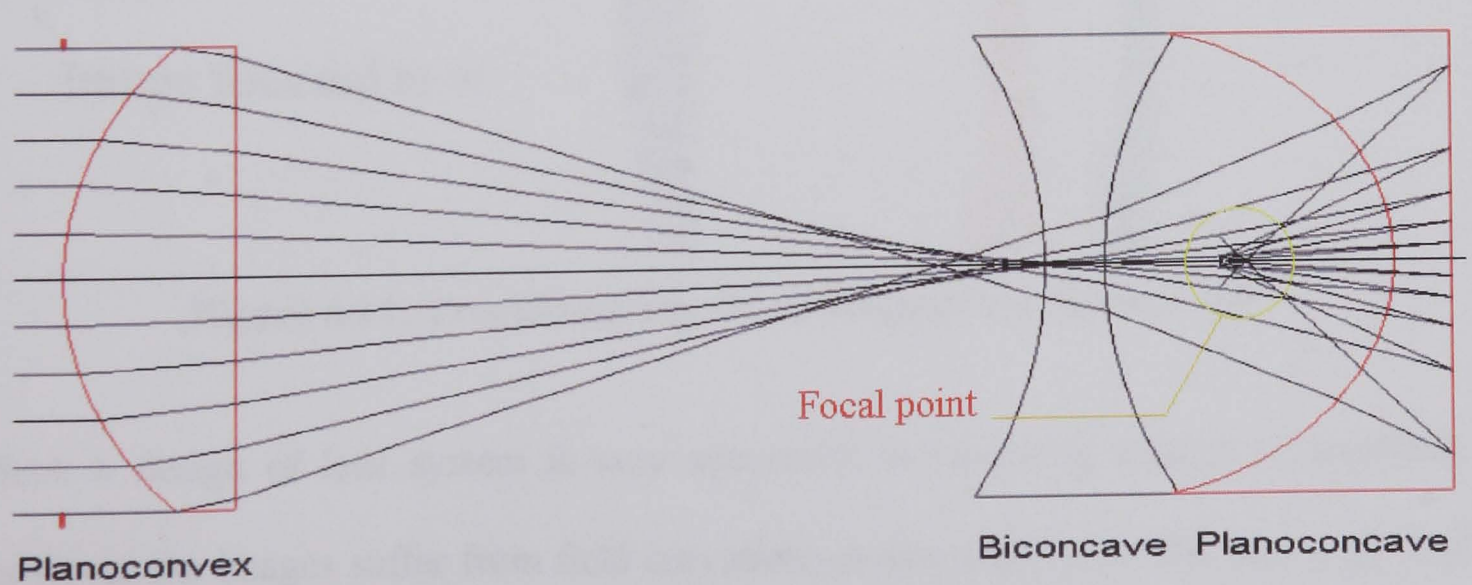

Figure 6.10, Ray trace diagram of lens system. (Reproduced from [76])

In essence, the two concave lenses collect the image at both a wide field of view and a large depth of field, whereas the convex lens is used to focus the image at infinity for viewing. This is shown in a traditional ray trace diagram in Figure 6.11.

This traditional ray trace diagram helps explain the optical mechanisms at work. The first concave lens reduces the object to a smaller imaginary image. The second concave lens reduces this imaginary image further, into a much smaller imaginary image. The convex lens simply acts as a telescope to focus this small image at infinity. In essence, the large field is reduced to a very small imaginary image and focused for viewing or image collection.

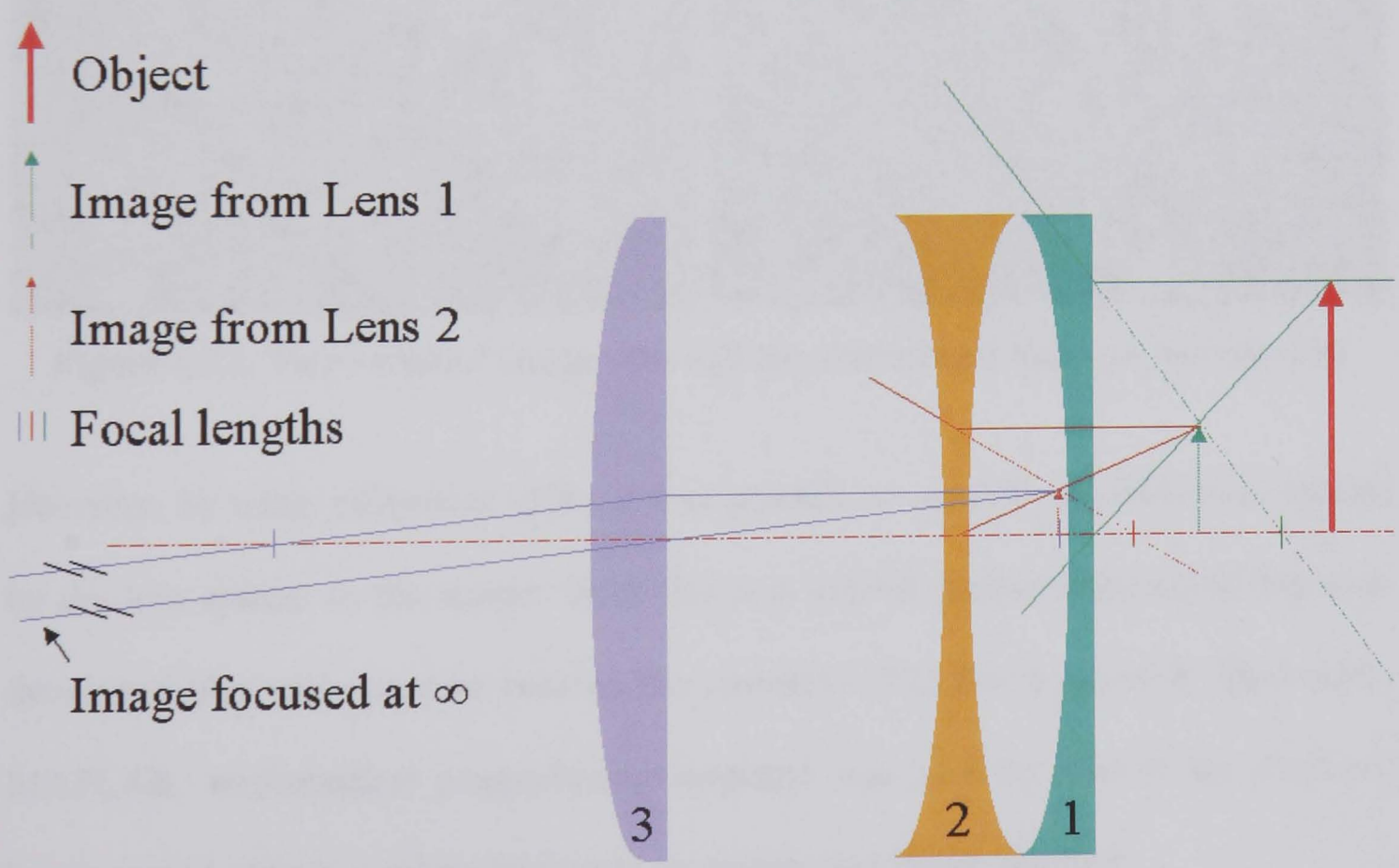

Figure 6.11, Traditional ray trace diagram for fish-eye lens.

Such a design of lens system is very successful in capturing images as described, however the images suffer from field curvature, or warping due to the very large field of view. One must accept these side effects when using such lenses, however they are

unacceptable when quantitative measurements must be made from the images. In order to correct for the field curvature, a de-warping algorithm was developed.

6.5.3 Correcting for Field Curvature

Figure 6.12 shows two original images photographed through the wide-angle lens system. It is obvious how the field curvature effects have distorted the images.

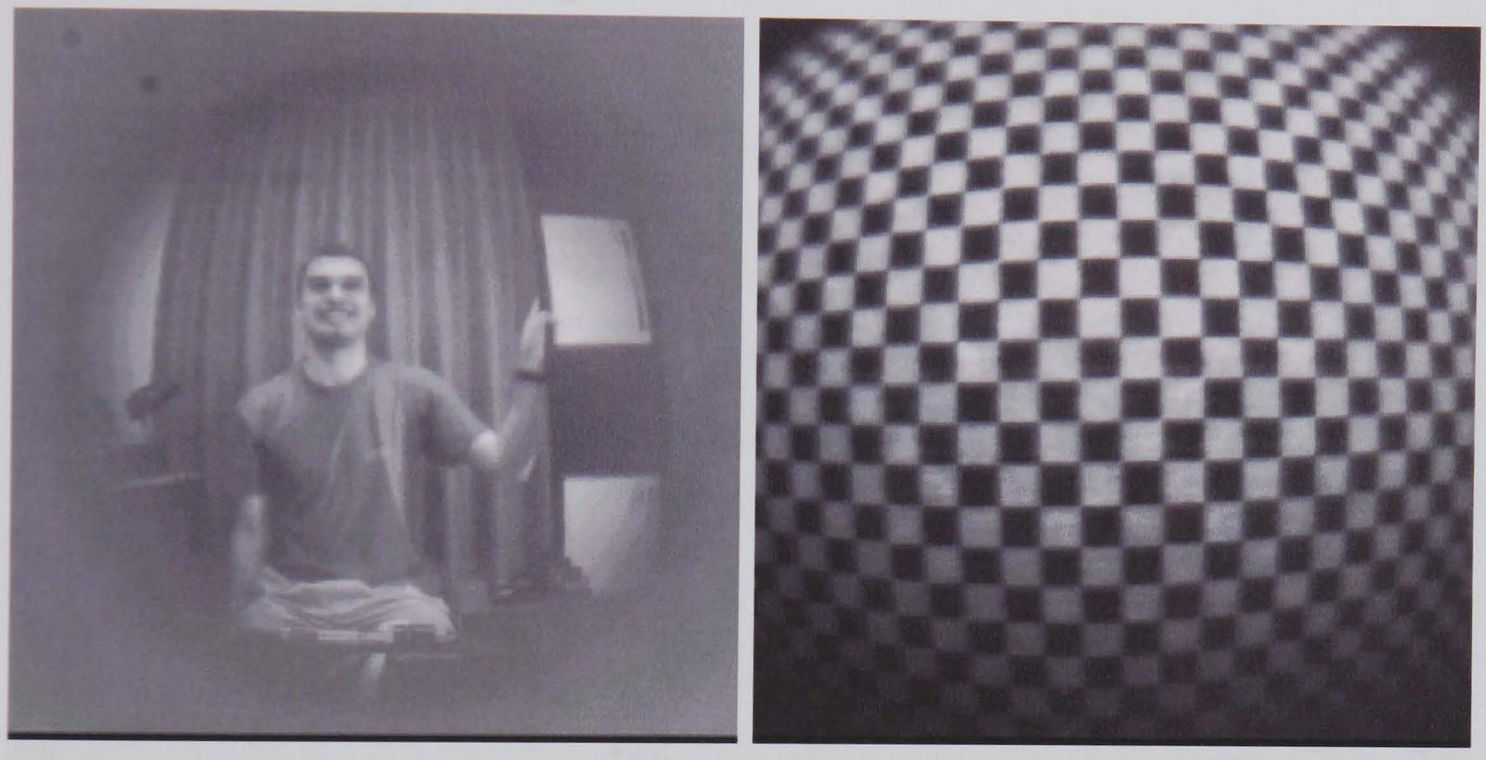

Figure 6.12, Two original images though the redesigned fish-eye lens system.

However, by using calibration grids, it was possible to quantify the distortion applied by the lens system to the image. Once this was known mathematical equations were developed that were used to remove the curvature. For this correction, Mathworks MATLAB, mathematical programming language was used to read in the distorted image and to correct pixel by pixel until an undistorted image resulted.

It performed this correction essentially by reading in the original monochrome digital image file. This array stores the grey level of each pixel in the image. From a separate calibration image, the centre of the lens is known, and so working from this point out,

the Matlab script can 'move' each pixel to the correct position. The distance a pixel is moved is a function of the distance from the lens centre; pixels at the centre are not moved, whereas pixels at the edge are moved the furthest. As described above, calibration images are used to calculate this function. Once matlab has corrected each pixel in the original image, a corrected processed image is output.

The corresponding processed images from Figure 6.12 are shown in Figure 6.13.

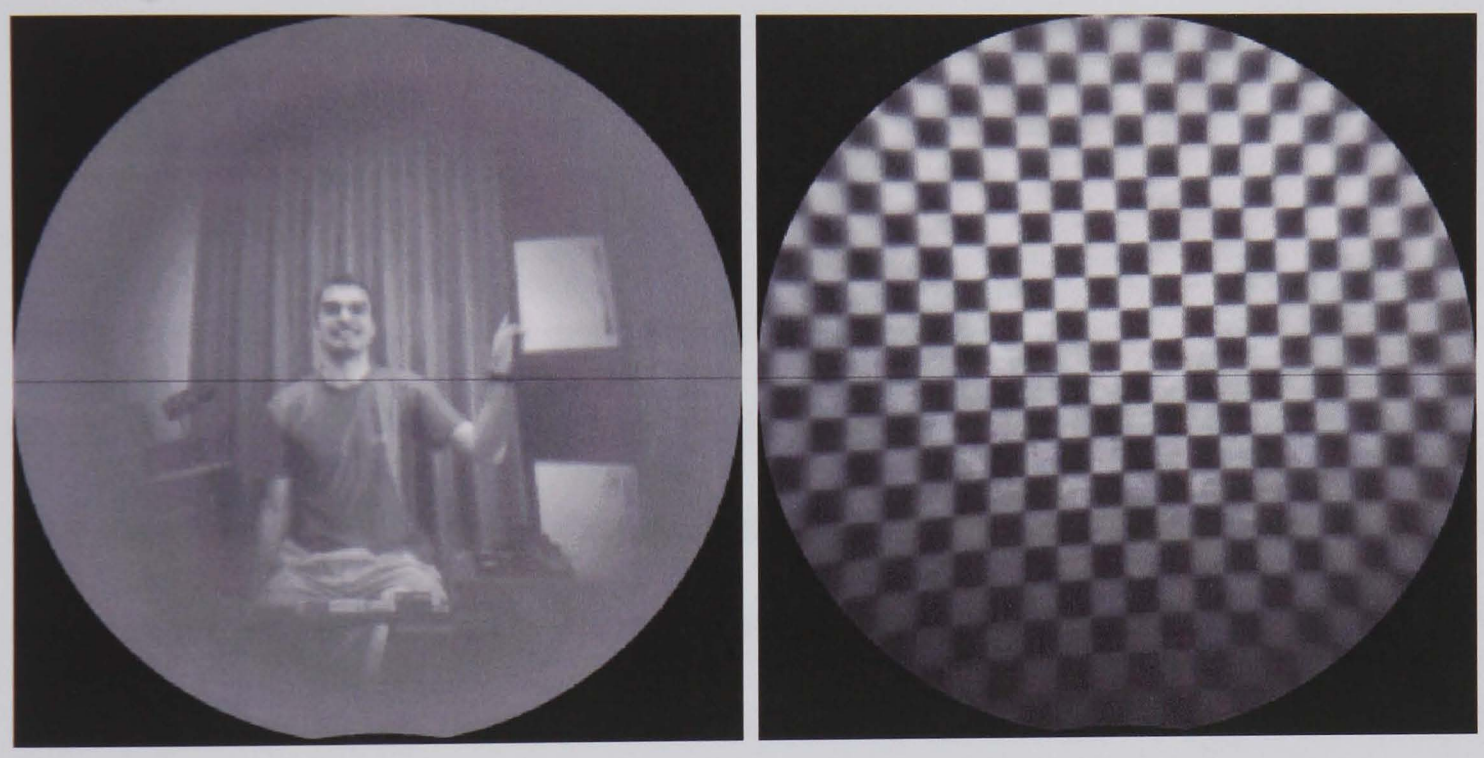

Figure 6.13, Images corrected for distortion.

Further details of the de-warping algorithm and the Matlab script can be found in Appendix D.

6.5.4 System to Relay Image

With a light collecting lens system mounted close to the combustion chamber wall to provide a wide angle of view through a small access point, some method of recording the light is required. Either a small charge coupled device (CCD) camera could be

mounted within the chamber wall, or some secondary optics must be used to relay the image to a point where imaging is possible.

CCD cameras are available in small packages, typical diameters as small as 10 mm, however not only are the resolutions, refresh rates and light sensitivity of these small cameras limited, but the package diameter is still too large. It is necessary therefore to relay the image. Alternatives include: using a series of relay lenses, as used in a borescope, a bundle of coherent optical fibres, using a light pipe or using a GRIN (GRaded refractive INdex) lens.

6.5.4.1 Relay Lens

Using two identical converging lenses of focal length *f*, placed 4*f* apart, with the object placed at 2*f* from the first lens, the image plane will be 2*f* from the second lens with magnification -1. This is illustrated in Figure 6.14 and is the theory used in a simple relay lens system; such a system could be implemented to transmit the image far enough from the combustion chamber where the temperatures are less hostile and physical space permits high resolution, fast frame cameras to collect the images.

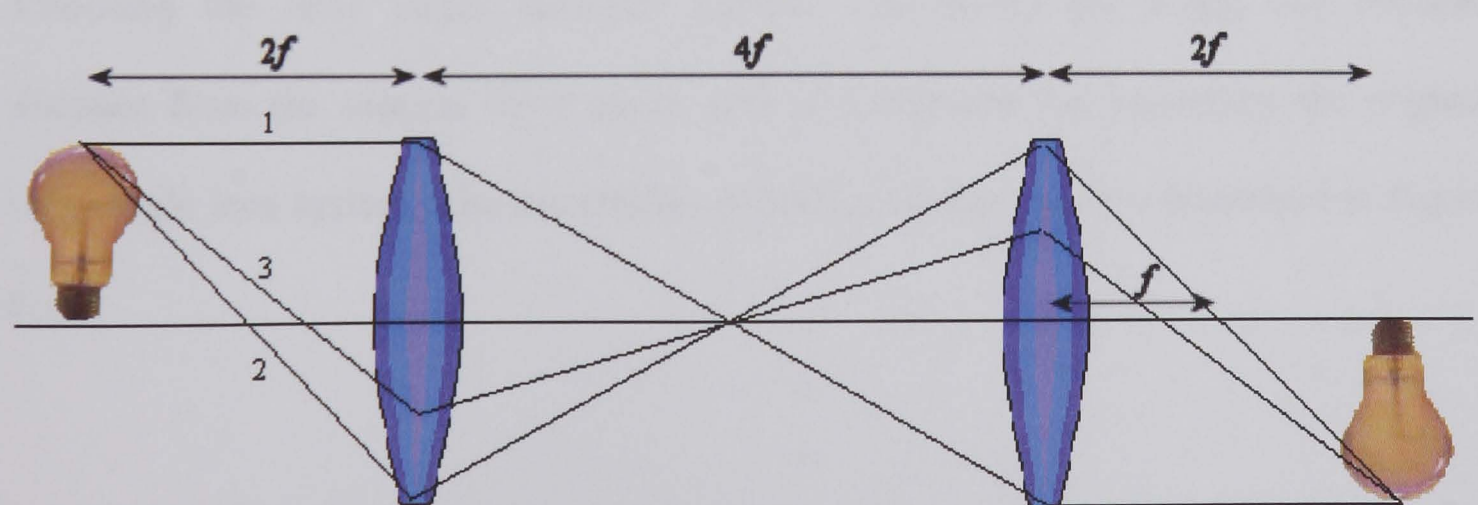

Figure 6.14, Simple relay lens system. (Modified from [76])

It is possible to improve the efficiency of a simple relay lens system by introducing more lenses. This is similar to the design used in a borescope and is illustrated in Figure 6.15. It operates along similar principles to that of the simple relay optics, however by using more lenses, the light is refracted a smaller amount by each lens and so less light is lost. It is a much more complex and fragile design, requiring precision locating of each element, however offers advantages such as reduced losses as each lens refracts the light by a much smaller amount, improved image clarity and the ability to introduce small curvatures or bends in the transmission optics. This ability to withstand small curvatures means alignment of the relay optics is no longer critical and can withstand small vibrations. Unfortunately the significant cost and difficulties in construction of such a design restrict its use.

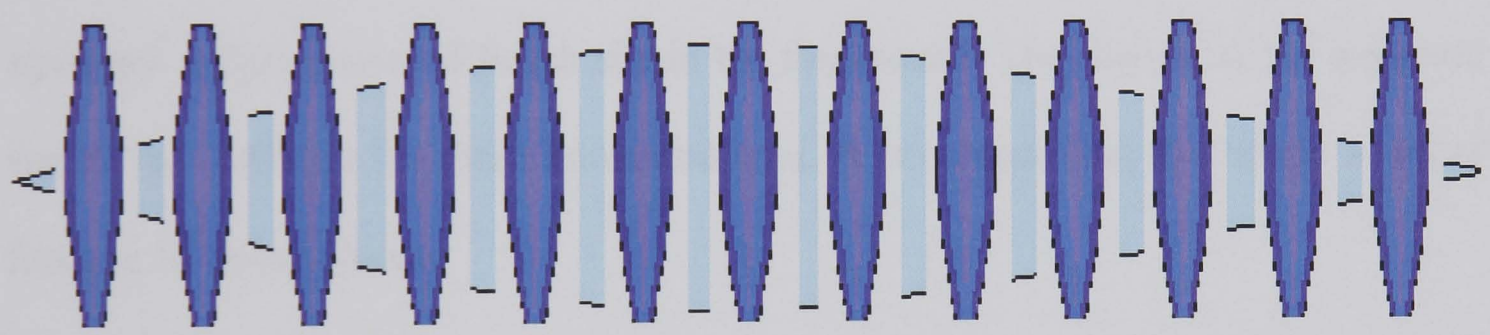

Figure 6.15, Complex relay lens system, as used in a borescope. (Reproduced from [76])

Choosing the relay lenses carefully permits transferring the image any required distance from the original focal plane, and at a diameter not exceeding the original wide-angle lens system. The ray tracing of such a configuration is illustrated in Figure 6.16.

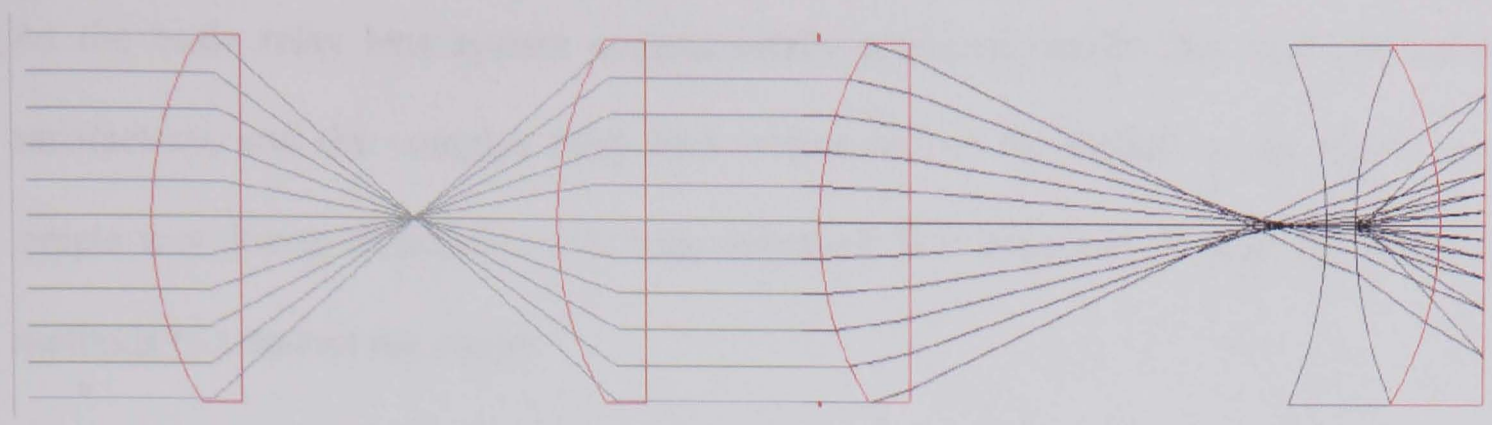

Figure 6.16, Ray trace diagram of fish-eye lens system (3 lenses on the right) and the relay optics (two lenses to the left).

In order to evaluate the performance of a relay lens system, it was tested experimentally. Various lenses of differing diameter and focal length were used, however the results were less than satisfactory. Marsh describes the test and results in [76]. Essentially Figure 6.17 is the image captured with the best clarity and focus. It was created using a relay lens system in conjunction with the fish-eye lens and a CCD camera to capture the image. In the background a cupboard is visible with its doors open and a light coloured bench sits in the foreground. The shelves of the cupboard are barely visible as the three horizontal lines. It is obvious that this image is out of focus in all object planes.

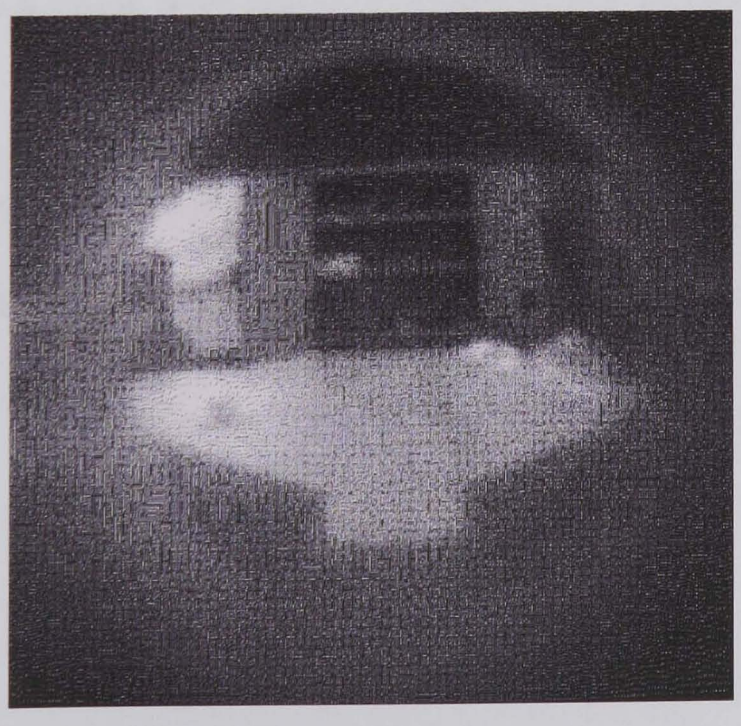

Figure 6.17, Image captured through fish-eye lens and relay optics.

As the basic relay lens system experimentally provided results that were less than satisfactory, and the complex relay lens system cannot be applied to the engine in a simple way due to difficulties with lens alignment, it is necessary to seek other optical methods to transmit the image.

6.5.4.2 Coherent Fibre Bundle

One single fibre optic core cannot relay an image; instead it relays the sum of the light it collects from its cone of vision. However, if many single fibres are held together coherently, that is each fibre position at one end relates exactly to the same position at the other end, then an image can be transmitted down a flexible cable containing many fibres, as illustrated in Figure 6.18.

The most significant advantage of such a system is the flexibility in routing. As shown, the cable can be subjected to many sharp turns and even knots with no effect on the image. Disadvantages of such a system include the high cost, high levels of light loss, image resolution limited by number of fibres and the system being very fragile due to the ease a single fibre could be shattered due to vibration.

Since the flexibility of a coherent fibre is not required for transmitting the image through the rigid engine walls, the disadvantages of this option outweigh the advantages.

Figure 6.18, Example of coherent fibre bundle. (Reproduced from [129])

6.5.4.3 Light Pipe

A light pipe works on a similar principle to a coherent fibre in that it effectively contains many coherent thin fibres, however a light pipe is a solid rod that may be permanently bent by the addition of heat. Generally constructed from a plastic, it avoids the cost and fragility problems with a coherent fibre; however, a light pipe is still limited by resolution.

6.5.4.4 Grin Lens

A GRaded INdex lens departs from the conventional lens design where the refraction of light occurs only at the polished surface due to the refractive index change. Instead in the GRIN design the light is refracted inside the lens as well as on its surface. To achieve this, the refractive index actually varies at different points in the glass resulting in light bending. A GRIN lens avoids lens aberrations and yields a lens that is of reduced size and weight to an equivalent conventional lens.

The use of a GRIN lens is investigated for this application as this type of lens may be constructed in a rod that can transmit an image, see Figure 6.19. Such a lens is not limited in resolution as a light pipe or coherent fibre bundle would be, however must be evaluated for light loss, ease of use and fragility.

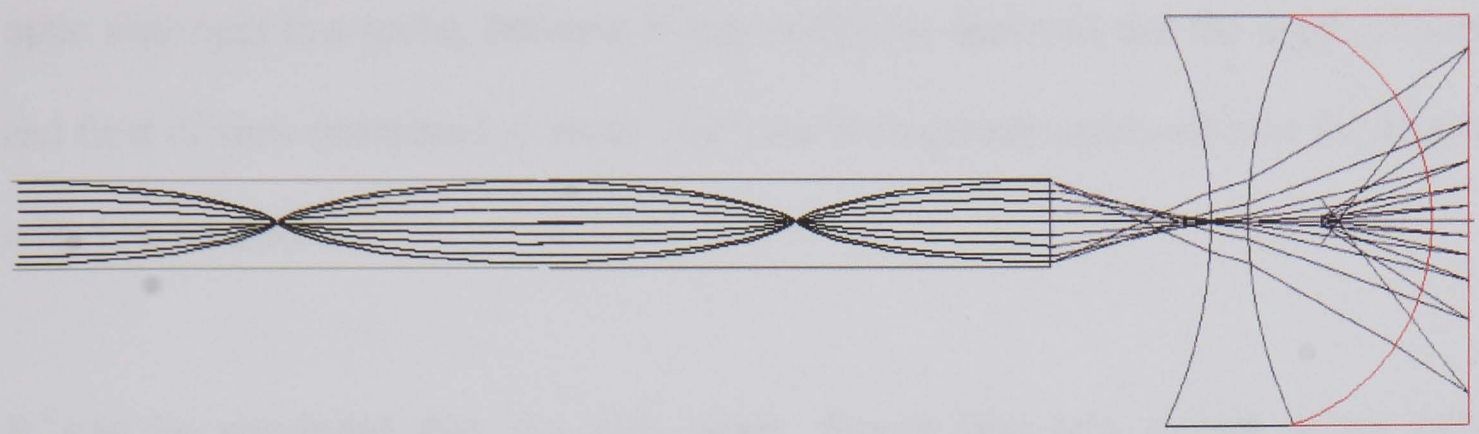

Figure 6.19, Ray trace diagram of GRIN and fisheye system. (Reproduced from [76])

As shown in Figure 6.19, two concave lenses collect the wide-angle image and a GRIN lens is used to transmit the image away from the combustion chamber. The GRIN lens can be manufactured in a variety of lengths and diameters; the imaging system is simply focused onto the image at the end of the system.

Figure 6.20, Image through GRIN and fisheye lens system.

To evaluate the GRIN lens system, an image was captured that was to be compared to the less than satisfactory image collected through the relay lens system shown above in Figure 6.17. The GRIN lens provided an image that was greatly improved in terms of resolution, focus and clarity, and is shown above in Figure 6.20. The slight defocus noted was due to mal-alignment of the optics and is easily corrected with precision optic alignment in a probe, however it may readily be observed that the depth of field and field of view (estimated at about 100°) are both greatly improved over the simple relay lens method.

It may be concluded that the wide angle, fisheye type lens system is not only attractive in terms of large field of view and large depth of view, but is also a feasible lens system for capturing both qualitative and quantitative images. Out of all the lens systems investigated to relay the images away from the hostile combustion chamber, it may also be concluded that the GRIN lens system provides sufficient resolution and limited light loss, in a lens that avoids problems of aberrations and is physically compact and rugged enough to be mounted in this region.

6.6 Conclusions

In summary therefore, the development of an optical spark plug for combustion imaging is described. The spark plug access point was chosen to provide the necessary optical access to the combustion chamber of an internal combustion engine. The use of the spark plug access point enables the optical probe to be applied to any thermal engine from a single or multi-cylinder research engine, through to a standard production engine operating within a vehicle. Results obtained using this optical spark plug are presented in Chapter 8, Optical probe results.

CHAPTER 7

DEVELOPMENT OF OPTICAL PROBES AND COMBUSTION IMAGING

7.1 Summary

Simple probes developed for measuring the intensity and spectral content of the light emitted from the flame during combustion are described, followed by the description of an optical cylinder head used for simple flame visualisation. The probes described provide information of flame speed and flame front species composition.

The work described below was performed with the assistance of Alex Picarelli as part of his MSc research project [130].

7.2 Light Emission Measurements of Combustion

It has previously been shown in Chapter 2, that the character of light emission during combustion holds information on the nature of flames and the burning conditions [12,13]. This section follows the development of simple optical sensors for the monitoring of light emission of a flame within an internal combustion engine.

7.3 Requirement

It is required that optical access of the combustion chamber is achieved through a method that neither disturbs the in cylinder flows or affects the temperature profiles

within the chamber. Therefore the use of optical engines or even engines with windows fitted is an unsuitable method for optical access; an alternative must be identified. In addition, the wavelength range of interest from the light collected from the chamber is from 200 to 500 nm. The use or standard 'glass' is therefore unsuitable and fused silica or similar must be used for any optics transmitting light where the spectral light emission is required. Finally, sampling must occur at greater than 1° CA resolution for the spectral measurements, this is equivalent to a sampling rate of 18 kHz per channel at 3000 RPM.

7.4 Probe Designs

Other than the use of the optical spark plug, two probe designs were used to collect light emission from the combustion. They were fitted across the combustion chamber of the side valve 4-stroke engine, see Figure 7.1, and were used for correlation with heat flux results and to monitor flame speed, flame front composition, and to evaluate light sensors for the tomographic array. These probes have been designed for the purpose set out above; it is not intended (due to difficulties in achieving convenient non-intrusive access) to apply these probes to the combustion chamber of a 'normal' 4-stroke overhead valve engine. Rather the optical spark plug described previously has been designed for that purpose.

As previously mentioned, two designs of optical probes were used. For the first, an optical fibre of 600 μm diameter was mounted flush with the combustion chamber wall. This fibre is constructed from fused silica, which was chosen for its optical transmission at the wavelengths of interest (200 – 500 nm). Simply mounting the fibres flush with the chamber wall, as shown in Figure 7.2, was the simplest to

manufacture and suffered the fewest losses in collected light. However, this type of mounting does not allow any adjustment to the acceptance cone profile, which was measured and calculated to be ≈ 23° half angle.

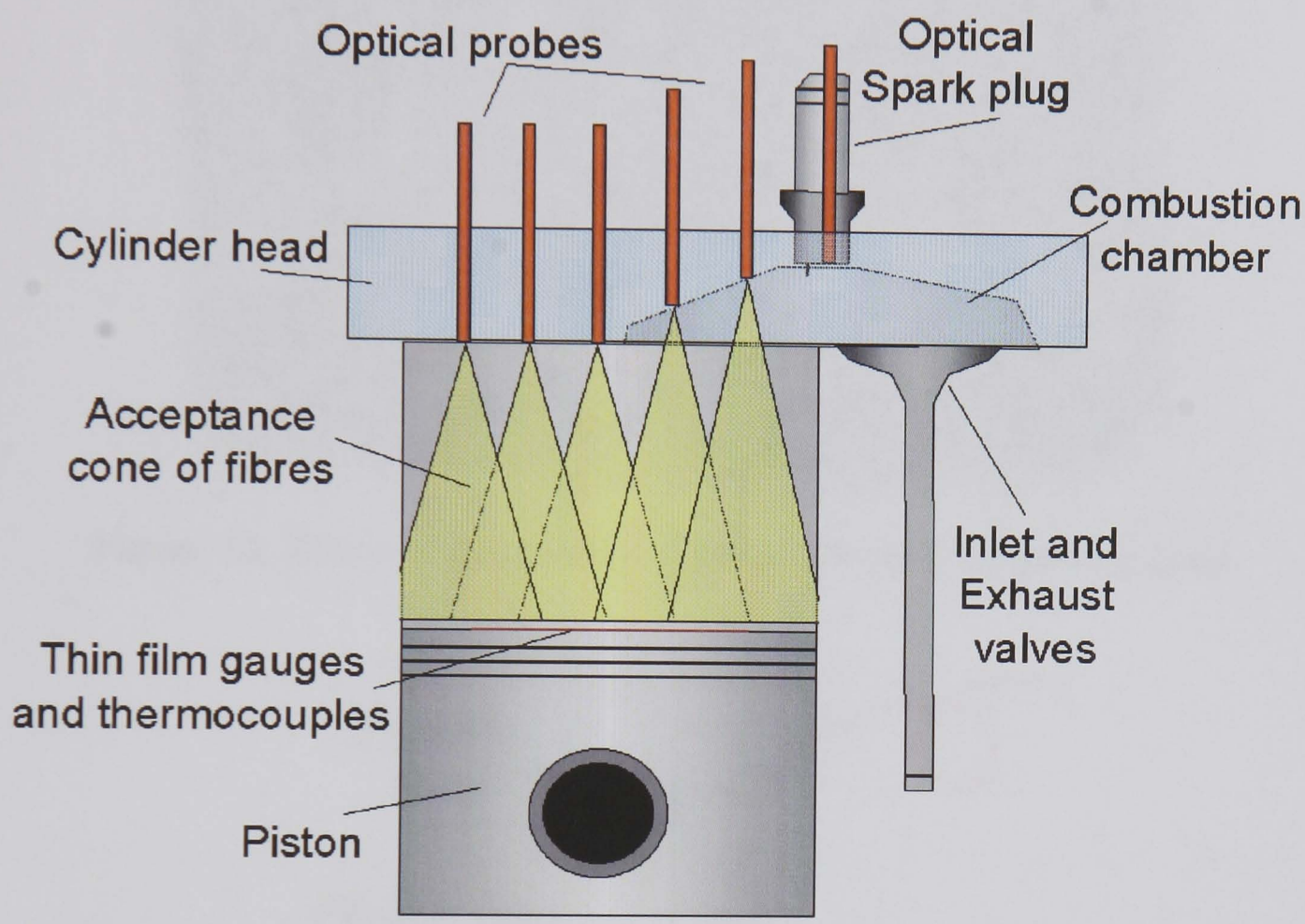

Figure 7.1, Schematic of optical probes mounted in the side-valve engine.

The second design of optical probe was slightly more complex. It uses two fibres to transfer the light emission to the collecting device. The first fibre is a 1mm diameter, fused silica metal-coated fibre mounted in a brass tube. This fibre can be positioned any distance from the combustion chamber surface and the access point to the chamber (the end cap) can be adjusted to vary the acceptance angle and shape. The second fibre is flexible and is coupled to the first. This fibre is used to carry the light away from the hostile and electrically noisy conditions in the region surrounding the engine. This is illustrated in Figure 7.3 and Figure 7.4.

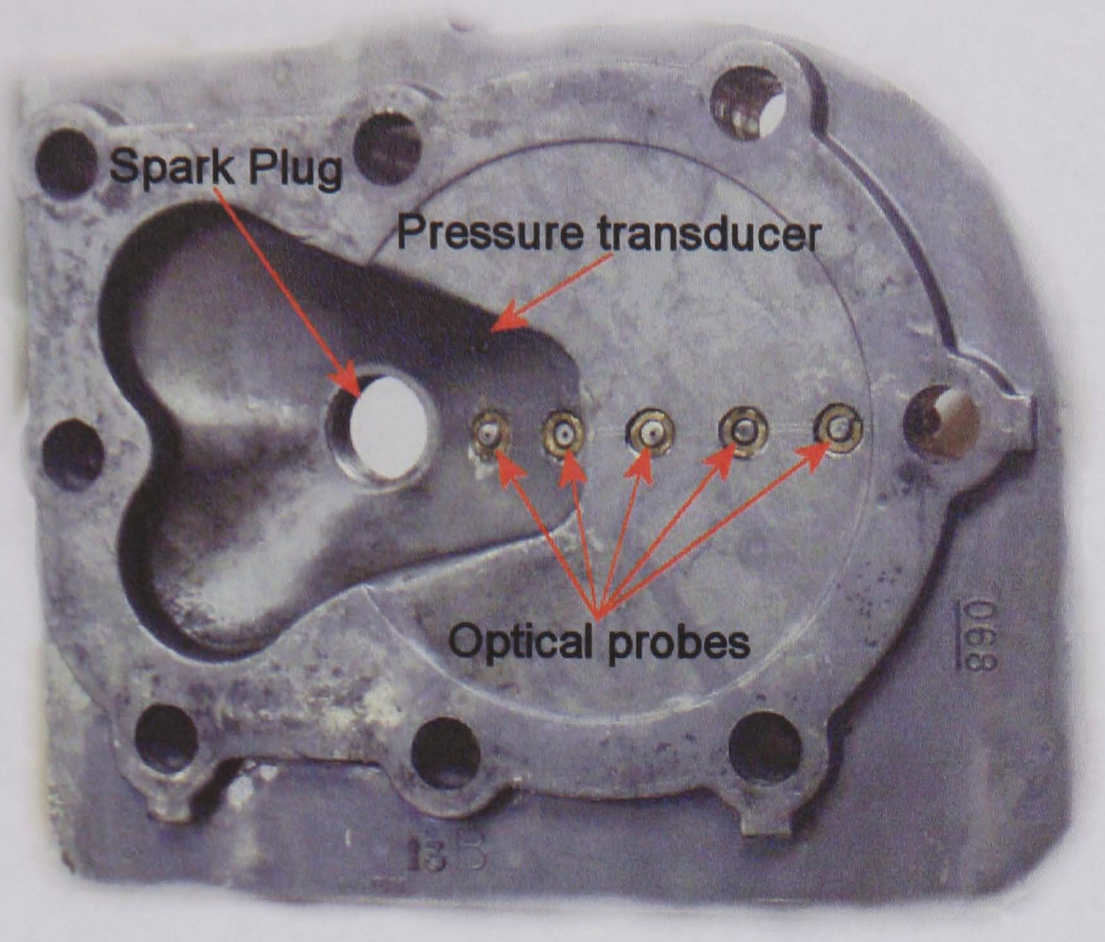

Figure 7.2, Photo of simple optical probe mounted in cylinder head.

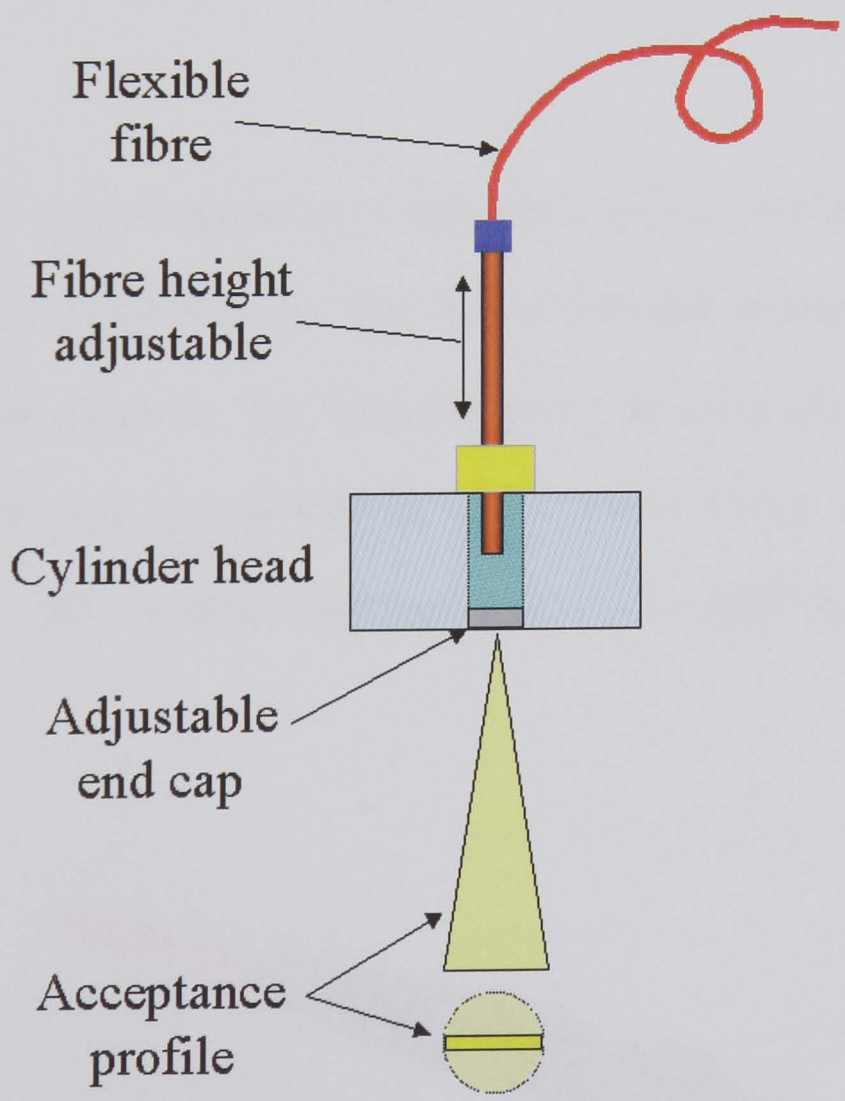

Figure 7.3, Schematic of adjustable probe showing the end cap that may be adjusted to vary acceptance angle and shape.

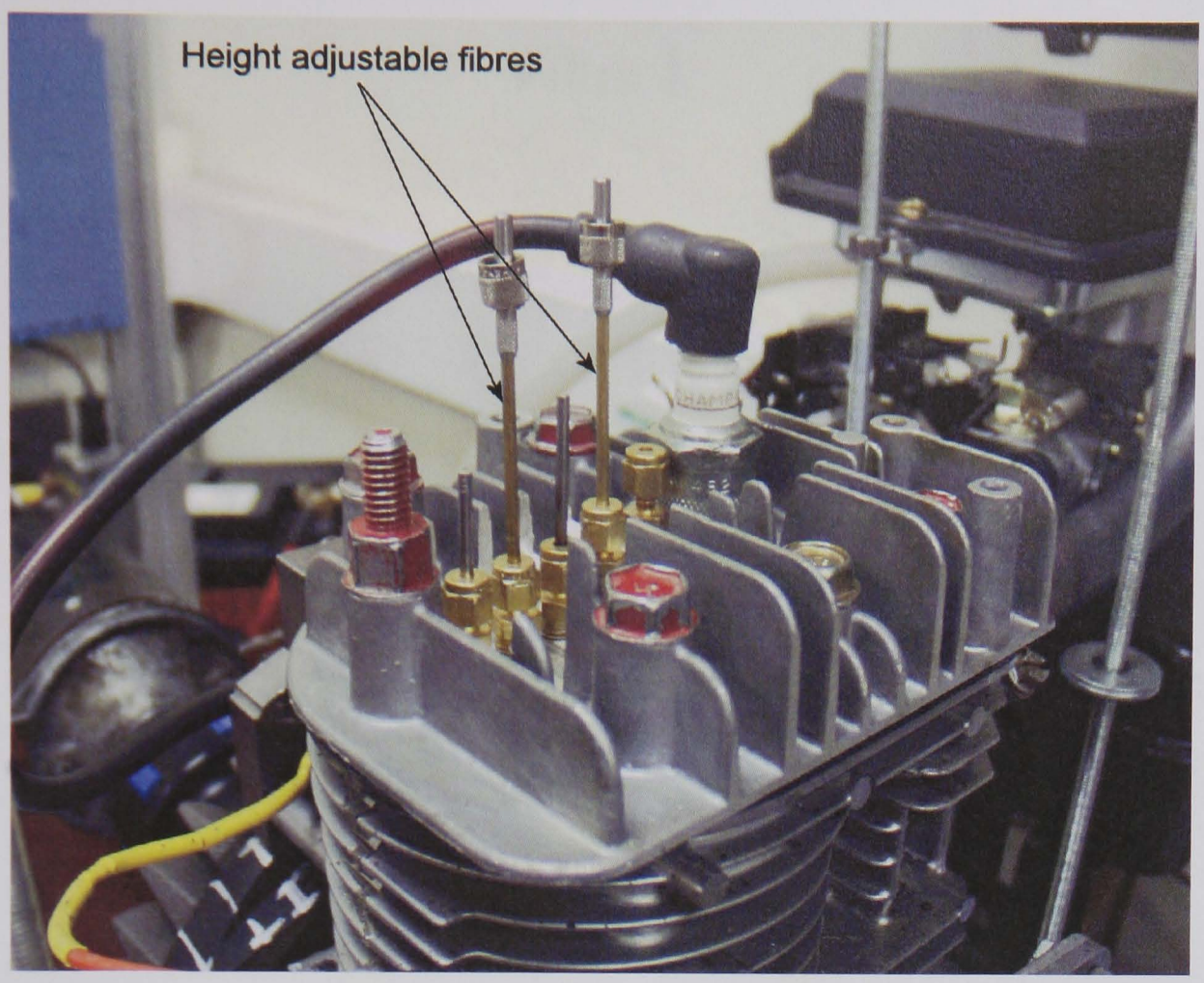

Figure 7.4, Photograph showing height adjustable fibres mounted on cylinder head.

7.4.1 Fibres

Both probe designs use the same patch fibre optic to carry the light to the sensory devices. In the non-adjustable probe, this fibre is mounted in direct contact with the combustion chamber gases. In the adjustable probe the same fibre is used, but this time only as a patch cord to carry the light to the sensory device, see Figure 7.6. The fibre is terminated with an SMA connector, Figure 7.5, which is used to hold it in position.

Figure 7.5, Photo showing SMA connector (black and silver) on fibre 1 (red).

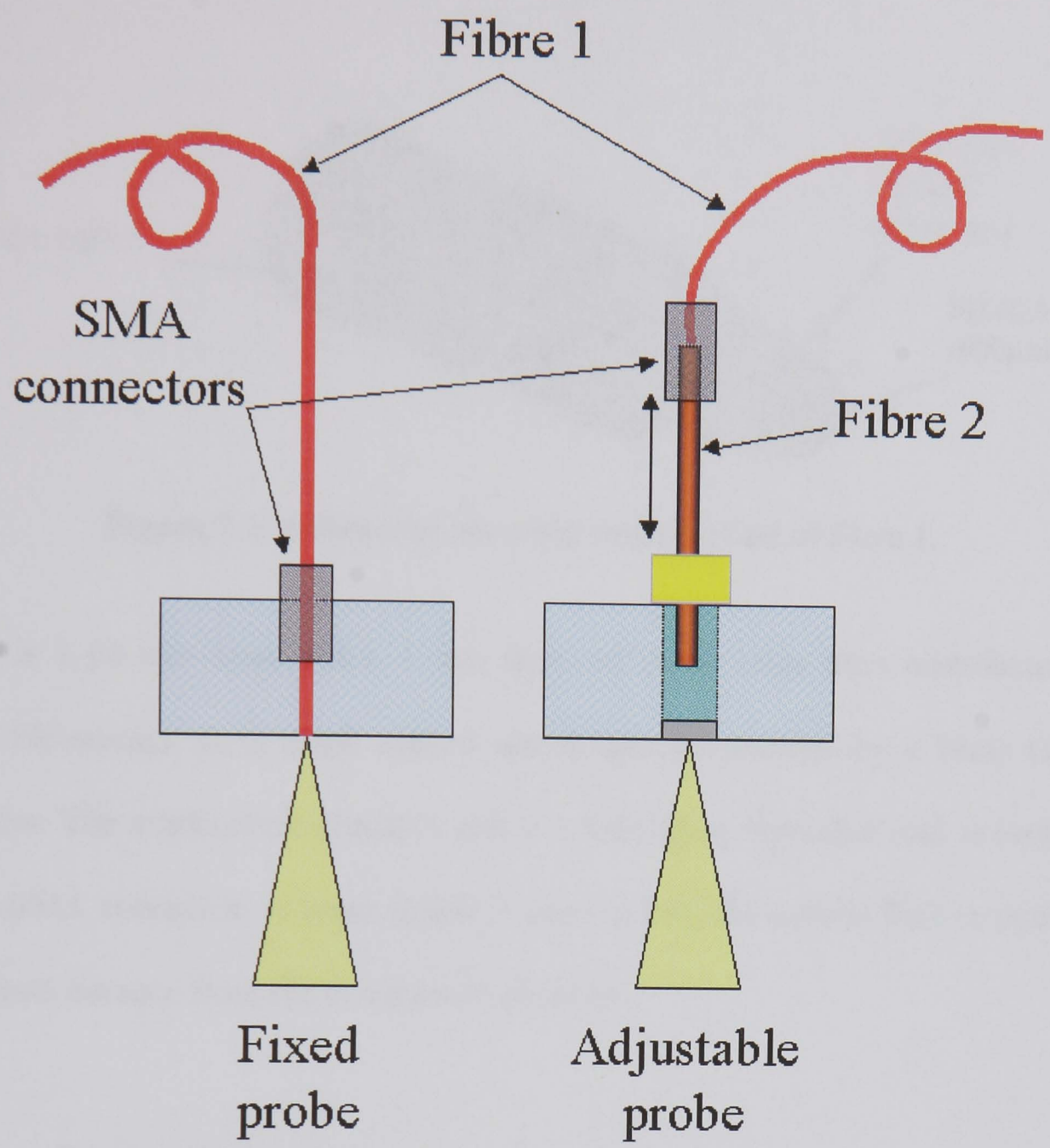

Figure 7.6, Schematic illustrating the differences between the two optical probes.

Fibre 1 is constructed with a 600 μm fused silica core, surrounded with a 300 μm TECS cladding that is covered with a TEFZEL buffer layer. See schematic in Figure 7.7. The fused silica core ensures high transmission levels required in the UV wavelengths since the chemical species of interest naturally emit light in this region. The silica also has a high melting point allowing its use in direct contact with the flame; this reduces losses and simplifies construction. The high numerical aperture (0.39) of the core defines its acceptance cone of vision, but also reduces light loss due to any tight bends in the fibre routing. Both the cladding and buffer surrounding the fibre were selected to be electrical insulators therefore avoiding any transmission of electrical or electromagnetic interference from the spark to the light sensors.

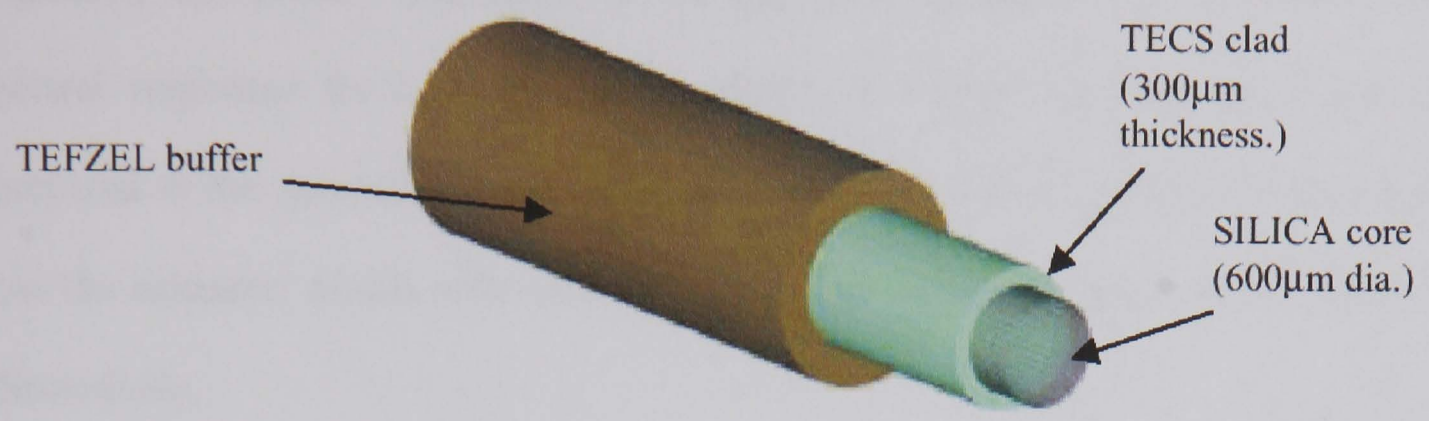

Figure 7.7, Schematic showing construction of fibre 1.

Fibre 2 is a 60 mm long, solid, 1 mm diameter fused silica fibre manufactured by Oxford Electronics. It is metal coated and is also surrounded by a brass tube for protection. The combustion chamber end is a bare fibre, the other end is terminated with an SMA connector. A brass ferrule is used to hold the second fibre in position at any defined distance from the combustion chamber.

7.4.2 Sensory Devices

Two methods of recording light levels were used, either with a photo multiplier tube or an amplified photodiode. Five identical photodiodes could be measured simultaneously yielding the relative light emission across the chamber at each of the access points; however, only two photomultiplier tubes were available, therefore simultaneous measurements at more than two locations within the chamber could not be performed using the photomultiplier tubes. Each is described along with the associated problems.

7.4.2.1 Photodiodes

Two types of photodiodes are used in the experiments. They are both manufactured by IPL (Integrated Photomatrix Ltd.). Both photodiodes have on-board amplifiers and

are enhanced for UV-light. Although both photodiodes have similar spectral responses, the primary difference is the gain and bandwidth of the diodes. The spectral responses for both diodes are shown in Figure 7.8 (blue line) and are compared to the spectral response of a standard silicon diode (red line). It is obvious how the enhanced diodes offer increased sensitivity in the UV region than a standard silicon diode.

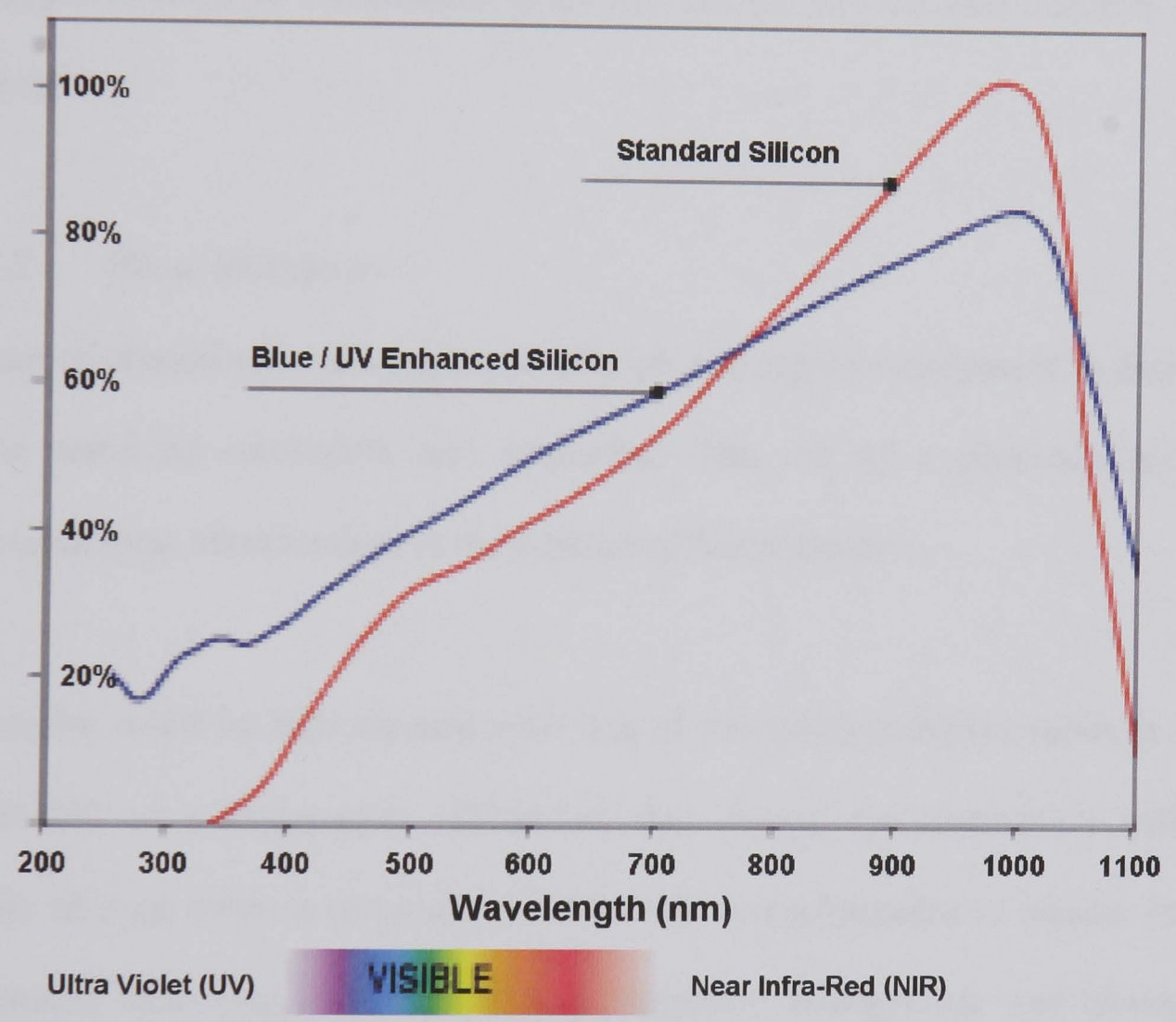

Figure 7.8, Graph showing the spectral response of normal and UV-enhanced IPL 10000 series photodiodes. [131]

In this series of experiments, primary interest is optically viewing the flame front. It is known that OH is found solely in this flame front and that it emits light at approximately 308nm. Therefore the UV enhanced photodiodes are advantageous over the standard silicone photodiode with a cut-off at 430nm.

As the photodiodes are being used to track the flame front, analyse the flame front speed and to identify if there is any turbulent structure measurable within the flame front, the diodes view the flame from five predefined positions in the cylinder head as described above.

Both types of photodiode are mounted in a specially designed case that not only shields the diodes from electrical and electromagnetic interference, but also provides the supply voltage for the onboard amplifiers and permits the easy selection of each diode type.

7.4.2.2 Photo Multiplier

The use of photodiodes, although cost efficient and rapid to implement, is limited due to the restricted bandwidth and sensitivity. The use of a photomultiplier tube overcomes these shortcomings at the expense of financial cost.

The engine could be instrumented with one of two photomultiplier tubes (a Dantec 9055X0084 or a Hamamatsu H5784-04) that viewed the combustion within the cylinder through either a Optometrics DMC1-02 monochromator or narrow bandpass interference filter (Appendix E). This experimental arrangement was chosen as it permits sampling of light at any chosen wavelength with a selectable resolution of between 0.37 and 7.41 nm for the monochromator, or at 308 nm with a bandpass of 10.8 nm if the filter is used, at one of five access points in the cylinder head, as described above.

It is useful to be able to view the emitted light spectrum of the combustion as this enables chemical species identification. There are two ways this can be achieved, either by passing light through a diffraction grating before sampling for example with a CCD chip or photodiode array, or alternatively by the use of the above arrangement, simply sampling several cycles repeatedly each time at a different wavelength until an entire spectrum is recorded. Each method has drawbacks associated, after passing through a diffraction grating, the light intensities are so low that either a large gain or long integration time is required. The large gain cannot be achieved with a standard CCD chip and a long integration time results an averaged reading over the entire cycle that obviously looses all temporal resolution; however, with the use of the monochromator, a spectrum can be built up where each wavelength is given by the average light emission sampled from a different engine run. This means that a cycle resolved emission spectrum could not be measured with this method. For the purposes of this investigation it is sufficient to use an emitted light spectrum that is averaged over many cycles, yet which shows the relative crank angles and intensities for each wavelength, for this reason the monochromator approach is used although results from a diffraction grating and CCD are also presented for comparison.

Two different photomultiplier tubes were used in this series of experiments. Initially access to only the Dantec photomultiplier was possible for testing, however the limitations of only one point measurement in a given run quickly became apparent and a second photomultiplier was sourced from Hamamatsu. Rapidly it became apparent that the two photomultiplier tubes gave very different results, the Dantec gave a very averaged in-cylinder signal whereas the Hamamatsu provided what

initially appeared to be a very noisy signal. An investigation into the cause of this discrepancy was obviously called for and the results are shown in Figure 7.9.

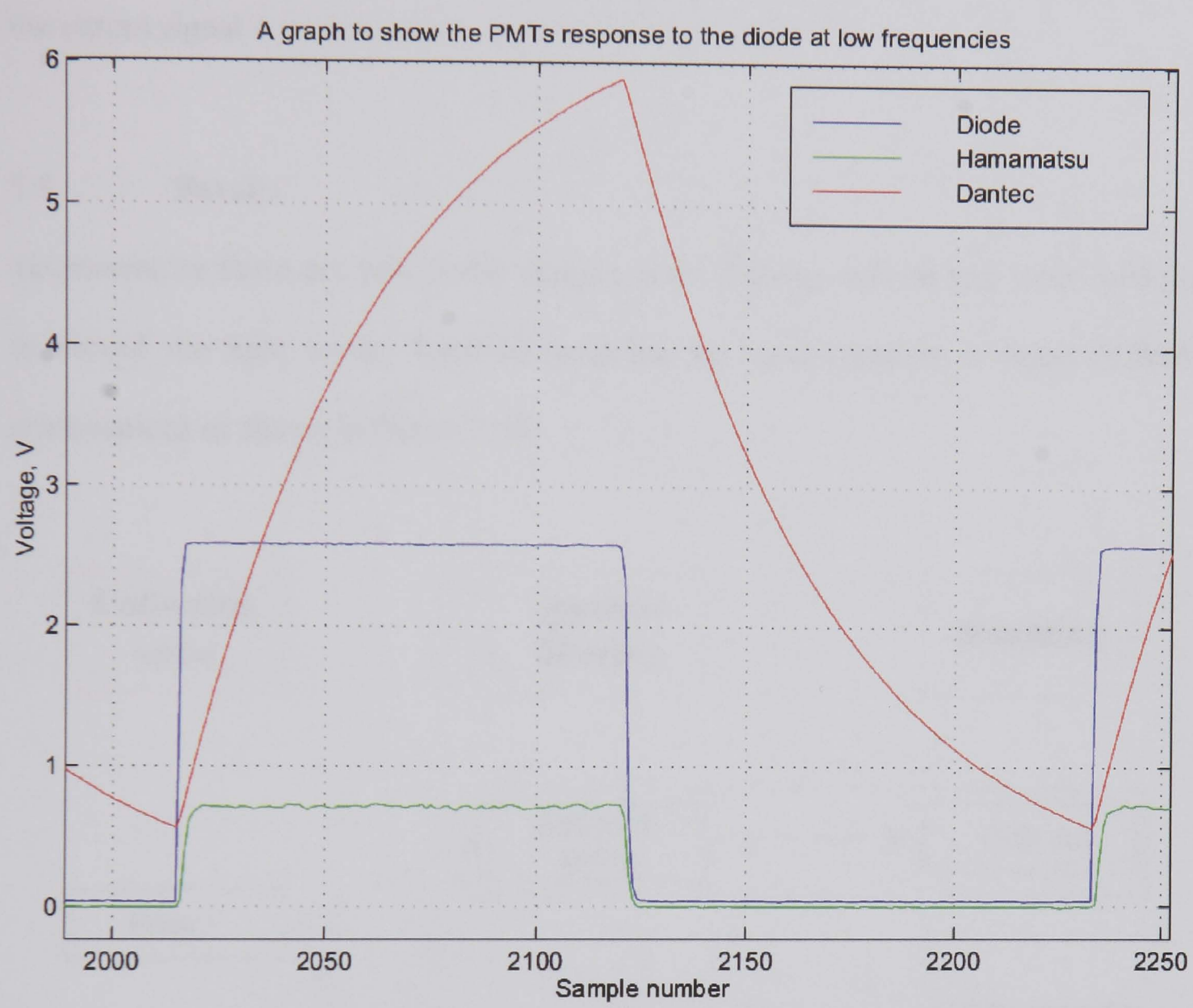

Figure 7.9, Response of each photo multiplier tube to a given light source (blue).

Essentially a light emitting diode was fed a square wave from a signal generator. This voltage signal was sampled with an A2D simultaneously to the signals returned from the two photomultiplier tubes. The voltage supplied to the diode is the blue line in Figure 7.9, note that strictly speaking this is not exactly the plot of actual light emitted from the diode as the diode only switches on when the voltage rises above a threshold level, thus the signal from the Hamamatsu (green line) and the signal from the Dantec (red line) show a short delay before recording light emission. Immediately obvious from this plot is that the construction of the Dantec photomultiplier continues to rise

with a steady light input. In summary, the Hamamatsu photomultiplier provides a signal more representative of the light collected in terms of frequency response, whereas the use of the Dantec must be carefully considered due to the integration in the output signal.

7.5 Results

To summarise there are two probe designs, three filtering options and three methods to record the light levels. Each of these can be used together in many different combinations as shown in Figure 7.10.

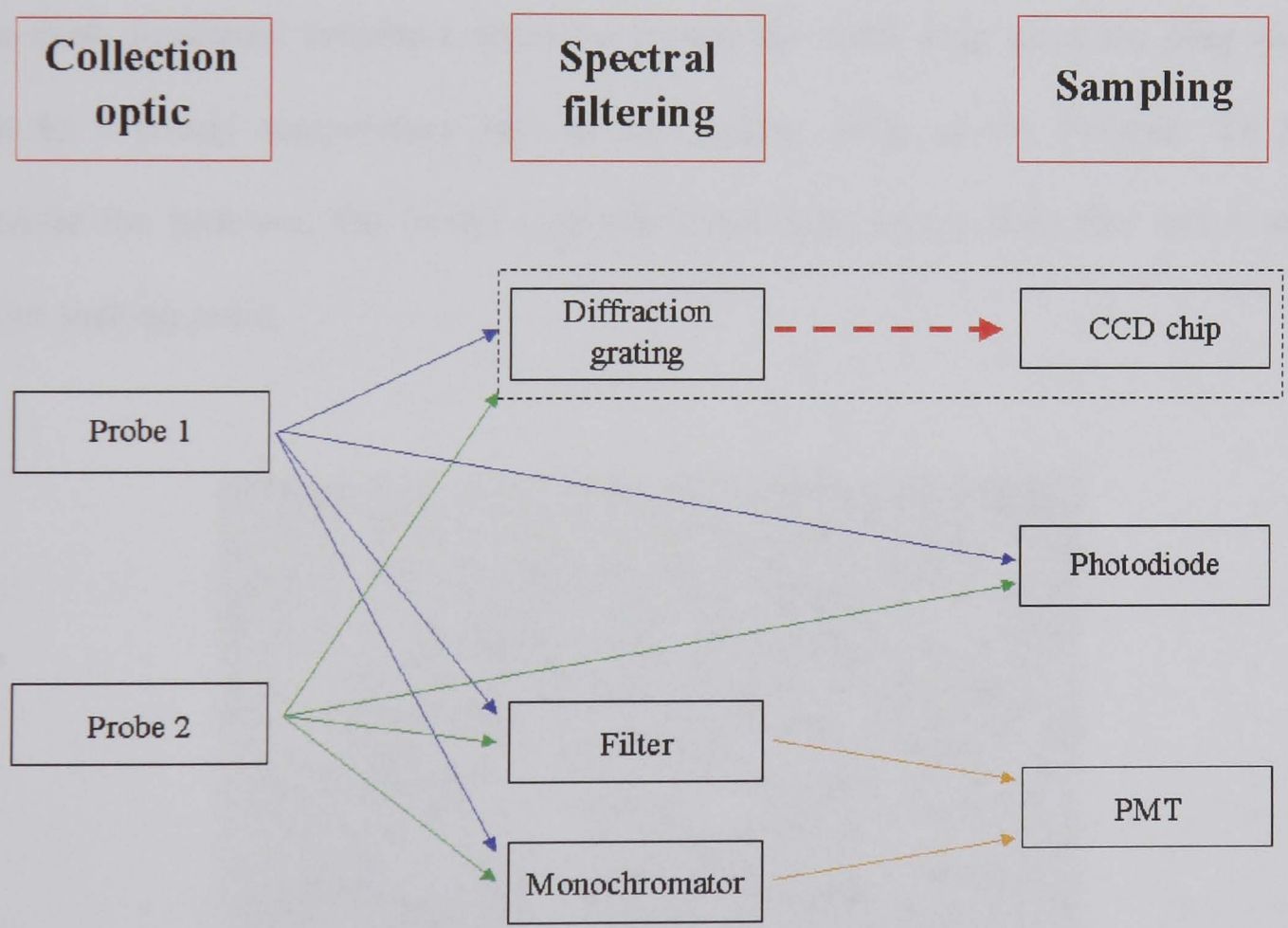

Figure 7.10, Options for light collection, filtering and recording.

Results are presented in Chapter 8, Optical Probe Results.

7.6 Imaging Through Transparent Cylinder Head

In order to image the complete area of the combustion chamber, a transparent cylinder head was manufactured from Perspex, Figure 7.11. The combustion chamber geometry of this head was machined to match the original.

Although Perspex is a thermoplastic material, meaning it is possible to bend or deform the material when heated; the cyclic nature of the temperatures and the short duration of each test proved sufficient to prevent permanent damage to the transparent cylinder head over most of the combustion chamber.

The most significant problems occurred around the spark plug since the plug would heat to a steady temperature beyond the melting point of the Perspex. To help alleviate the problem, the thread was reinforced with epoxy resin that has a much higher melting point.

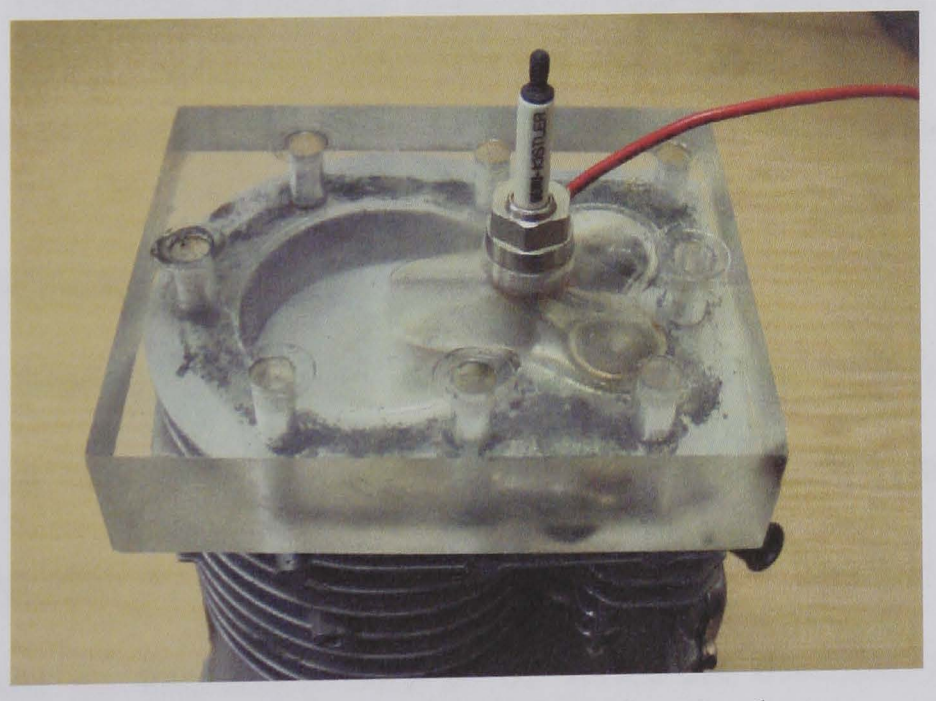

Figure 7.11, Optical Cylinder Head.

A high frame-rate video camera (NAC, HSV 500) was used to record a video sequence of the firing cycle. The camera was positioned vertically and viewed the

combustion chamber through the transparent cylinder head, Figure 7.12. Markings on the flywheel allowed determination of crank angle to within ± 1.5°. A frame rate of 500 frames/second (1 frame every 2 ms), shutter speed of 1/1000s and a gain of 12 dB was used to record the 510 x 112 pixel resolution sequences.

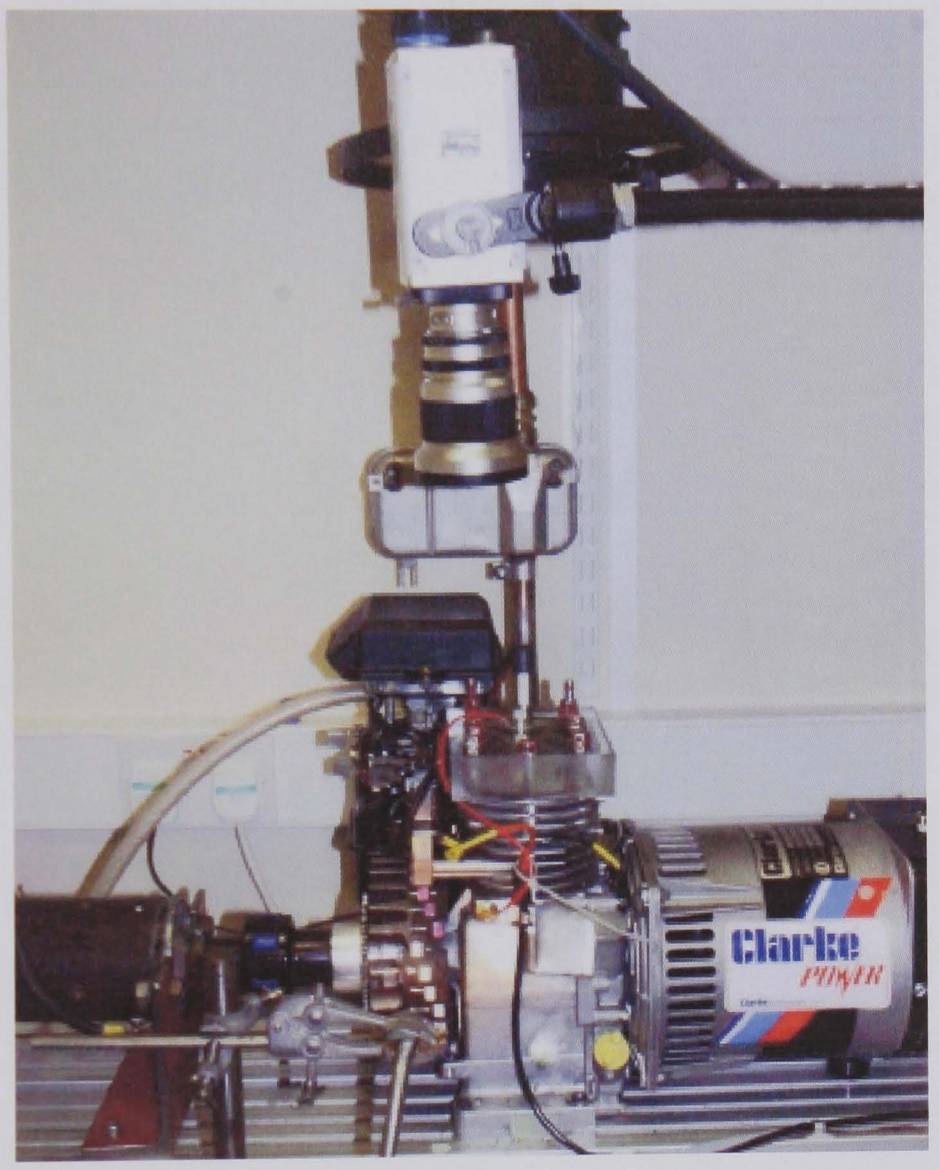

Figure 7.12, Photo showing High speed camera viewing the combustion chamber.

7.7 Conclusions

Described are probes for monitoring of in-cylinder light emission from the combustion event. These probes will be evaluated in the low-cost engine facility described in Appendix A1 for application to the I.C. engine. Fixed probes, as well as designs that allow the acceptance cone to be varied are described as are the three methods of light sampling: photodiodes measuring light intensity, photomultiplier tube and spectrometer measuring spectral content. Finally, the development of a simple optical cylinder head for basic flame imaging has been described.

PART IV

RESULTS

CHAPTER 8

OPTICAL PROBE RESULTS

8.1 Summary

This chapter presents the various results obtained from the different optical probes described previously. Included is flame visualisation, flow visualisation, PIV, spectral and light intensity results. The sections on flame visualisation and light intensity were partly performed in conjunction with Alex Picarelli [130] as part of his MSc thesis; similarly, the section on PIV was in part performed in association with Richard Marsh [76] as part of his MRes thesis.

8.2 Flame Visualisation

Colour images of combustion were recorded using the high-speed digital camera viewing the combustion chamber through a transparent cylinder head, as previously described in Chapter 7. Markings on the flywheel permitted identification of engine timing; engine speed, fuelling and load were all fixed in any run.

Figure 8.1 shows a sequence of flame images acquired with the engine running at 2100 RPM, and not loaded. At this engine speed the frame spacing is approximately 24°, sufficient to permit the capture of up to 5 frames of the flame. The blue flame front propagating from the spark plug may be observed, as can the cooler 'red'

burning region behind the front. The chamber is shown schematically in Figure 8.2. It may be observed that the spark plug partially obscures the view and that the chamber is not symmetric since the inlet valve is larger than the exhaust.

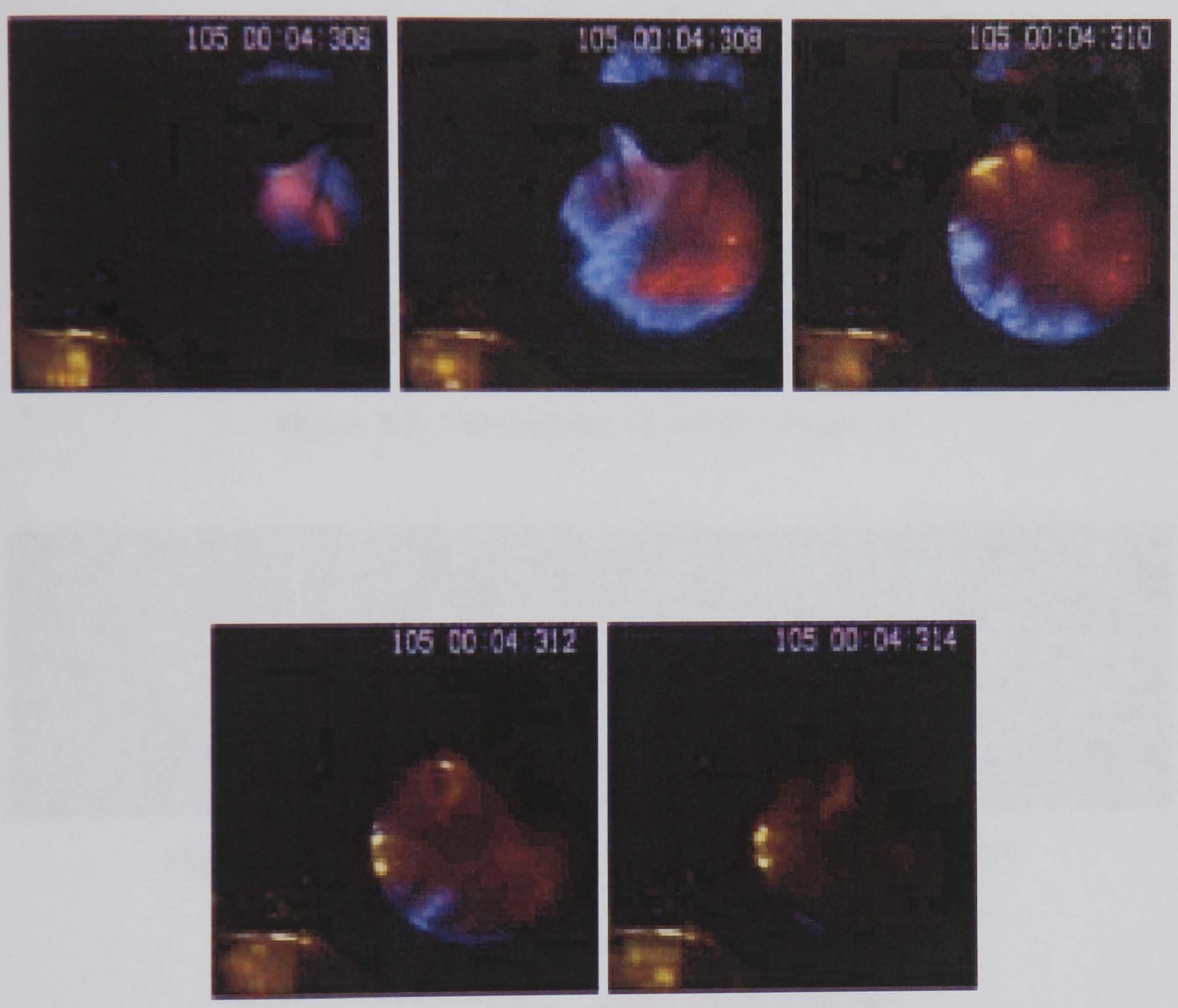

Figure 8.1, Sequence of flame images at 2100 RPM, no load. Shutter speed is $^{1}/_{1000}$ s at 500 frames per second.

The direct flame imaging enabled a more complete understanding of the results from the other instrumentation. In particular it is obvious from images such as Figure 8.1 above and Figure 8.3 below that the flame propagation direction is not straight across the chamber, instead is at an angle to the centreline as illustrated schematically in Figure 8.4. This is due to the barrel tumble introduced due to the off centre inlet valve.

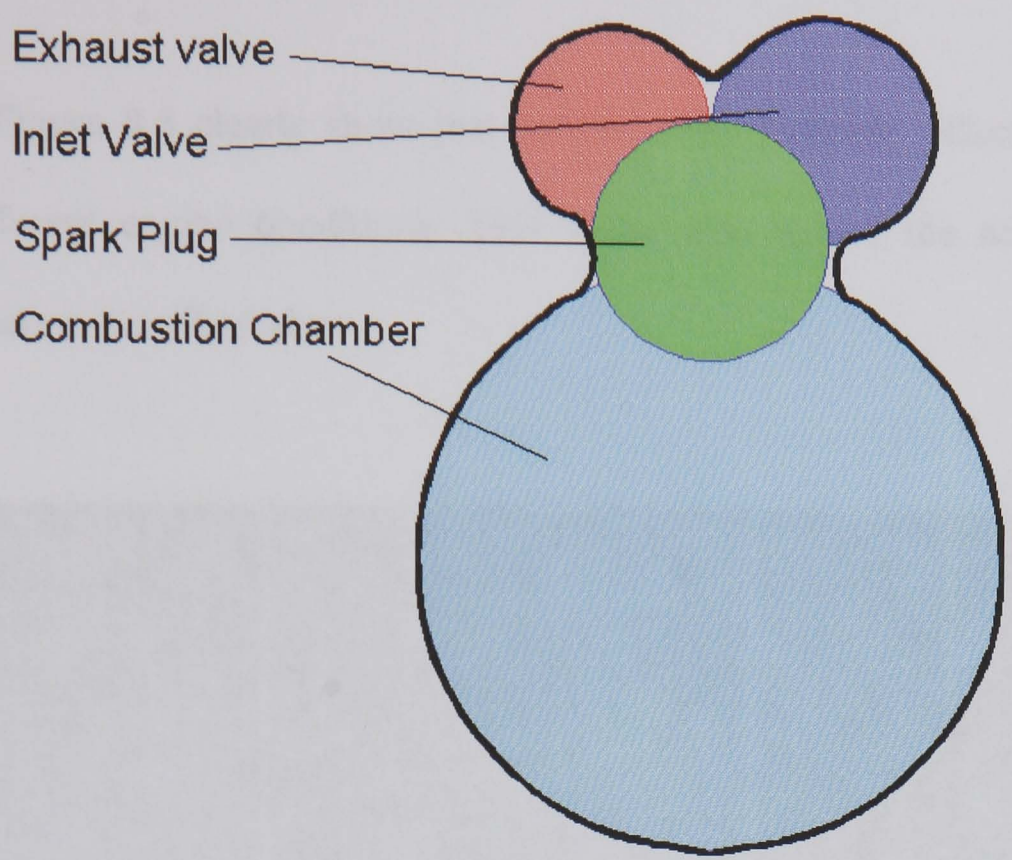

Figure 8.2, Combustion chamber schematic.

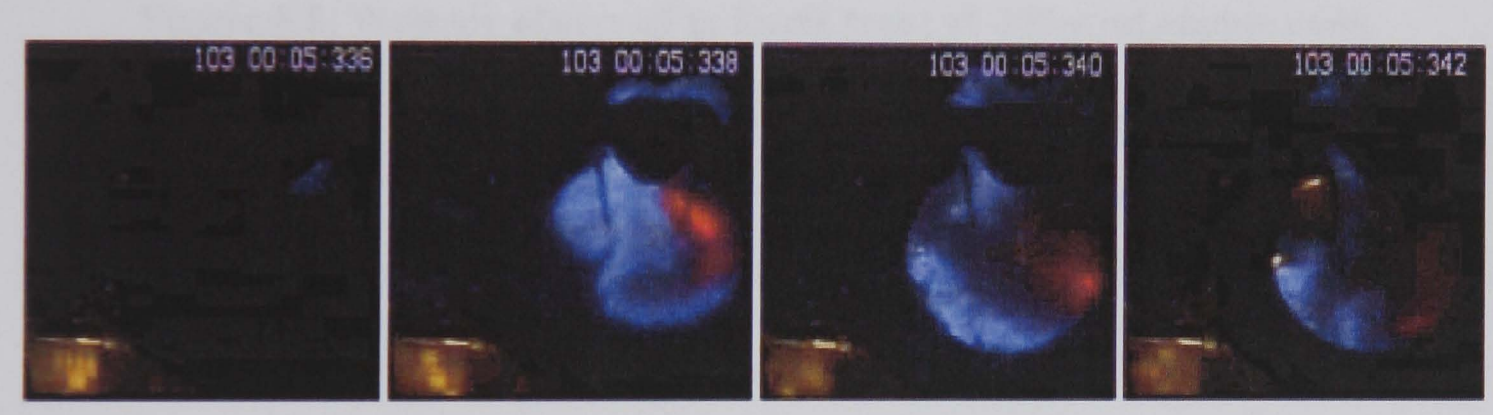

Figure 8.3, Sequence of flame images at 2100 RPM, loaded.

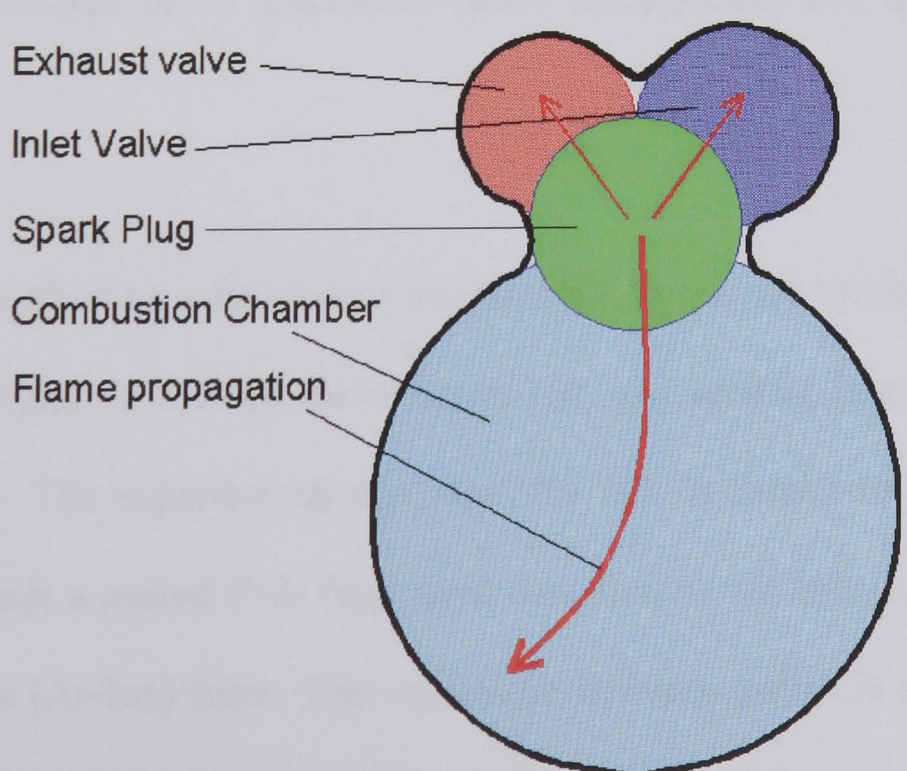

Figure 8.4, Flame front direction illustrated schematically.

In addition, Figure 8.5 clearly show the turbulence or 'wrinkle' effect on the flame front for different engine conditions. This figure also shows the non-symmetrical flame propagation described above.

Figure 8.5, Wrinkle observed in flame front of different engine runs.

8.3 Flow Visualisation & PIV

Knowing and being able to control the flow speeds and directions spatially resolved within the combustion chamber is important for an understanding and control of the flame development. Images of the in-cylinder charge seeded with particles that follow the flow are recorded for a qualitative (flow visualisation) and quantitative (PIV) understanding.

For the flow visualisation a DC motor provides the torque for turning the engine at a fixed speed, the laser is a fixed wave Argon-Ion, and seeding is an oil mist created with a nebuliser. The experimental apparatus for PIV is similar to that for the flow visualisation except a pulsed (Nd-Yag) lased was used as the light source instead of a continuous wave (Ar-Ion) laser. The separation between pulses is accurately known and from a calibration image each pixel location is known in x-y mm co-ordinates. The flow speeds and direction at localised points can easily be calculated.

Two experimental arrangements were used to collect the data, these are shown in Figure 8.6. In **(A)**, the light sheet enters through the cylinder head via the probe illustrated in Figure 8.7 and imaging is performed through the cylinder wall using a second variation of this probe. In **(B)** a laser light sheet enters the combustion chamber through the optical adapter (Figure 8.7) mounted in the cylinder wall and imaging is performed though the spark plug designed for optical access, as described previously in Chapter 6.

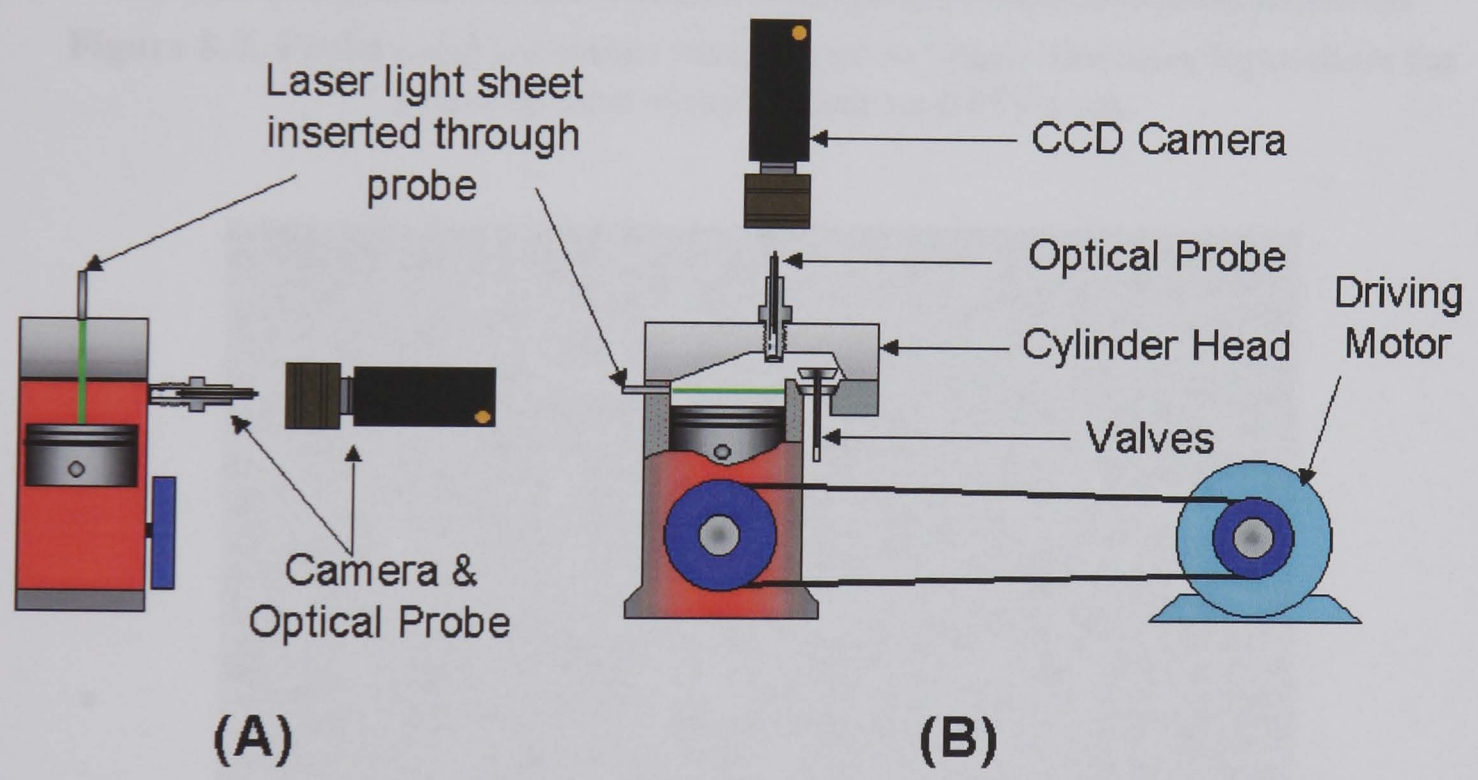

Figure 8.6, Experimental arrangements for Flow Visualisation and PIV.

Figure 8.8 and Figure 8.9 each show frames from two separate flow visualisation video sequences. The images clearly show the flow motion within the combustion chamber.

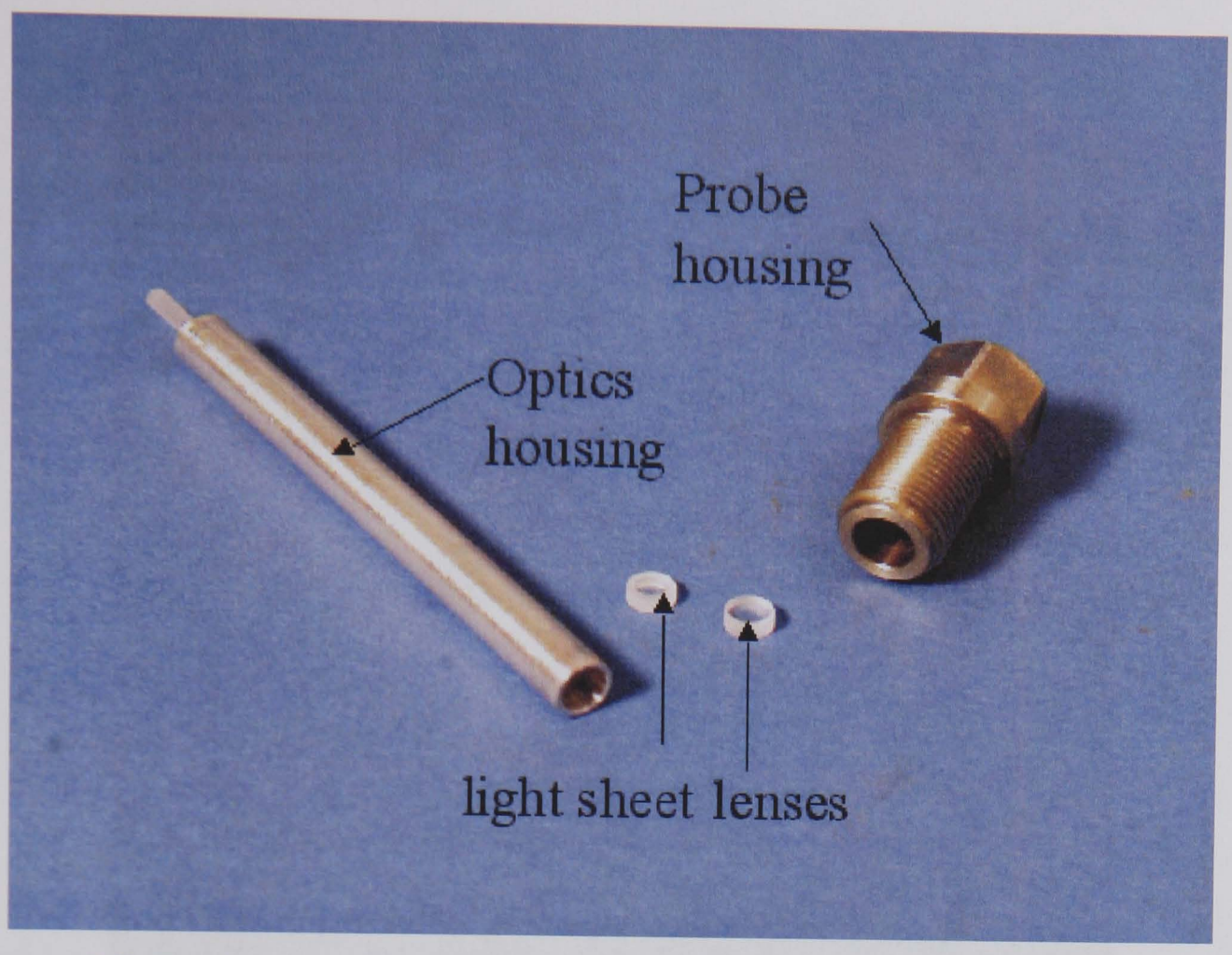

Figure 8.7, Probe used for either imaging or to create the laser light sheet for motored flow visualisation and PIV tests.

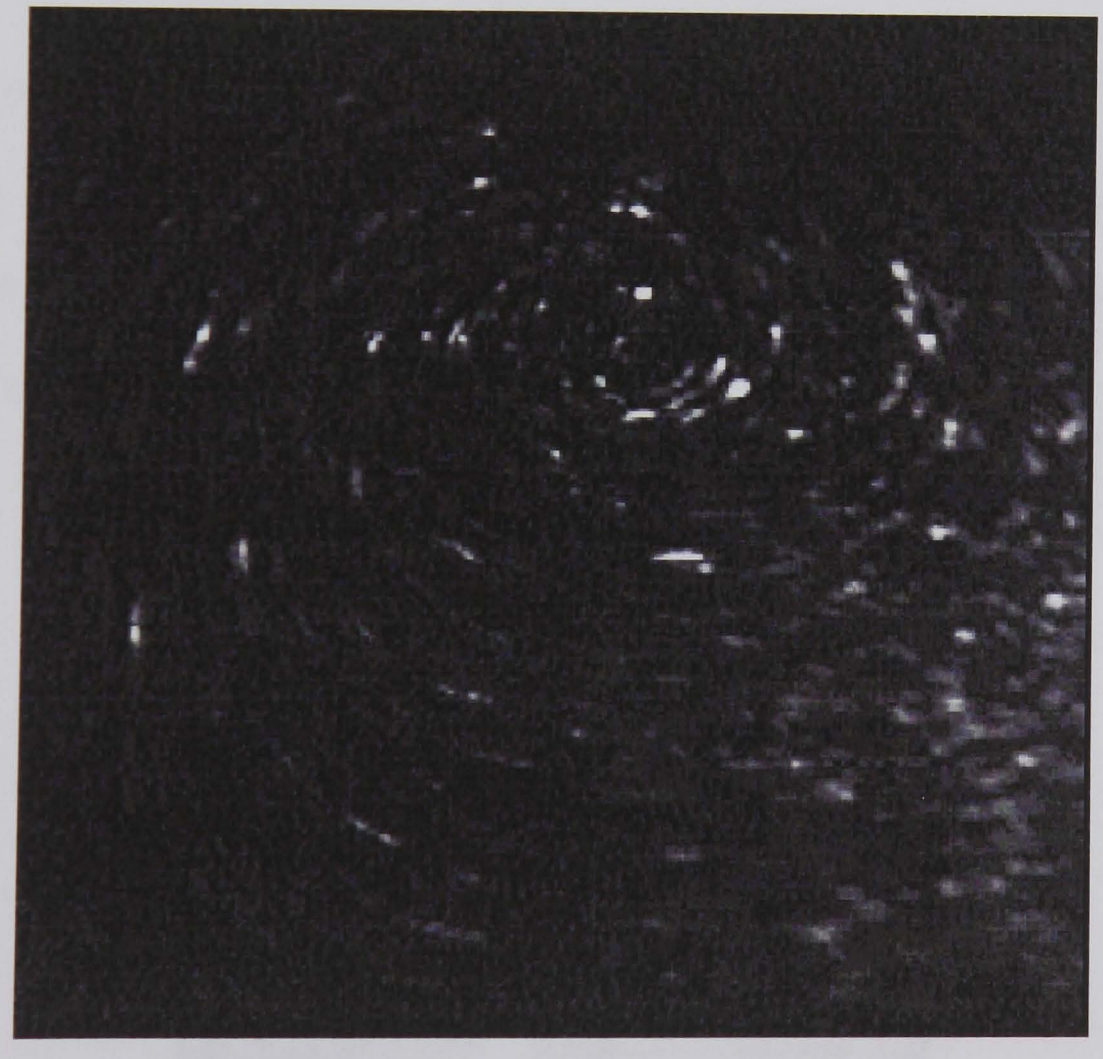

Figure 8.8, Flow visualisation image captured with the camera viewing through engine block and light sheet inserted through cylinder head. (Arrangement A)

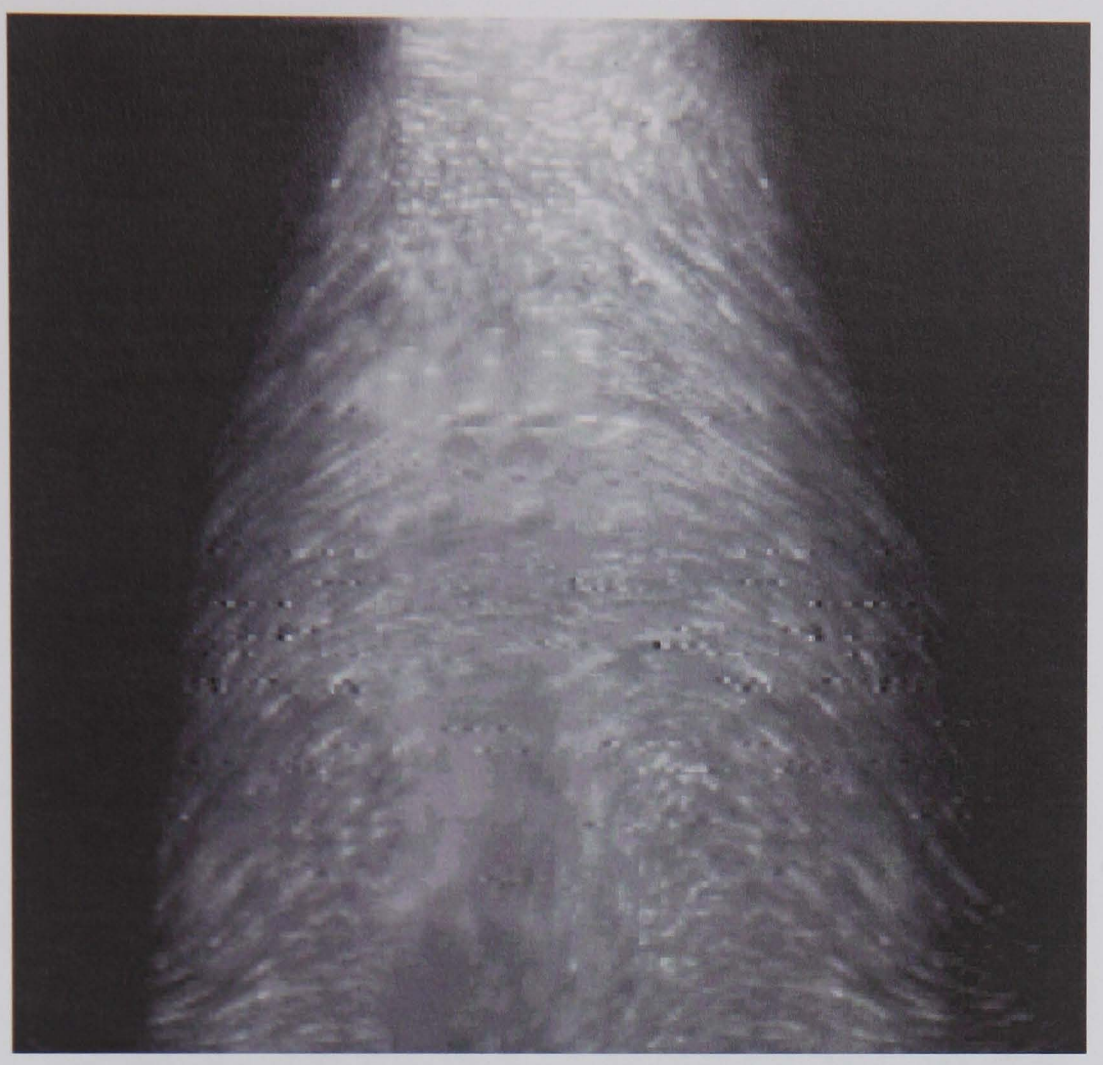

Figure 8.9, Flow visualisation image captured with camera viewing through cylinder head and light sheet inserted through block. (Arrangement B)

Figure 8.10 and Figure 8.11 show raw PIV images within the chamber. The output from four ensemble averaged velocity maps generated from the configuration in Figure 8.10 is shown in Figure 8.12. Figure 8.13 is ensemble averaged over a greater number of cycles.

Figure 8.10, Double exposed PIV image though spark plug. The glare is due to laser reflections off the piston. (Arrangement B)

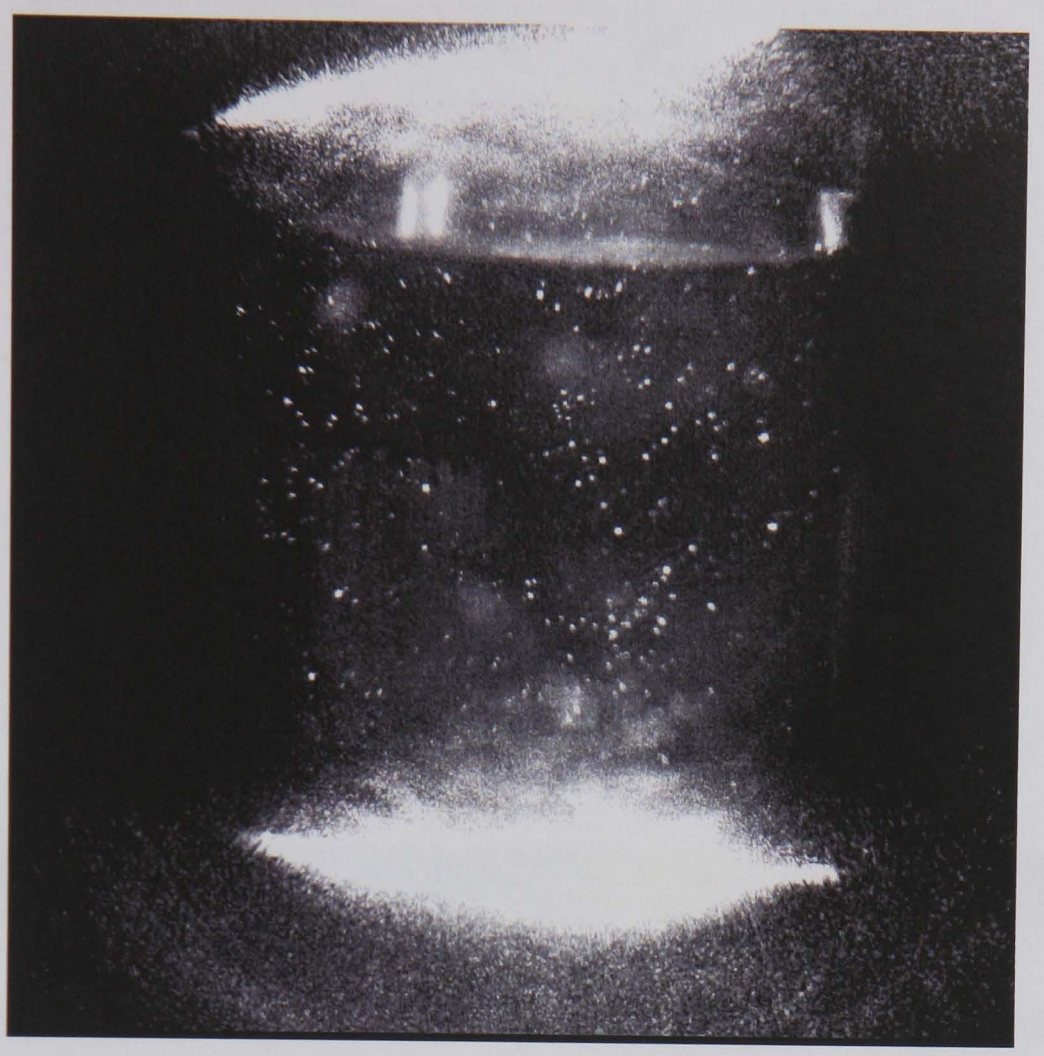

Figure 8.11, Double exposed PIV image taken through optical probe mounted in barrel. The glare is due to laser reflections off the piston. (Arrangement A)

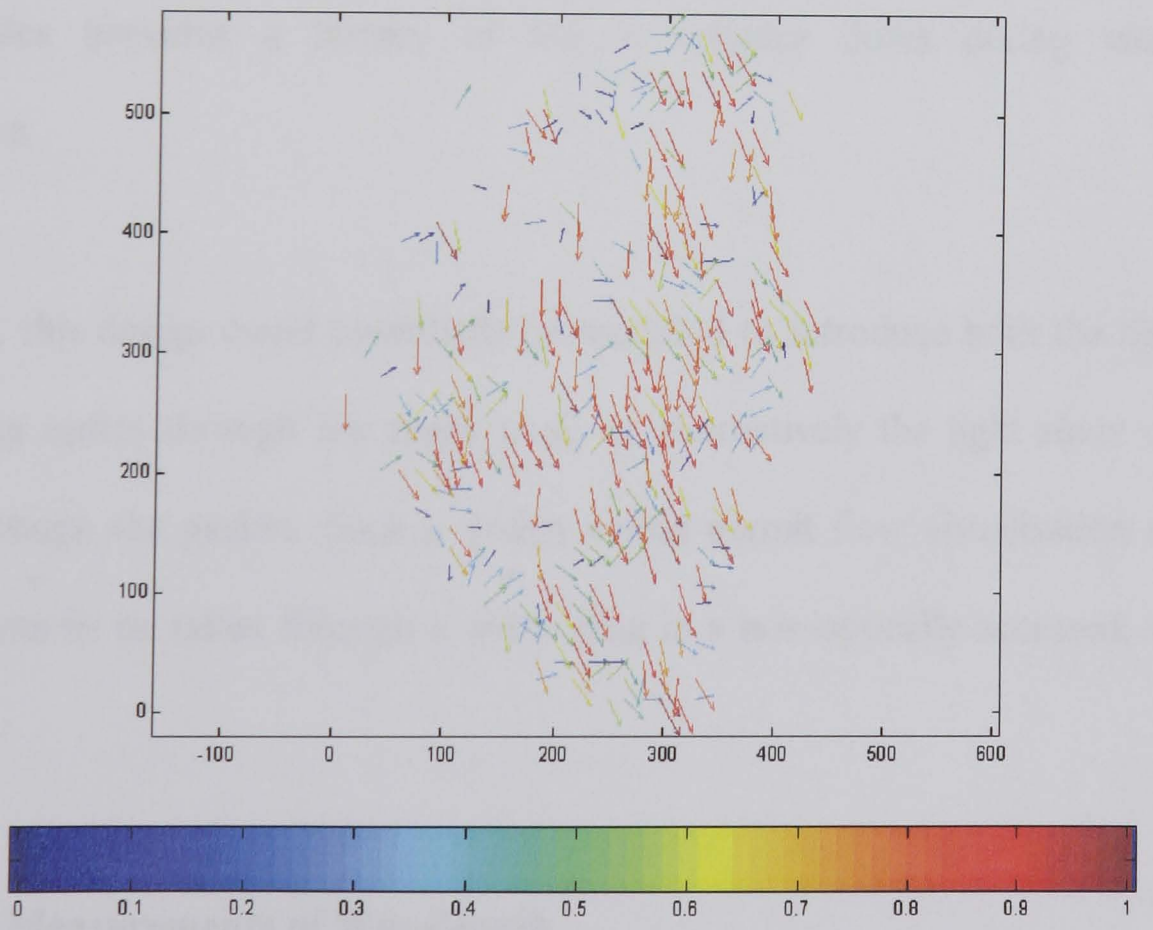

Figure 8.12, Averaged vector plot for experimental arrangement B.

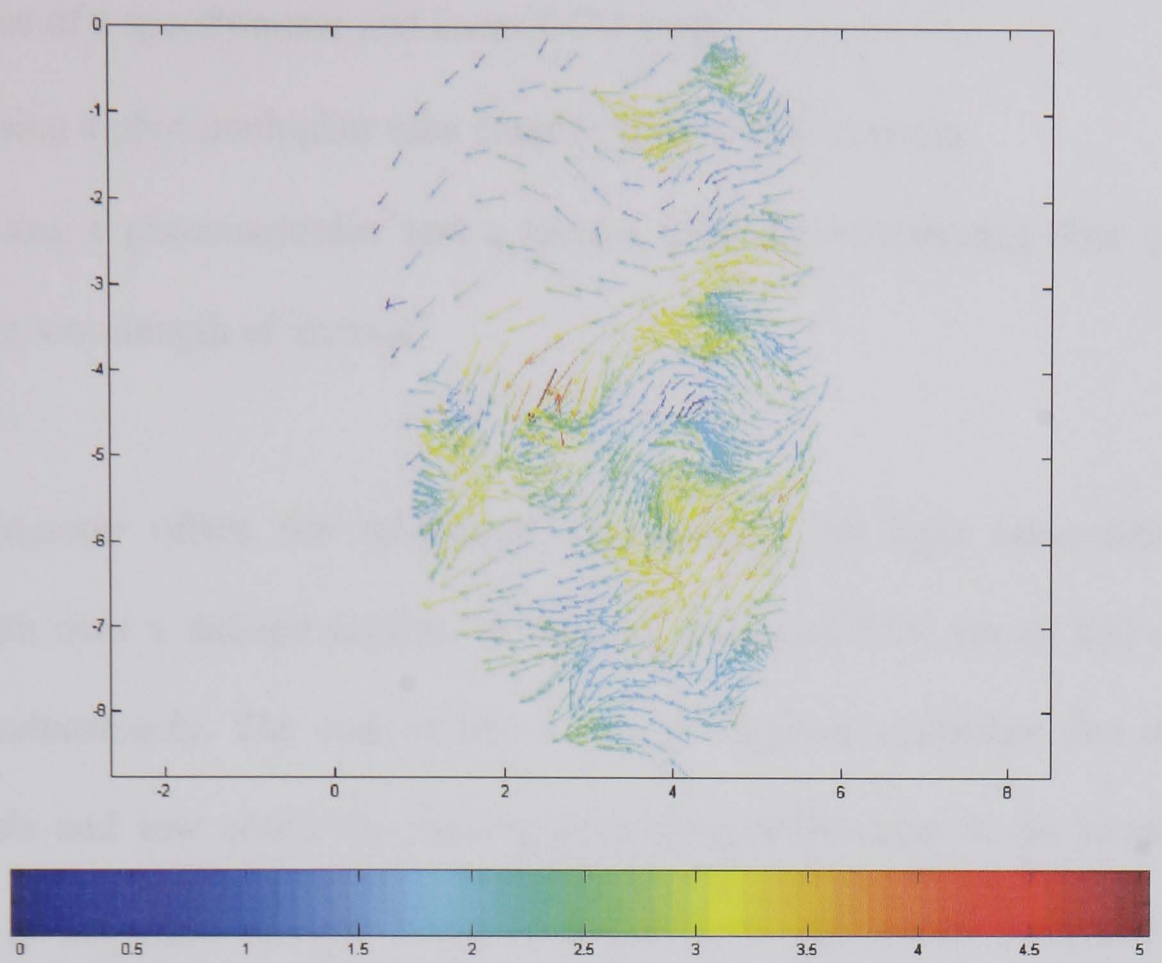

Figure 8.13, Averaged vector plot for experimental arrangement of B.

For each image the laser and camera were triggered at the same crank angle during the compression stroke. Results from ensemble averaging vector results from different crank angles provides a history of the in cylinder flows during intake and compression.

If required, this design could potentially be modified to introduce both the light sheet and imaging optics through the spark plug, or alternatively the light sheet could be inserted through the gasket. Such a design would permit flow visualisation and PIV measurements to be taken through a spark plug in a non-optically accessed, motored engine.

8.4 Measurements of Wavelength

The spectral content of the light emitted from the combustion was determined by one of three methods:

- Use of a spectrometer and linear CCD array
- Using a photomultiplier tube coupled to a monochromator
- Using a photomultiplier and a narrow bandpass interference filter centred on the wavelength of interest.

A spectrometer offers the advantage of capturing the light intensities at each wavelength over a defined portion of the light spectrum (200 nm to 800 nm in this case) simultaneously. The cost of this is loss in temporal resolution due to the low light levels and low sensitivity causing long integration times to be required. This resulted in the light spectra being averaged over the entire combustion event; therefore, all time resolved detail is lost. A spectrum sampled with the spectrometer is shown in Figure 8.14. It may be noted from this plot that the signal intensity over the dark level is very low, typically only up to 3 counts; consequently the noise level is high and little useful information may be gleaned from the data.

A photomultiplier tube has a fast response and therefore when coupled with a monochromator or bandpass filter, the light emission at one wavelength can be tracked at greater than 1° CA resolution. With the use of tables [12], it is possible to identify the wavelength that each chemical species emits light at. For example, it is known that the OH radical emits light at 309 nm [12]; therefore, by measuring the emitted light intensity at 309 nm from the flame, it is possible to qualitatively show the development of OH within the volume sampled.

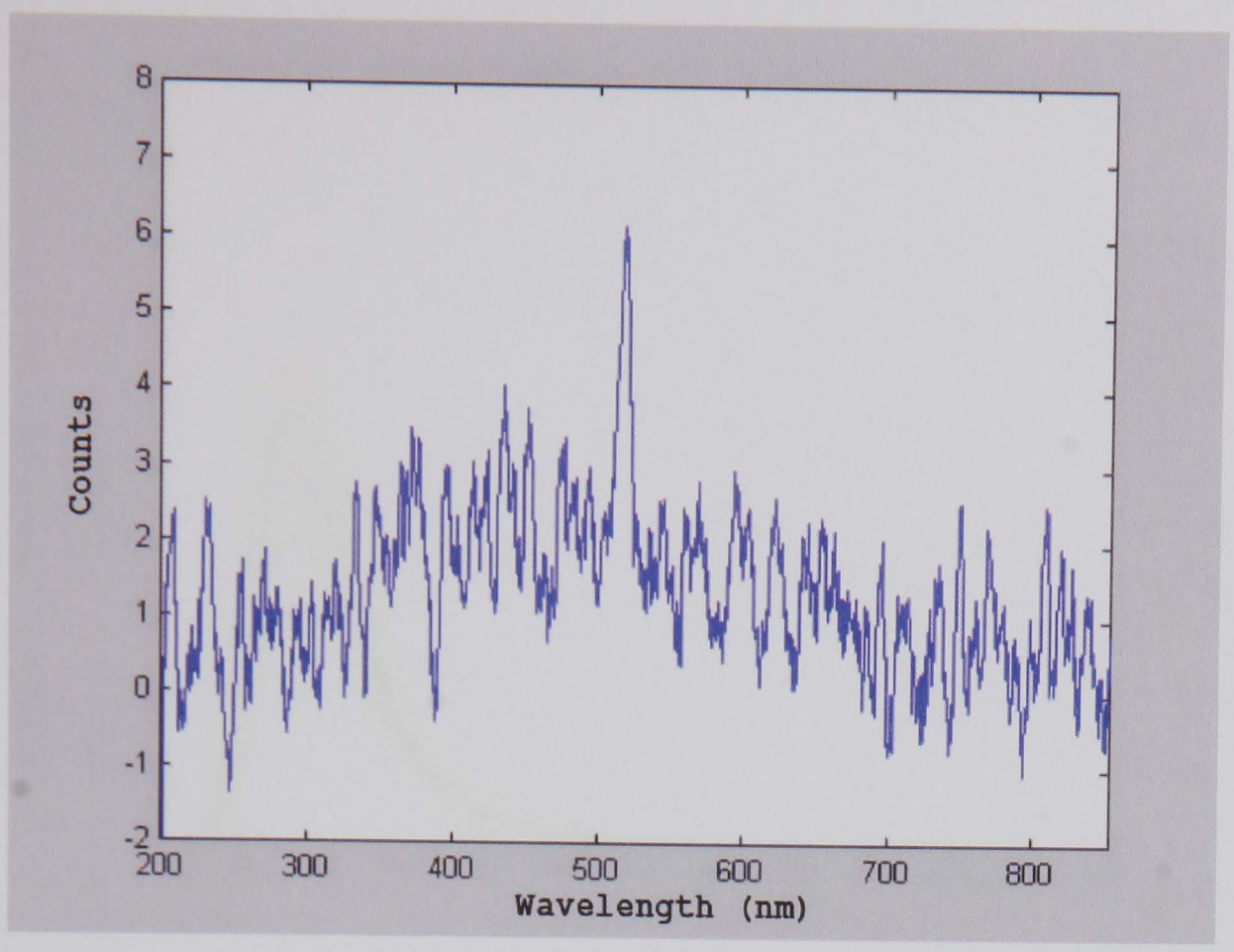

Figure 8.14, Spectrum averaged over entire combustion cycle with spectrometer.

The following graphs show the instantaneous, average and standard deviation from the mean of the development of certain wavelengths measured using a photomultiplier tube and monochromator with an optical fibre mounted in the cylinder head.

By changing the input slit width, the resolution of the monochromator may be varied up to a resolution greater than 1 nm, the following results use a slit width that yields a resolution of $\approx \pm 5$ nm. The following wavelengths are plotted below as examples as they are the wavelengths that peak when plotted as a spectra Figure 8.24.

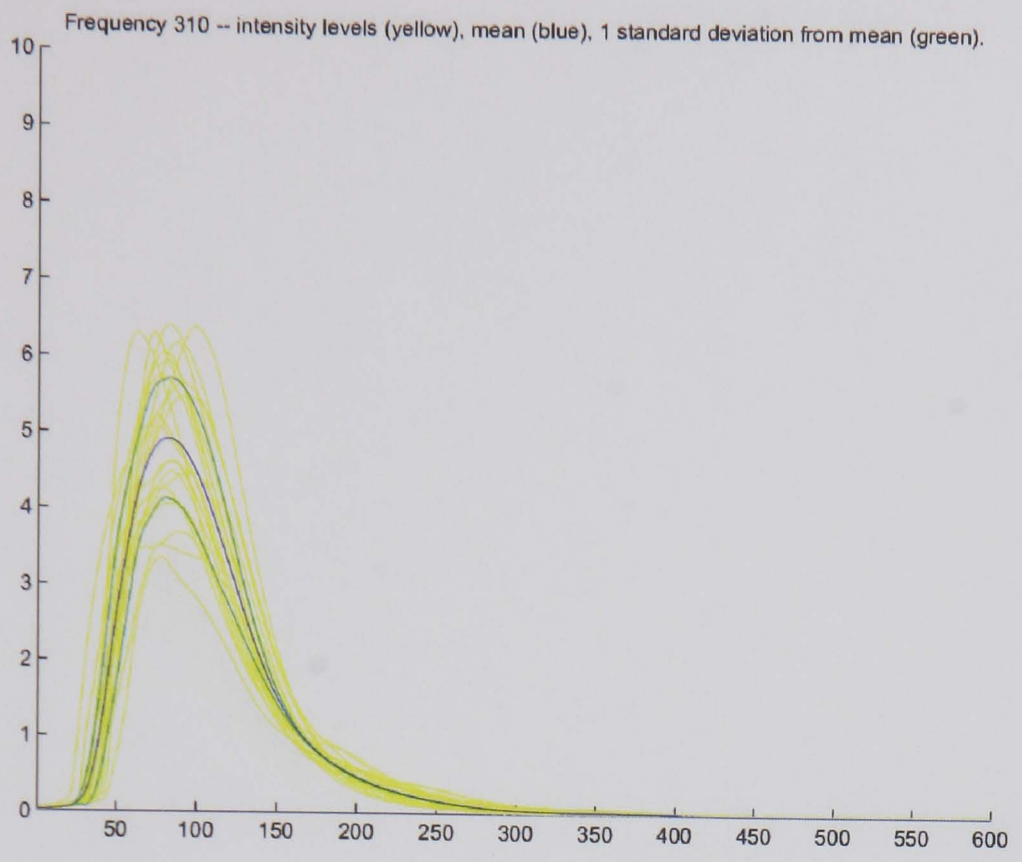

Figure 8.15, Light emitted from flame at 310 (≈ 309) nm (OH). Y-axis: intensity, X-axis: crank angle.

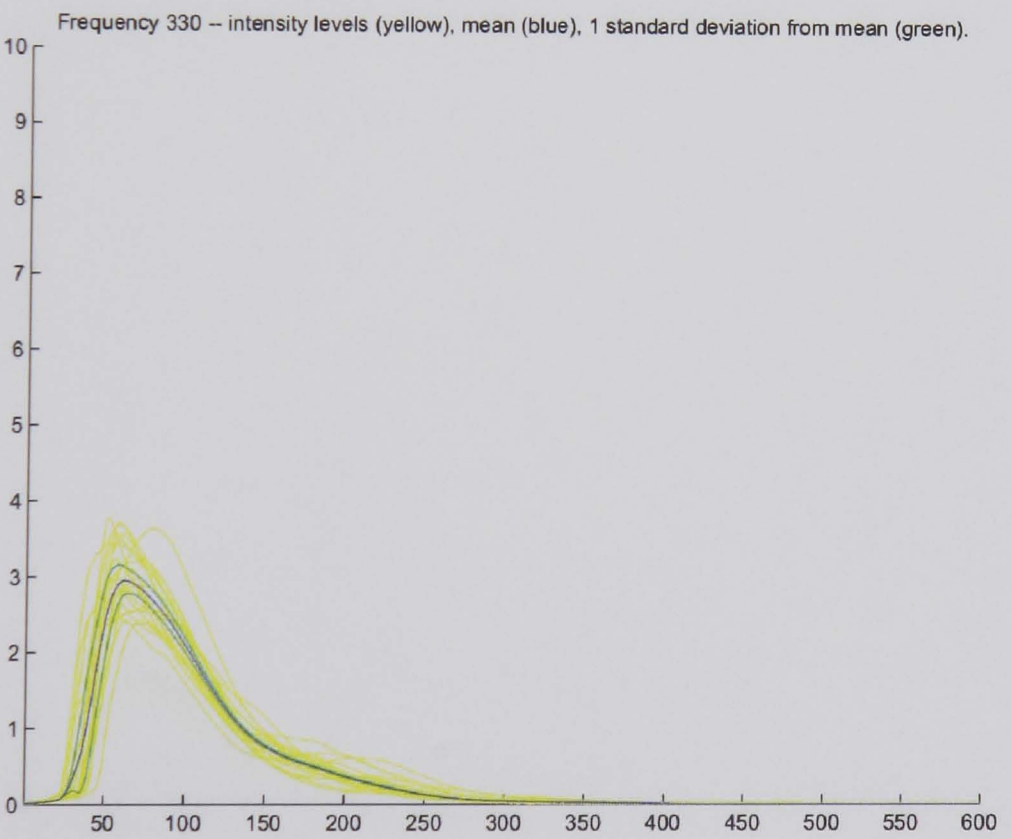

Figure 8.16, Light emitted from flame at 330 nm. Y-axis: intensity, X-axis: crank angle.

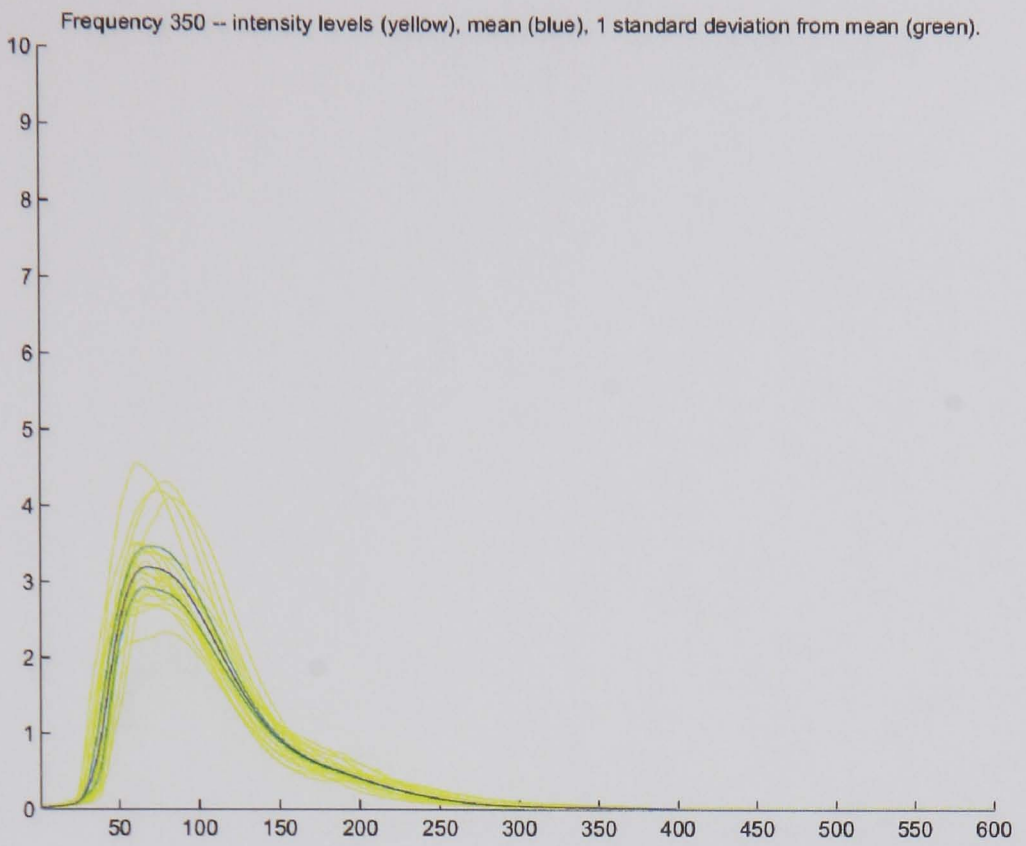

Figure 8.17, Light emitted from flame at 350 nm. Y-axis: intensity, X-axis: crank angle.

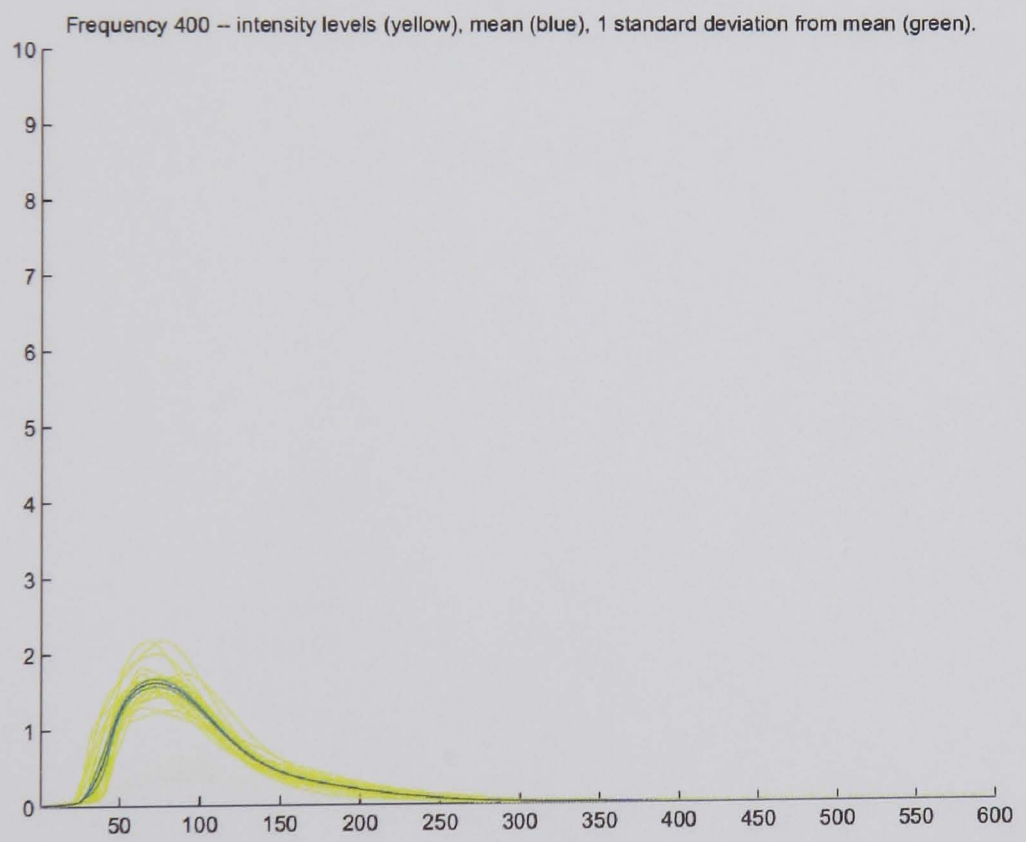

Figure 8.18, Light emitted from flame at 400 nm. Y-axis: intensity, X-axis: crank angle.

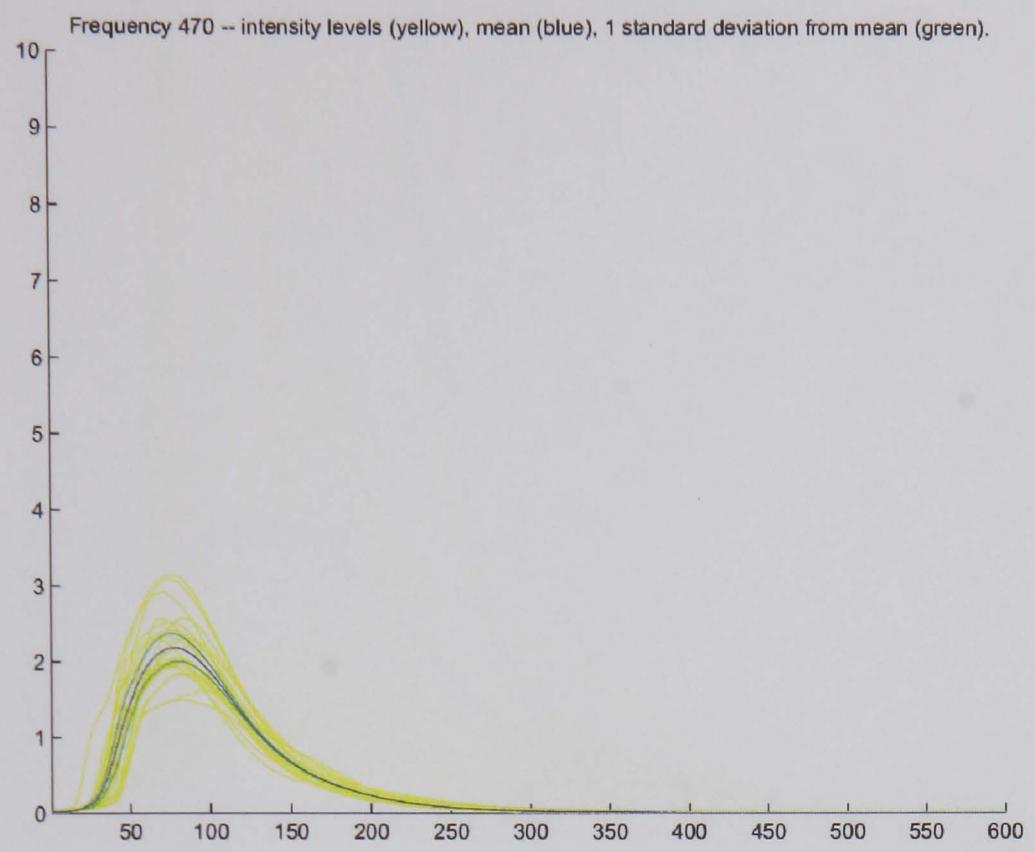

Figure 8.19, Light emitted from flame at 470 nm. Y-axis: intensity, X-axis: crank angle.

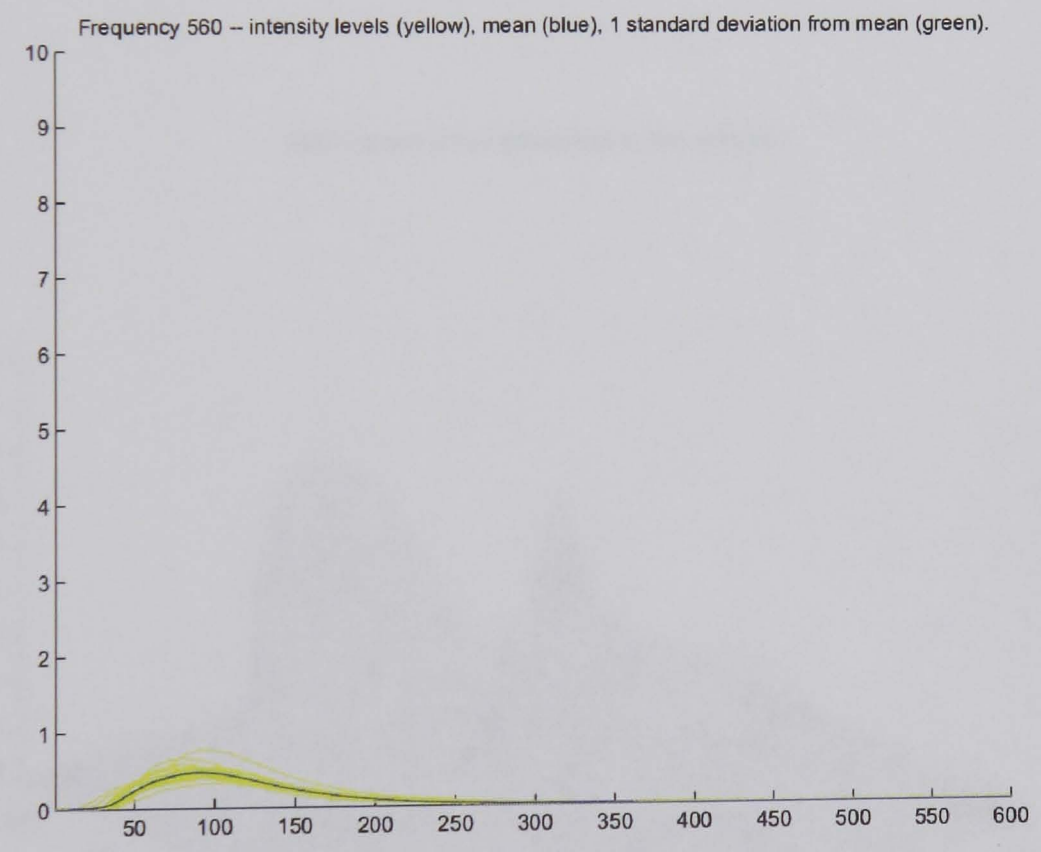

Figure 8.20, Light emitted from flame at 560 nm. Y-axis: intensity, X-axis: crank angle.

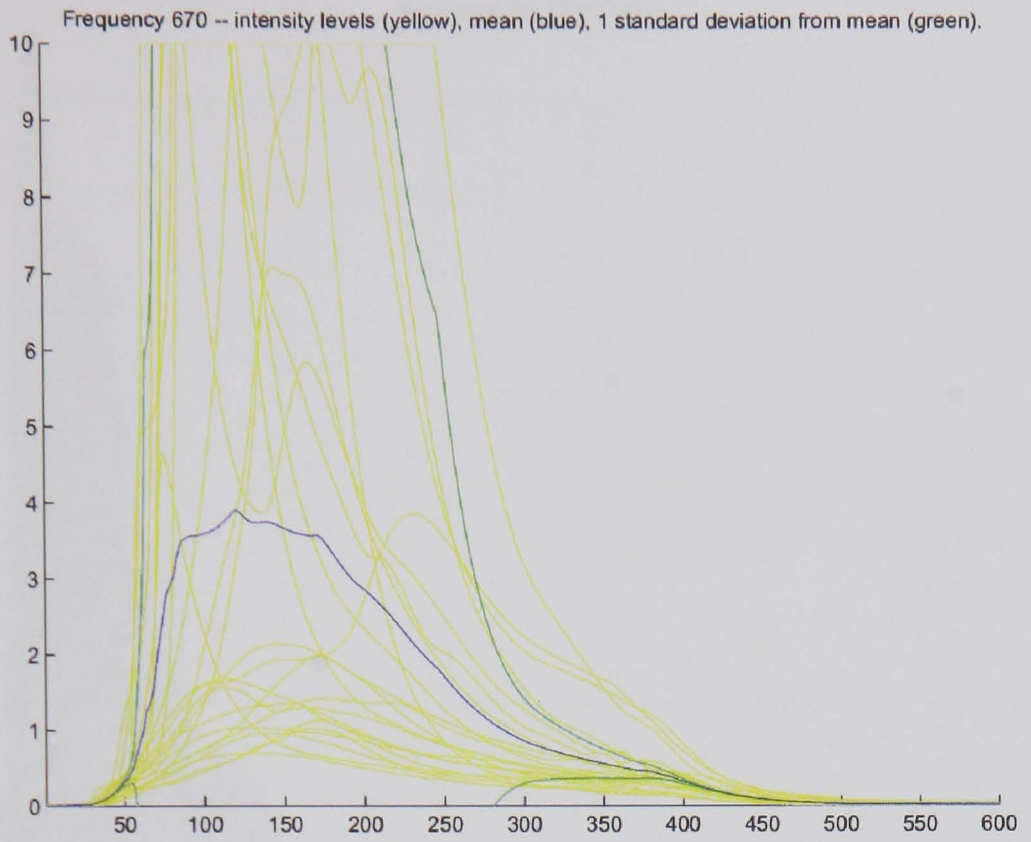

Figure 8.21, Light emitted from flame at 670 nm. Y-axis: intensity, X-axis: crank angle.

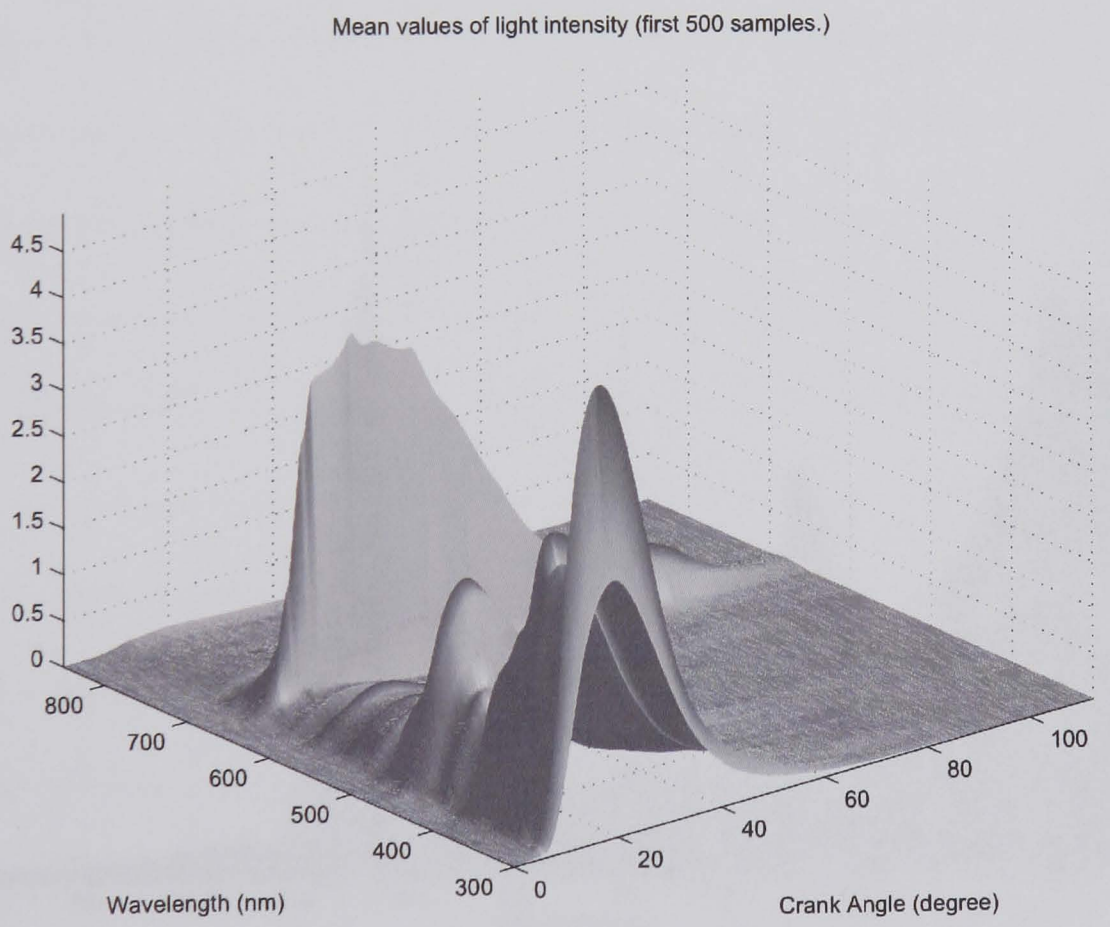

Figure 8.22, Three-dimensional plot of light emission for each wavelength against time (crank angle).

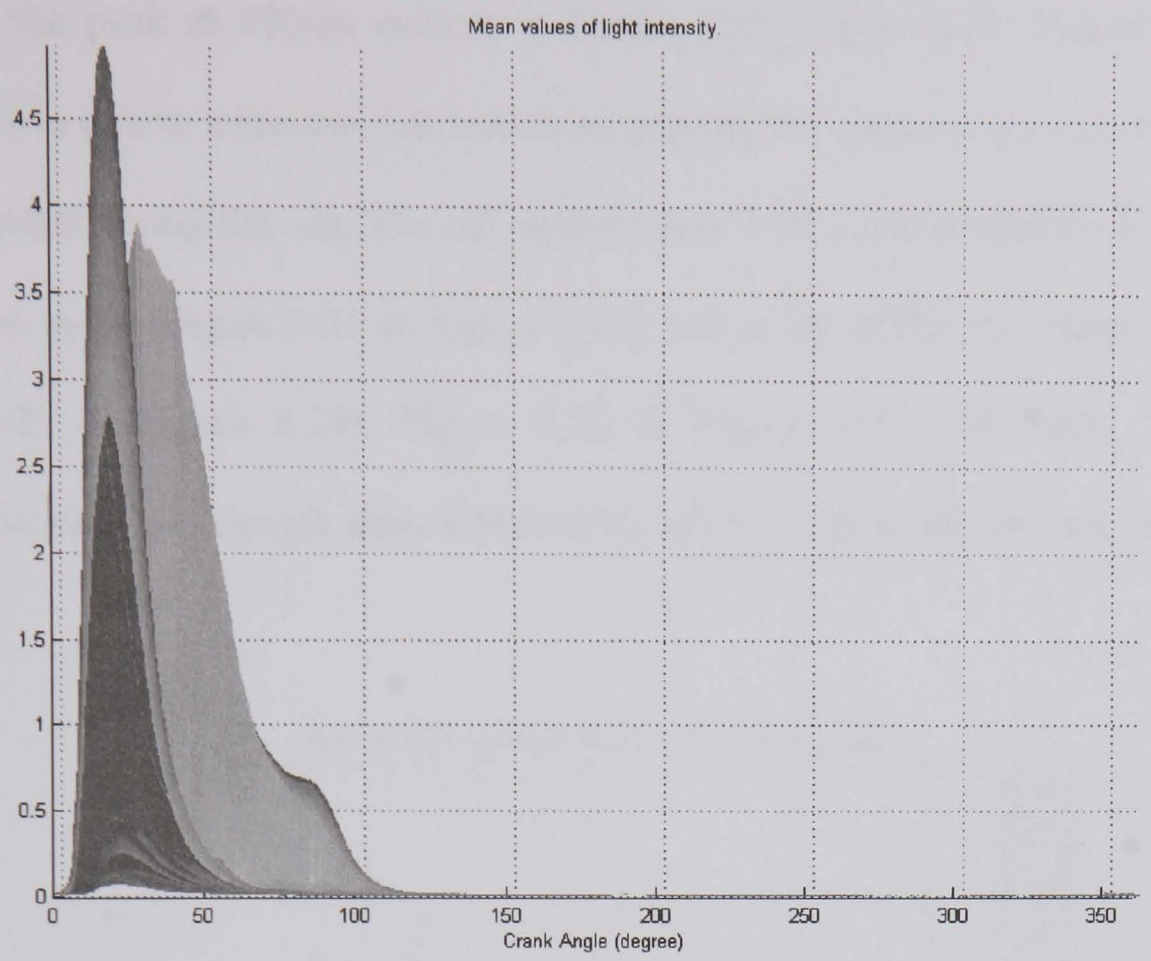

Figure 8.23, End-on view of light emission illustrating how different wavelengths occur at different timings and have different durations. Y-axis: intensity.

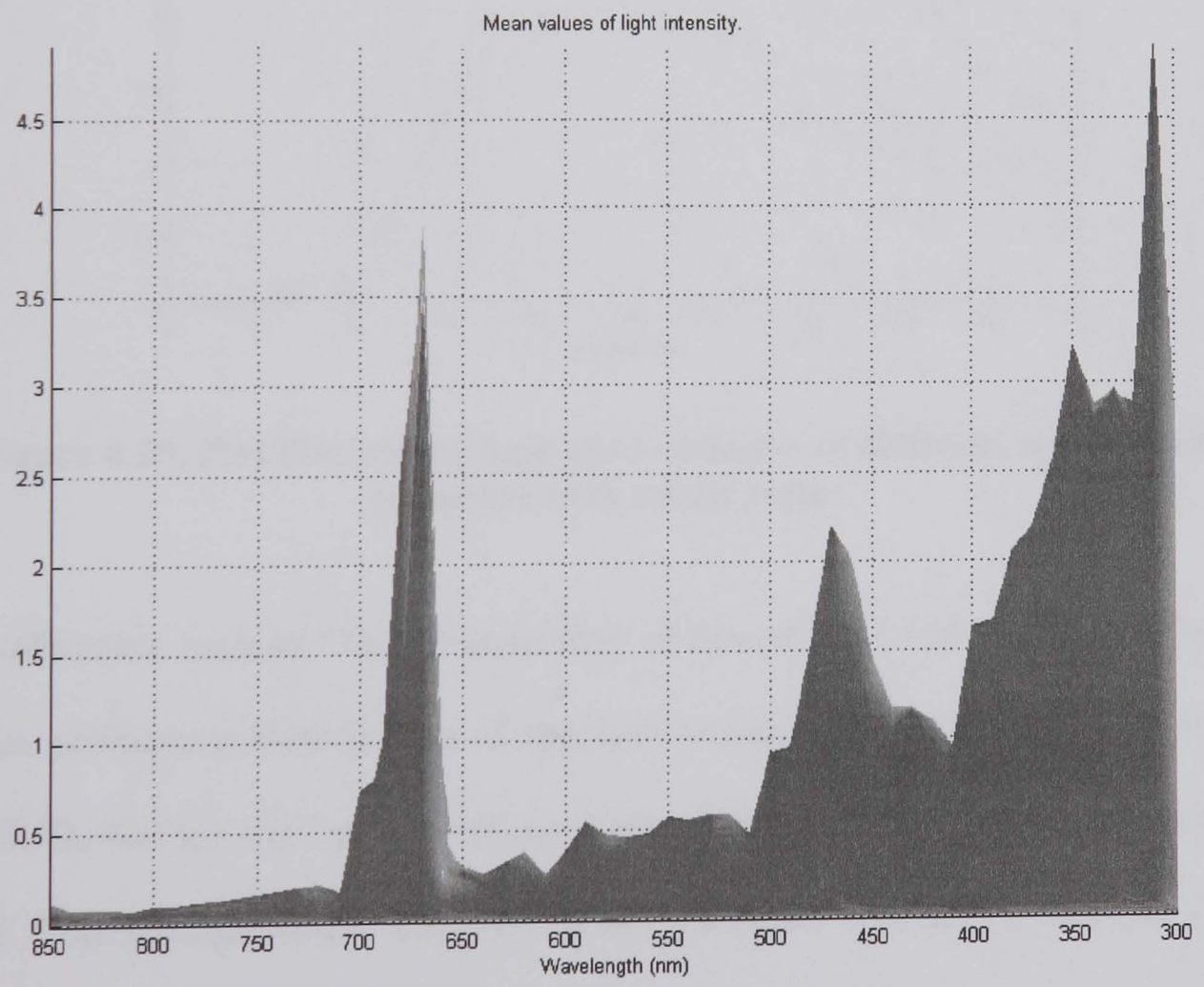

Figure 8.24, 'Spectrum' of light emission averaged over 100 cycles for each wavelength and measured at 10nm steps. Y-axis: intensity.

Note that the peak at 670nm evident in Figure 8.21, Figure 8.22, Figure 8.23 and Figure 8.24 is due to excessive lubrication oil passing the piston rings and combusting in the chamber during the run. The oil vapour burns with a low temperature late in the combustion cycle (Figure 8.21 & Figure 8.22) and emits in the red / near IR region (Figure 8.21 & Figure 8.24). Figure 8.22 & Figure 8.23 both show how light emissions at each wavelength show different durations, peak intensities and profiles.

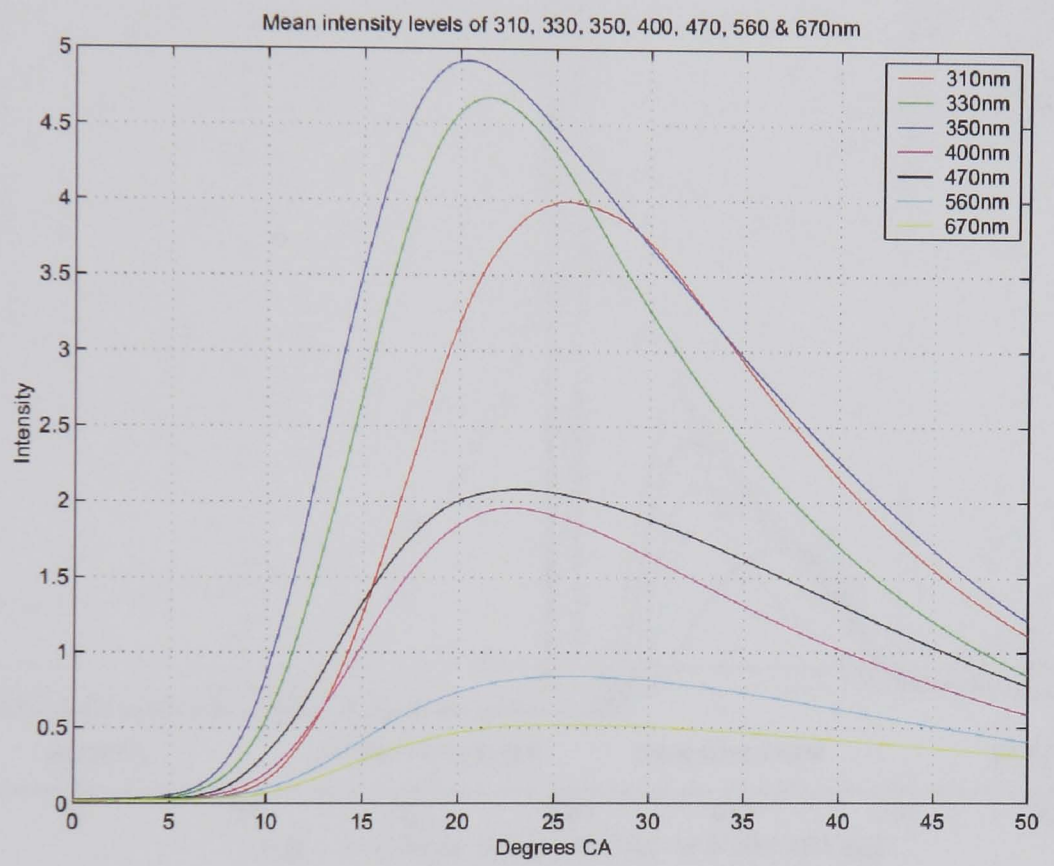

Figure 8.25, Plot illustrating how light emission at different wavelengths compares with crank angle.

From references such as "The spectroscopy of flames" by Gaydon [12], it is possible to make preliminary identification of species / wavelengths, such as 330 nm is likely to be HCO, 400 nm and / or 470 nm are likely to be CH_2O and 310 nm is expected to be OH. Only through further engine runs using a higher wavelength resolution will it be possible to correctly identify each corresponding species / wavelength.

8.5 Measurements of Emitted Light Intensity

Photodiodes with known spectral acceptance were used to measure the total emitted light of the flame at defined positions within the flame. These probes can be used to show how the light intensity changes across the chamber as the flame propagates.

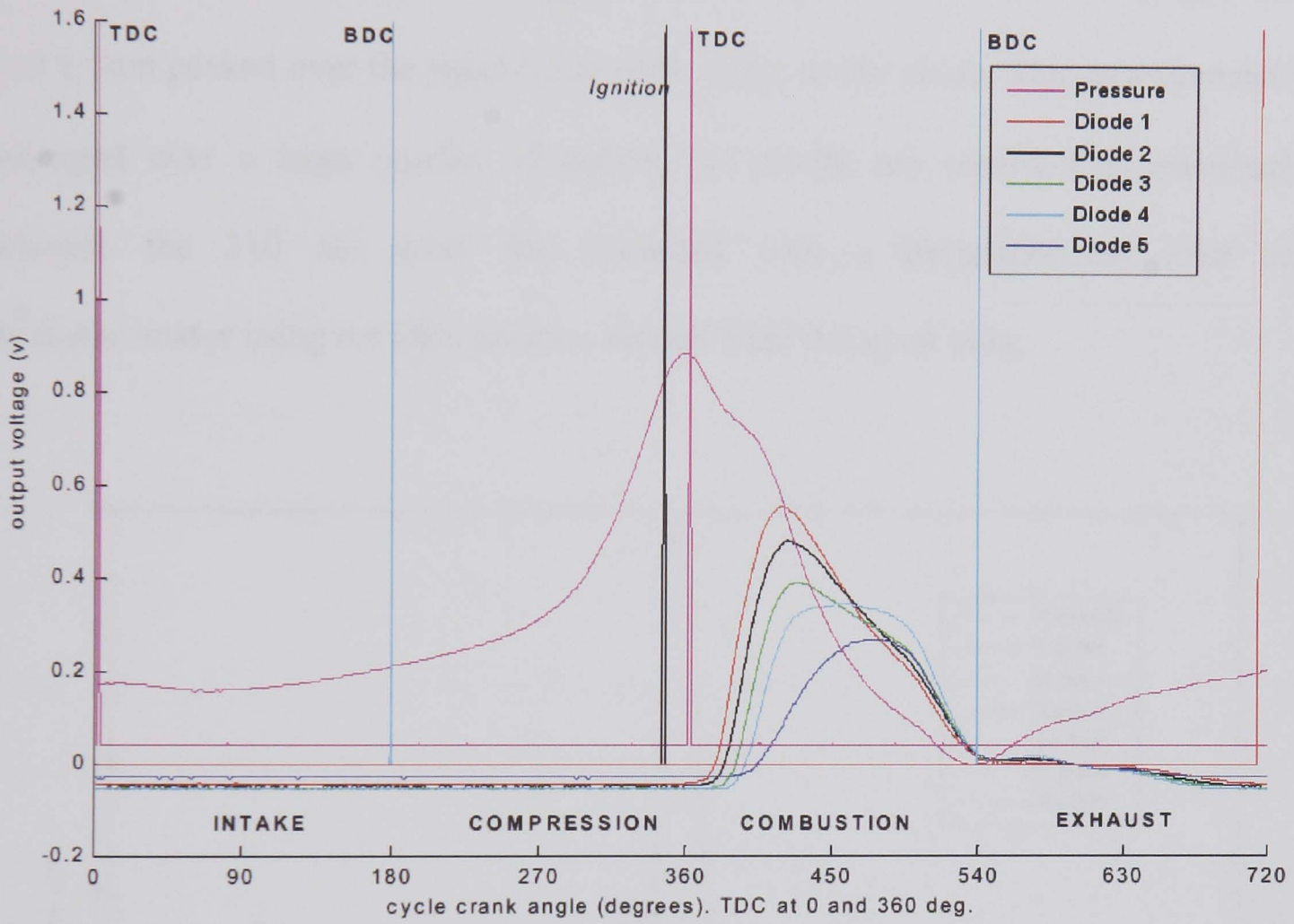

Figure 8.26, Plot of in-cylinder pressure and each photodiode level for 2000 RPM, no load.

By instrumenting a cylinder head with five diodes viewing the combustion chamber via fibre optics, as described in Chapter 7, it was possible to track the flame propagating across the chamber, as graphed in Figure 8.26. In this figure, the in-cylinder pressure is observed to peak at TDC, and each photodiode records a reduced light intensity as the flame propagates further from the spark plug. The rise of each photodiode signal indicates the plot order; in other words, the photodiode nearest the spark plug rises first, the diode furthest away rises last. It is observed that the light

emission and therefore also the combustion, is only present during the expansion stoke (360° ATDC - 540° ATDC) as expected.

Although the diodes are not spectrally filtered and therefore have a wide spectral acceptance, it was investigated which wavelength has the most significant impact on the recorded signal. As shown in Figure 8.27, it was found that the wavelength band 310 ± 5nm peaked over the same crank angle range as the diode. This measurement is averaged over a large number of cycles; the diodes are recorded as previously, whereas the 310 nm band was recorded with a photomultiplier tube and monochromator using the fibre position second from the spark plug.

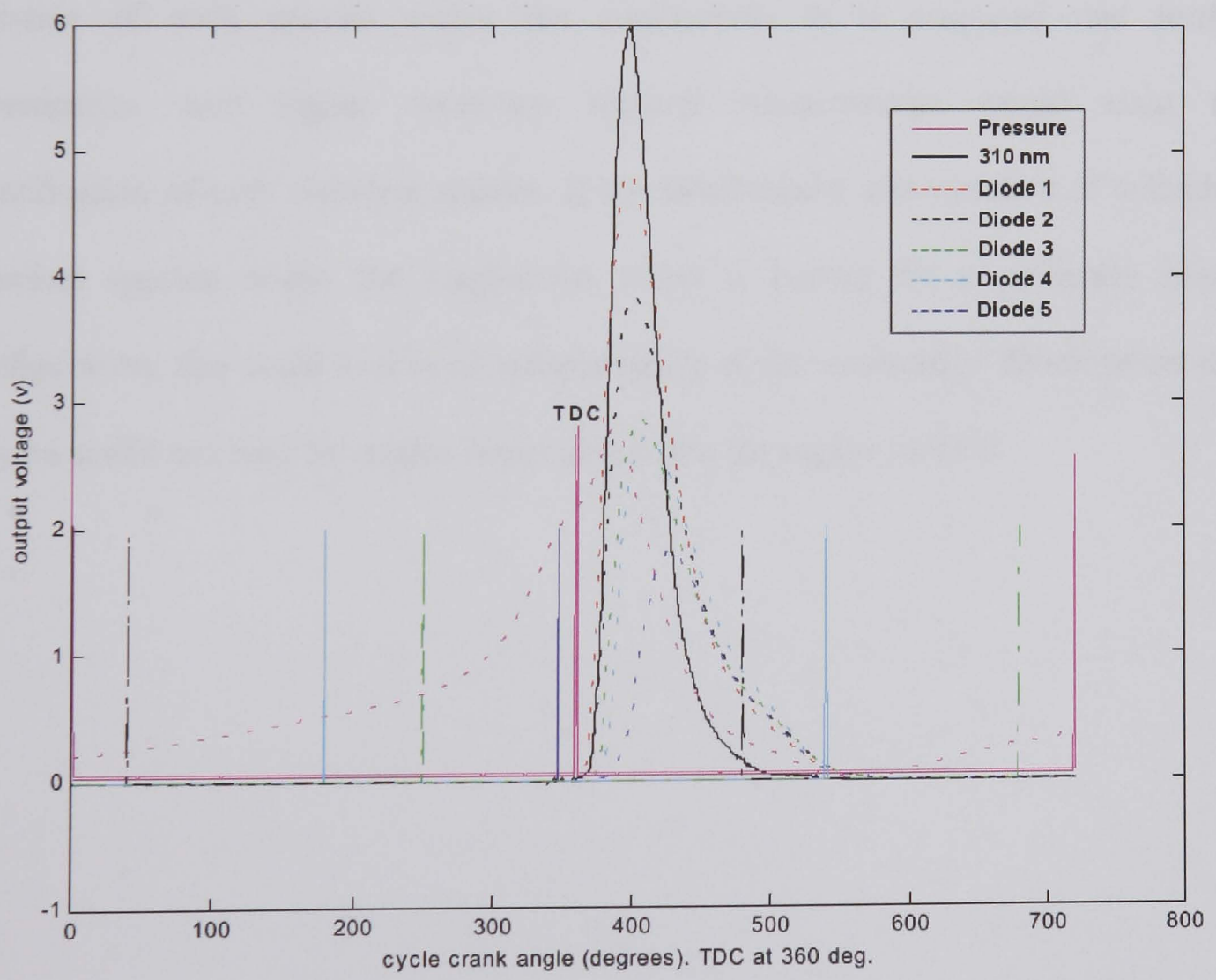

Figure 8.27, Plot of in-cylinder pressure, diode signals for the 5 fibre positions (dotted) and the 310 nm signal (solid, highest peak) recorded with a PMT and monochromator for 2000 RPM loaded.

8.6 Conclusions

It has been shown that it is possible to make qualitative (flow visualisation) and quantitative (PIV) measurements of in-chamber flow within an engine that has not had significant modifications to achieve optical access. This is the first PIV measurement of the flow within an internal combustion engine made through the spark plug.

The spectral and light intensity measurements have similarly been successful in recording in-cylinder light levels during the combustion event. It has been shown that plots of discrete light wavelengths show significant differences in intensity, timing, profile and duration. These differences are due to the chemical reactions and the light emission of each species within the combustion. It is proposed that further investigation with higher resolution spectral measurements would assist the identification of each chemical species. If the development and variation of individual chemical species within the combustion event is known for a particular engine configuration, this could lead to an understanding of the combustion development that may be useful not only for engine research but also for engine control.

CHAPTER 9

TEMPERATURE AND HEAT FLUX RESULTS

9.1 Summary

This chapter presents results obtained from the heat flux sensors applied to the engine. Each stage of results during processing is illustrated, from the raw data measured within the engine, the surface temperature plots before finally the heat transfer rate plots.

9.2 Raw Data

As previously described in Chapter 5, the instrumentation varies the voltage applied to the gauges in order to maintain a constant low current passing through the gauge. This varying voltage is proportional to the gauge temperature.

A typical example plot of the raw data is shown in Figure 9.1. Five cycles worth of raw data is also shown in Figure 9.2. Both of these plots were generated for data recorded from gauge 7 (gauge nearest the spark plug). A noticeable change in raw signal is observed after approximately the third cycle when the engine fires. A further less noticeable change occurs after approximately the eighth cycle caused by the generator switching on and applying a load to the engine. Note that the recorded signal is inverted, *i.e.* decreasing voltage = increasing temperature.

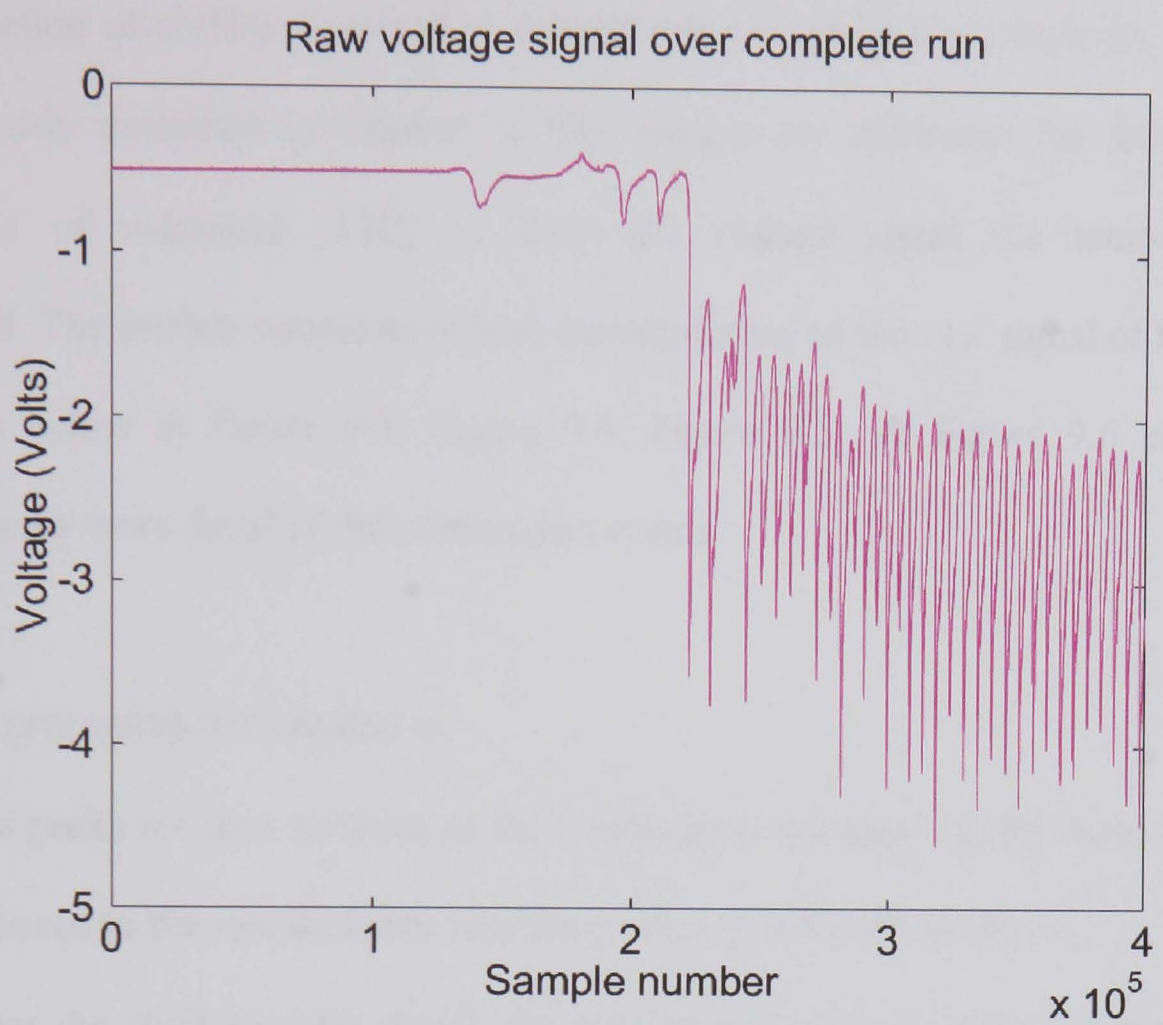

Figure 9.1, Raw data for the complete run, recorded from gauge 7.

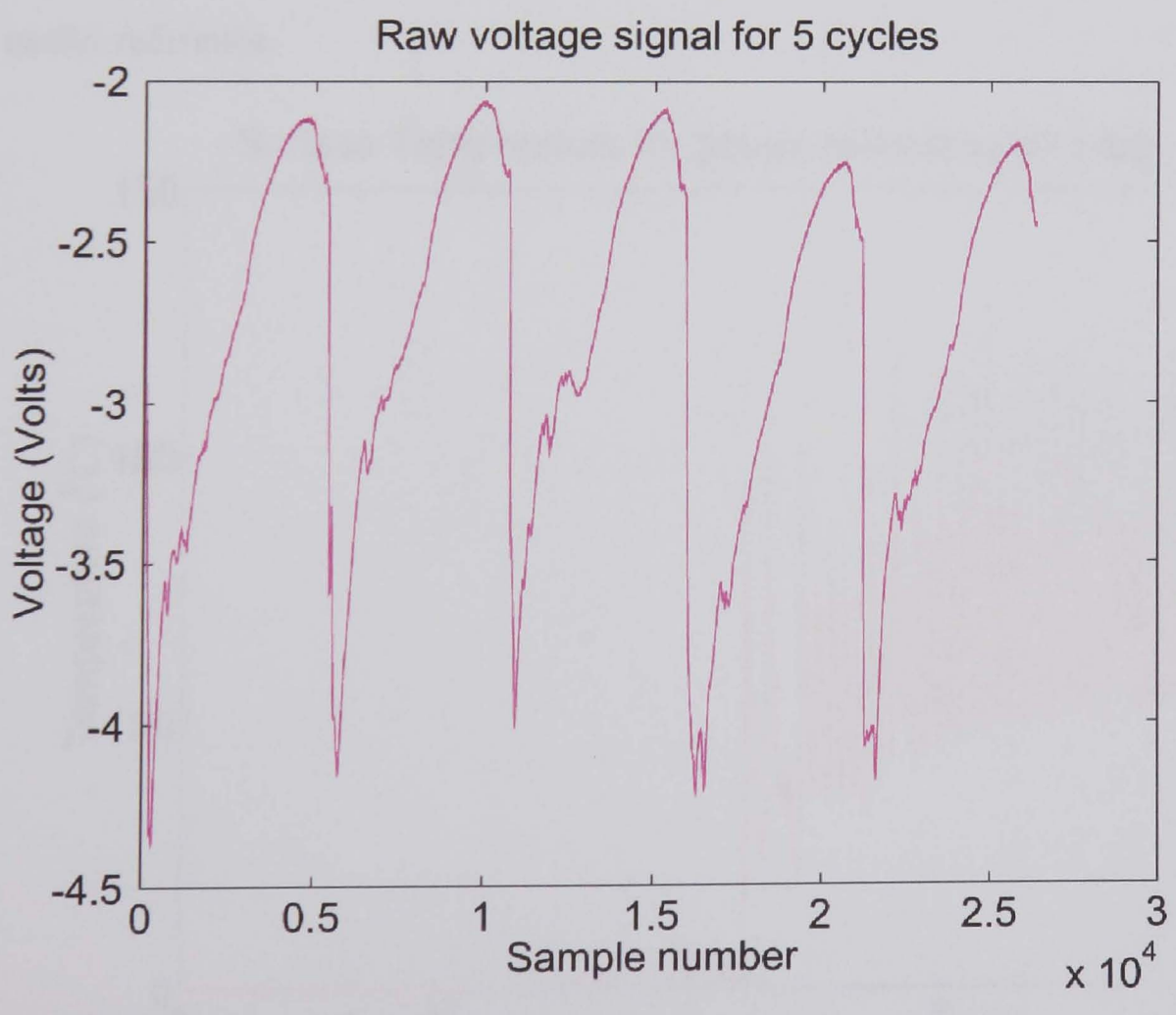

Figure 9.2, 5 cycles of raw data from gauge 7.

9.3 Surface Temperature Determination

Determination of surface temperature is relatively straightforward from the raw data, as previously described in Chapter 5. The gauges are calibrated for their thermal coefficient of resistance [122], so from the voltage signal the temperature is calculated. The surface temperature plot corresponding to the raw signal of Figure 9.1 is shown below in Figure 9.3. Figure 9.4, Figure 9.5 & Figure 9.6 each show progressively more detail of the combustion events.

The data processing has resulted in,

- The peaks are now positive as the temperature increases as the flame passes, as opposed to the raw data that was the inversion of the temperature.
- From the shaft encoder signal, the corresponding crank angle for each sample has been calculated. Plots are now against crank angle, which is known to be a useful reference.

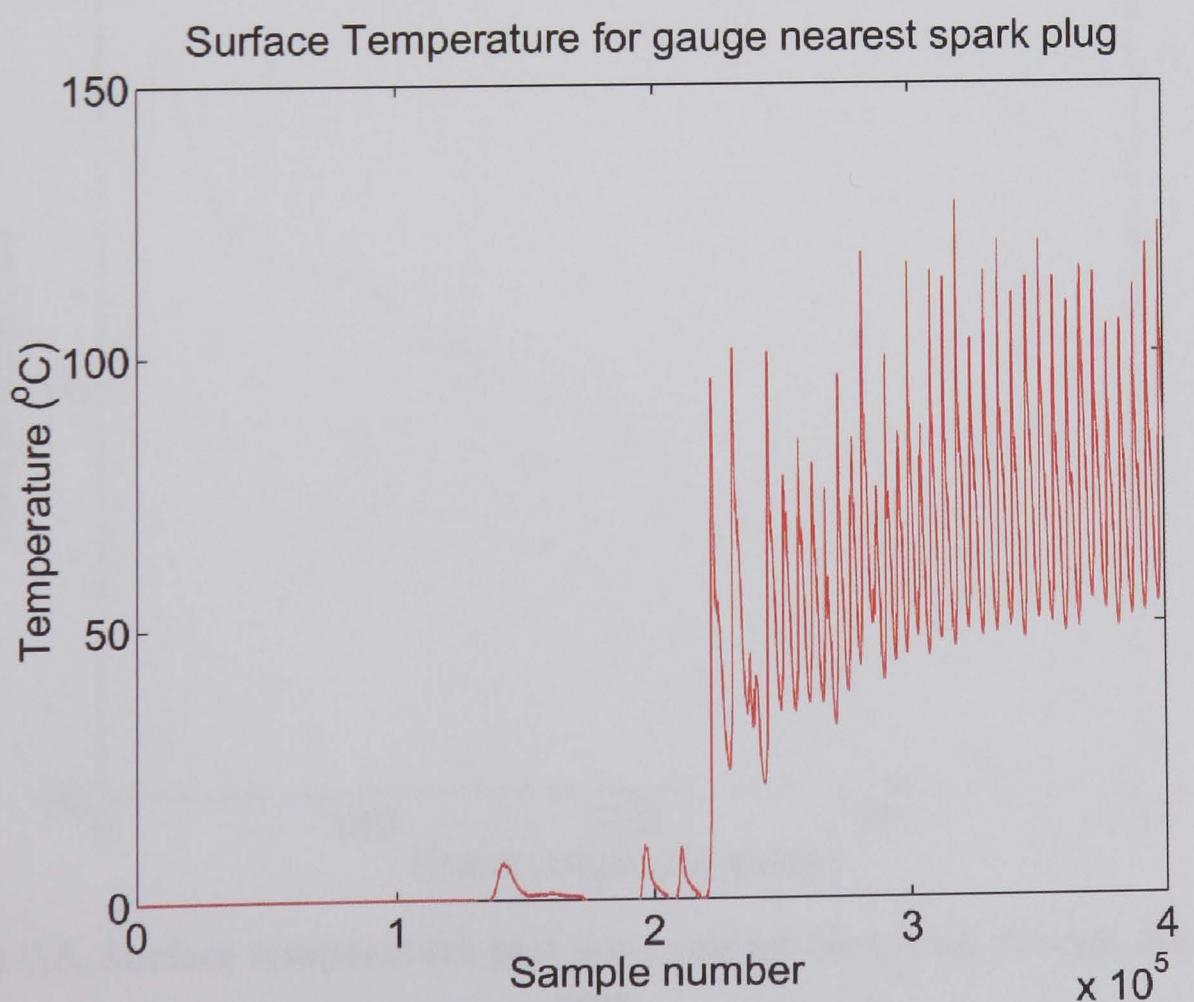

Figure 9.3, Temperature for gauge nearest spark plug for the complete run.

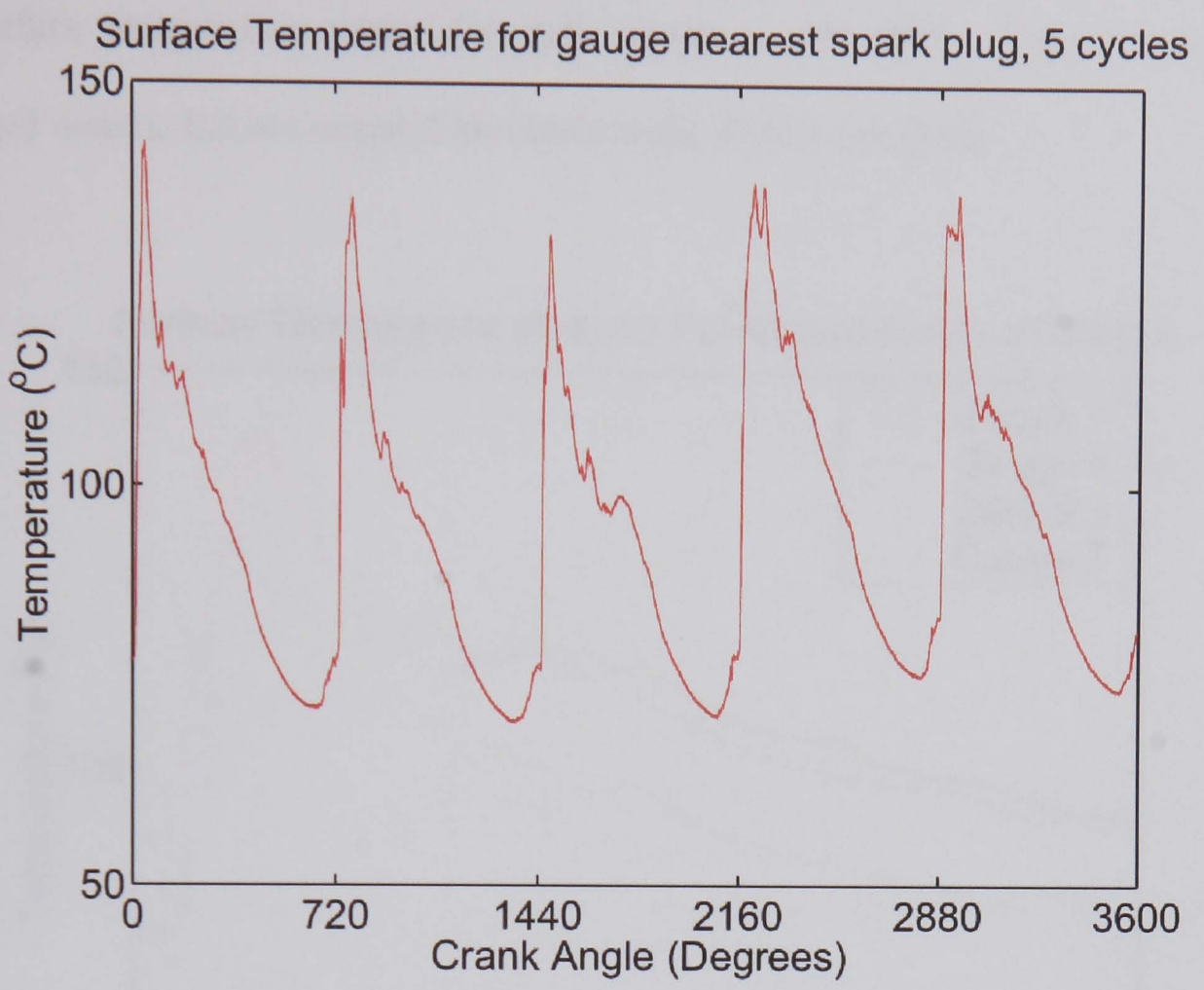

Figure 9.4, Surface temperature for the gauge nearest the spark plug for 5 cycles.

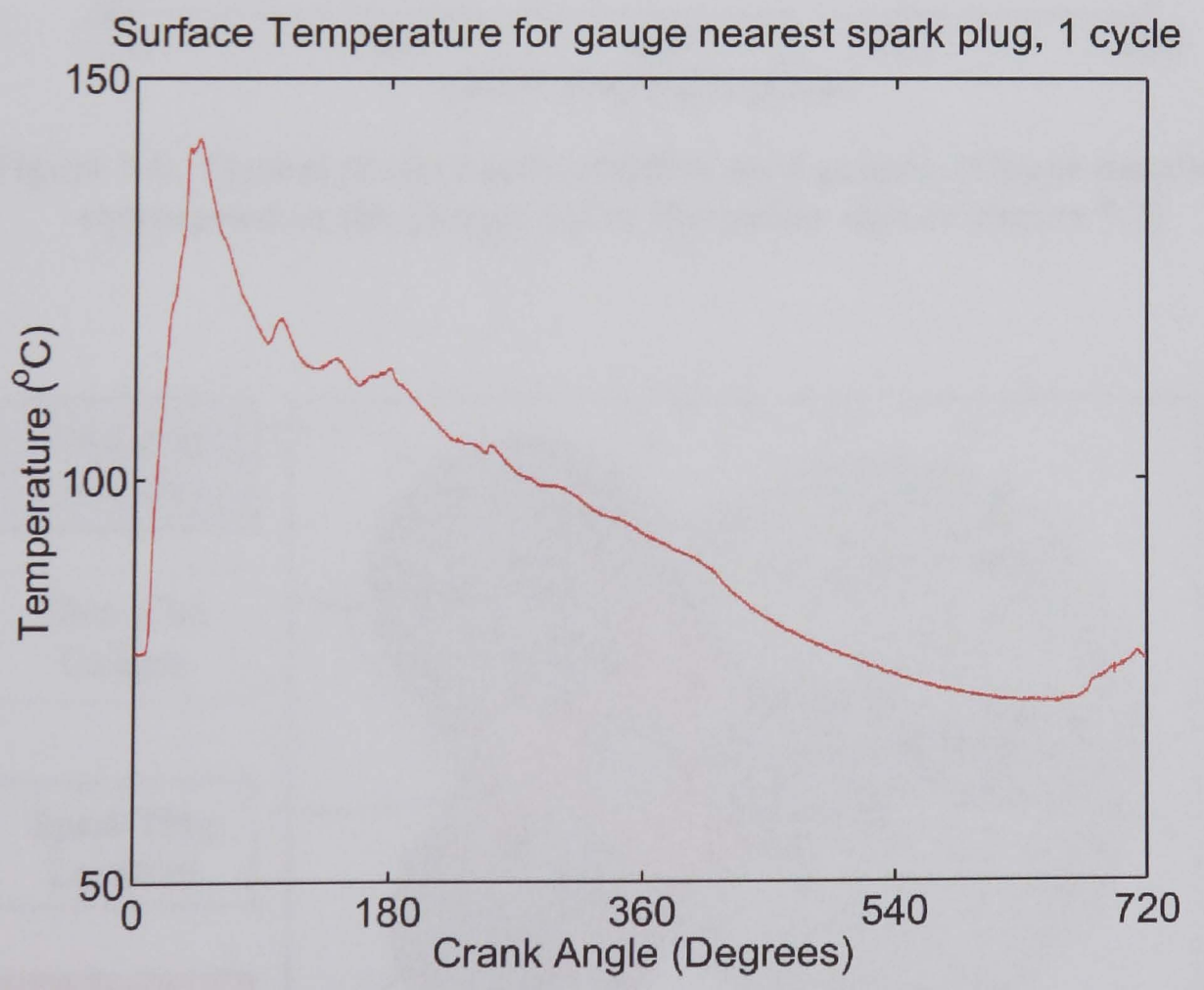

Figure 9.5, Surface temperature plot one cycle on the gauge nearest the spark plug.

The above plots are only for one gauge. The following figure, Figure 9.6, shows how the surface temperature varies for each gauge in one cycle. These are not cycle averaged results, but are sampled simultaneously during one cycle.

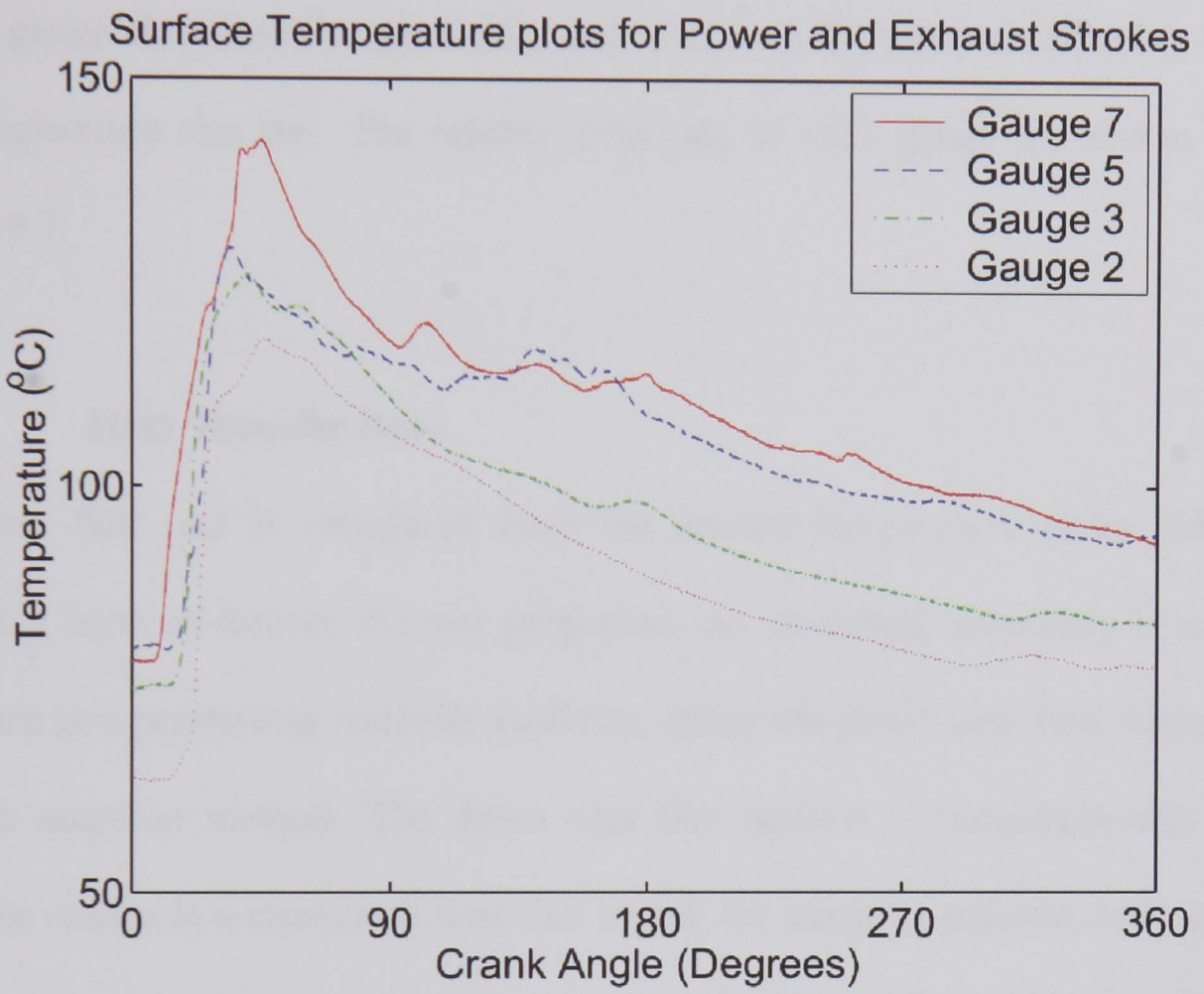

Figure 9.6, Typical surface temperatures on 4 gauges. (Gauge numbers correspond to the gauges above the piston area in Figure 9.7)

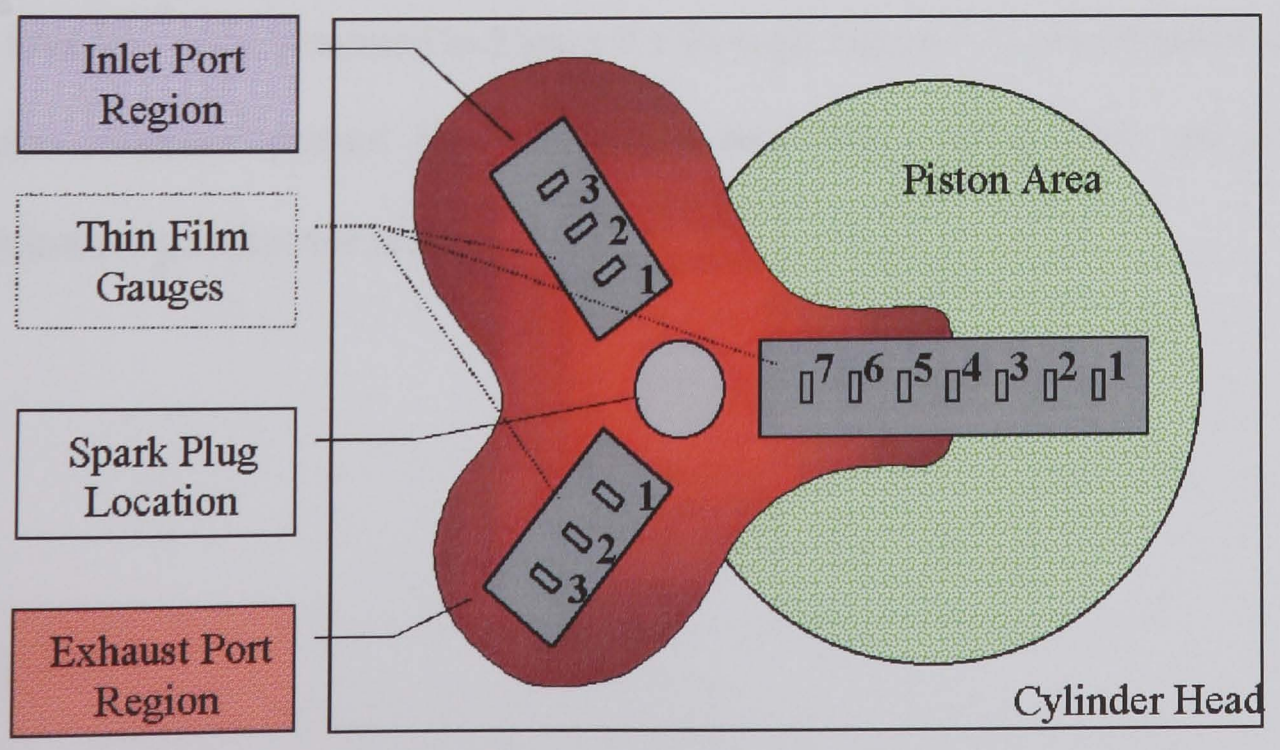

Figure 9.7, Schematic of gauge numbers on cylinder head and piston.

Figure 9.6 shows the relative surface temperatures at various points within the chamber. In particular it may be observed that determination of the flame propagating across the chamber is possible, with an increase in surface temperature observed first on the gauge closest to the spark plug and the gauge furthest from the plug recording the temperature rise last. The relative positions of each gauge are shown above in Figure 9.7.

9.4 Heat Transfer Rate

The heat flux rate is calculated from the known temperature either side of the insulating layer of known thermal properties. As described previously in chapter 5, there are two processing methods available, either the direct heat flux method or the impulse response method. The direct heat flux method is computationally quicker, however results in a dampened heat flux signal; the impulse response method is much slower, however provides a much improved response rate. The results from these two processing methods are compared in Figure 9.8.

The heat flux rates presented in Figure 9.9 through Figure 9.13 are obtained using the impulse response method since the direct heat flux method does not provide a sufficiently high response rate.

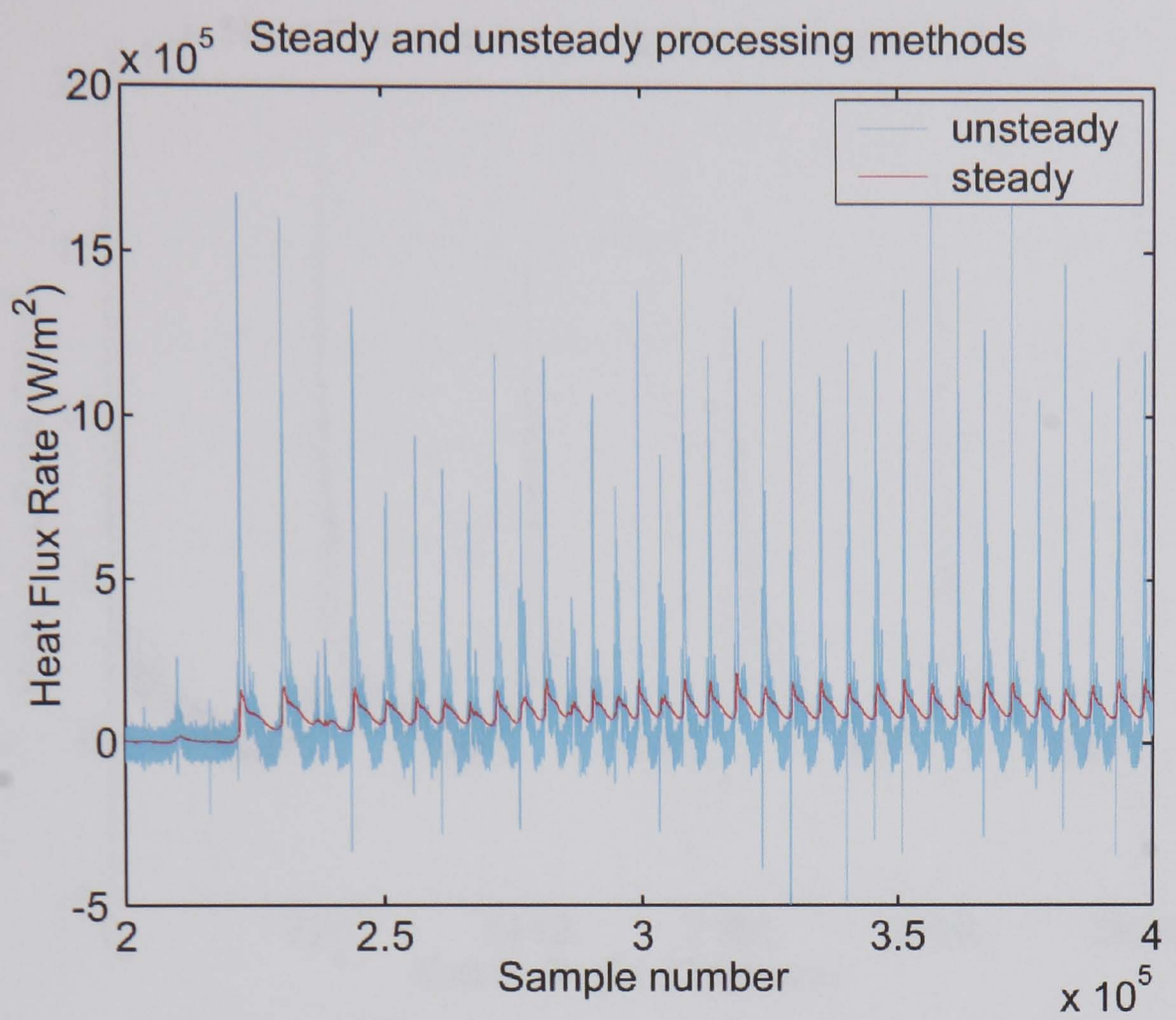

Figure 9.8, Comparison of steady (direct) and unsteady (impulse response) methods of heat flux rate processing.

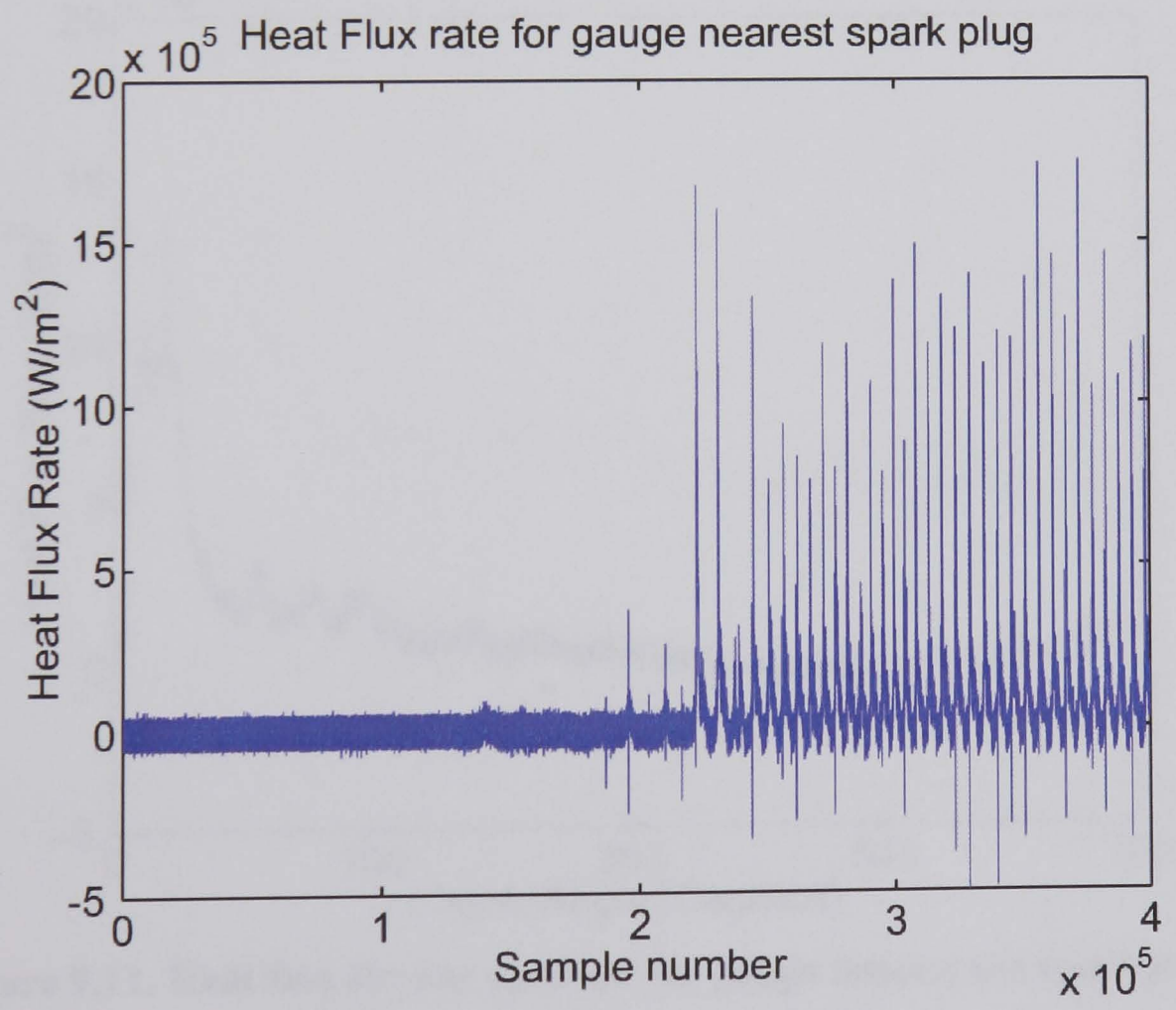

Figure 9.9, Heat flux for the gauge nearest the spark plug during the complete run.

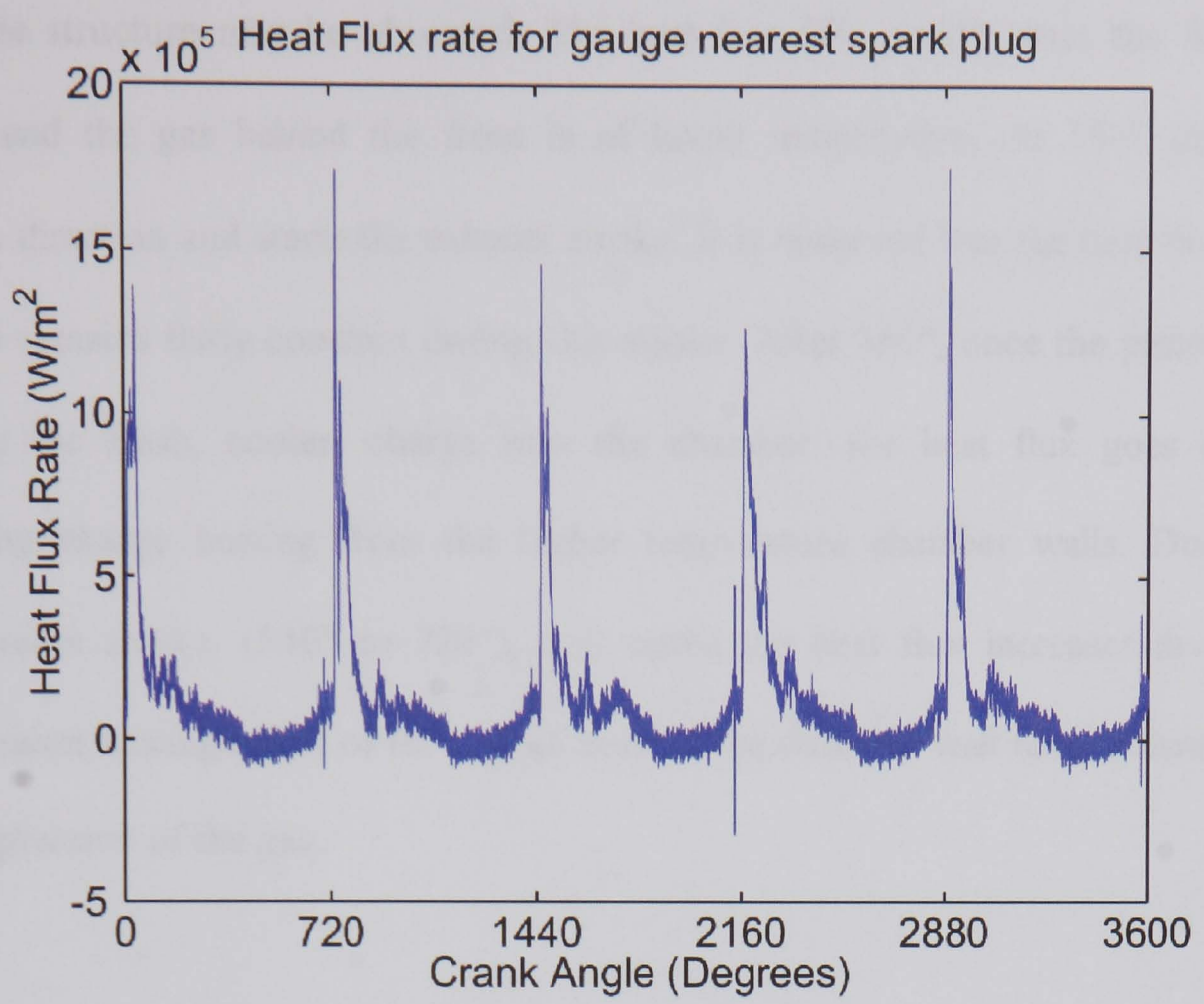

Figure 9.10, Heat flux for the gauge nearest the spark plug for 5 cycles.

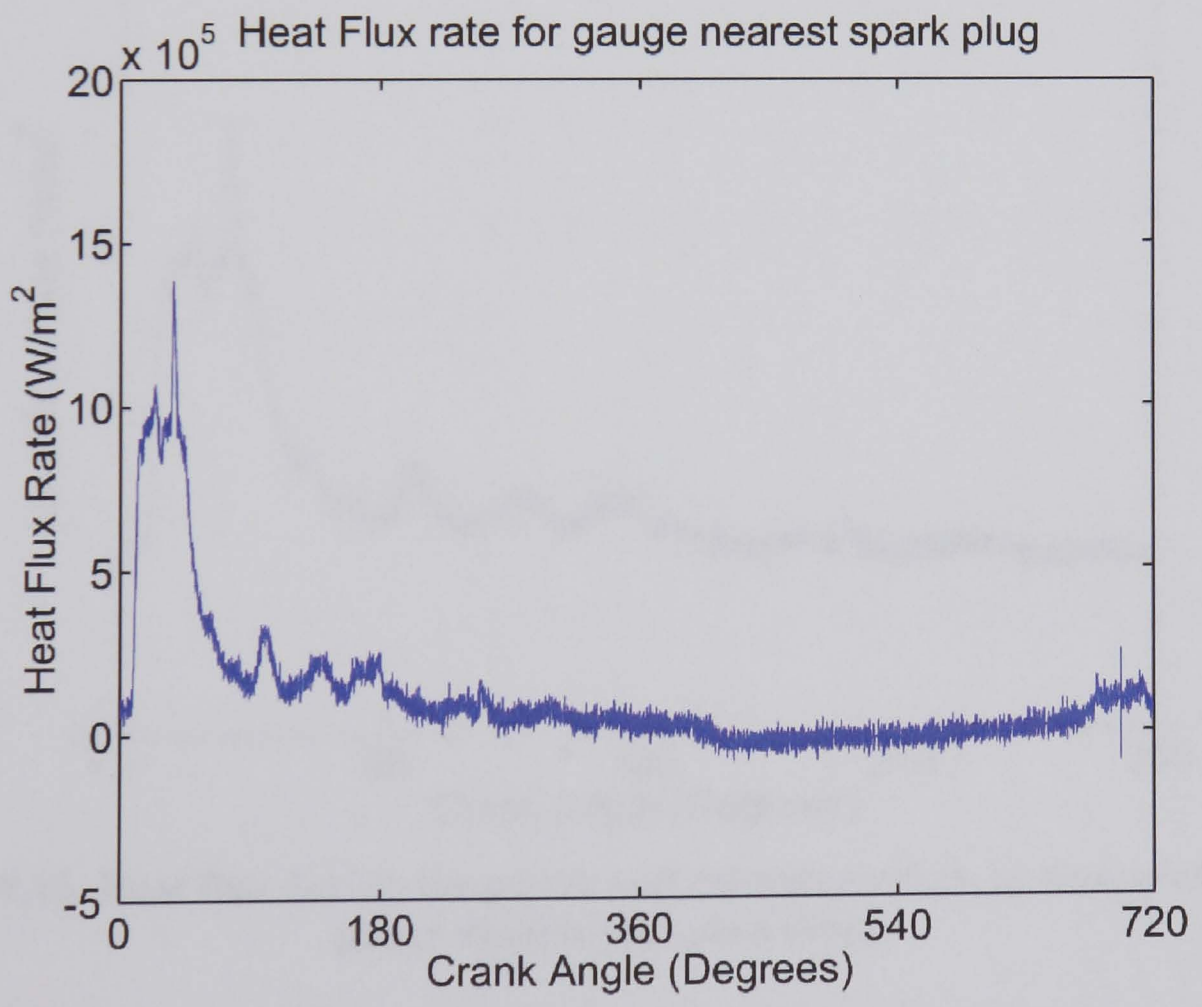

Figure 9.11, Heat flux for one cycle on the gauge nearest the spark plug.

Figure 9.11 shows the heat flux for one cycle. It may be observed that initially the heat flux rises rapidly as the flame passes the gauge. On the 'peak' of the plot some of

the flame structure may be observed. The heat flux falls rapidly once the flame has passed and the gas behind the front is of lower temperature. At 180° the piston changes direction and starts the exhaust stroke. It is observed that the heat flux at this position remains fairly constant during this stroke. After 360°, once the piston begins drawing the fresh, cooler, charge into the chamber, the heat flux goes negative indicating charge heating from the higher temperature chamber walls. During the compression stroke, (540° to 720°), it is noted the heat flux increases due to the compression heating effect of the charge beyond the chamber wall temperature caused by compression of the gas.

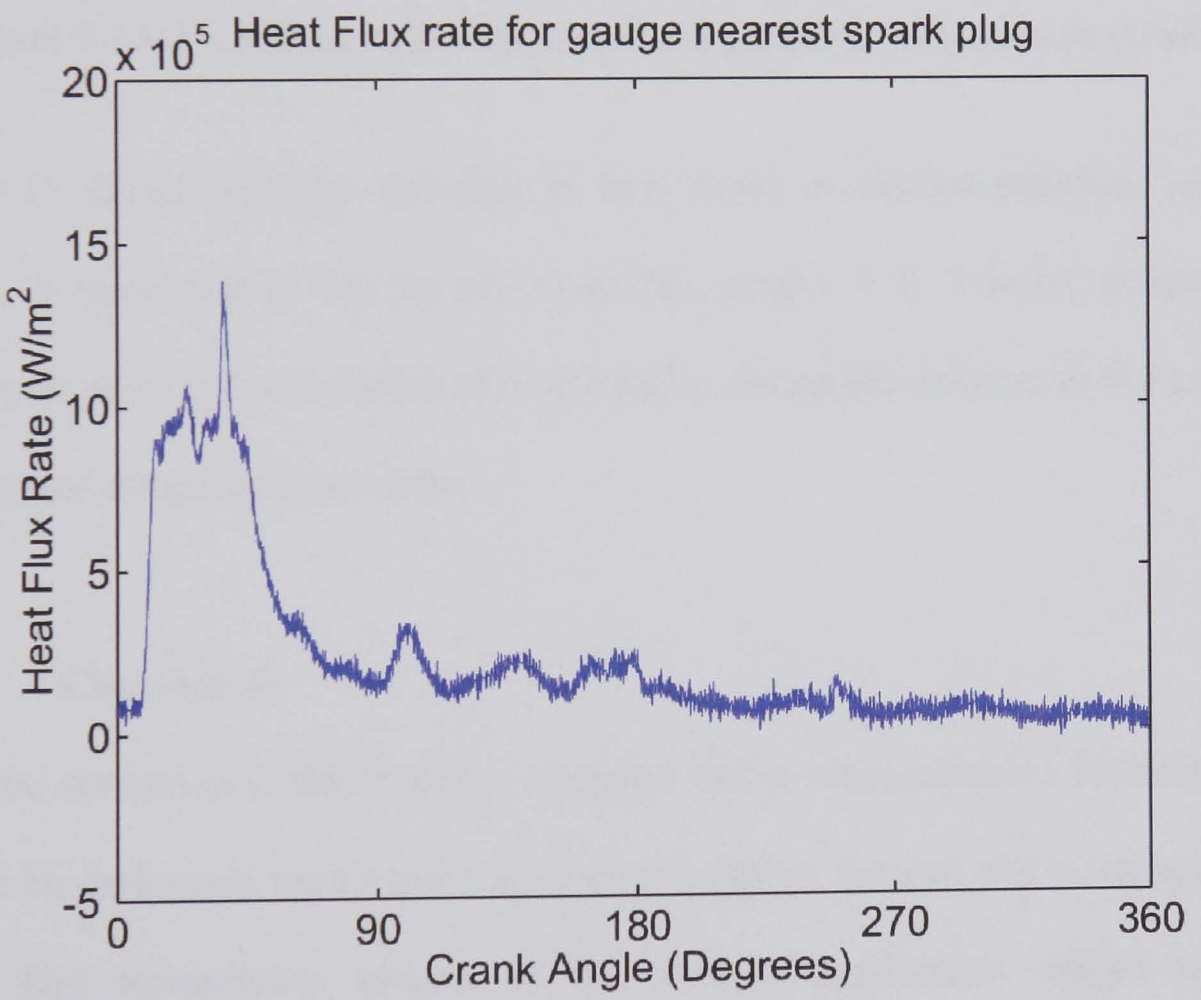

Figure 9.12, Heat flux during the power and exhaust strokes, as measured on the gauge nearest the spark plug.

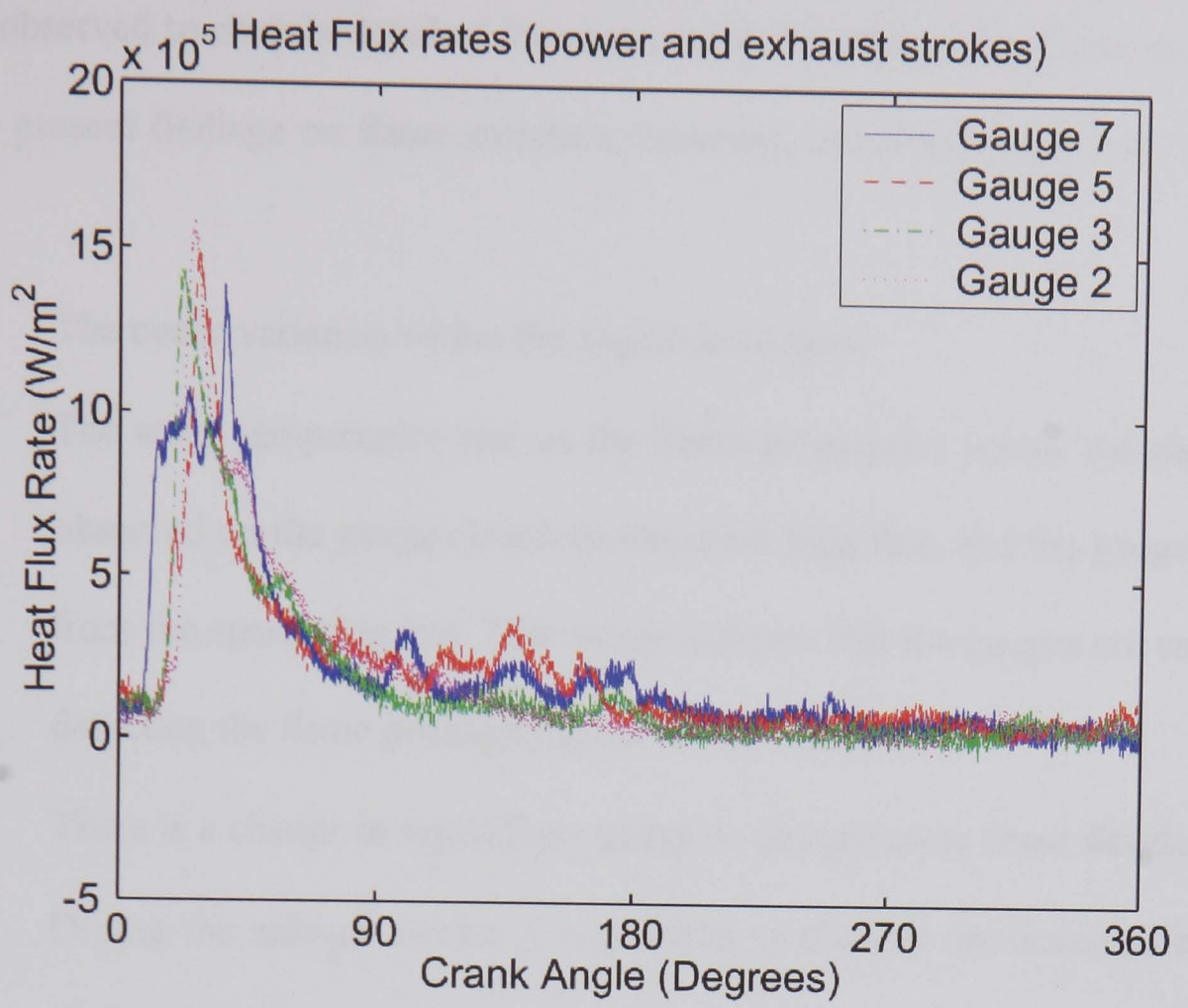

Figure 9.13, Heat fluxes for 4 gauges during power and exhaust strokes.

Figure 9.13 shows the large variation in heat fluxes at various positions within the chamber, in particular it may be observed that gauges 5 & 7 being closest to the exhaust port show increases rates of heat transfer during the exhaust stroke as the hot exhaust gases are pushed past them.

9.5 Conclusions

It must be remembered that it is not intended that a comprehensive investigation of heat flux be performed within this engine configuration. Instead, the novel application of thin film temperature gauges to the internal combustion engine has been demonstrated. The results above are presented to illustrate the typical temperature and heat fluxes determined within the chamber. As expected the results are, due to the much increased probe bandwidth, yielding temperature variations much higher than previous investigations with thermocouples (typically 10-20K [69,71,85,93,98,114])

and are observed to contain detail of flame structure. No attempt has been made at this stage to present findings on flame structure, however, conclusions that may be drawn include:

- The cyclic variation within the engine is obvious
- The steep temperature rise as the flame propagates across the chamber is observed on the gauge closest to the spark plug first, and the gauge furthest from the spark plug last. This would indicate that the gauges are capable of detecting the flame propagating across the chamber.
- There is a change in signal from gauge to gauge due to flame development
- During the exhaust stroke, it is possible to observe the increased heat flux as the hot gases are expelled past the gauges.

CHAPTER 10

DATA INTERPRETATION

10.1 Summary

The optical and temperature signals have been further processed in an attempt to yield information useful for assessing engine processes and performance. These analysis techniques may be used to asses the stableness of a given engine configuration and here provide an investigation into the associated advantages, disadvantages and limitations of each measurement technique. Such processing is not intended to be exhaustive, rather simply to illustrate the versatility of optical and temperature measurements and as a starting point for further study.

10.2 Complementary Measurements

Figure 10.1 & Figure 10.2 illustrate the nature of both the heat flux measurement and the narrow band optical measurement recorded in three successive loaded engine runs at 2300 RPM. Experimentally, the fibre optic is mounted in the cylinder head above the heat flux gauges; therefore, note that the fibres integrate the light over a larger area than the temperature gauges sample.

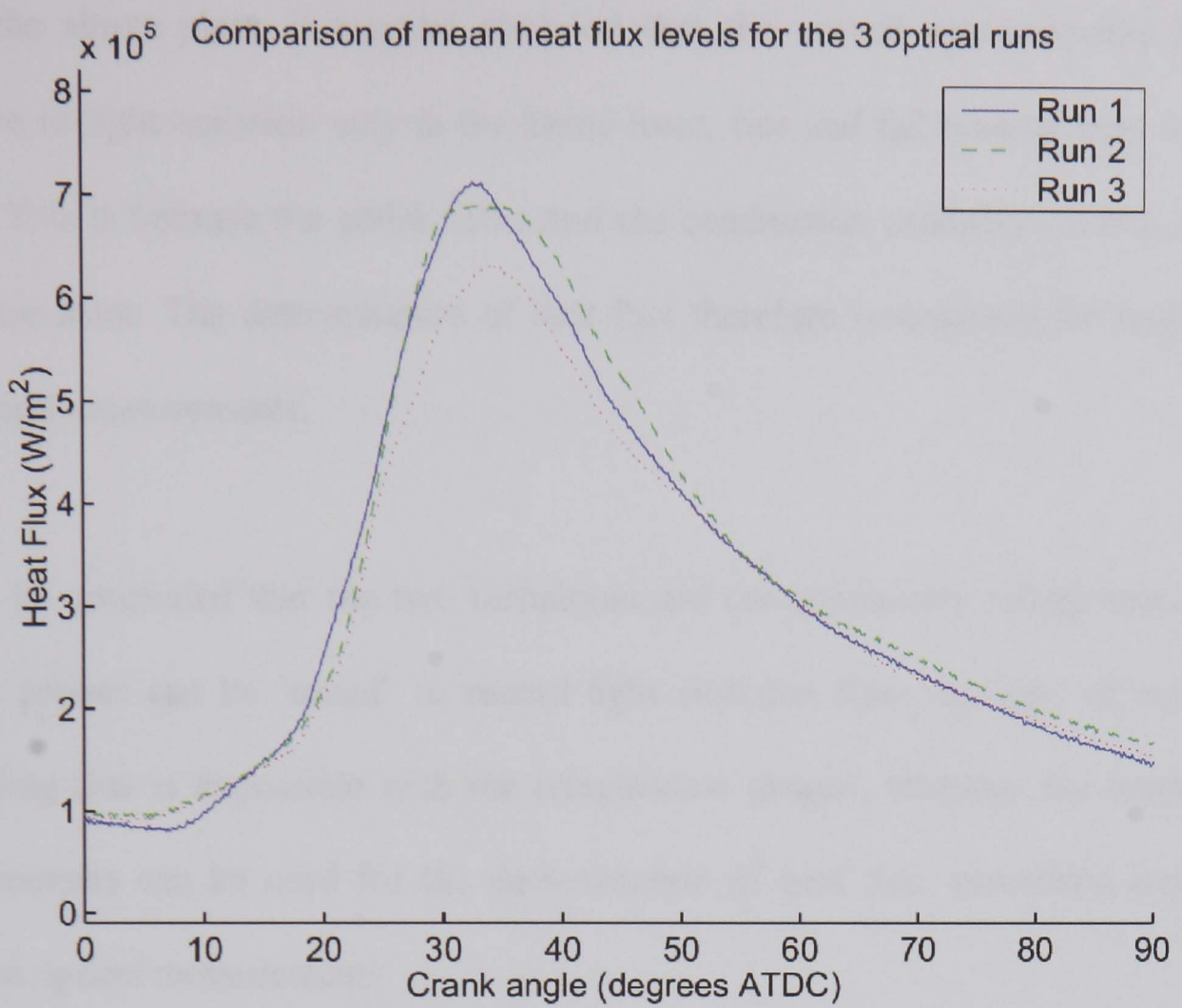

Figure 10.1, Heat flux levels for runs shown in Figure 10.2.

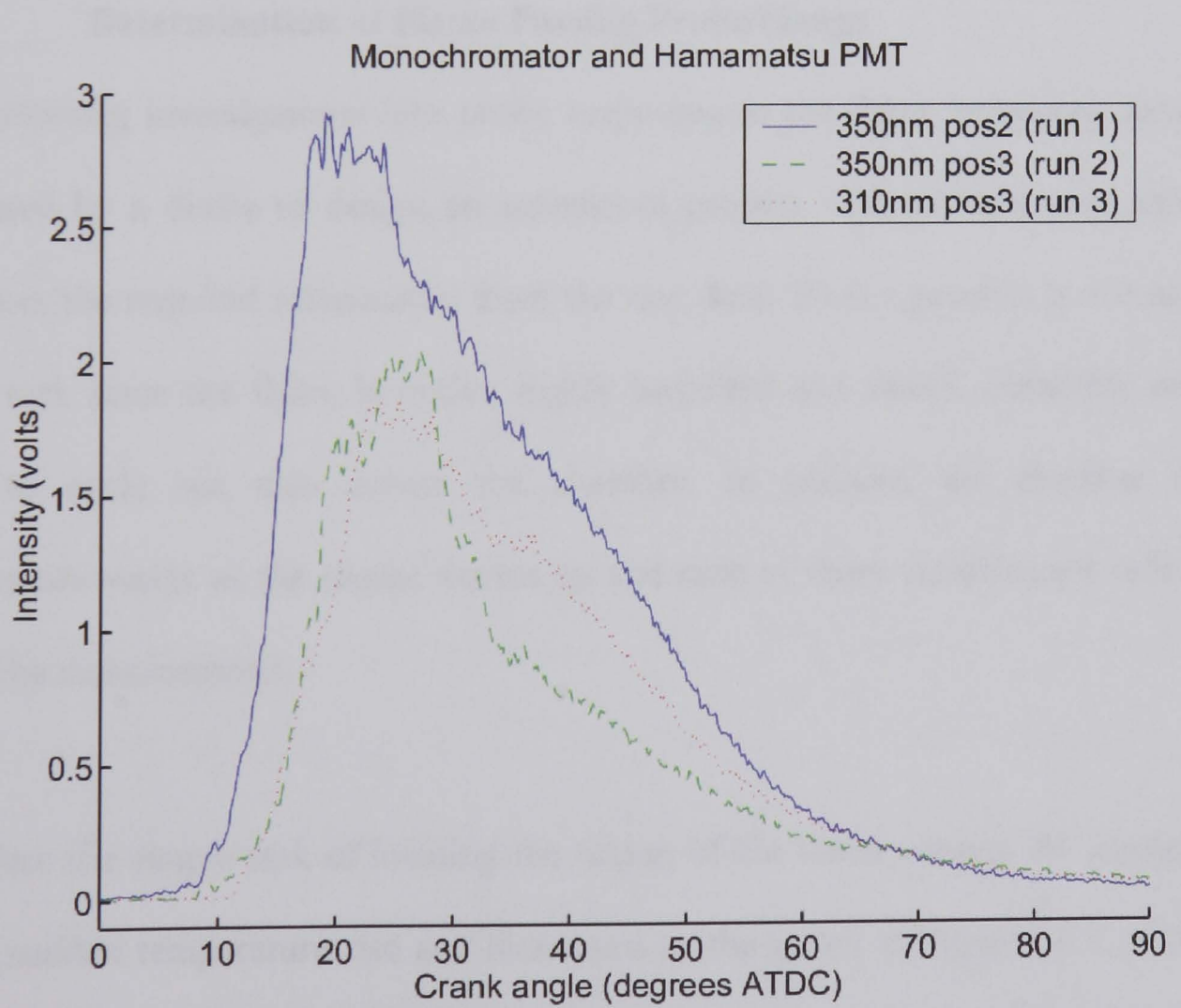

Figure 10.2, Emission intensities of 310 and 350 nm for 2 fibre positions.

From the above plots, it may be observed that the optical measurements that are sensitive to light emission only in the flame front, rise and fall quicker than heat flux signal. This is because the entire flame and the combustion products are hot, not just the flame front. The determination of heat flux therefore is sustained for longer than the optical measurements.

It may be concluded that the two techniques are complementary measurements. The optical probes can be 'tuned' to record light emission from any part of the flame, something that is impossible with the temperature gauges; whereas, the temperature measurements can be used for the determination of heat flux, something impossible with the optical measurements.

10.3 Determination of Flame Passing Probe/Gauge

The following investigations into probe responses to the flame behaviour have been motivated by a desire to design an automated process with minimal user input that generates the required information from the raw data. Such a process is not always a trivial task since the flame is cyclic, highly turbulent and shows variability not only cycle to cycle but also across the chamber. In addition the chamber surface temperature varies as the engine warms up and each of these variables are reflected in the probe measurements.

Therefore the simple task of locating the timing of the flame passing the gauge, given by the sudden temperature rise and illustrated by the arrow in Figure 10.3, is obvious to determine to the human eye. However, it is not a simple problem to solve computationally. Possible techniques involve recording the sample number when the

temperature rises above a predetermined temperature, but the slow temperature rise as the engine heats up over many cycles leaves this unsuitable. Even setting the threshold level at a temperature rise from the beginning of the cycle is unsuitable since the temperature can sometimes rise slowly from trapped exhaust gases remaining or show a very small temperature rise if a poor burn occurs in a cycle.

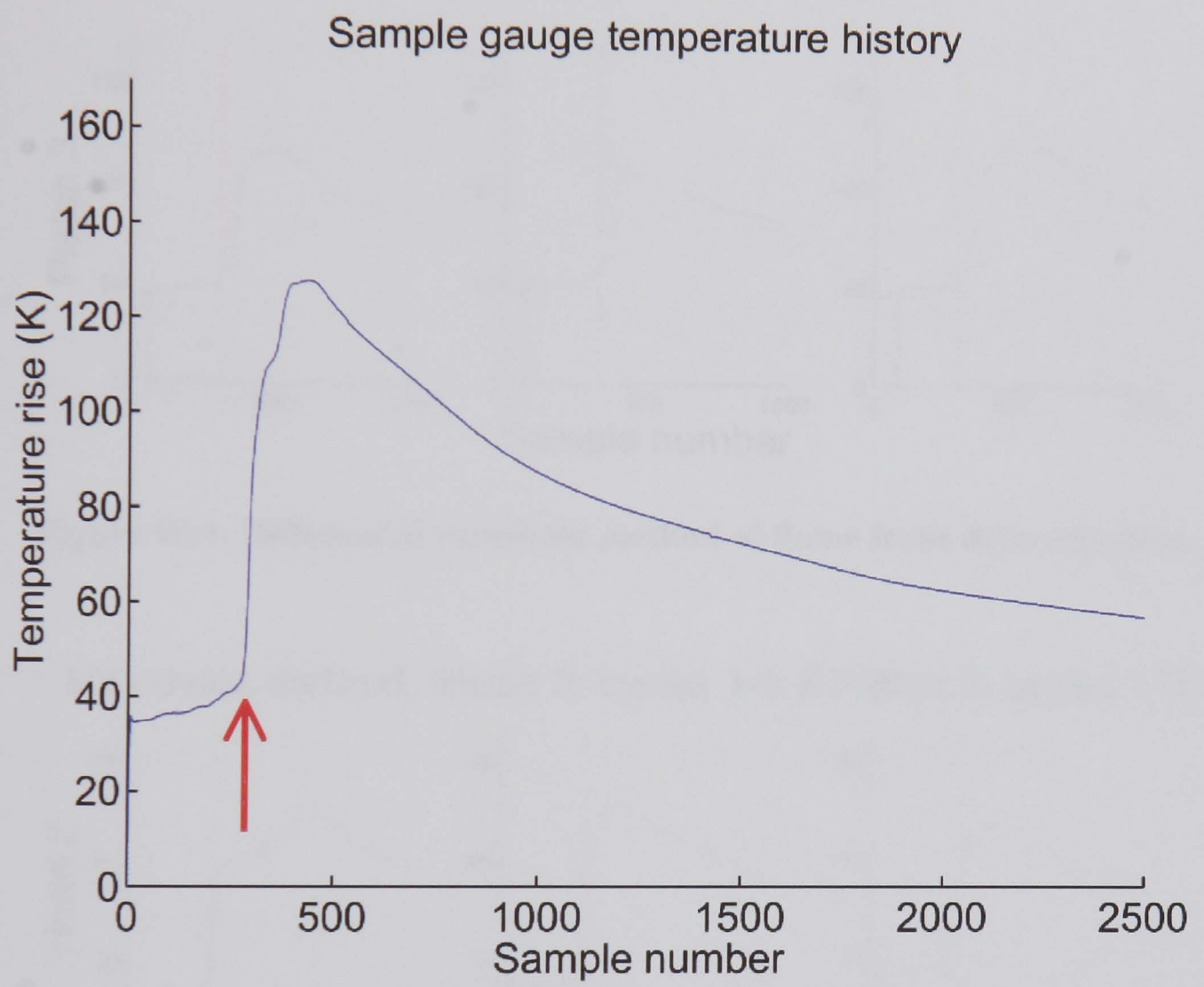

Figure 10.3, Example of gauge temperature history.

Alternatively the arrival of the flame front may be calculated from the differential of a temperature plot by choosing the point either when the differential value exceeds a threshold or when it reaches a maximum. This is illustrated in Figure 10.4 and Figure 10.5. (There are many methods of differentiating a signal, it should be noted that in this context the simple method of applying a smoothing filter and subtracting one data point from the previous was utilised. It is acknowledged that this is a poor method of performing a differentiation; however, in this instance it provides sufficient accuracy.)

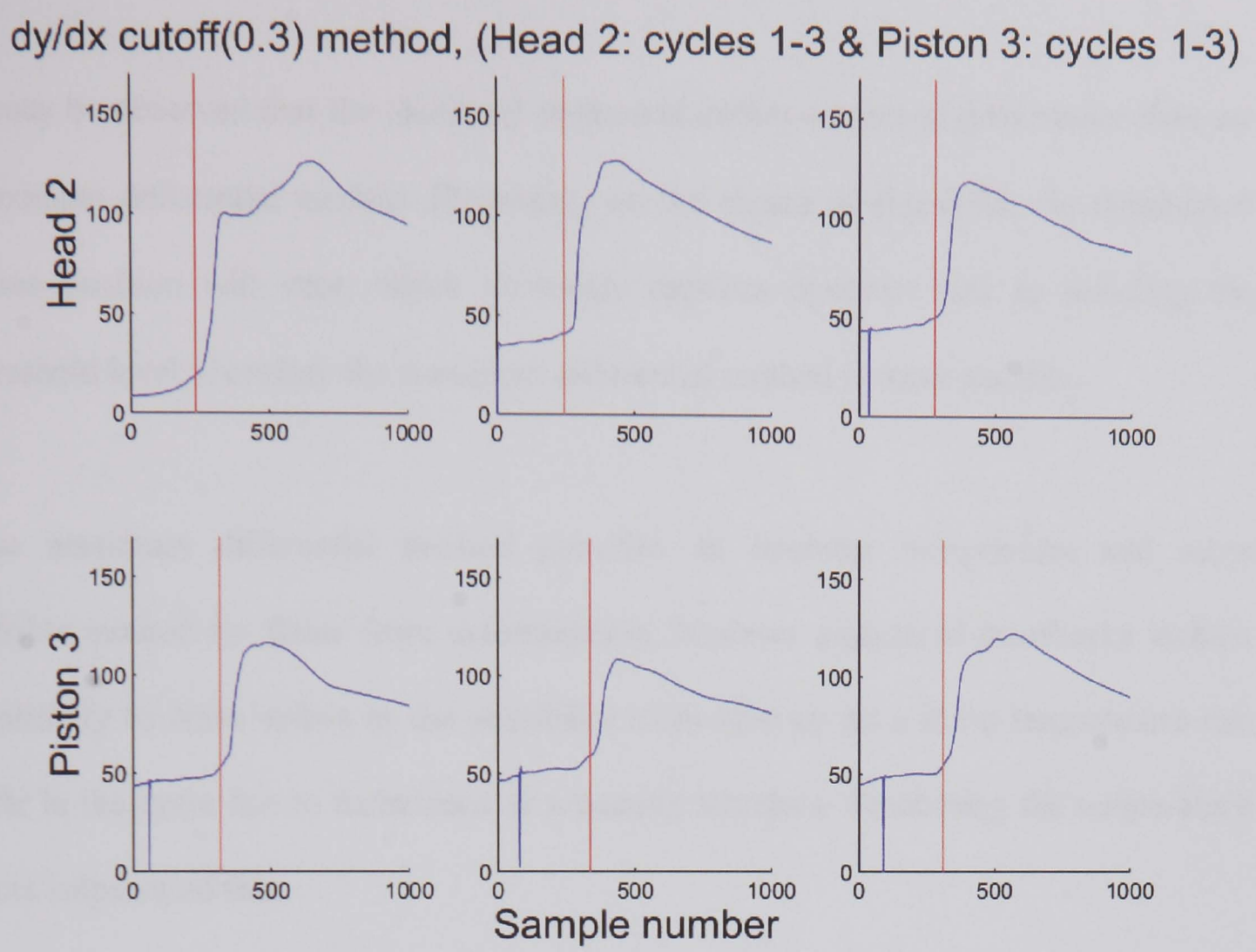

Figure 10.4, Differential threshold method of flame front determination.

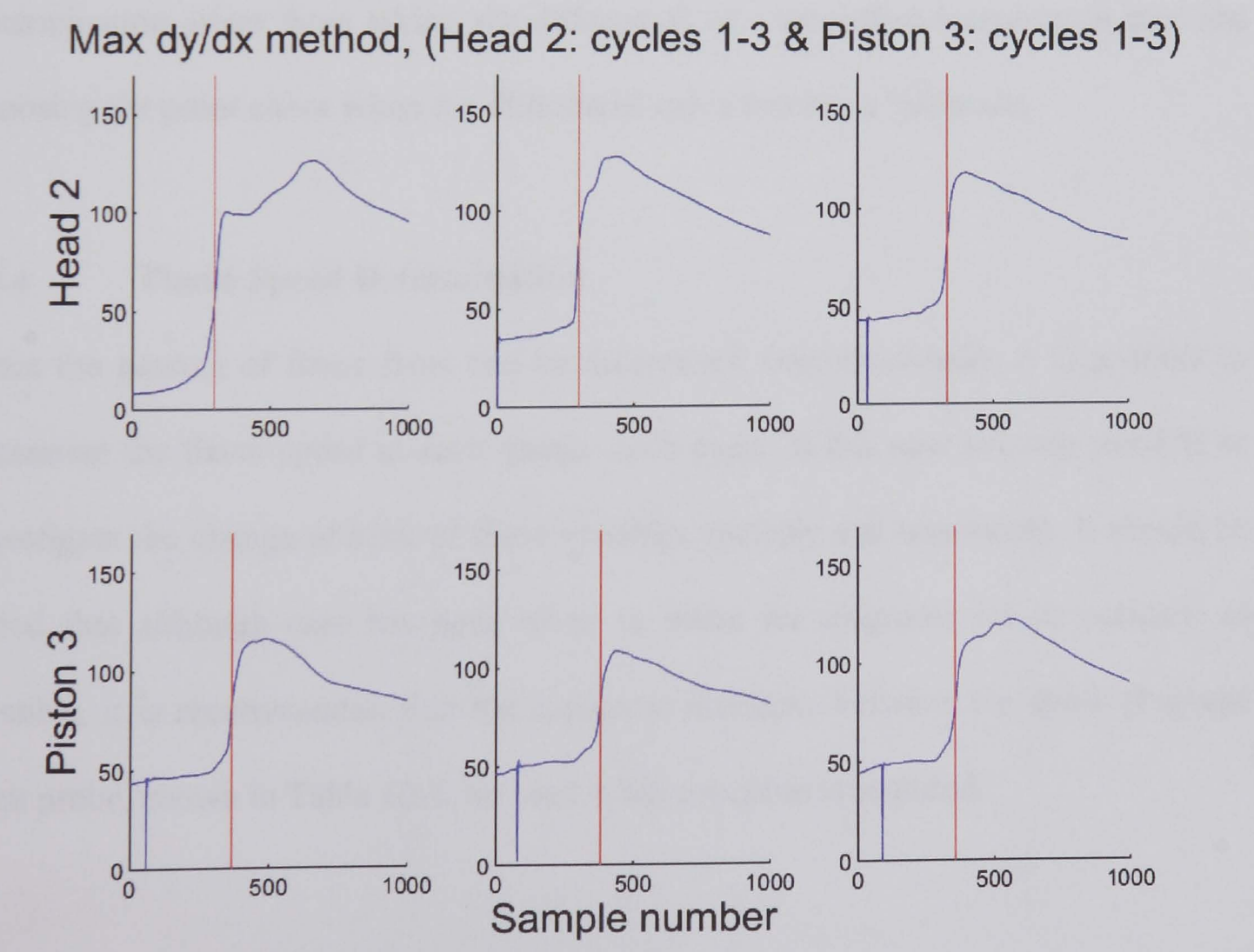

Figure 10.5, Maximum differential method of flame front determination.

It may be observed that the threshold method identifies a point slightly earlier than the maximum differential method. Depending on the choice of threshold, the determined flame position will vary, which obviously requires operator skill in selecting the threshold level, therefore the maximum differential method is more suitable.

The maximum differential method provides an operator independent and more reliable method for flame front determination, however associated drawbacks include sensitivity to noise spikes or the possibility of picking up on a sharp temperature rise later in the cycle due to turbulence or a passing structure. Smoothing the temperature plots helps avoid this.

It may therefore be concluded that the most successful method of flame front determination arises from taking the differential of a smoothed temperature plot and choosing the point either when the differential value reaches a maximum.

10.4 Flame Speed Determination

Once the passing of flame front can be determined computationally, it is possible to determine the flame speed at each gauge, each cycle. It has now become possible to investigate the change of both of these variables spatially and temporally. It should be noted that although care has been taken to make the diagrams are as accurate as possible, it is recommended that the measured distances between the spark plug and each probe, shown in Table 10-1, be used when precision is required.

Distance from Spark plug to:	(mm)	Distance from Spark plug to:	(mm)
Gauge 7	10.0	Optical probe 1	16.0
Gauge 6	16.5	Optical probe 2	27.0
Gauge 5	23.0	Optical probe 3	38.0
Gauge 4	29.5	Optical probe 4	49.0
Gauge 3	36.0	Optical probe 5	60.0
Gauge 2	42.5		
Gauge 1	49.0		

Note that piston gauges are directly below head gauges.

Table 10-1, Measured distances between spark plug and each probe.

10.4.1 Flame Speed From Temperature Gauges

This section shows that it is possible to determine the flame speed from the gauges. In addition, use of either the gauges mounted in the head or on the piston shows good agreement in flame speeds. Further, the flame speeds calculated from the maximum dy/dx method and the dy/dx cut-off method are compared. In the following plots the flame speeds are calculated between the spark plug and each gauge in turn.

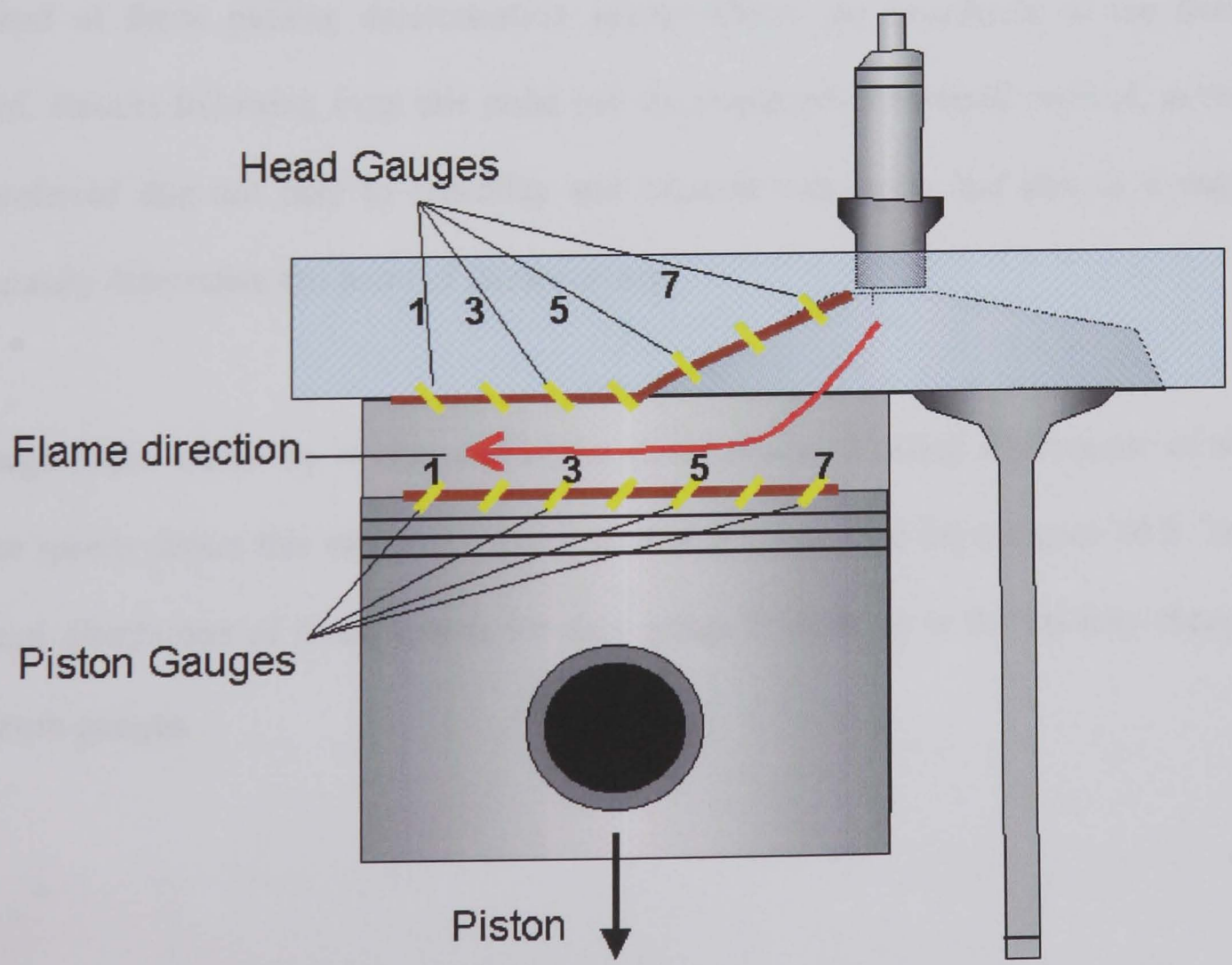

Figure 10.6, Flame propagation across gauges at known locations.

Initially the flame speed is determined by dividing the known distance from the spark plug to each probe by the measured time taken for the flame to propagate from the spark plug (time given by spark timing), to the gauge (time calculated from the sample number the flame passes the gauge), Figure 10.6. This provides an average flame speed from the spark plug to the probe.

The following two graphs show the calculated average flame speeds from the spark plug to each gauge. For the first graph, Figure 10.7, the flame position is determined using the differential threshold method, but for the second graph, Figure 10.8, the flame position is determined with the maximum differential method.

It may be noted that the general trend and relative flame speeds are unchanged, the method of flame passing determination simply affects the magnitude of the flame speed. Results following from this point use the maximum differential method, as this is preferred due not only to reliability and minimal user input, but also as it more accurately determines the point of flame passing.

A large cyclic variability is observed in the above results. Plotting a histogram of the flame speeds shows this variation. Figure 10.9 is the histogram from Figure 10.8. The normal distribution of flame speeds for each gauge is clear, as is the velocity change between gauges.

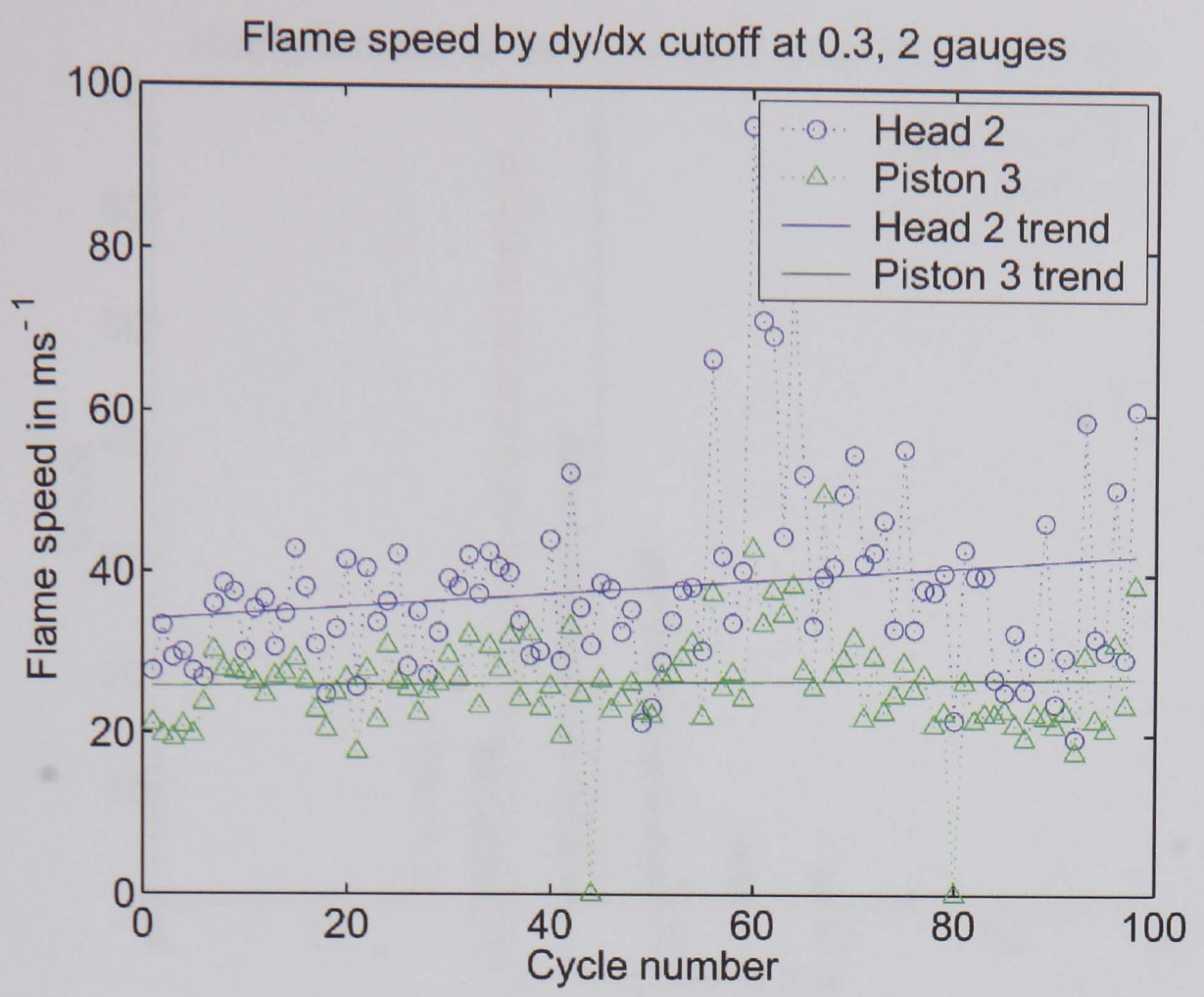

Figure 10.7, Flame speed determined over 100 cycles using differential threshold method.

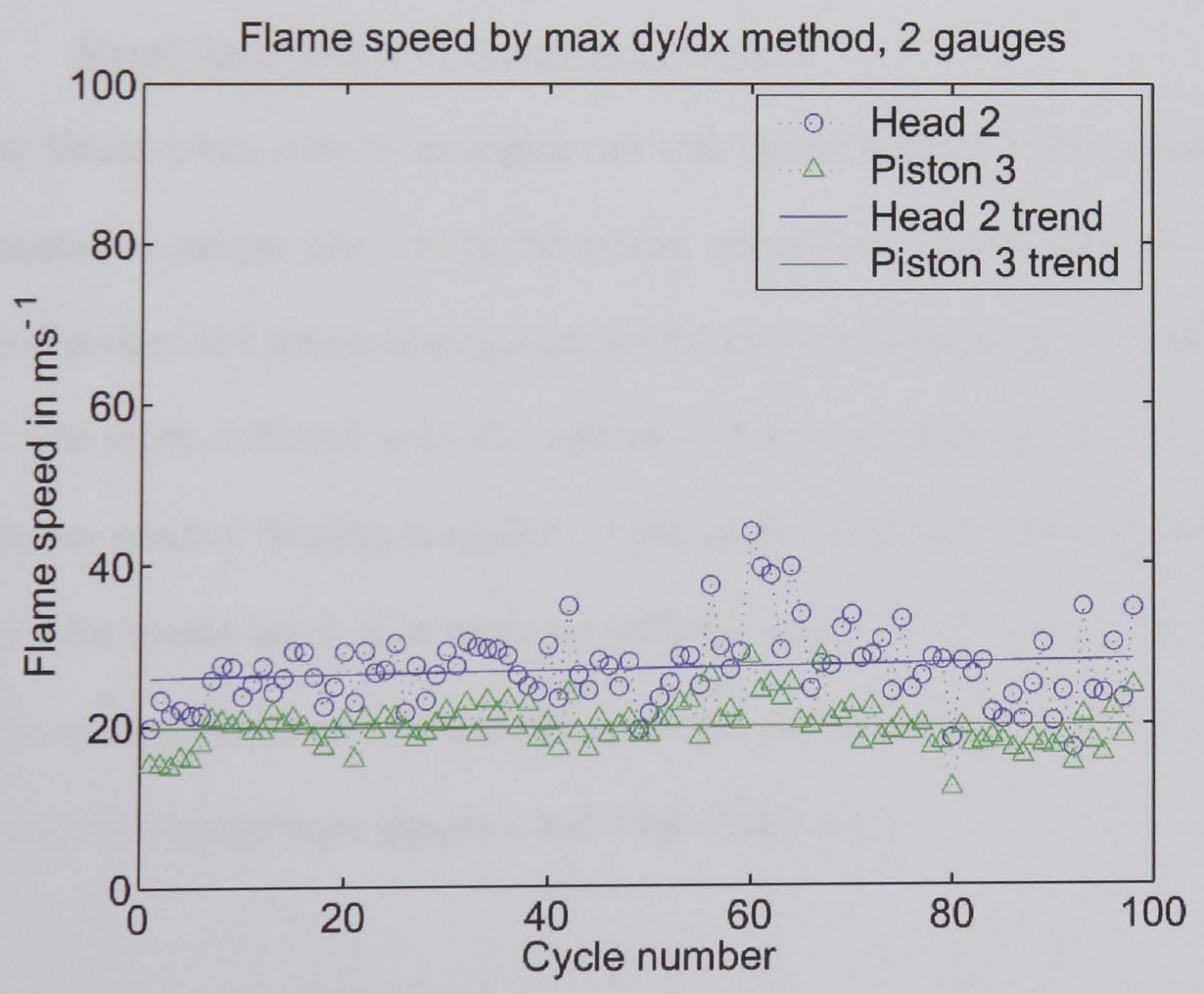

Figure 10.8, Flame speed determined over 100 cycles using the maximum differential method.

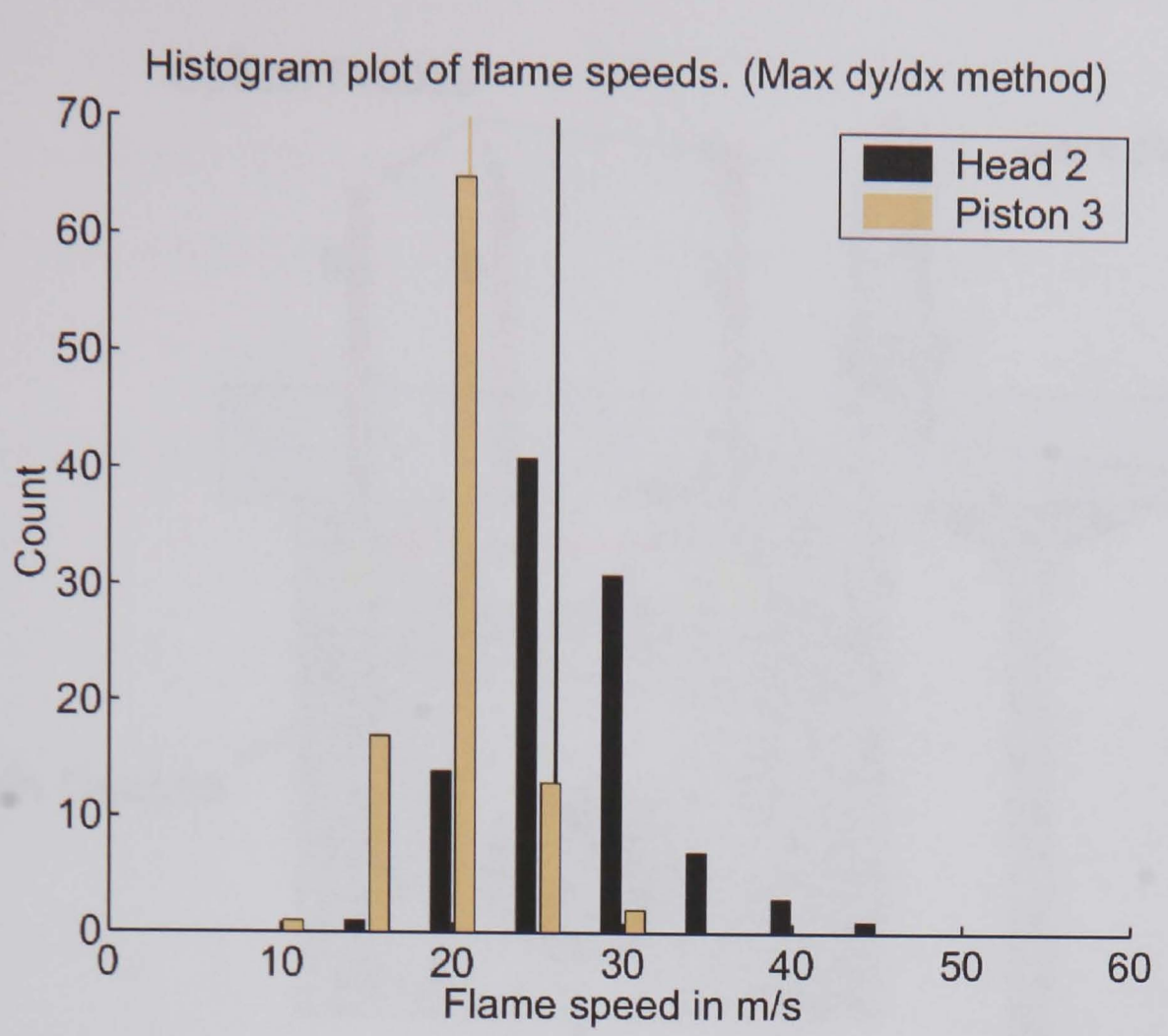

Figure 10.9, Histogram of average flame speed from spark plug to each gauge. (Thin vertical lines represent the mean flame speeds)

10.4.2 Speed from Optical & Temperature Gauges

Applying similar processing to an engine run with optical sensors in the cylinder head and temperature gauges attached to the piston, permits the investigation of whether the optical probes and temperature gauges detect the flame passing at the same instant in time. The light collected with the optical probes is sampled using photodiodes; therefore, no spectral filtering is applied. If one probe suggests a time lag relative to the other, this would imply each detects a different aspect of the flame. Figure 10.10 shows the relative positions of the temperature gauges and optical probes. Fibres 1,3 and 5 along with temperature gauges 2 and 4 have been used.

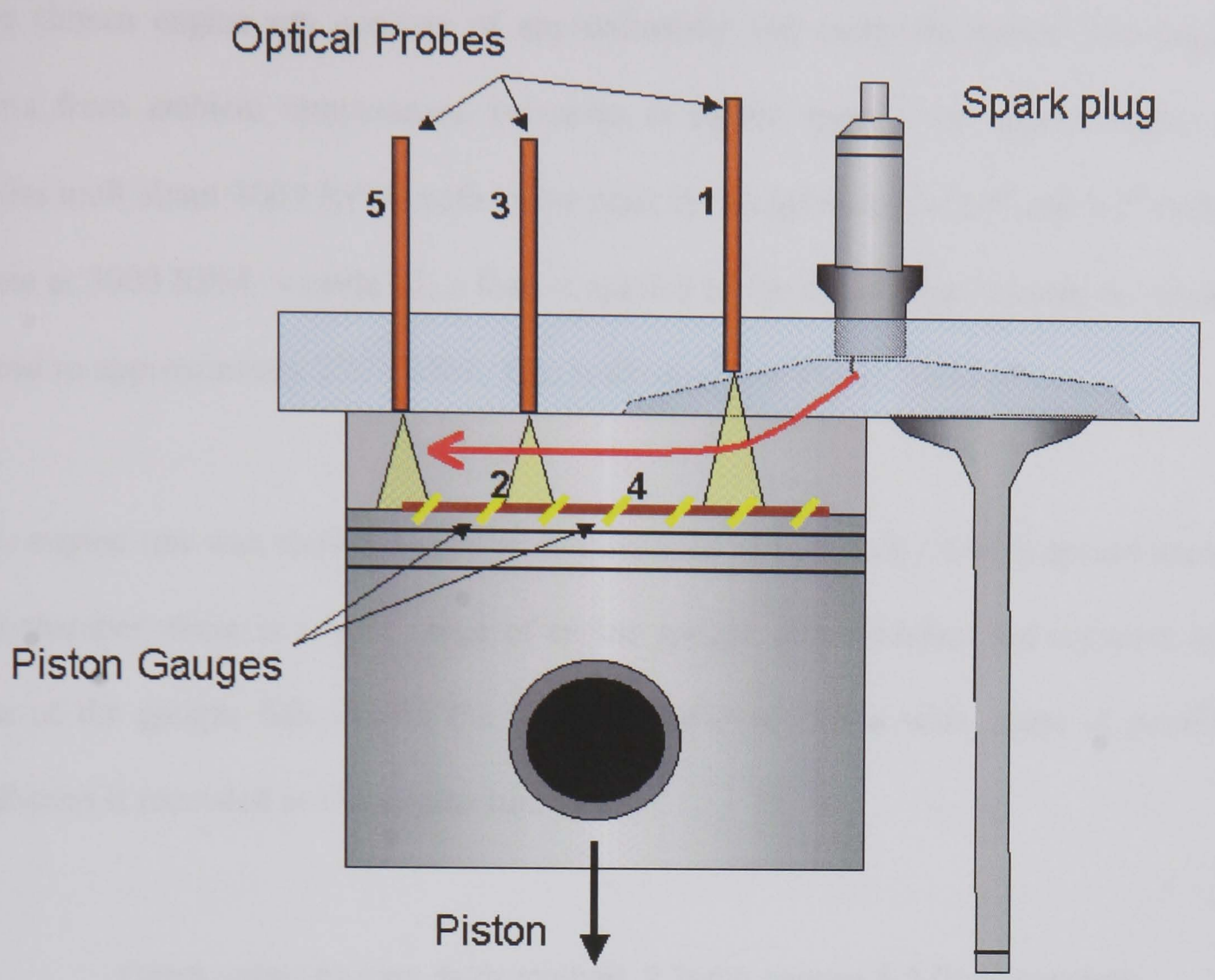

Figure 10.10, Relative positions of temperature gauges and optical probes.

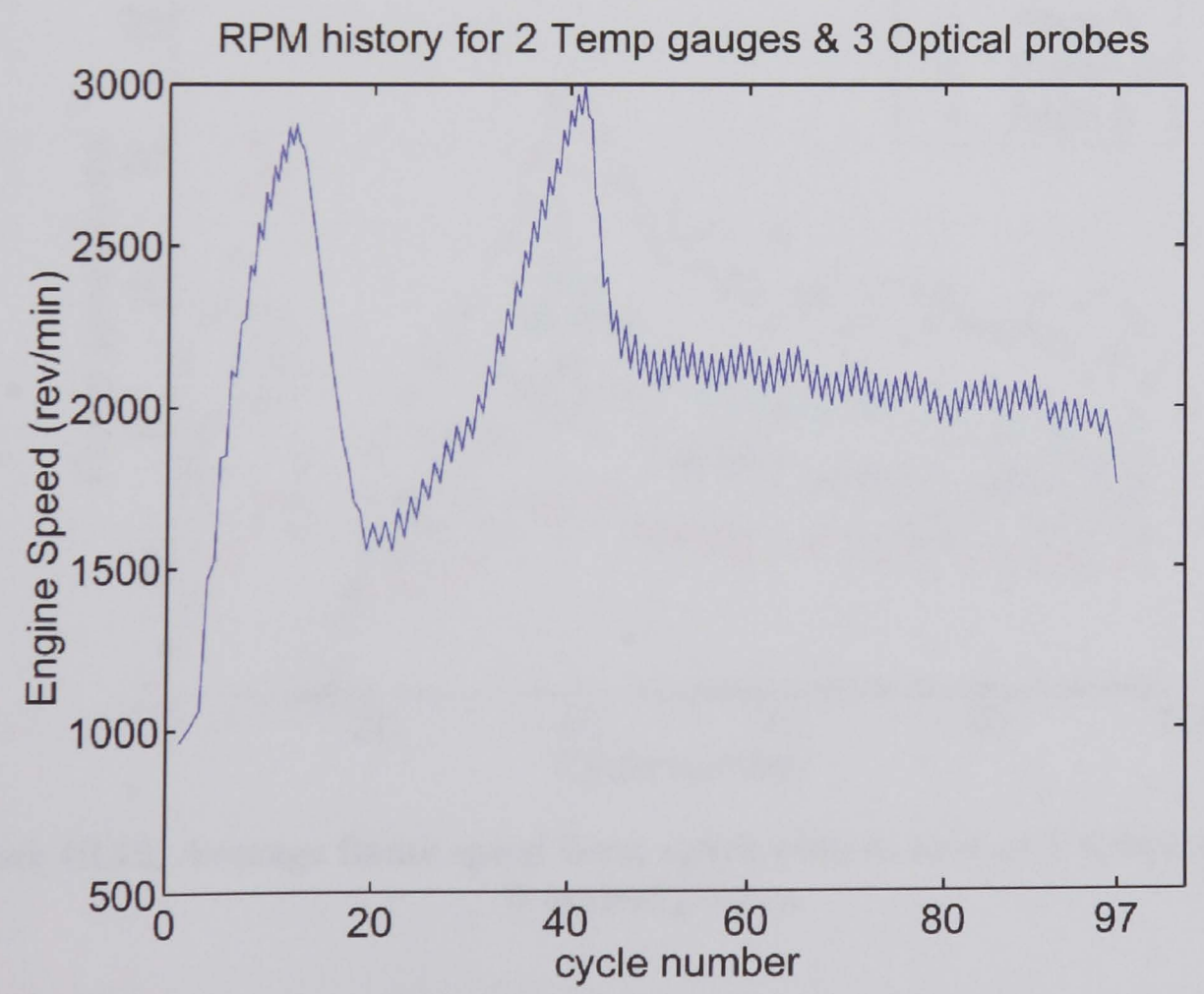

Figure 10.11, Engine speed plot for second flame speed investigation.

The chosen engine run consists of approximately 100 complete cycles. The engine starts from ambient temperature, increases in engine speed over approximately 40 cycles until about 3000 RPM, with a few poor cycles between the 10th and 20th cycles. Once at 3000 RPM, ≈ cycle 43, a load is applied to the engine that reduces the engine speed to approximately 2000 RPM. This is illustrated in Figure 10.11.

The engine run was chosen as the probes sampled are relatively evenly spread across the chamber, there is a wide range of engine speeds, some misfires are recorded and one of the gauges fails during the run. It is believed that a wide range of possible scenarios is recorded in one engine run.

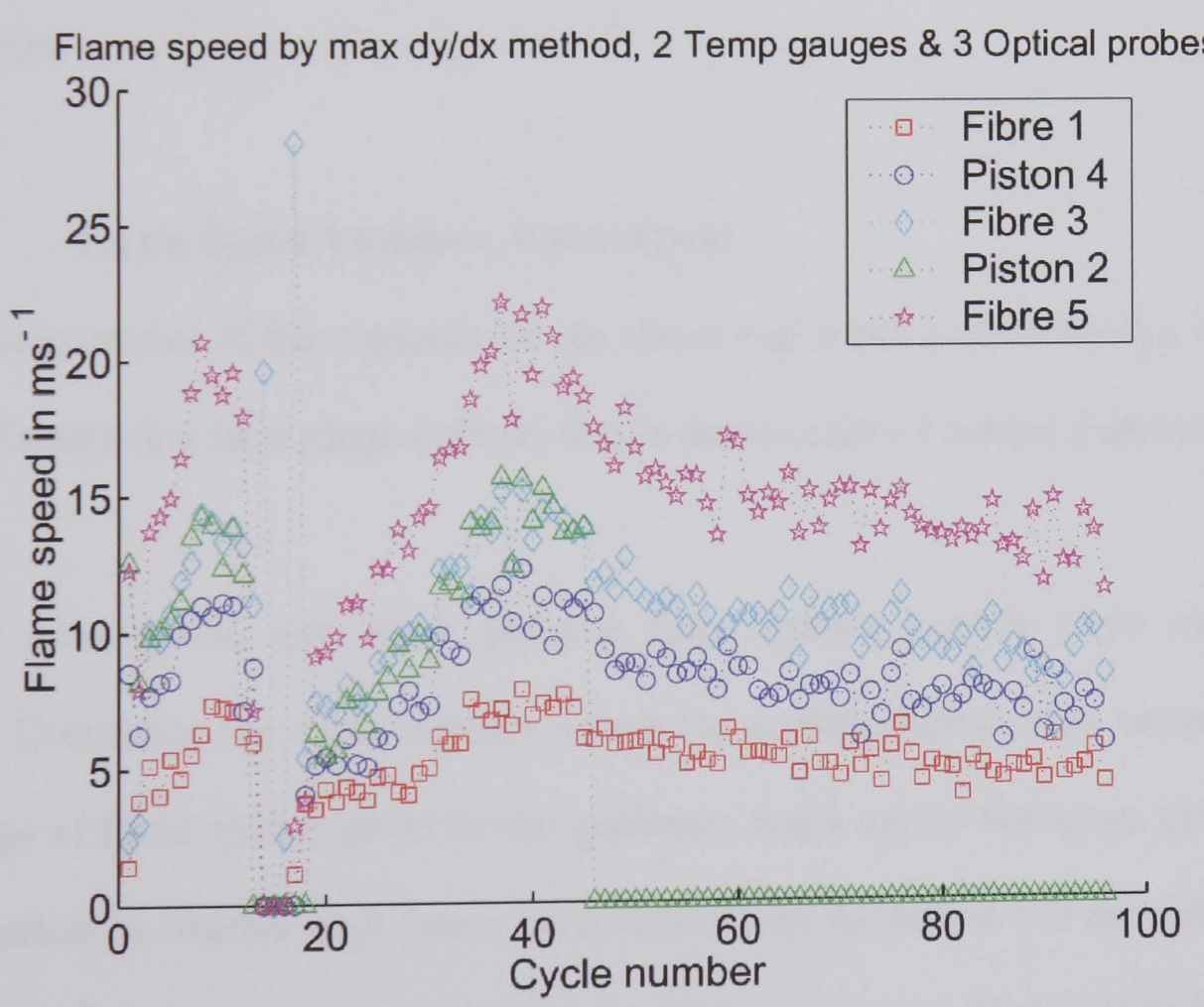

Figure 10.12, Average flame speed from spark plug to each of 2 temperature and 3 optical probes.

The plot of flame speeds is shown in Figure 10.12. It may be observed that the second temperature gauge on the piston failed during the run at approximately cycle 45. This

was traced to the failure of the gauge wiring. The zero readings of flame speed on cycles 13 to 18 were automatically filtered out due to unrealistic engine speeds being reported. A rise in the average flame speeds from spark to probes is observed while the engine speed increases, and a more gentle fall in flame speeds is noted as the engine speed slowly falls after the application of the loading; compare this to the plot of engine speed history in Figure 10.11.

Increasing distance from the spark plug (Optical gauge 1, temperature gauge 4, optical 3, temperature 2 and optical 5) leads to steadily increasing average flame speeds (square, circle, diamond, triangle and pentagon markers), permitting the conclusion that the temperature and optical probes are consistent in identifying the passing of the flame front.

10.5 Flame Speed Variation, Cycle-Cycle

The histogram plot of flame speeds for the above engine run is shown below in Figure 10.13. Considering each gauge (colour) in turn demonstrates a normal distribution.

Further investigation into these grouped flame speeds provide some interesting results. Comparing the cycle numbers where the average flame speed occurs within the range of flame speeds given by the maximum count on the histogram plot allows investigation on whether each sensor is consistent with the others. For example optical probe 1 and temperature probe 4 share 35 cycles where the fibre reported a flame speed of between 5 and 7.5 m/s and the temperature gauge reported a speed between 7.5 and 10 m/s. More significantly in 29 common cycles fibre 1 reports a flame speed between 5-7.5 m/s, piston 4 between 7.5-10 m/s and fibre 3 between 10-12.5 m/s,

where each flame speed range is determined from the histogram plot. These 29 cycles are plotted in Figure 10.14.

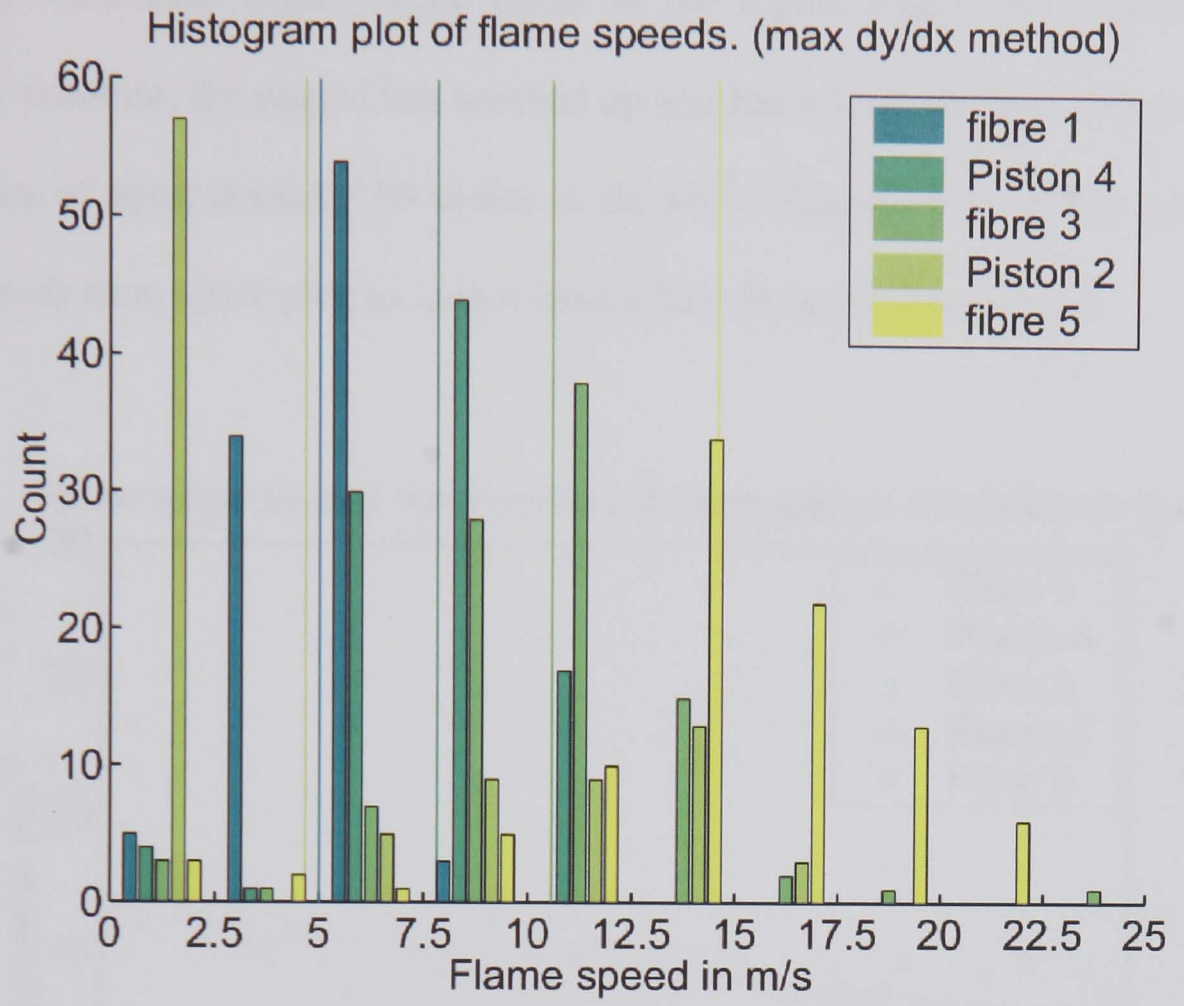

Figure 10.13, Histogram of average flame speeds from spark plug to sensors. (Thin vertical lines represent the mean flame speeds)

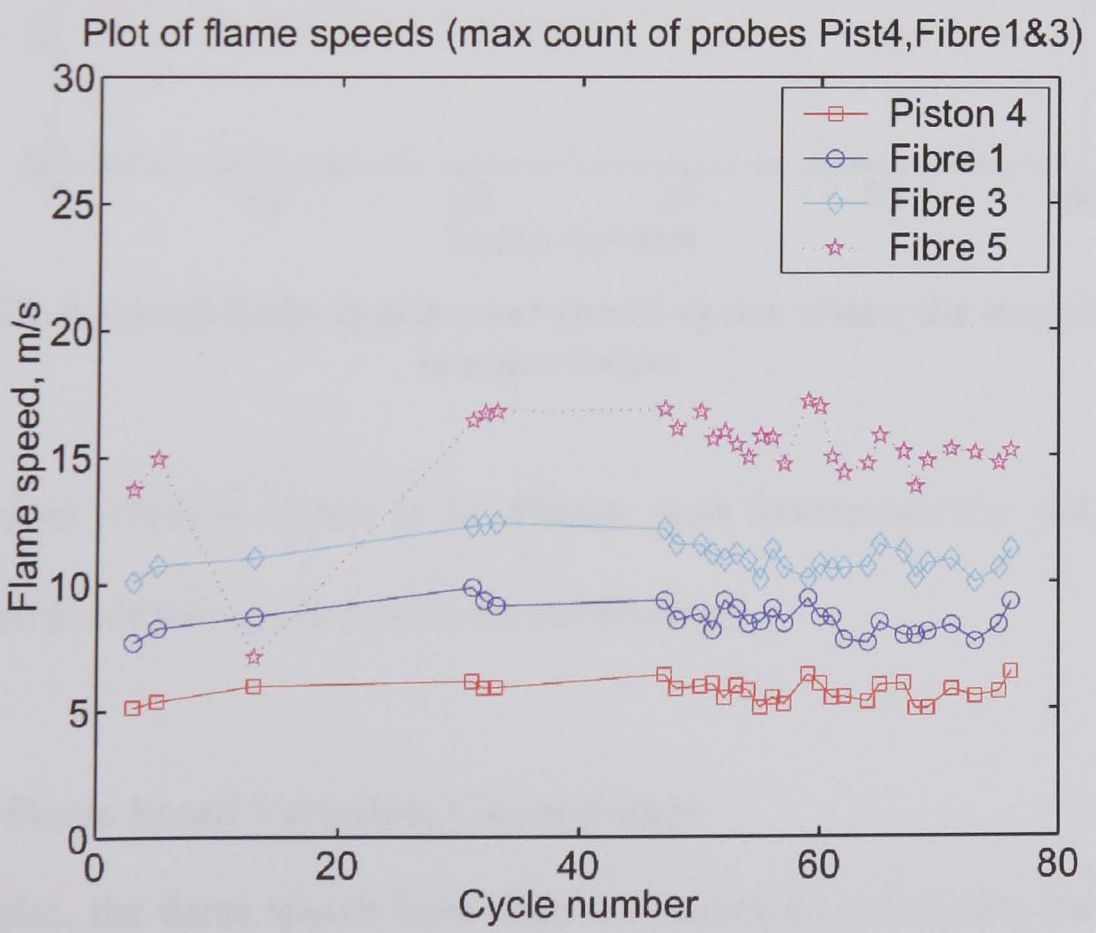

Figure 10.14, Plot of average flame speeds for the 29 cycles where each gauge shared the maximum frequency of flame speed.

It may be noted that the cycles where the gauges report flame speeds that are consistent with each other mainly occur in the region where the engine speed is relatively constant, the engine has warmed up and has a load applied. This final region of the run of approximately 50 cycles is shown in Figure 10.15 where the average flame speeds from spark plug to sensor have a best-fit (solid) line applied.

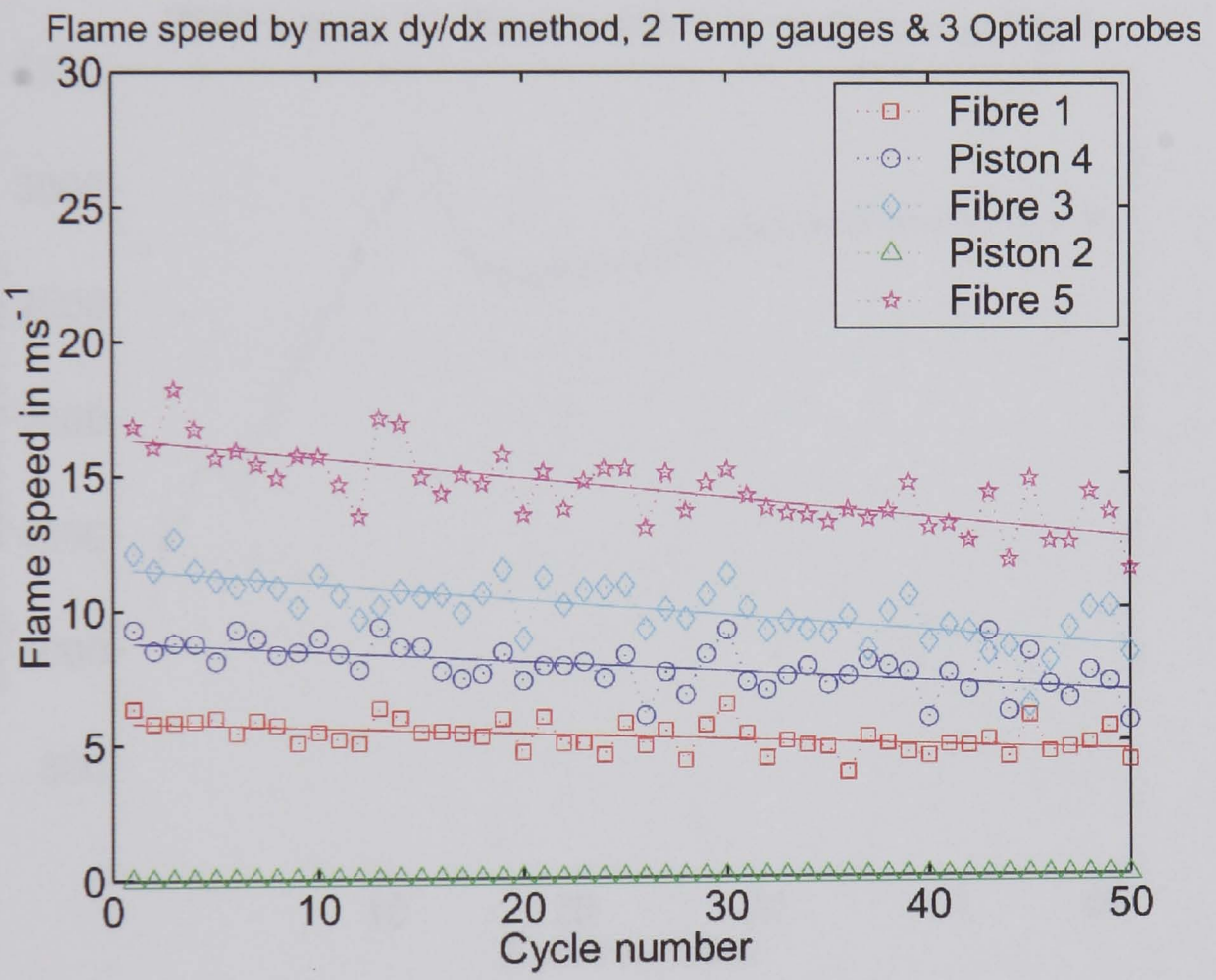

Figure 10.15, Average flame speeds over the 50 cycles where the engine operation is more stable.

The question is therefore raised as to whether such instrumentation and processing could be used to identify cycles with poor combustion.

10.6 Flame Speed Variation, Gauge-Gauge

Until this point, the flame speeds have been determined by calculating the time taken for the flame to propagate from the spark plug to each gauge. While this is a more

robust technique to calculate the flame speed, it yields only an average flame speed over the chamber and does not permit the study of the flame speed variation between gauges. For this, an engine run with 4 temperature gauges instrumented in a ray moving out from the spark plug in the direction of flame travel was chosen. The engine speed history is shown in Figure 10.16.

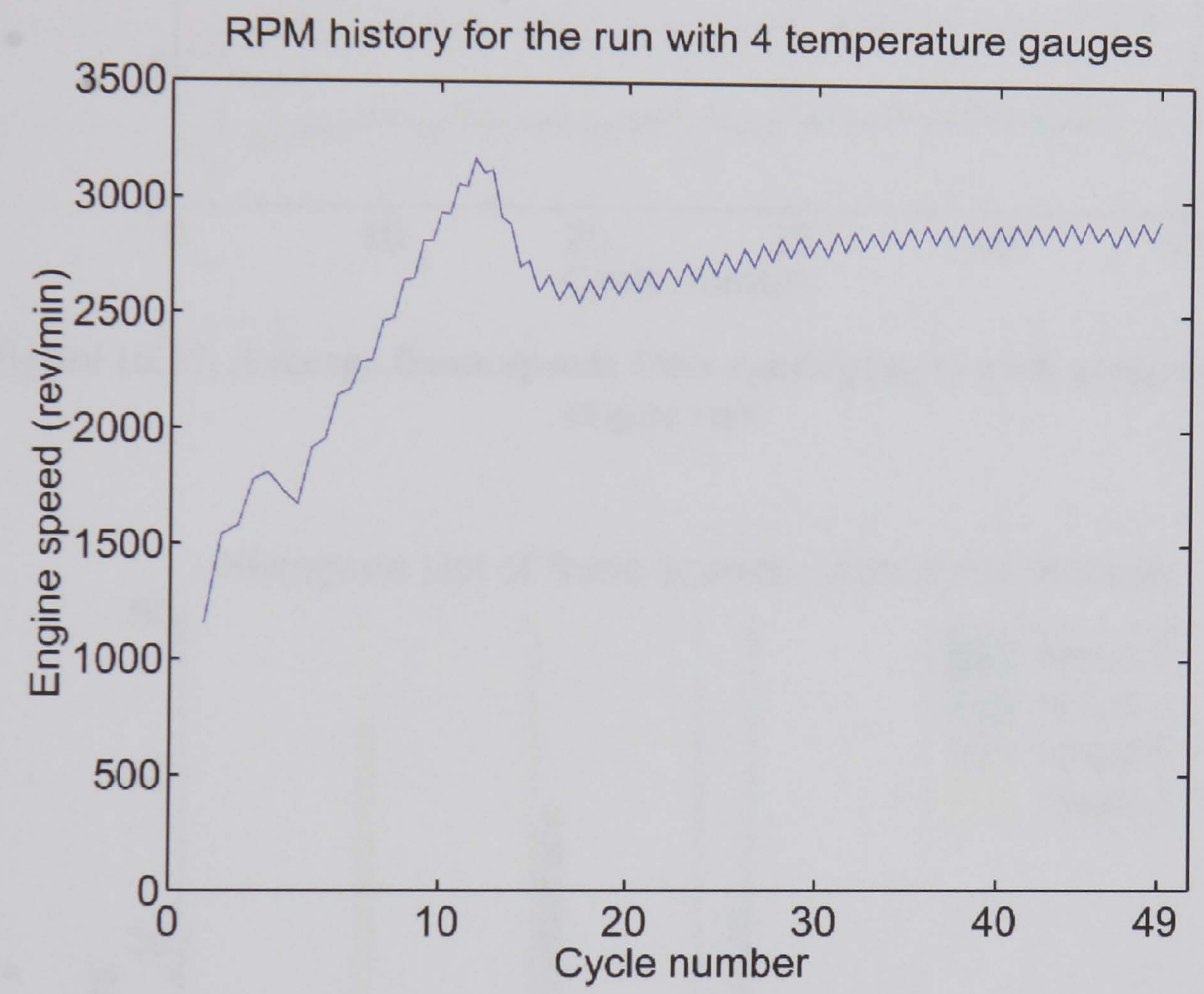

Figure 10.16, Engine speed plot for third flame speed investigation.

For the above run the engine was not loaded, instead it was run up to a steady speed of approximately 2700 RPM. The above plot shows one misfire occurred on the 3rd engine cycle and that the steady engine speed was reached just before the 15th cycle.

The average flame speeds from the spark plug to each gauge in turn is shown for comparison purposes in Figure 10.17, below.

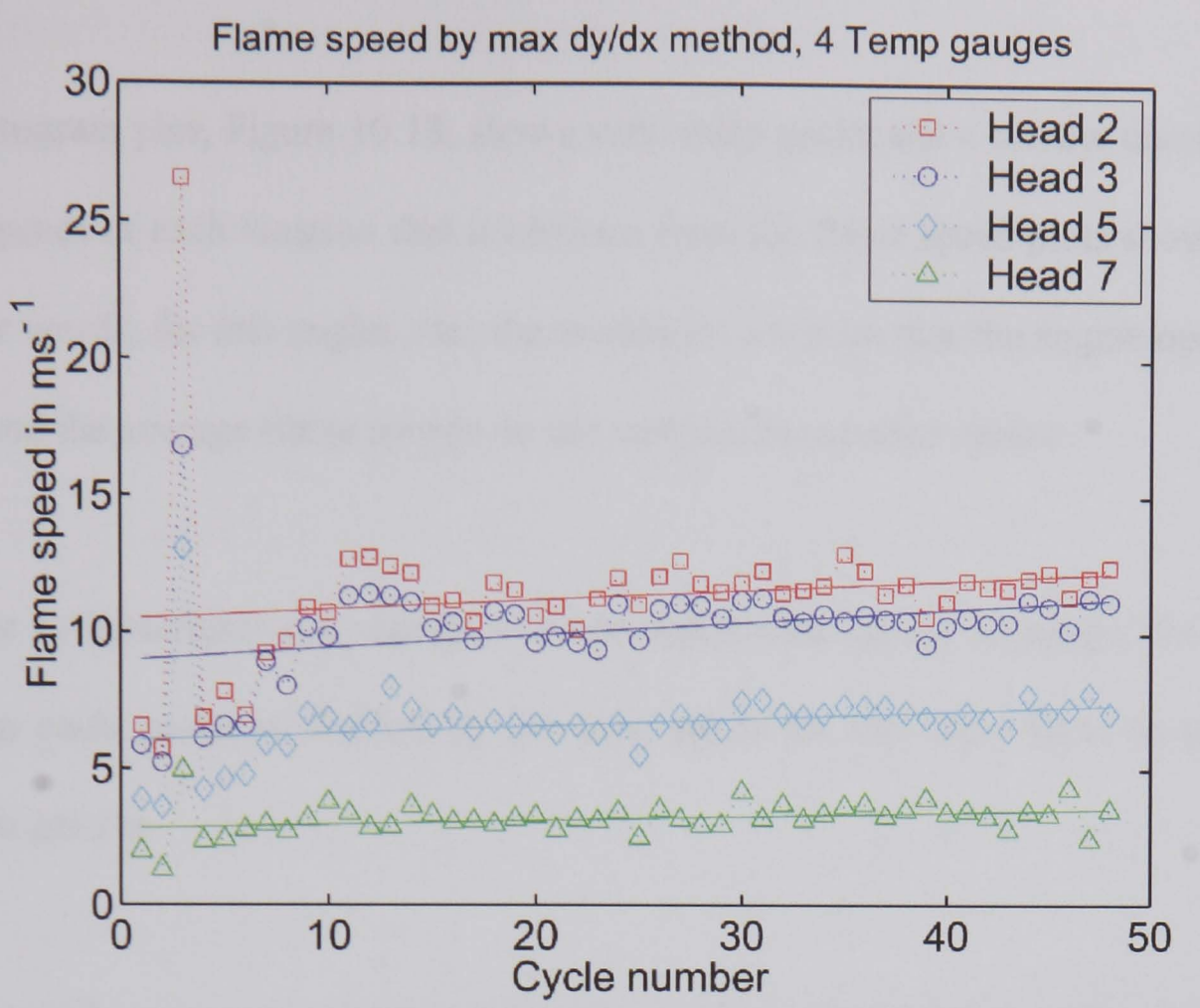

Figure 10.17, Average flame speeds from spark plug to each gauge for thrid engine run.

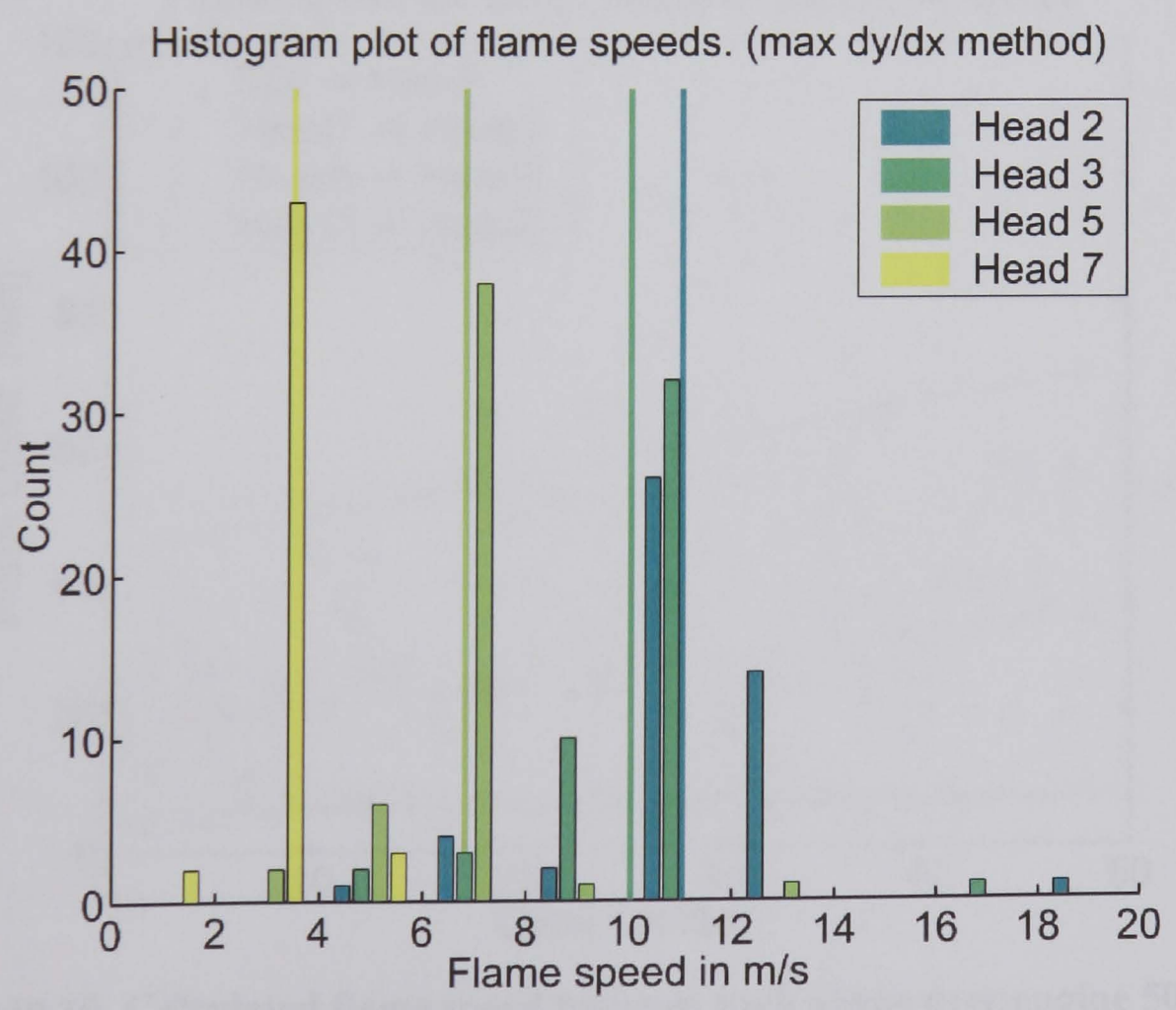

Figure 10.18, Histogram of average flame speeds from the spark plug to each of the 4 temperature gauges.

(Thin vertical lines represent the mean flame speeds)

The histogram plot, Figure 10.18, shows very sharp peaks and a narrow distribution in flame speeds at each location that is obvious from the flame speed plots shown above. In other words, for this engine run, the conditions are such that the engine operation is stable and the average flame speeds do not vary much between cycles.

In order to investigate the change in flame speed from gauge to gauge, the distance between each gauge is divided by the time taken for the flame front to propagate between gauges.

The plot of flame speeds calculated between gauges is shown below in Figure 10.19.

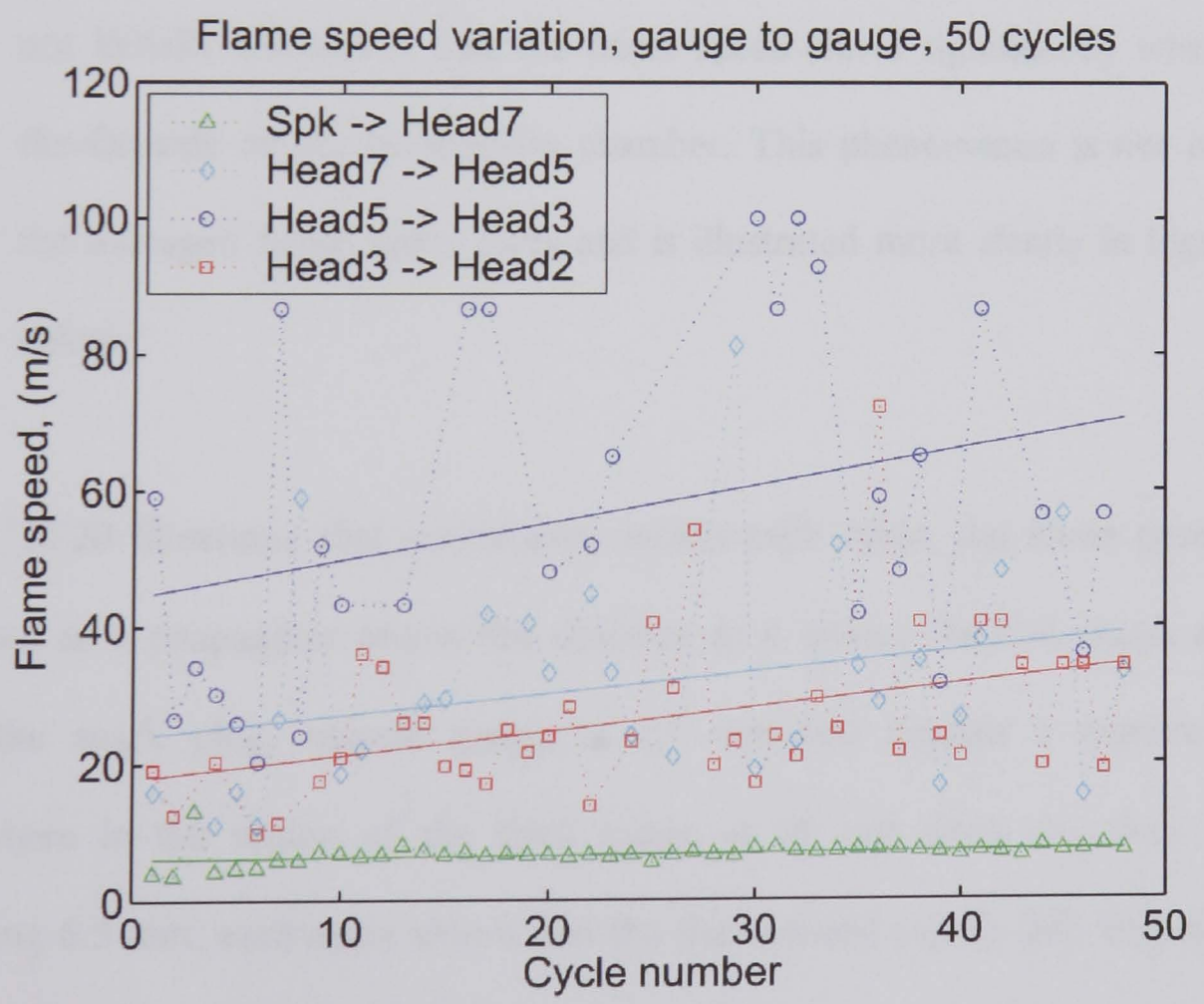

Figure 10.19, Calculated flame speed between each gauge over engine 50 cycles.

Several conclusions may be drawn from the above plot.

- The variation between cycles of the flame speed between each gauge is much higher than between the spark plug and each gauge. In other words by calculating the flame speed between the spark plug and the gauge, as done previously, a much more spatially averaged flame speed is found.
- The general trend of the flame speeds between gauges is consistent with that of the flame speeds calculated between the spark plug and the gauges.
- As the distance from the spark plug increases, the variation from cycle to cycle also increases, therefore suggesting that the flame becomes more turbulent and 'unpredictable' as it grows.
- The flame speed increases rapidly over the first portion of the chamber, as is also shown to a less extent in the averaged flame speed plots, however what is not initially obvious is that the flame speed slows significantly when nearing the far side of the combustion chamber. This phenomenon is not obvious in the averaged flame speed plots and is illustrated more clearly in Figure 10.20 below.

Figure 10.20 illustrates that consistently within each cycle, the flame speed rapidly increases as it propagates across the chamber as it passes the first gauge at 10 mm from the spark plug, second gauge at 23 mm and reaches a maximum speed somewhere in the region of the third gauge at 36 mm from the plug. Over the following 6.5 mm, each cycle shows that the flame speed rapidly falls before reaching the far chamber wall.

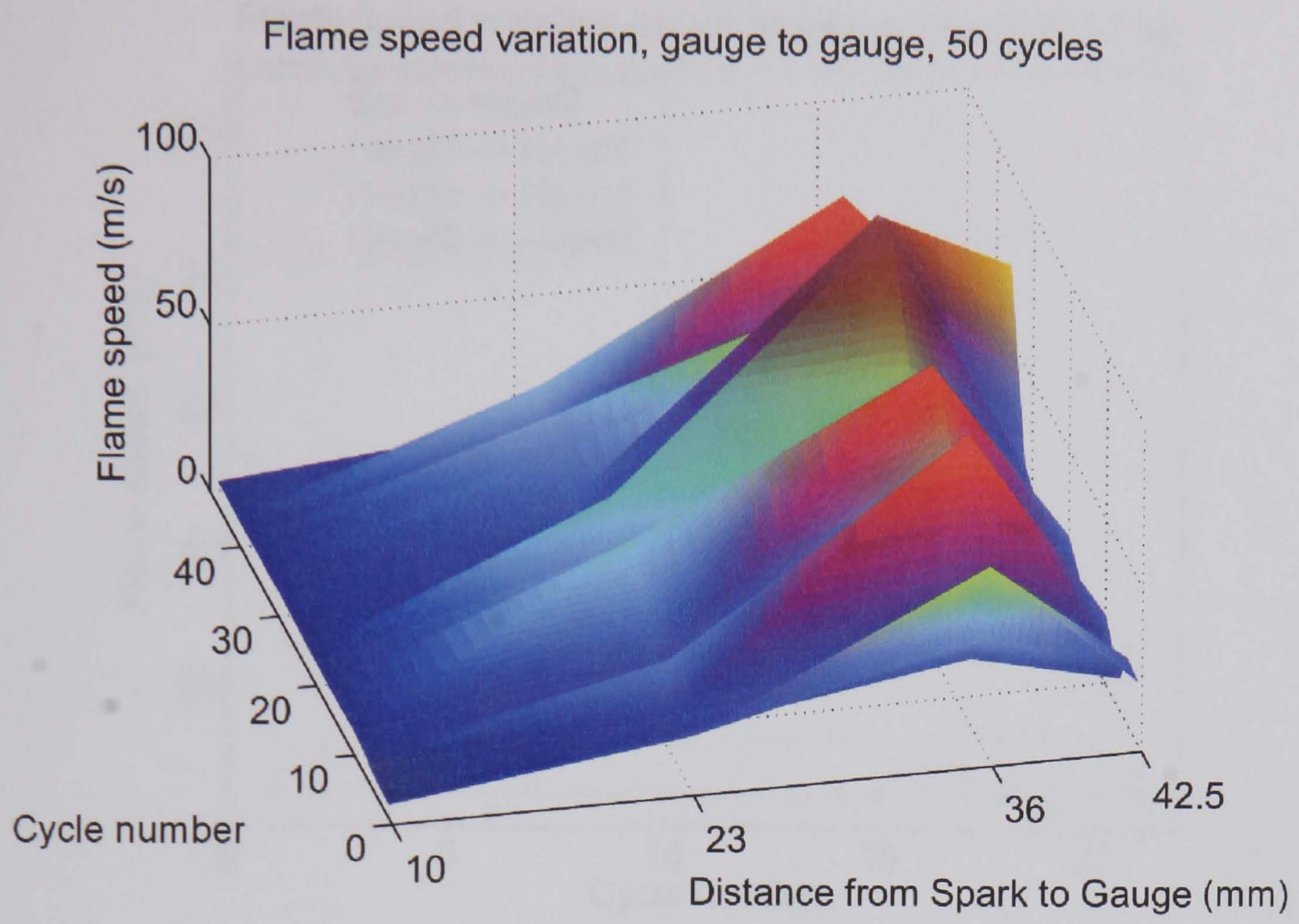

Figure 10.20, Surface plot of the spatial variation in flame speed.

10.7 Effect of Engine Conditions on Flame Speed

A series of short tests were performed at fixed engine speeds and varying load to investigate the effect of engine speed and load on the flame speed. The results are presented below.

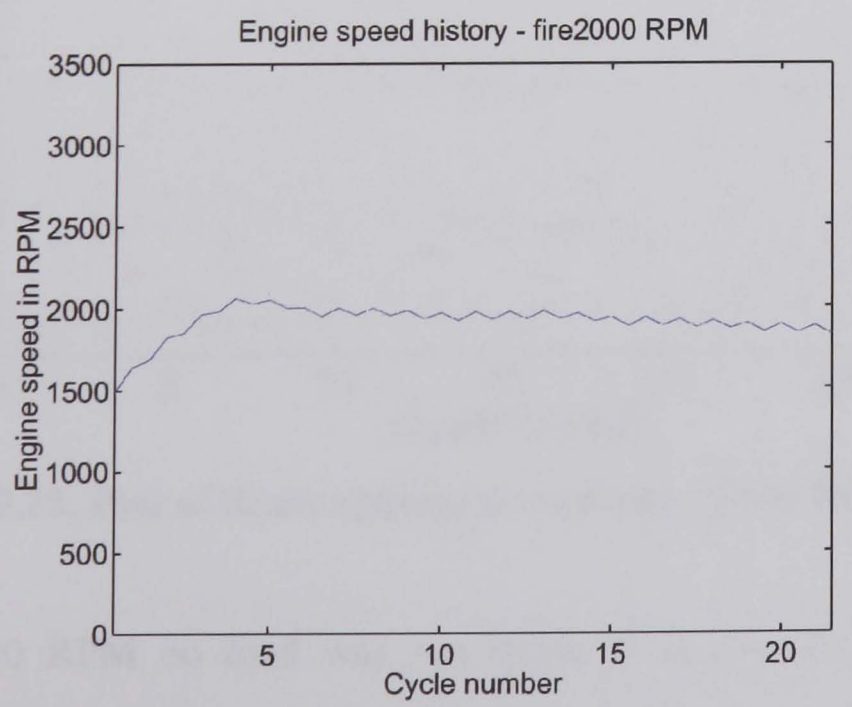

Figure 10.21, Plot of engine speed. (First run at 2000 RPM, no load)

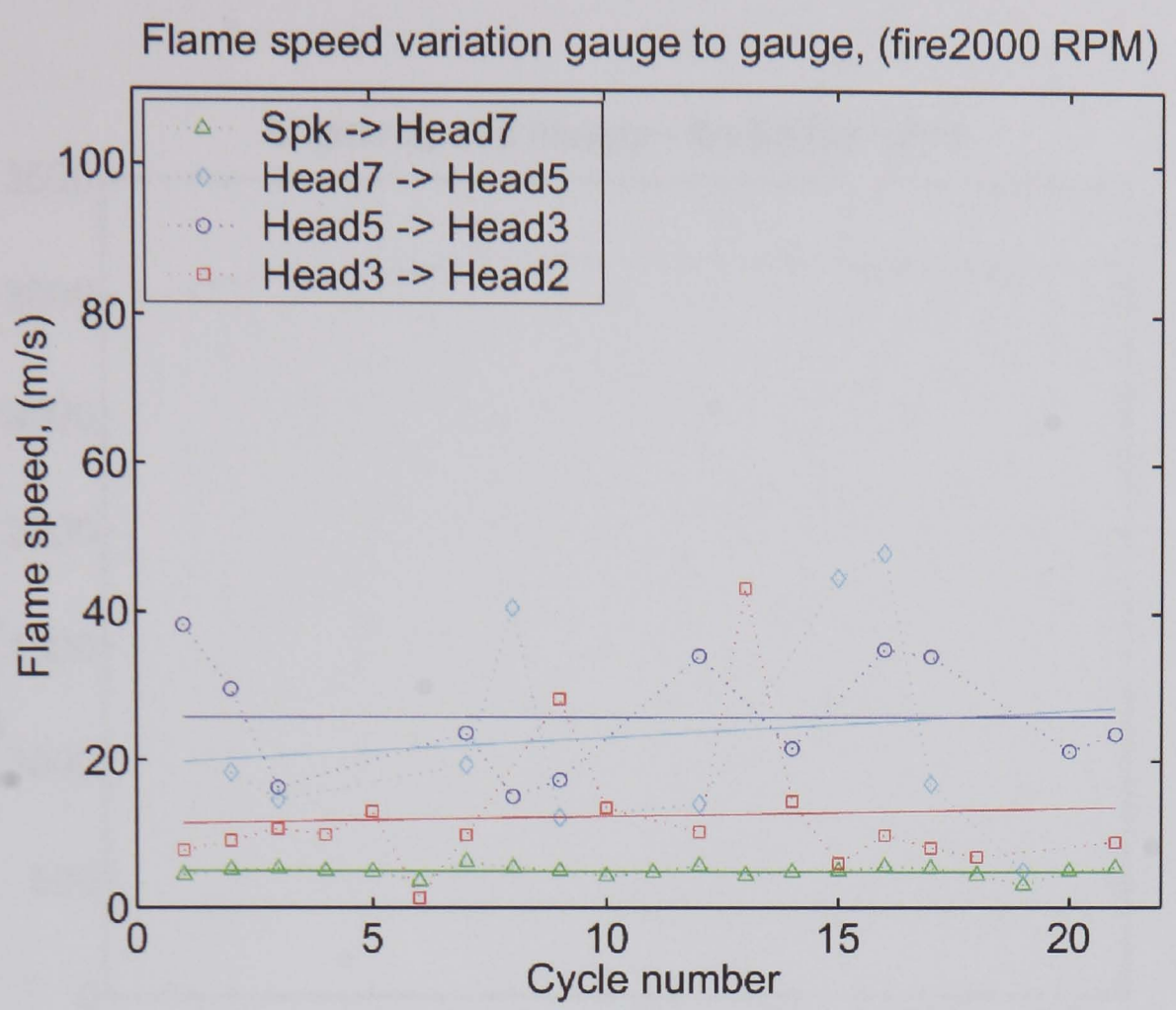

Figure 10.22, Plot of flame speeds, first run. (2000 RPM, no load)

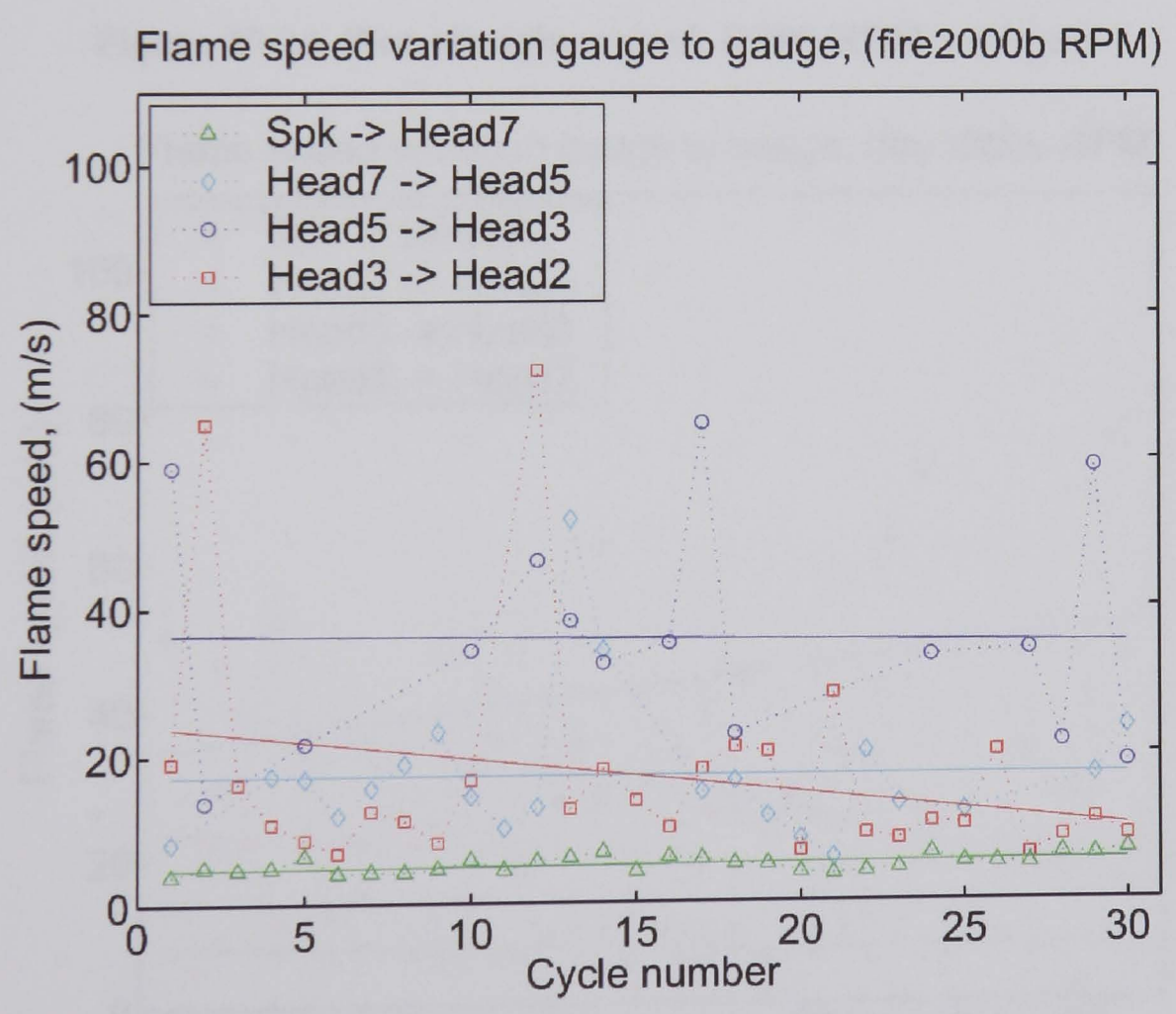

Figure 10.23, Plot of flame speeds, second run. (2000 RPM, no load)

The test at 2000 RPM no load was run twice. It is obvious the results are not repeatable.

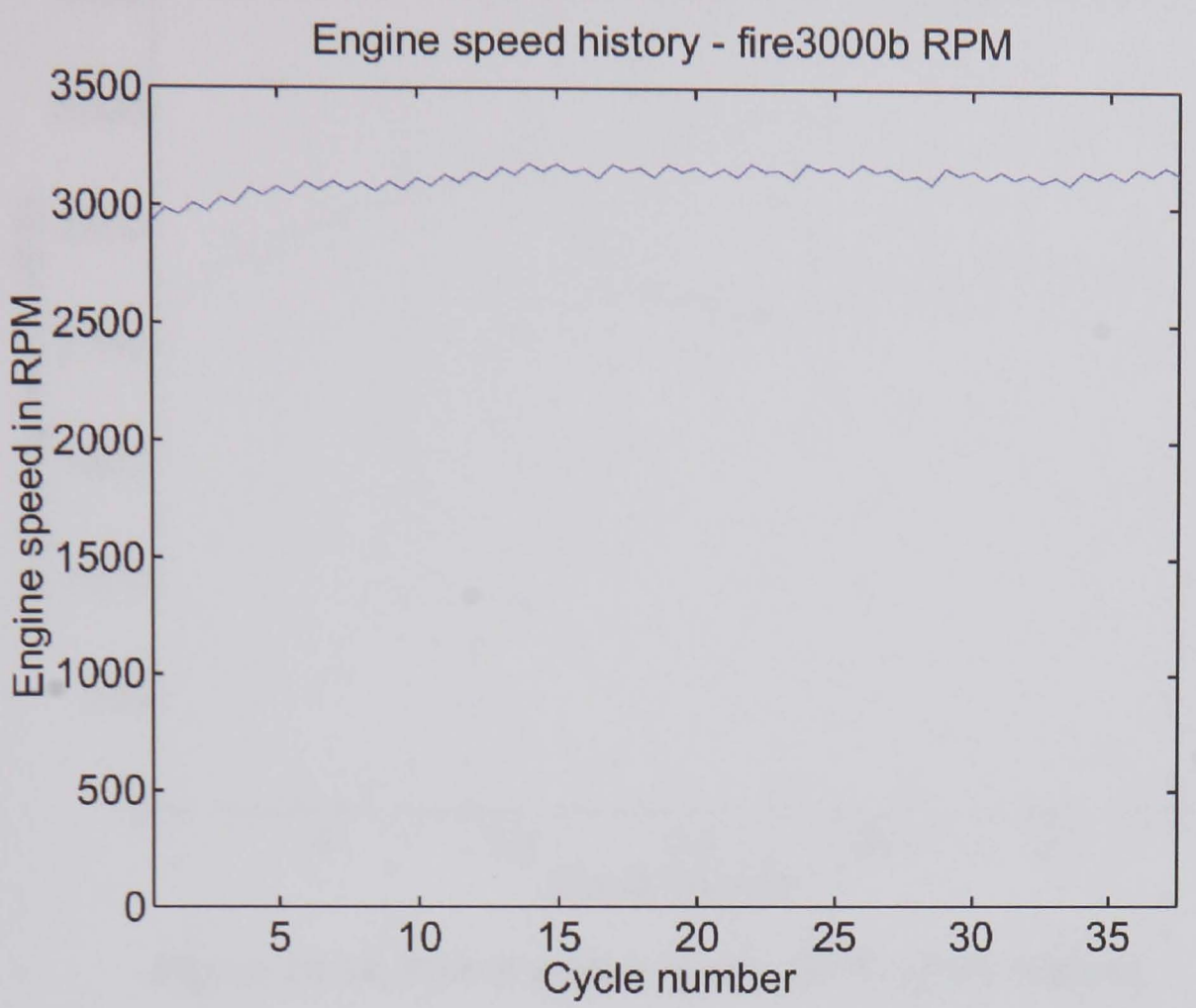

Figure 10.24, Plot of engine speed. (3000 RPM, no load)

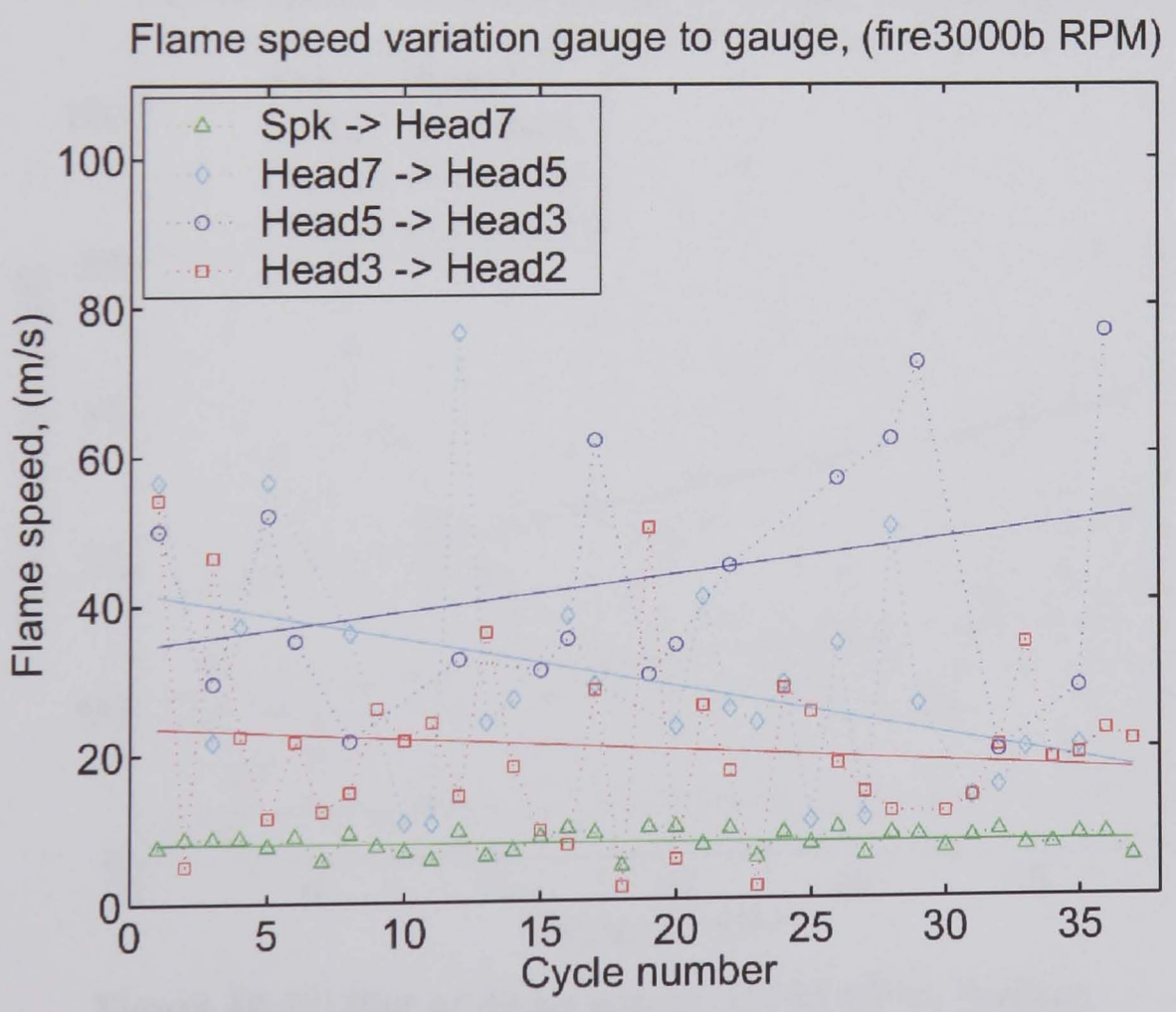

Figure 10.25, Plot of flame speeds. (3000 RPM, no load)

Although it is acknowledged that this difference exists, it is believed to have a small effect on predicted gas temperatures and therefore heat flux rates. Certainly though, this is difference that should be corrected in any further investigations.

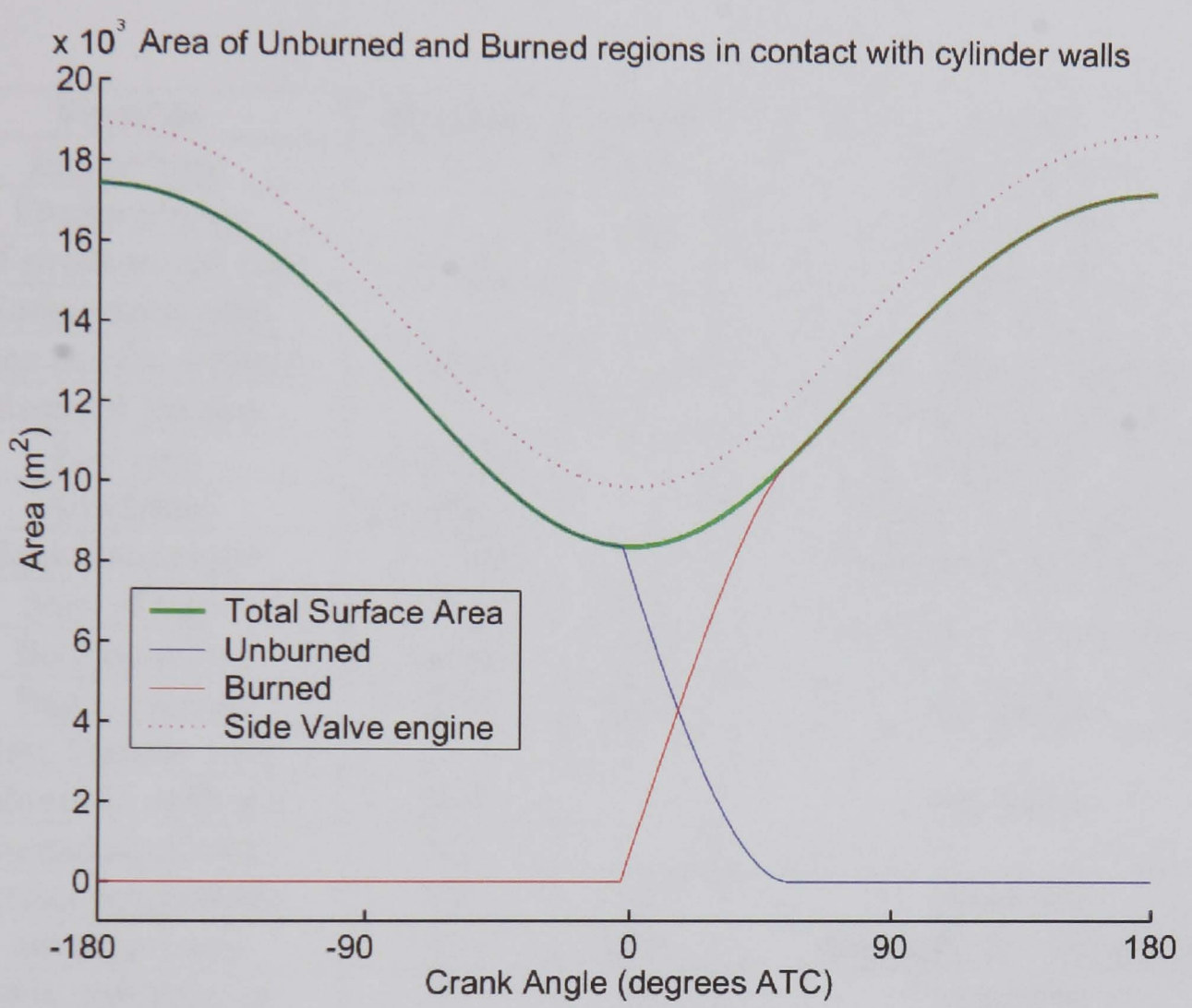

Figure 11.1, Plot of A_u and A_b as determined for calculating heat loss during combustion compared to total chamber surface area for pentroof and side valve engine designs.

11.2.3 Expansion

The calculations during the expansion stroke after the completion of combustion are the same as during the compression phase, except that the combustion chamber now consists of 100% residual gas, and therefore different species concentrations. This is considered and the differential equations integrated accordingly.

11.3 Choice Of Input Variables

In order to predict the operation of a particular engine configuration, the user must input the variables that define that particular engine. See Table 11-1 for a list of these variables and how they are selected.

Variable	Symbol	Units	Choice
Engine bore	b	m	Measured
Engine Stroke	s	m	Measured
Half stroke to rod ratio	ε (eps)	-	Measured
Compression ratio	r	-	Measured
Piston blowby constant	Cblowby	-	Estimated - see below
Residual fraction	f	-	Estimated - see below
Fuel type	fueltype	-	Known
Airscheme	airscheme	-	Choice - see below
Equivalence ratio	ϕ (phi)	-	Estimated - see below
Start of burn	theatas	CA	Estimated - see below
Burn duration	thetab	CA	
Engine Speed	RPM	rpm	Measured
Heat Transfer Law	-	-	See below
Unburned coefficient	hcu		
Burned coefficient	hcb		
Surface temperature	Tw	K	Measured
Initial pressure	p1	kPA	Atmospheric – Measured
Initial temperature	T1	K	Measured

Table 11-1, Engine model inputs.

Piston blowby constant: Piston rings are used to seal the piston into the bore to ensure that as much as possible of the raised pressure in-cylinder is turned into useful work moving the piston. However, piston rings require a gap to facilitate not only fitting of the rings, but also to allow for heat expansion as the engine warms up. This gap results in some hot gasses being able to escape past the rings. The amount of gas that escapes is characterised with the piston blowby constant. This is measurable for any given piston, ring pack and bore, but in this case was not measured; instead a typical value has been chosen. This choice is valid as the effect of piston blowby

constant on predicted performance is minimal, see Figure 11.2, especially when compared to the other assumptions made.

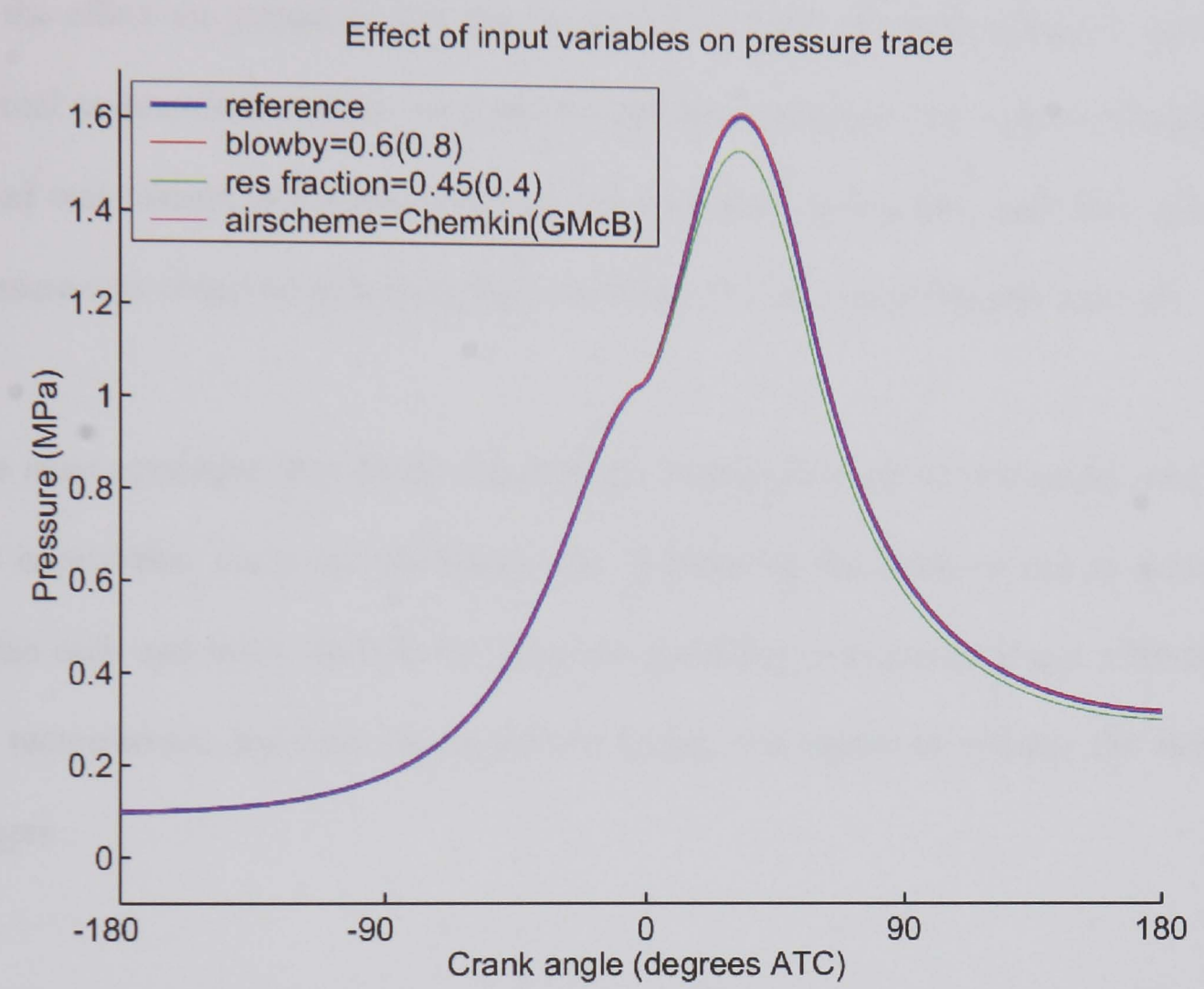

Figure 11.2, Influence of blowby, residual fraction and air scheme on predicted pressure.

Residual fraction: Not all of the combustion products are exhausted during the exhaust stroke; instead, some remain and are present during the intake stroke and thus also present during compression and combustion. This residual fraction is not unwanted as in some cases it can be used to benefit combustion emissions; however, to measure the residual fraction is not trivial. Typically this is found by sampling a small portion of the in-cylinder gas during the compression stroke using a specially designed sampling valve in the chamber and comparing this gas composition to the exhaust composition to get a ratio of exhaust to fresh charge.

Again, such complex analysis was not appropriate to the essence of the investigation, however it is acknowledged that the choice of residual fraction does have a significant effect on both in-cylinder pressure and combustion gas temperature, (see Figure 11.2 for the effect on pressure). For the prediction, a value of residual fraction typical of internal combustion engines, and specifically appropriate to the engine configuration tested was chosen, and it may be observed later that a good agreement with measured pressure was observed indicating that the choice of 0.4 was sufficiently accurate.

One must remember that many assumptions have been made in this model, and while this is probably the most significant, the purpose of this study is not to accurately define each and every variable for accurate modelling, but instead to get a flavour for the temperatures and heat fluxes present within this engine to validate the heat flux gauges.

Airscheme: A choice of two air schemes are offered whilst defining the model initial conditions, both of which define the thermodynamic properties of CO_2, H_20, N_2, O_2, CO, H_2, H, O, OH and NO. Both Gordon and McBride (GMcB) and the Scandia National Laboratories (Chemkin) have attempted to curve fit the experimental JANAF data [135] of thermodynamic properties for each of the above species. A choice is offered as to which scheme is preferred, however very little (typically <1%) difference exists between the curves, which results in an insignificant difference in predicted pressure and temperature. See Figure 11.2 for the effect on pressure. The GMcB curves were chosen.

Equivalence ratio, Start of burn & Burn duration: It is acknowledged that typically one would measure air and fuel flow and therefore have a measurement of equivalence ratio; however, such measurements were not available at the time of writing, instead the equivalence ratio variable was added to that of start of burn and burn duration, being parameters that are chosen by curve fitting to experimental data, see p80 of [133] for more information.

As the parameters are chosen one considers how practical such values are. The equivalence ratio of unity is as expected, the values of burn start and duration not only yield a good agreement with measured pressure but are similar to that observed with the flame imaging.

It is noted however that equation (11.5) defining mass fraction burned (mfb) does not accurately reflect the rate of burn within the engine, (although is sufficiently accurate for this initial investigation). The plot of mfb is shown in Figure 11.3 along with cylinder volume. When one considers that the spark occurs at -20° ATDC, compared to -3° ATDC before any pressure rise due to combustion is observed, it is obvious that equation (11.5) over predicts the burn rate.

$$x = \begin{cases} 0 & \vartheta < \vartheta_s \\ \frac{1}{2}\left\{1 - \cos\left[\frac{\pi(\vartheta - \vartheta_s)}{\vartheta_b}\right]\right\} & \vartheta_s < \vartheta < \vartheta_s + \vartheta_b \\ 1 & \vartheta > \vartheta_s + \vartheta_b \end{cases} \tag{11.5}$$

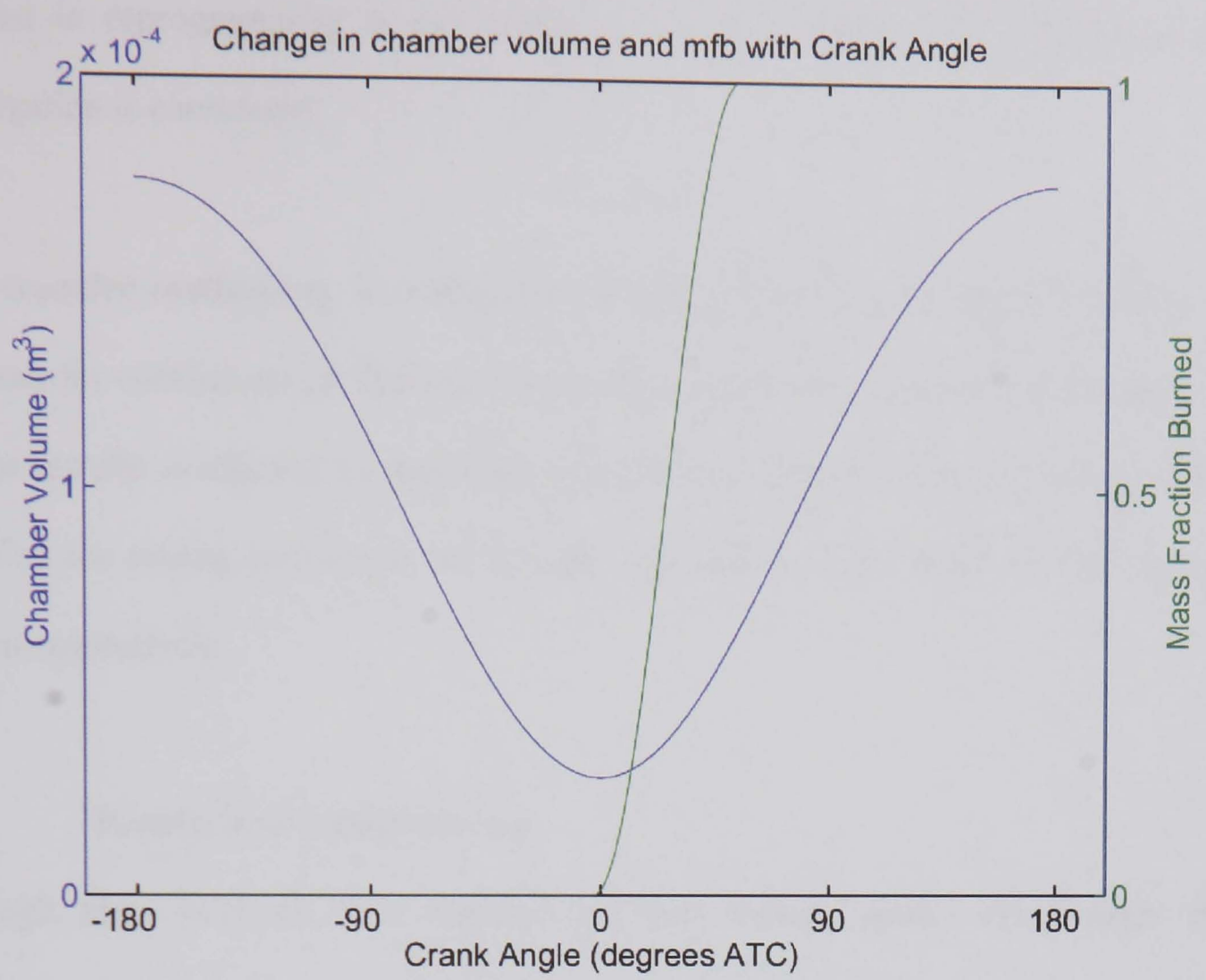

Figure 11.3, Plot of mass fraction burned and chamber volume against crank angle.

A more accurate burn rate would start at -15° ATDC to correspond with the spark timing, show a very small increase in mfb until just before TDC when it would initially slowly rise but speed up towards the 100% mass burned. This in turn would result in an improved match in predicted pressure (note the deviation from measured pressure during the high rate of pressure rise in Figure 11.4) and improve the heat flux comparison in the region just after TDC in Figure 11.7. It is expected this deviation from the standard burn rate is due to the side valve engine configuration as opposed to the radial burn typically observed with a pent roof combustion chamber.

Note that burn rate is not defined as an engine parameter, rather is built into the modelling code. Again, an exact match in burn rate has not been pursued, as the effort

required in reprogramming is not justified when the essence and purpose of the investigation is considered.

Heat transfer coefficients: The Woschni correlation [92] may be used to predict the heat transfer coefficients for the unburned and burned regions instead of a single value of heat transfer coefficient as described previously. In this case hcu and hcb are used to define the scaling factors for the Woschni correlation in the unburned and burned regions respectively.

11.4 Results and Interpretation

Although plots of work, heat transfer and heat leakage against crank angle are available, the interest is in the in-cylinder pressure, unburned and burned gas temperatures and heat flux rates. These plots are shown and discussed below.

11.4.1 Pressure

As previously described, pressure is an important parameter to compare as it is easily measured and any deviation of the input parameters from practice will be evident in the pressure trace.

In addition, for the purpose of this investigation, it is the in-cylinder temperatures that are of interest rather than building an accurate model of the engine; and since the temperatures are related to pressure, if a good agreement can be found with pressure, it naturally follows that the temperatures should be close to those found in the engine.

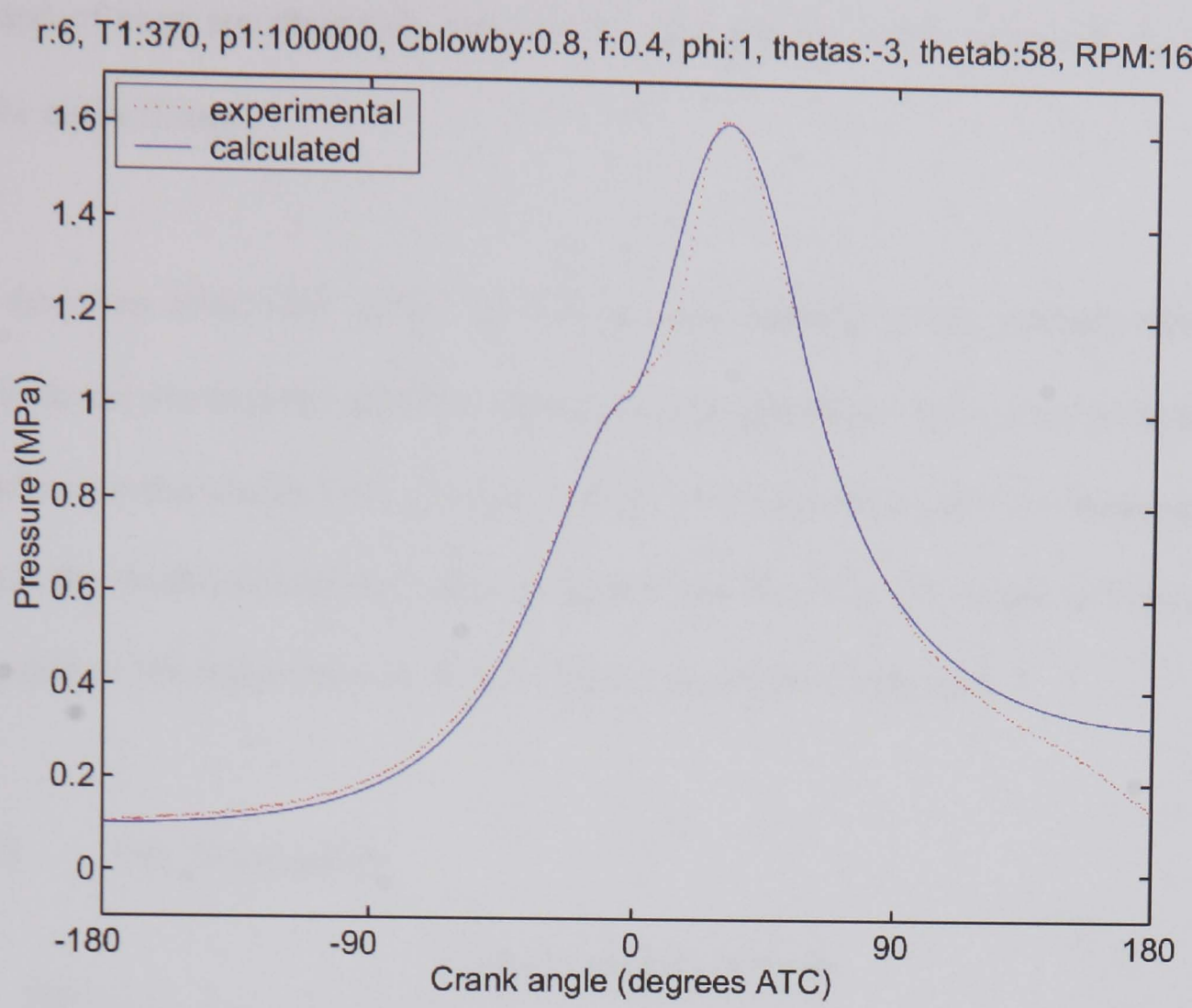

Figure 11.4, Plot comparing predicted to measured pressure. The variables in the plot title correspond to the model inputs of Table 11-1.

Figure 11.4 shows the predicted in-cylinder pressure generated with the model compared to the pressure measured experimentally. It may be observed that an excellent agreement is found during the compression stroke until TDC, similarly an excellent agreement is observed with the peak pressure and the pressure fall due to the expanding combustion chamber until approximately 120° ATDC. The significant differences are observed between TDC and peak pressure and after 120° ATDC on expansion.

The deviation between TDC and peak pressure is due to differences in the burn rate as described previously, and are assumed to be the best achievable without reprogramming the model. It is believed that more significant than the deviation during the pressure rise due to combustion is the fact that start of burn, peak pressure

and end of burn are accurately matched by changing the 3 user inputs (ϕ, θ_s and θ_b) left for curve fitting.

The deviation after 120° ATDC is due to early opening of the exhaust valve that results in the combustion products venting during expansion. This is not an important deviation as the combustion process has by now completed, it does however help explain the predicted slightly higher sustained heat fluxes in this region in Figure 11.7 compared to the measured heat fluxes which drop off from this point.

11.4.2 Gas Temperature

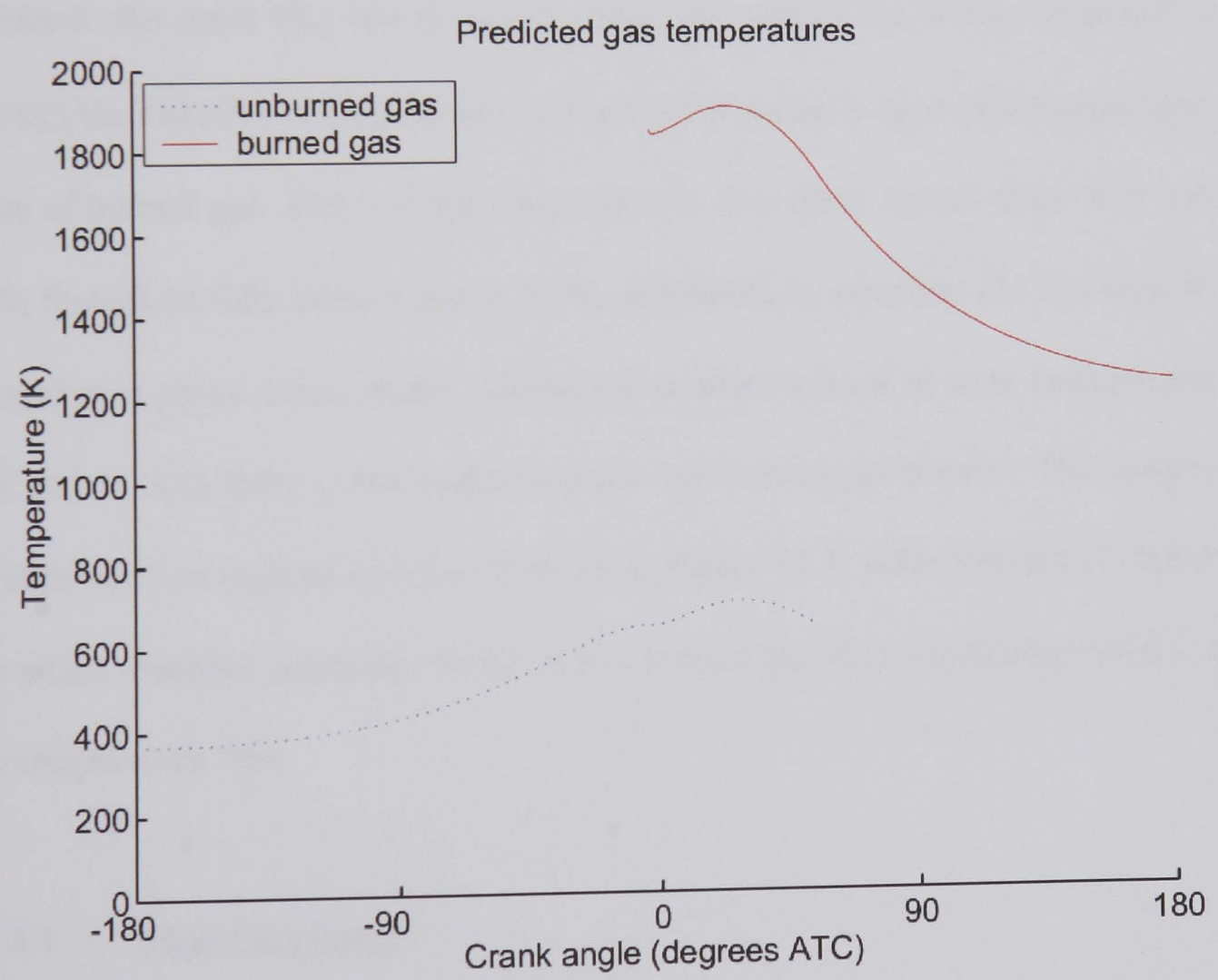

Figure 11.5, Plot of predicted gas temperatures.

Gas temperature is an intermediately step in the determination of predicted heat flux. From this temperature prediction and the values of heat transfer coefficient from the

Woschni correlation, values of heat flux may be determined. Gas temperature is not measured in this engine as there are currently no reliable gas temperature methods available that will accurately operate within the internal combustion engine.

The overlap in temperatures can be explained when one considers the method the model is operating. Initially the entire chamber is full of the fresh charge mixed with the remaining residual gas. This is compressed from -180° through to roughly TDC therefore causing the temperature to rise as shown by the unburned gas temperature plot in this region of the graph.

Between this point (θ_s) and the point where the charge has been completely burned ($\theta_s+\theta_b$) the chamber is considered to consist of 2 zones, a zone of unburned gas and a zone of burned gas. The boundary between the two zones moves from fully unburned at θ_s though to fully burned gas at $\theta_s+\theta_b$ as defined by equation (11.5) (mass fraction burned at a given crank angle). Obviously at any moment in time between the start and end of burn there is both unburned gas and burned gas present. The temperatures of each of these regions are plotted above in Figure 11.5. After the end of burn ($\theta_s+\theta_b$) the entire chamber contents consist of hot burned gas in an expanding volume and so the temperature falls.

11.4.3 Heat Flux Rates

The heat flux rates calculated using the model, those measured with each of the thin film gauges and the mean measured heat flux are all plotted below in Figure 11.6. Note again that the two blue curves relate to the predicted heat flux in the burned and unburned regions. The model uses the predicted gas temperatures in each of these

regions, as described above, and the values of heat transfer coefficient previously defined, to calculate and plot the heat flux for each region.

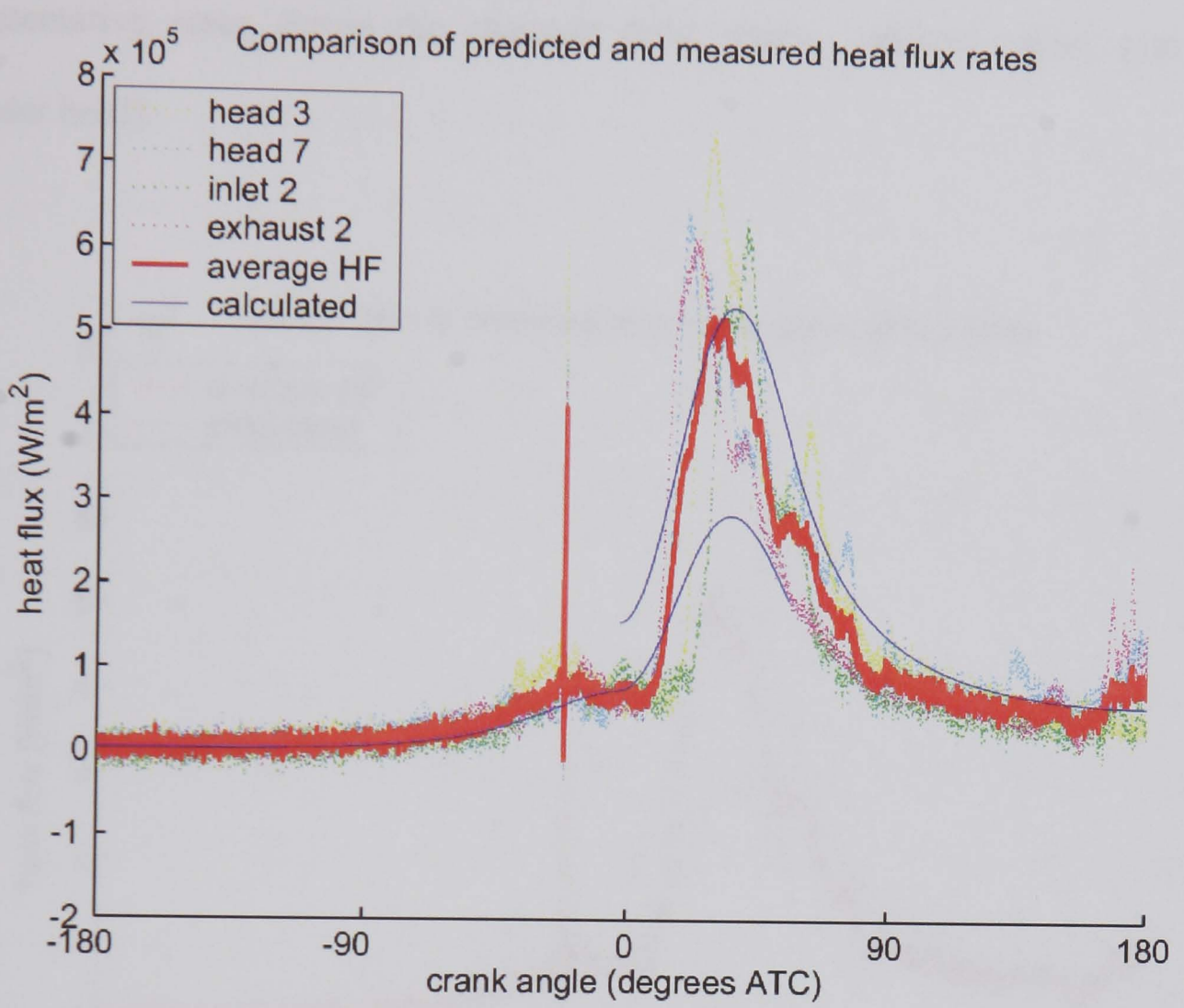

Figure 11.6, Measured heat flux rates compared to predicted heat flux.

It is observed that a good agreement is found during the compression stroke (-180° to 0° ATDC). Similarly during the burn even though individual gauges differ substantially in terms of both peak value and duration from the predicted heat flux, the mean heat flux from the 4 gauges in general shows a very good agreement to the predicted heat flux. This is shown more clearly below in Figure 11.7.

Figure 11.7 is a slightly simplified version of Figure 11.6 showing only predicted and mean measured heat fluxes. From this plot it is possible to compare the measured with predicted on a more like for like basis since the prediction is only for cylinder

averaged heat flux. The mean measured heat flux is not an exact measurement of cylinder averaged heat flux since the heat flux levels within the chamber vary significantly with spatial position, but instead is the mean of 4 gauges positioned in 4 representative areas across the chamber (inlet region, exhaust region, piston and cylinder head).

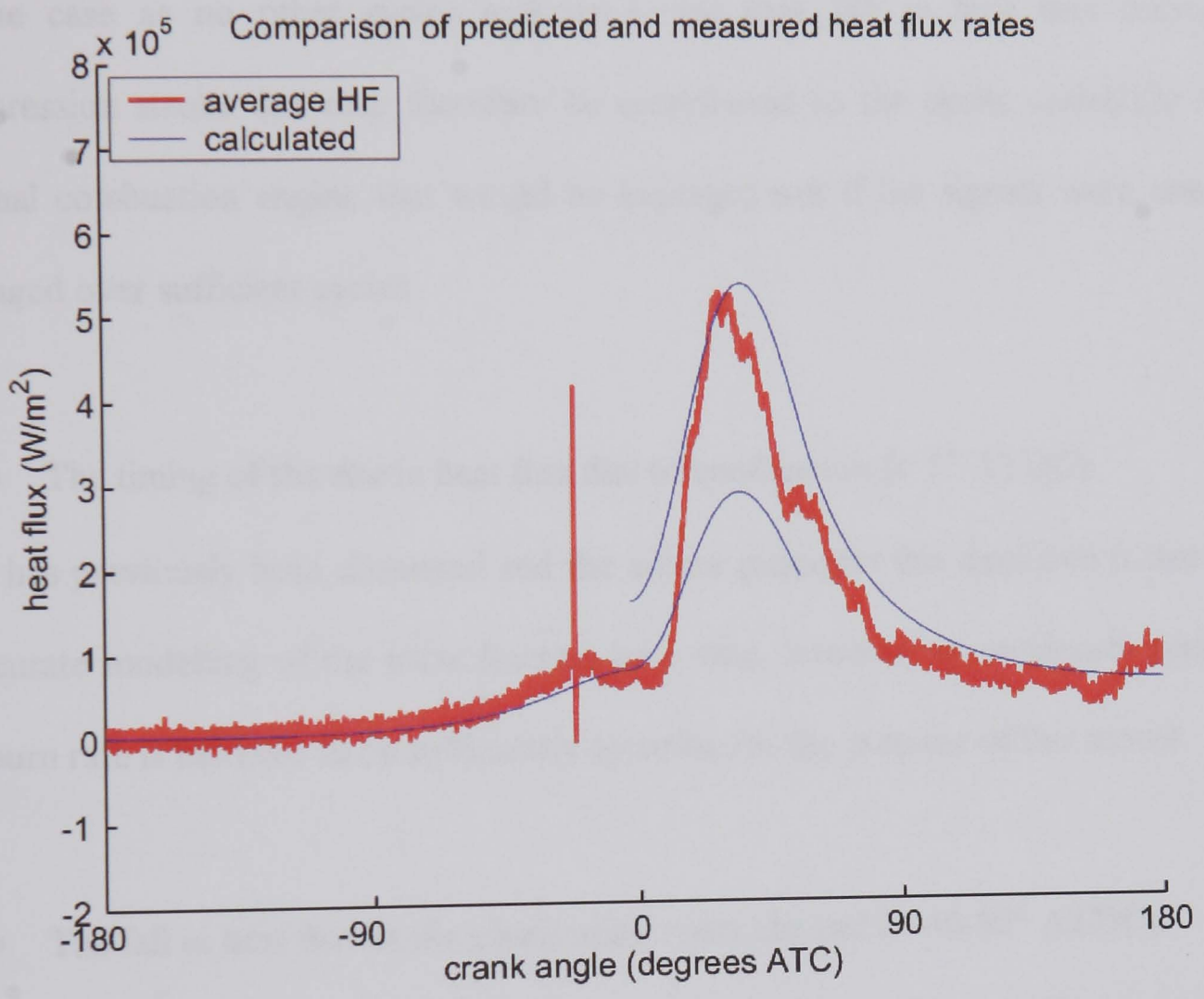

Figure 11.7, Mean measured chamber heat flux compared to predicted heat flux.

The deviations from predicted heat flux occur mainly in the following areas:

- In the time around the spark (≈ -15° ATDC)

Initially this raised the question whether the spark affected the measurement of heat flux, but as may be observed in Figure 11.8 where the predicted motored heat flux is compared to the measured motored heat flux with and without the spark operating it is

obvious that the spark has no affect on the measurement (other than the 1°-2° interference spike).

Instead this deviation from predicted heat flux was traced to a raised temperature signal on one of the gauges in this region and therefore is assumed to be a small region of hot residual gas that was temporarily next to the gauge in question.

Comparing this result to heat flux signals from other engine runs indicate this was a unique case as no other cycles indicate a rise then fall in heat flux during the compression stroke and may therefore be contributed to the cyclic variability of the internal combustion engine that would be averaged out if the signals were ensemble averaged over sufficient cycles.

- The timing of the rise in heat flux due to combustion (≈ 5° ATDC)

This has previously been discussed and the author proposes this deviation is due to an inaccurate modelling of the mass fraction burn rate, however as previously specified, the burn rate is believed to be sufficiently accurate for the purpose of this model.

- The fall in heat flux as the combustion nears the end (≈ 40-90° ATDC)

This may not easily be explained, but it is assumed that given sufficient heat flux measurements spread across the chamber, this deviation would probably be reduced.

- The rise in heat flux observed in the measurements but not the prediction at (≈ 180° ATDC)

Quite simply this is the hot combustion products passing through exhaust valve. The rise in heat flux is observed on only one gauge, the gauge in the combustion chamber above the exhaust valve. Since not only is this a local phenomenon but also since the

model does not account for valve events but instead considers a closed system from -180° through 180° it is expected that the model would not predict this feature.

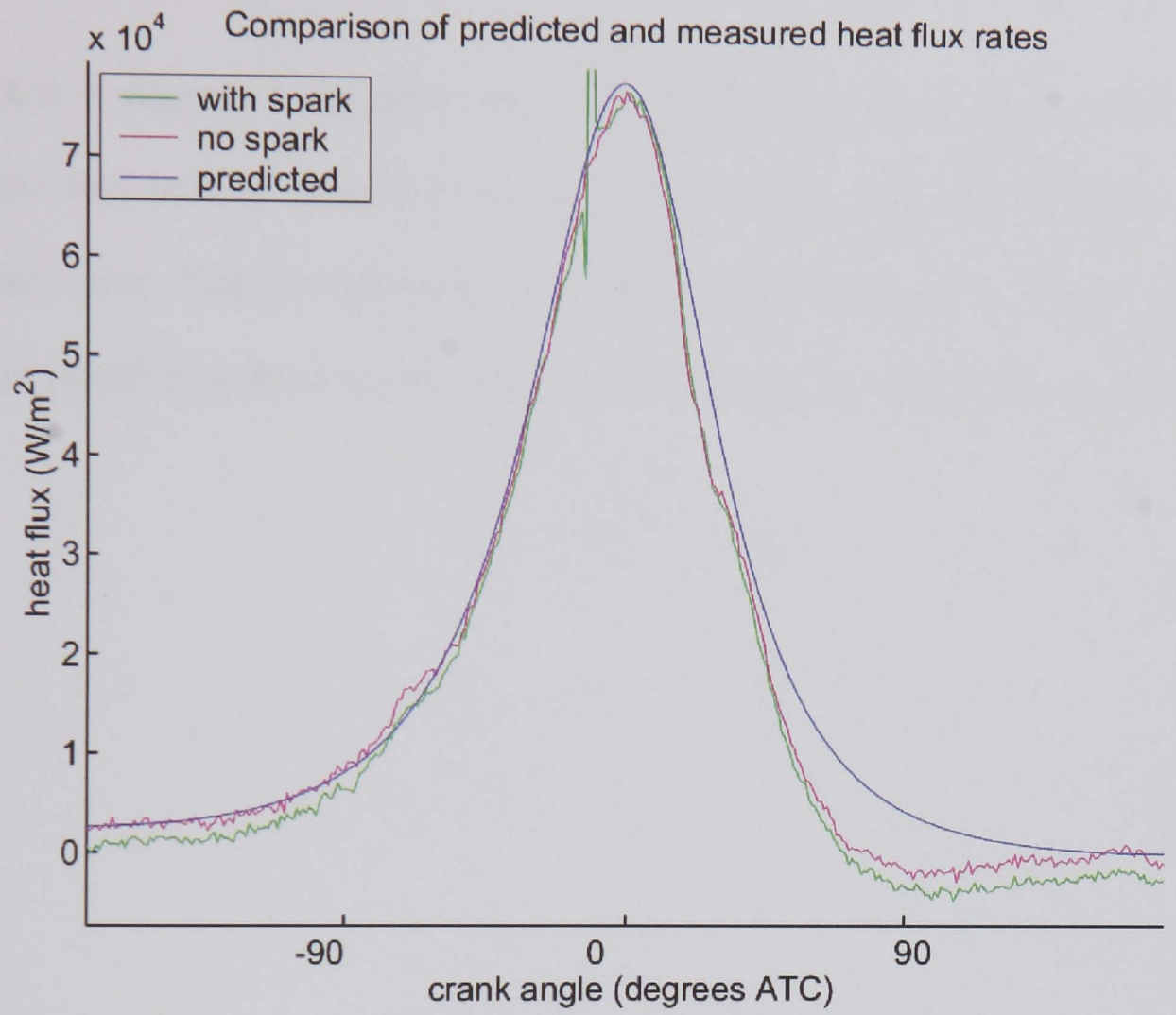

Figure 11.8, Comparison of motored heat flux with and without the spark operating compared to predicted heat flux when motored.

11.5 Conclusions

The mean measured values of heat flux compared very favourably to those predicted by the model. This is a significant result since as the model is based on historically accepted thermodynamic laws applied to the internal combustion engine it comes pre-validated, therefore the agreement observed between measured and predicted serves to validate the measurements.

Further, as expected, agreement is observed between mean measured heat flux and predicted values of heat flux. This in turn provides evidence that the signals from the

individual gauges are themselves genuine and believable. Such a fast response, one-dimensional heat flux measurement within the internal combustion engine is a breakthrough from existing technology.

In turn it is suggested that given such high bandwidth measurements of heat fluxes, advances may now be made in computer models that consider and model the thermal boundary layer. This is of particular importance when designing coolant systems since the heat rejection, as has been observed, is not constant throughout the chamber.

PART V

CONCLUSIONS AND FURTHER WORK

CHAPTER 12

CONCLUSIONS AND FURTHER WORK

12.1 Conclusions

The current "state of the art" experimental techniques for internal combustion engine measurement have been evaluated and assessed in terms of measurement quality and 'usefulness'. It has been shown that new, high frequency, less intrusive techniques for measurements of flow, surface temperature and light emission within this harsh environment are required.

The use of a small single cylinder test engine has demonstrated that it is possible to create a low cost environment suitable for this fundamental research. The use of natural gas and a self-contained, single cylinder, air-cooled engine has significantly reduced the complications and cost normally associated with engine testing and opened routes for technology transfer to the gas turbine engine. This low operating overhead has permitted the evaluation of instrumentation measuring the highly turbulent flame front.

This instrumentation includes:

- The novel application of heat flux gauges to the combustion chamber of an internal combustion engine
- Temporal and spectral fibre optic measurement of the flame front development
- The first PIV measurement of the flow within a combustion chamber made through the spark plug of an essentially unmodified internal combustion engine

It has been shown that it is possible to apply techniques such as PIV, spectral analysis and temperature measurement to an internal combustion engine without significant engine modifications. This can be seen as step forward in the evolution of a new type of minimally intrusive intelligent instrumentation.

In addition, a two-zone combustion model has been used to model the combustion and provide a validation of the temperature measurements.

12.2 Further Work

Significant progress has been completed in each of the areas investigated. Below a brief discussion is provided with recommended routes for further development.

12.2.1 Heat Flux Gauges

These gauges proved effective at recording at a high bandwidth the surface temperatures within the combustion chamber. From the surface temperature and the metal temperature it has been possible to calculate local heat flux levels at a frequency rate sufficiently high (100 kHz) to record the turbulent structures passing the gauges. However, since there are currently no techniques available that provide a sufficiently

robust and reliable gas temperature measurement, determination of the heat transfer coefficient has not been possible.

In order for this technique be used for internal combustion engine computer model development, it is required that the heat transfer coefficient be measured experimentally. A proposed new generation of heat flux gauge holds the potential for making this measurement [136]. This new gauge would work on a similar principal; however, in addition it is proposed that a protrusion on the gauge surface would extend through the boundary layer and measure the gas temperature with a further thin film temperature sensor, Figure 12.1. The work required on such a project must assess not only probe durability, but also ensure the measurement is non-intrusive. In addition, it is suggested that the wire routing is reconsidered to reduce problems with wire fatigue and wire breakage.

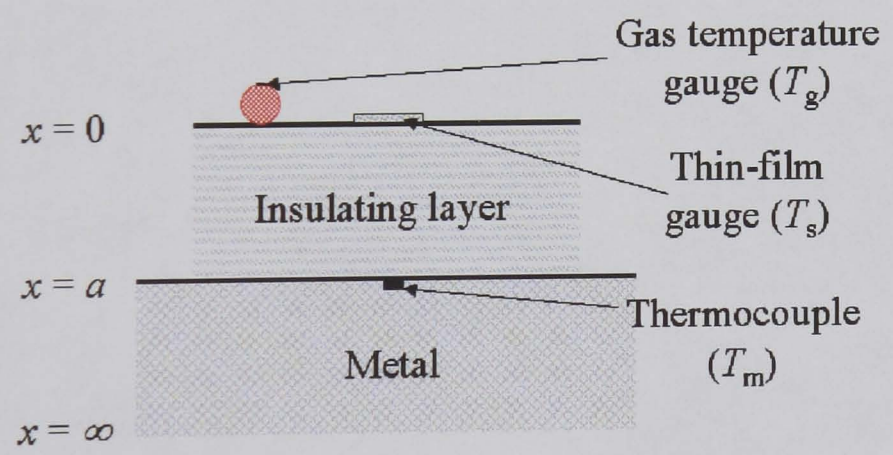

Figure 12.1, Schematic of proposed heat flux gauge measuring gas temperature (T_g) as well as the existing wall temperature (T_w) and metal temperature (T_m).

Investigation of the turbulent structure of the flame could also be explored. Difficulty in correlation between gauges was experienced due to the small signals from the structures observed on the large surface temperature signal. Further investigation and

statistical modelling is required. Alternative gauge orientations should be explored as a part of such research.

Finally it is suggested that the gauges be assessed for both rapid prototyping ability and durability over a wide range of fuels and operating extremes. For example, investigation into 'writing' the gauges onto a ceramic coating on the piston or cylinder head surface, or performing more pre-preparation of the gauges so that they may simply be 'stuck' onto the surface when required without requiring any soldering. Obviously issues such as calibration require addressing.

12.2.2 Tomography

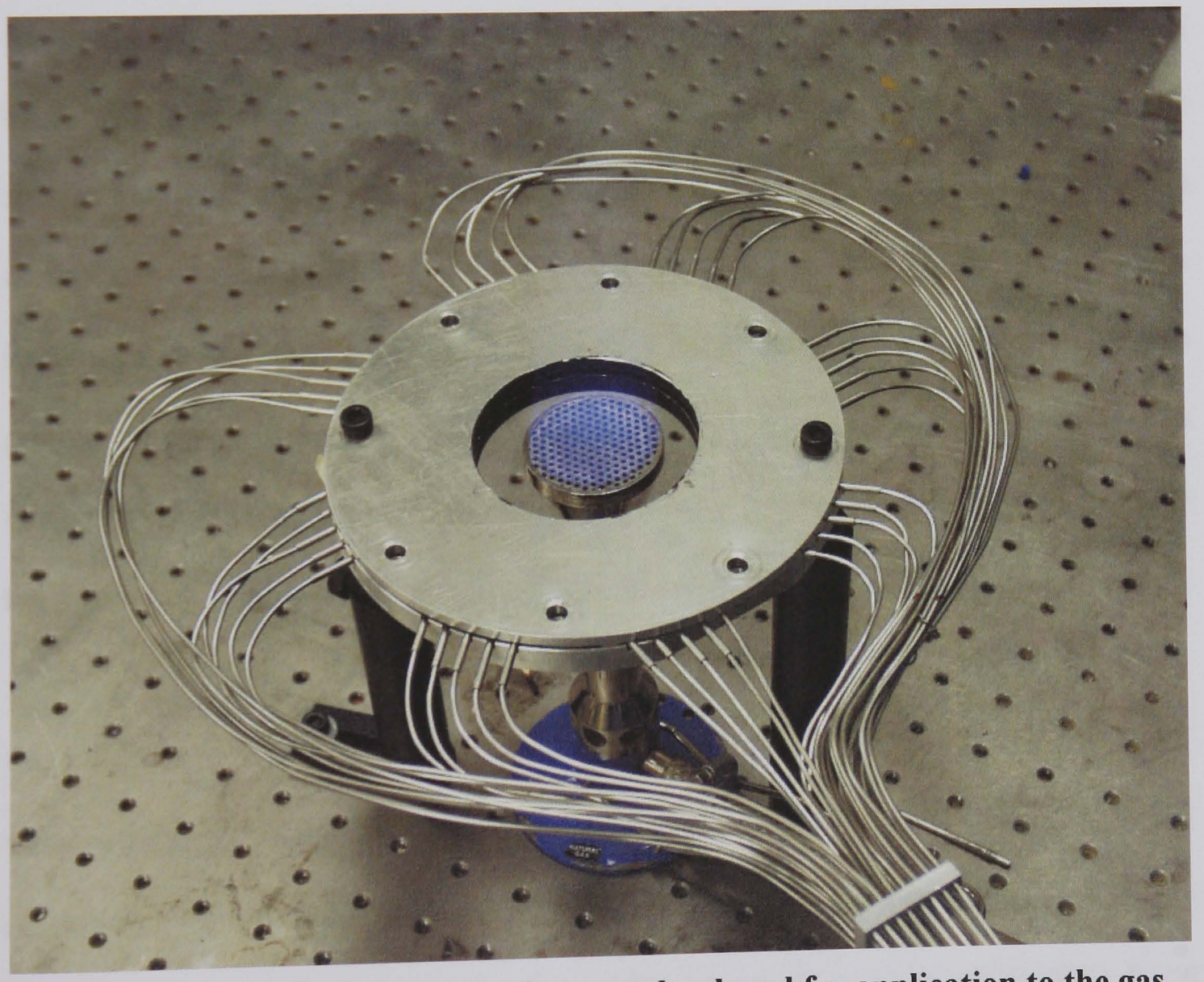

Figure 12.2, Photo of tomographic array developed for application to the gas turbine combustor.

The preliminary photodiode research has proven the use of low cost light sensors for application to flame studies in the internal combustion engine. This work has already assisted in the choice of light sensors for a novel tomographic heat release visualisation tool for a gas turbine combustor [137], as shown in Figure 12.2. It is suggested that this tomographic work be extended and applied to the internal combustion engine as a low cost, gasket mounted, 2d flame emission visualisation tool.

12.2.3 Spectral Measurements

Initial investigation with the spectral optical probes identified wavelengths of significant light emission. It is proposed that further investigation with higher resolution spectral measurements, should seek to ascertain the correct species for each band of light emission. It is suggested the work presented has proved that sufficient species light emission exists within the chamber to justify an approach such as the use of an image intensified fast frame CCD camera. This would be sufficient for flame imaging, species imaging through narrow pass band filters and also with a diffraction grating to obtain a light spectrum over a short ($\approx$ 5 ns) gating time. The species imaging with such an arrangement meets the spatial resolution requirements, whereas the diffraction grating could meet the temporal resolution requirements.

As a further development, the CCD could be modified to use the fast pixel shift transfer time to record the development of each species at greater than a 1° CA resolution by illuminating only one row of the CCD and using the rest of the CCD as a fast storage area. Such an approach would yield a time resolved emission spectrum of the combustion within one cycle.

12.2.4 Flame Imaging, Flow Visualisation and PIV

The use of the spark plug for flame imaging, flow visualisation and PIV measurements is a unique measurement; however, significant difficulties were experienced with aligning the probe and collection optics. It is highly recommended that a study of precision imaging alignment be performed.

In particular, as CCD cameras are reducing in size, weight and cost, the possibility of mounting the camera close to and attached to the engine should be considered. With such an option available, the choice between a small locally mounted camera and a remotely mounted fibre optic linked camera becomes possible. The obvious advantage of mounting the camera on the engine is reduced losses and simplified optics. The advantages with remote mounting include a wider choice of cameras as size and weight are no longer an issue and the camera can be isolated from the engine vibrations.

An improved version of the optical spark plug that facilitated simpler operation would facilitate its application to multi-cylinder internal combustion engines outside of the research environment. A self-contained combustion imaging package would be useful for diagnostics in engine and combustion development, engine test, and workshop repair.

Finally for flow visualisation and PIV, launching options for the light sheet should be considered including gasket, spark plug and probe mounted systems. In particular,

with laser diodes continually reducing in size and increasing in power, the option of mounting the diode and optics within the gasket itself should be investigated.

12.2.5 Computer Model

The two-zone computer model utilised in Chapter 11 is similar to that used industrially for preliminary investigations of thermal efficiency. It is suggested that the model be adapted in the following ways in order to improve the modelling of this particular engine configuration. This is especially important as the heat flux gauges are developed further to provide heat transfer coefficient measurement. An improved model is essential for investigating the effects of discrepancies between measured and assumed heat coefficient values.

The engine is based on a pent-roof combustion chamber geometry. In order to improve modelling of the side valve design used experimentally, the following points must be addressed:

- The surface area used for heat flux calculation is incorrect. This should be modified to account for the side valve engine configuration
- The rate of burn assumed by the model is observed to be incorrect. Again, this should be modified to account for this particular engine design.

In addition it is suggested that longer duration testing be performed at a fixed engine speed to facilitate improved comparisons between predicted and measured values. The rig configuration did not permit such a test and as a result ensemble averaging over a large number of cycles was not possible. A modification to the method of load application would facilitate such a test. It is also suggested that measurements of air

mass flow and fuel mass flow are performed in order to reduce the unknown model variables. Similarly, measurements or further calculations of residual gas trapping should be performed to again reduce the unknown model variables.

REFERENCES

1. Faraday Partnership Flagship Project (1999) "The Application of Data Fusion to a Multi-Sensored Intelligent Engine." EPSRC grant number MR/48444.
2. R. Stone (1992) *Introduction to Internal Combustion Engines*, The Macmillan Press Ltd, London.
3. C. R. Ferguson & A. T. Kirkpatrick (2001) *Internal Combustion Engines*, Wiley.
4. S. R. Turns (2000) *An Introduction to Combustion*, McGraw Hill.
5. "The plastic car", Department of Materials, Queen Mary College, University of London, (2001) (Website - available at: http://www.materials.qmul.ac.uk/mat604/2001/intro.htm)
6. UPI (1995) "Folgen der Globalen Motorisierung," Internal Report No. 35, Environmental Prognosis Institute (UPI), Heidelberg.
7. A. J. Haagen-Smit (1952) "Chemistry and Psychology of Los Angeles smog" *Ind Engng Chem,* **44**(6), pp. 1342-6
8. N. Docquier & S. Candel (2002) "Combustion control and sensors: a review" *Progress in Energy and Combustion Science,* **28**(2), pp. 107-150
9. A. C. Alkidas (1999) "Combustion-chamber crevices: the major source of engine-out hydrocarbon emissions under fully warmed conditions" *Progress in Energy and Combustion Science,* **25**(3), pp. 253-273
10. BBC News On-line, (2002) "What is the Kyoto treaty?," (Website - available at: http://news.bbc.co.uk/1/hi/world/europe/2233897.stm)
11. UNEP/WMO Information Unit on Climate Change, Geneva Executive Center, Box 356, 1219 Châtelaine, Switzerland, (1994) "Understanding Climate Change: A Beginner's Guide to the UN Framework Convention," (Website - available at: http://unfccc.int/resource/beginner.html)
12. A. G. Gaydon (1957) *The Spectroscopy of Flames*, Chapman & Hall, London.
13. A. G. Gaydon & H. G. Wolfhard (1970) *Flames*, Chapman & Hall, London.
14. S. Cheskis (1999) "Quantitative measurements of absolute concentrations of intermediate species in flames" *Progress in Energy and Combustion Science,* **25**(3), pp. 233-252
15. G. P. Smith, D. M. Golden, M. Frenklach, N. W. Moriarty, B. Eiteneer, M. Goldenberg, C. T. Bowman, R. K. Hanson, S. Song, W. C. Jr. Gardiner, V. V. Lissianski & Z. Qin, (1997) "GRI-Mechanism 3.0 available for download," (Website - available at: http://www.me.berkeley.edu/gri_mech/)
16. H. Soyhan, P. Amneus, T. Lovas, D. Nilsson, P. Maigaard, F. Mauss & C. Sorusbay (2000) "Automatic Reduction of detailed Chemical Reaction

Mechanisms for Autoignition Under SI Engine Conditions". SAE 2000-01-1895, Presented at SAE Journal of Fuels and Lubricants.

17. J. B. Heywood (1988) *Internal Combustion Engine Fundamentals*, McGraw Hill.
18. J. K. Ball, R. R. Raine & C. R. Stone (1998) "Combustion analysis and cycle-by-cycle variations in spark ignition engine combustion - Part 1: an evaluation of combustion analysis routines by reference to model data" *Proceedings of the Institution of Mechanical Engineers Part D- Journal of Automobile Engineering,* **212**(D5), pp. 381-399
19. G. H. Abd Alla (2002) "Computer simulation of a four stroke spark ignition engine" *Energy Conversion and Management,* **43**(8), pp. 1043-1061
20. D. Lee, J. Shakal, S. Goto, H. Ishikawa, H. Ueno & N. Harayama (1999) "Observation of Flame Propagation in an LPG Lean Burn SI Engine" *SAE Journal of Engines,* **108**(3).SAE 1999-01-0570.
21. E.P. Lim (1998) "Temperature and Heat Flux measurements in a Spark Ignition Engine." MSc Thesis, Oxford University.
22. M. Pischinger, W. Salber, F. Staay, H. Baumgarten & H. Kemper (2000) "Benefits of the Electromechanical Valve Train in Vehicle Operation" *SAE Journal of Engines,* **109**(3).SAE 2000-01-1223.
23. S. B. Fiveland & D. N. Assanis (2000) "A Four-Stroke Homogeneous Charge Compression Ignition Engine Simulation for Combustion and Performance Studies" *SAE Journal of Engines,* **109**(3).SAE 2000-01-0332.
24. J. Martinez-Frias, S. M. Aceves, D. L. Flowers, J. Smith & R. Dibble (2000) "HCCI Engine Control by Thermal Management". SAE 2000-01-2869, Presented at SAE Journal of Fuels and Lubricants.
25. J. Olsson, O. Erlandsson & B. Johansson (2000) "Experiments and Simulation of a Six-Cylinder Homogeneous Charge Compression Ignition (HCCI) Engine" *SAE Journal of Engines,* **109**(3).SAE 2000-01-2867.
26. R. H. Stanglmaier & C. E. Roberts (1999) "Homogeneous Charge Compression Ignition (HCCI): Benefits, Compromises, and Future Engine Applications" *SAE Journal of Engines,* **108**(3).SAE 1999-01-3682.
27. G. Kontarakis, N. Collings & T. Ma (2000) "Demonstration of HCCI using a Single Cylinder Four-stroke SI Engine with Modified Valve Timing" *SAE Journal of Engines,* **109**(3).SAE 2000-01-2870.
28. S. M. Aceves, D. L. Flowers, Westbrook C., J. Smith, W. Pitz, R. Dibble, Christensen M. & B. Johansson (2000) "A Multi-Zone Model for the Prediction of HCCI Combustion and Emissions". SAE 2000-01-0327, Presented at SAE Journal of Engines.
29. Z. Chen, M. Konno, M. Oguma & T. Yanai (2000) "Experimental Study of CI Natural-Gas/DME Homogeneous Charge Engine". SAE 2000-01-0329, Presented at SAE Journal of Engines.
30. F. W. Bowditch (1961) "A new tool for combustion research - A Quartz Piston Engine" *SAE Transactions,* **69,** pp. 17-23
31. M. Bakenhus & R. D. Reitz (1999) "Two-Color Combustion Visualisation of Single and Split Injections in a Single-Cylinder Heavy-Duty D.I. Diesel Engine Using an Endoscope-Based Imaging System" *SAE Journal of Engines,* **108**(3).SAE 1999-01-1112.
32. P. Bryanston-Cross, M. Burnett, B. Timmerman, W. K. Lee & P. Dunkley (2000) "Intelligent diagnostic optics for flow visualization" *Optics and Laser Technology,* **32**(7-8), pp. 641-654

33. M. Burnett, D. D. Udrea & P. Dunkley (2001) "Sensors for combustion." Report for INTErSECT, University of Warwick, Coventry.
34. D. D. Udrea (1997) "High Accuracy Flow Velocity Measurements using Particle Image Velocimetry: Development and Applications." PhD Thesis, University of Warwick, Coventry.
35. M. L. G. Oldfield (1990) "Experimental Techniques in Unsteady Flows," Internal Report No. OUEL 1843/90, University of Oxford, Oxford.
36. T. S. Wilson (1998) "Comparison of in-cylinder flows between 30 and 45 degree pentangle combustion chambers." 3rd Yr Project, University of Warwick, Coventry.
37. Dantec, (2002) "Dantec Dynamics," (Website - available at: www.dantecmt.com)
38. M. Tagawa, S. Nagaya & Y. Ohta (2001) "Simultaneous measurement of velocity and temperature in high- temperature turbulent flows: a combination of LDV and a three- wire temperature probe" *Experiments in Fluids,* **30**(2), pp. 143-152
39. A. Cairns & C. Sheppard (2000) "Cyclically Resolved Simultaneous Flame and Flow Imaging in a SI Engine" *SAE Journal of Engines,* **109**(3).SAE 2000-01-2832.
40. T. Obokata, N. Hanada & T. Kurabayashi (1987) "Velocity and Turbulence measurements in a Combustion Chamber of S.I. Engine Under Motored and Firing Operations by L.D.A. with Fiber-Optic Pick-Up". SAE paper 870166, Presented at SAE.
41. B. F. Gajdeczko & F. V. Bracco (1999) "Application of Two-Color Particle Image Velocimetry to a firing Production Direct-Injection Sratified-Charge Engine" *SAE Journal of Engines,* **108**(3).SAE 1999-01-1111.
42. D. D. Udrea, P. J. BryanstonCross, W. K. Lee & M. FunesGallanzi (1996) "Two sub-pixel processing algorithms for high accuracy particle centre estimation in low seeding density particle image velocimetry" *Optics and Laser Technology,* **28**(5), pp. 389-396
43. P. Bryanston-Cross, T. Wilson, P. G. Tucker, Z. Pan, P. Dunkley, D. Udrea & E. L. Hines (1999) In *Optical Diagnostics for Fluids/Heat/Combustion and Photomechanics for Solids,* "Application of fuzzy logic to the automatic processing of particle image velocimetry images of a flow induced by adjacent spinning cylinders" Vol. 3783. SPIE - INT SOC OPTICAL ENGINEERING, Bellingham, pp. 127-130.
44. P. J. BryanstonCross, D. Udrea, W. K. Lee & M. Burnett (1996) In *International Seminar on Optical Methods and Data Processing in Heat and Fluid Flow*, "The application of PIV (particle image velocimetry) to transonic flow measurements: Extracting three-dimensional measurements" Vol. 1996. MECHANICAL ENGINEERING PUBL, Edmunds, pp. 169-178.
45. E. L. Hines, D. D. Udrea, T. Wilson, P. Dunkley, M. Burnett & P. J. Bryanston-Cross (1999) "Application of fuzzy logic and neural networks to the automatic determination 2 and 3 dimensional PIV velocity distributions" *SPIE 44th General Meeting,* (Technical Conference 3783: Optical Diagnostics for Fluids/Heat/Combustion and Photomechanics for Solids)
46. D. D. Udrea, P. J. BryanstonCross, C. Driver, G. Calvert, E. Bennett, B. Black, S. Coats, J. Elworthy, B. Furlonger, K. Kirwan, A. Lee, J. Metcalfe & N. Todd (1997) In *New Image Processing Techniques and Applications: Algorithms, Methods, and Components II*, "The application of PIV (Particle

Image Velocimetry) and flow visualisation to the coolant flow through an automotive engine" Vol. 3101. SPIE - INT SOC OPTICAL ENGINEERING, Bellingham, pp. 221-226.

47. D. D. Udrea, C. Driver & G. Calvert (1998) In *International Conference on Optical Methods and Data Processing in Heat and Fluid Flow*, "The application of particle image velocimetry (PIV) and flow visualization to the coolant flow through an automotive engine" Vol. 1998. PROFESSIONAL ENGINEERING PUBLISHING LTD, Bury St Edmunds, pp. 343-350.
48. LaVision, (2002) (Website - available at: www.lavision.de and www.piv.de)
49. M. Ronnback, W. X. Le & J. R. Linna (1991) "Study of Induction Tumble by Particle Tracking Velocimetry in a 4-Valve Engine". SAE paper 912376, Presented at SAE.
50. A. Stella, G. Guj, J. Kompenhans, M. Raffel & H. Richard (2001) "Application of Particle Image Velocimetry to combusting flows: design considerations and uncertainty assessment" *Experiments in Fluids,* **20,** pp. 167-180
51. J. Hartmann, J. Kohler, W. Stolz & H. H. Flogel (1996) "Evaluation of instationary flow fields using crosscorrelation in image sequences" *Experiments in Fluids,* **20**(3), pp. 210-217
52. P. Calendini, T. Duverger, A. Lecerf & M. Trinite (2000) "In-Cylinder Velocity Measurements with Stereoscopic Particle Image Velocimetry in a SI engine". SAE 2000-01-1798, Presented at SAE Journal of Fuels and Lubricants.
53. W. Choi & Y. G. Guezennec (1999) "Study of the Flow Field Development During the Intake Stroke in an IC Engine Using 2-D PIV and 3-D PTV" *SAE Journal of Engines,* **108**(3).SAE 1999-01-0957.
54. M. Reeves, D. P. Towers, B. Tavender & C. H. Buckberry (1999) "A high-speed all-digital technique for cycle-resolved 2-D flow measurement and flow visualisation within SI engine cylinders" *Optics and Lasers in Engineering,* **31**(4), pp. 247-261
55. K. R. Kunkulagunta (2000) "Video Imaging and Analysis of Common Rail Sprays in an Optical Engine using Shadowgraphy Technique" *SAE Journal of Engines,* **109**(3).SAE 2000-01-1255.
56. L. Gillespie, M. Lawes, C. Sheppard & R. Woolley (2000) "Aspects of Laminar and Turbulent Burning Velocity Relevant to SI Engines". SAE 2000-01-0192, Presented at SAE Journal of Engines.
57. R. D. Reitz & C. J. Rutland (1996) "Development and testing of diesel engine CFD models" *Fuel and Energy Abstracts,* **37**(1), pp. 42
58. T. Yoshinaga, T. Igashira, H. Kawai & N. Nakamura (1995) "Research on formation and growth of flame kernel in spark ignition engine" *JSAE Review,* **16**(1), pp. 7-11
59. Y. Fukano, H. Hisaki, S. Kida & T. Kadota (1999) "In-Cylinder Combustion in a Natural Gas Fueled Spark Ignition Engine Probed by High Speed Schlieren Method and its dependence on Engine Specifications" *SAE Journal of Fuels and Lubricants,* **108**(4).SAE 1999-01-1493.
60. A. Asseban, M. Lallemand, J-B. Saulnier, N. Fomin, E. Lavinskaja, W. Merzkirch & D. Vitkin (2000) "Digital speckle photography and speckle tomography in heat transfer studies" *Optics & Laser Technology,* **32**(7-8), pp. 583-592

61. A. Hultqvist, M. Christensen, B. Johansson, A. Franke, M. Richter & M. Alden (1999) "A study of the Homogeneous Charge Compression Ignition Combustion Process by Chemiluminescence Imaging" *SAE Journal of Engines,* **108**(3).SAE 1999-01-2680.
62. C. Kaminski, J. Hult, J. Nygren, A. Franke, M. Alden, S. Lindenmaier, A. Dreizler, U. Maas & R. Williams (2000) "Development of High Speed Spectroscopic Imaging Techniques for the Time Resolved Study of Spark Ignition Phenomena". SAE 2000-01-2833, Presented at SAE Journal of Fuels and Lubricants.
63. M. J. Hall & P. Zuzek (2000) "Fiber Optic Sensor for Time-Resolved Measurements of Exhaust Gas Recirculation in Engines". SAE 2000-01-2865, Presented at SAE Journal of Fuels and Lubricants.
64. M. Hilton & A. H. Lettington (1997) "Application of FTIR Spectroscopy to Measurement of Gas Turbine Engine Exhaust Emissions", pp. 8. Presented at Advisory Group for Aerospace Research & Development; Propulsion and Energetics Panel; Advanced non-intrusive instrumentation for propulsion engines, AGARD; 1998, Brussels.
65. B. Lawton & G. Klingenberg (1996) *Transient Temperature in Engineering and Science*, Oxford University Press, Oxford, UK.
66. V. Aust, G. Zimmermann, P-W. Manz & W. Hentschel (1999) "Crank-Angle Resolved Temperature in SI Engines Measured by Emission-Absorption Spectroscopy" *SAE Journal of Fuels and Lubricants,* **108**(4).SAE 1999-01-3542.
67. A. E. M. Barrag & B. Lawton (1993) "Computer Optical Tomography in the Study of Internal Combustion Engine Soot Concentration", pp. 423-430. 93EN061, Presented at Automotive technology and automation The motor vehicle and the environment - demands of the nineties and beyond, Croydon; Automotive Automation Ltd; 1993, Aachen; Germany.
68. M. C. Burrows, S. Shimizu, P. S. Myers & O. A. Uyehara (1961) "The measurement of unburned Gas Temperatures in an engine by an Infrared Radiation Pyrometer" *SAE Transactions,* **69,** pp. 514-528
69. C. R. Stone, E. P. Lim, P. Ewart, G. Lloyd & R. Williams (2000) "Temperature and Heat Flux measurements in a Spark Ignition Engine" *SAE Journal of Engines,* **109**(3).SAE 2000-01-1214.
70. A. C. Eckbreth (1996) *Laser Diagnostics for Combustion Temperature and Species*, Gordon & Breach Science Publishers, Amsterdam.
71. B. Grandin, I. Denbratt, J. Bood, C. Brackmann & P. Bengtsson (2000) "The effect of Knock on the Heat Transfer in an SI Engine: Thermal Boundary Layer Investigation using CARS Temperature Measurements and Heat Flux Measurements" *SAE Journal of Engines,* **109**(3).SAE 2000-01-2831.
72. B. Grandin & I. Denbratt (2002) "The Effect of Knock on Heat Transfer in SI Engines". SAE paper 2002-01-0238, Presented at SAE 2002 World Congress, SAE, Detroit, MI.
73. M. Haste (2000) "An Investigation of In-Cylinder Flow and Combustion in a Spark Ignition Engine using Particle Image Velocimetry." PhD Thesis, Loughborough University.
74. E. Winklhofer & H. Fuchs (1996) "Laser Induced Fluorescence and Flame Photography--tools in Gasoline Engine Combustion Analysis" *Optics and Lasers in Engineering,* **25**(6), pp. 379-400

75. N. Georgiev & M. Alden (1997) "Developments of laser-induced fluorescence for two-dimensional multi-species imaging in flames" *Spectrochimica Acta Part B: Atomic Spectroscopy,* **52**(8), pp. 1105-1112
76. R. Marsh (2000) "MRes Report." MRes Thesis, University of Warwick, Coventry.
77. T-M. Liou (2001) "Some applications of experimental and numerical visualization in fluid flow, heat transfer, and combustion" *Experimental Thermal and Fluid Science,* **25**(6), pp. 359-375
78. P. O. Witze, M. J. Hall & J. S. Wallace (1988) "Fiber-Optic Instrumented Spark Plug for Measuring Early Flame Development in Spark Ignition Engines". SAE paper 881638, Presented at SAE.
79. AVL, "AVL- Powertrain Engineering, Advanced Simulation, Instrumentation and Test Systems," (Website - available at: http://www.avl.com/)
80. C Nwagboso & M. Pendlebury (2001) "Kinematics of fibre optics sensory systems for control of a natural gas engine" *Proceedings of the I MECH E Part D Journal of Automobile Engineering,* **215**(D), pp. 713-723
81. M. Christensen, A. Hultqvist & B. Johansson (1999) "Demonstrating the Multi Fuel Capability of a Homogeneous Charge Compression Ignition Engine with Variable Compression Ratio" *SAE Journal of Engines,* **108**(3).SAE 1999-01-3679.
82. C. Mobley (1999) "Non-Intrusive In-Cylinder Pressure Measurement of Internal Combustion Engines" *SAE Journal of Engines,* **108**(3).SAE 1999-01-0544.
83. H.S. Rai, M. F. J Brunt & C.P Loader (1999) "Quantification and reduction of IMEP Errors Resulting from Pressure Transducer Thermal Shock in an S.I. Engine" *SAE Journal of Engines,* **108**(3).SAE 1999-01-1329.
84. P. Tobias, P. Martensson, A. Goras, I. Lundstrom & A. L. Spetz (1999) "Moving gas outlets for the evaluation of fast gas sensors" *Sensors and Actuators B-Chemical,* **58**(1-3), pp. 389-393
85. A. C. Alkidas, P. V. Puzinauskas & R. C. Peterson (1990) "Combustion and Heat Transfer Studies in a Spark-Ignited Multivalve Optical Engine". SAE paper 900353, Presented at SAE.
86. A. E. Catania, D. Misul, A. Mittica & E. Spessa (2000) "Unsteady Convection Model for Heat Release Analysis of IC Engine Pressure Data" *SAE Journal of Engines,* **109**(3).SAE 2000-01-1265.
87. A. Franco & L. Martorano (1999) "Methods to evaluate In-Cylinder Heat Transfer and Thermal Load in the Small Internal Combustion Engines" *SAE Journal of Engines,* **108**(3).SAE 1999-01-1252.
88. B. Donkin (1894) "Temperature of cylinder walls" *Railway Review,* **34**(558)
89. E. G. Coker & W. A. Scoble (1913) "Cyclic Changes in Temperature in a Gas-Engine Cylinder" *Proceedings of the Institution of Civil Engineers,* **196**(2)
90. W. Nusselt (1914) "Der Warmeubergang in der Gasmaschine" *Zeitschrift der Vereines Deutscher Ingenieure,* **58**(1)
91. G. Eichelberg (1939) "Some New Investigations on Old Combustion-Engine Problems" *Engineering,* **148**
92. G. Woschni (1967) "A Universally Applicable Equation for the Instantaneous Heat Transfer Coefficient in the Internal Combustion Engine" *SAE Transactions.*SAE 670931.
93. V. D. Overbye, J. E. Bennethum, O. A. Uyehara & P. S. Myers (1961) "Unsteady Heat Transfer in Engines" *SAE Transactions,* **69,** pp. 461-494

94. TC Ltd. (2002) *Guide to Thermocouple and resistance Thermometry*, TC Ltd., PO Box 130, Uxbridge, England.
95. L. J. Forney & G. C. Fralick (1994) "Two wire thermocouple: Frequency response in constant flow" *Review of scientific instruments,* **65**(10), pp. 3252
96. L. J. Forney, E. L. Meeks, J. Ma & G. C. Fralick (1993) "Measurement of frequency response in short thermocouple wires" *Review of scientific instruments,* **64**(5), pp. 1280
97. NANMAC, (Website - available at: www.nanmac.com)
98. K. Huber, G. Woschni & K. Zeilinger (1990) "Investigations on Heat Transfer in Internal Combustion Engines under Low Load and Motoring Conditions". SAE paper 905018, Presented at SAE.
99. P. J. Shayler, S. A. May & T. Ma (1993) "The Determination of Heat Transfer from the Combustion Chambers of SI engines". SAE paper 931131, Presented at SAE.
100. J. A. Gatowski, M. K. Smith & A. C. Alkidas (1989) "An Experimental Investigation of Surface Thermometry and Heat- Flux" *Experimental Thermal and Fluid Science,* **2**(3), pp. 280-292
101. D. R. Buttsworth (2002) "Transient Response of an Erodable Heat Flux Gauge using Finite Element Analysis" *Proceedings of the I MECH E Part D Journal of Automobile Engineering,*
102. D. J. O. Nijeweme, J. B. W. Kok, C. R. Stone & L. Wyszynski (2001) "Unsteady in-cylinder heat transfer in a spark ignition engine: experiments and modelling" *Proceedings of the Institution of Mechanical Engineers Part D-Journal of Automobile Engineering,* **215**(D6), pp. 747-760
103. Y. Harigaya, F. Toda & M. Suzuki (1993) "Local Heat Transfer on a Combustion Chamber Wall of a Spark-Ignition Engine". SAE paper 931130, Presented at SAE.
104. A. C. Alkidas (1980) "Heat Transfer Characteristics of a Spark-Ignition Engine" *ASME Journal of Heat Transfer,* **102**(2), pp. 189-193
105. A. C. Alkidas & J. P. Myers (1982) "Transient Heat-Flux Measurements in the Combustion Chamber of a Spark-Ignition Engine" *ASME Journal of Heat Transfer,* **102**(4), pp. 62-67
106. A. Ishii, H. Nagano, K. Adachi, S. Kimura, M. Koike, N. Iida, H. Ishii & Y. Enomoto (2000) "Measurement of Instantaneous Heat Flux Flowing into Metallic and Ceramic Combustion Chamber Walls" *SAE Journal of Engines,* **109**(3).SAE 2000-01-1815.
107. A. Wimmer, R. Pivec & T. Sams (2000) "Heat Transfer to the Combustion Chamber and Port Walls of IC Engines - Measurement and Prediction", pp. 101-116. SAE Paper 2000-01-0568, Presented at Modeling of SI engines, Society of Automotive Engineers; 2000, Detroit, MI.
108. K.S. Chana, T. S. Wilson, M. Burnett, P.J. Bryanston-Cross & T.V. Jones (2001) "High-bandwidth heat-transfer measurements in an internal combustion engine under low load and motored conditions". Presented at the Applied Vehicle Technology Panel: Symposium on Advanced Flow Management, Leon, Norway.
109. T. S. Wilson, P. Bryanston-Cross, K. S. Chana, P. Dunkley, T. V. Jones & P. Hannah (2002) *Combustion & Flow Diagnostics (Part A&B).* "High Bandwidth Heat Transfer and Optical Measurements in an instrumented Spark Ignition Internal Combustion Engine". SAE paper 2002-01-0747, Presented at SAE 2002 World Congress, SAE, Detroit.

110. P. Gilaber & P. Pinchon (1988) "Measurements and Multidimensional Modeling of Gas-Wall Heat Transfer in a S.I. Engine". SAE paper 880516, Presented at SAE.
111. W-D. Bauer, J. Wenisch & J. B. Heywood (1998) "Averaged and time-resolved heat transfer of steady and pulsating entry flow in intake manifold of a spark-ignition engine" *International Journal of Heat and Fluid Flow,* **19**(1), pp. 1-9
112. D. R. Buttsworth & M. C. Wright "Observations of Combustion in a Spark Ignition Engine Using Transient Heat Flux Measurements"
113. C. D. Rakopoulos & G. C. Mavropoulos (2000) "Experimental instantaneous heat fluxes in the cylinder head and exhaust manifold of an air-cooled diesel engine" *Energy Conversion and Management,* **41**(12), pp. 1265-1281
114. C. D. Rakopoulos, G. C. Mavropoulos & D. T. Hountalas (2000) "Measurements and analysis of load and speed effects on the instantaneous wall heat fluxes in a direct injection air-cooled diesel engine" *International Journal of Energy Research,* **24**(7), pp. 587-604
115. E. Weisstein, Wolfram Research, "Eric Weissteins's World of Physics," (Website - available at: http://scienceworld.wolfram.com/physics/)
116. New Mexico Solar Energy Association, "Energy Physics Primer," (Website - available at: http://www.nmsea.org/Curriculum/Primer/how_is_energy_transferred.htm)
117. Fuel Cell Store, (Website - available at: http://www.fuelcellstore.com/)
118. D.L. Schultz & T.V. Jones (1973) "Heat transfer measurements in short duration hypersonic facilities" *NATO 1973,* (AGARDOGRAPH 165)
119. S. M. Guo, C. C. Lai, T. V. Jones, M. L. G. Oldfield, G. D. Lock & A. J. Rawlinson (1998) "The application of thin-film technology to measure turbine-vane heat transfer and effectiveness in a film-cooled, engine-simulated environment" *International Journal of Heat and Fluid Flow,* **19**(6), pp. 594-600
120. S. M. Guo, C. C. Lai, T. V. Jones, M. L. G. Oldfield, G. D. Lock & A. J. Rawlinson (2000) "Influence of surface roughness on heat transfer and effectiveness for a fully film cooled nozzle guide vane measured by wide band liquid crystals and direct heat flux gages" *Journal of Turbomachinery-Transactions of the Asme,* **122**(4), pp. 709-716
121. S. M. Guo, M. C. Spencer, G. D. Lock & T. V. Jones (1995) "The Application of Thin Film Gauges on Flexible Plastic Substrates to the Gas Turbine Situation", pp. ALL. Presented at Gas turbine and aeroengine, ASME; 1995, Houston; TX.
122. E. Piccini, S. M. Guo & T. V. Jones (2000) "The development of a new direct-heat-flux gauge for heat-transfer facilities" *Measurement science & technology,* **11 Part 4,** pp. 342-349
123. A. Hofeldt (1993) "Thin Film Techniques and Turbulent Spot Studies." First Year Report, Oxford University.
124. S. M. Guo (1994) "Thin Film Instrumentation on Plastic Substrates and Applications to Aerodynamics." First Year Report, Oxford University.
125. M. L. G. Oldfield (2000) "Guide to Impulse Response Heat Transfer Signal Processing," Internal Report No. 2233/2000, University of Oxford, Oxford.
126. A. Attenborough (1994) *Engineering Mathematics Exposed*, McGraw-Hill, Berkshire.

127. J.E. Doorly & M.L.G. Oldfield (1997) "The theory of advanced multi-layer thin film heat transfer gauges" *International Journal of Heat and Mass Transfer*, **30**(6), pp. 1159-1168
128. Science Joy Wagon, (1999) "Image Formation - Ray tracing basics," (Website - available at: www.sciencejoywagon.com)
129. E. Hecht (1997) *Optics*, Addison-Wesley.
130. A. Picarelli (2001) "MSc Report." MSc Thesis, University of Warwick, Coventry.
131. IPL, "Integrated Photomatrix," (Website - available at: www.ipl-uk.com)
132. D. R. Buttsworth (2001) "Spark Ignition Internal Combustion Engine Modelling using Matlab," Internal Report No. TR-2001-02, University of Southern Queensland, Toowoomba, Austrialia.
133. C. R. Ferguson (1985) *Internal Combustion Engines (1st Ed)*, Wiley.
134. C. Olikara & G.L. Borman (1975) "A Computer Program for Calculating Properties of Equilibrium Combustion Products with Some Applications to I.C. Engines". SAE 750468, Presented at, SAE.
135. (1971) *JANAF Thermochemical Tables*, NSRDS-N35 37, National Bureau of Standards, Washington D.C.
136. K. Chana (2002) Patent pending.
137. P. Dunkley (2002) "The investigation and application of OET (Optical Emission Tomography) as a combustion diagnostic." PhD Thesis, University of Warwick.
138. D. R. Buttsworth & T. V. Jones (1997) "Transient thin film heat flux measurements with finite film thickness" Ed. A. F. P. Houwing. pp. 477-482. Presented at Shock waves, Fyshwick; Panther Publishing; 1997.

APPENDICES

APPENDICES

APPENDIX A

TEST FACILITY

13.1 Overview

To facilitate the combustion investigations and the development of instrumentation, a special engine test cell was built; this test cell accommodates various engine ancillaries as well as the data acquisition units. The emphasis has been to build a self-contained, 'bench top' test environment for instrumentation development, not an industrial 'engine development' cell. Below, each item is described.

13.2 Choice of Engine

As the internal combustion engine has been identified as the source of combustion it is necessary to not only choose one of the many engines available, but to also build this engine into a test cell that is not only safe to use, but also simple and logical to operate while maintaining versatility.

Access to the combustion chamber in an internal combustion engine is not always easy. Often getting past the coolant jacket, oil supply rails, timing mechanism, adjacent cylinders and the valves is not a trivial task. Added to this the decision to use a four stroke engine and the job becomes harder. For these reasons it was decided to use a commercially available side valve engine from Briggs and Stratton. This engine

is air cooled, thus dispenses with the coolant jacket, has only one cylinder, dispensing with access problems due to adjacent cylinders and the inter-cylinder air and fuel supply effects, and being a side valve engine allows convenient access to the cylinder head, allowing easy removal, replacement and instrumentation.

The use of this configuration of engine is satisfactory, as it has no negative effect on the variables investigated. The engine is to be used only as a test bed for the developing, testing and implementation of instrumentation, it is not intended that the results from this engine are to be used in the development of a typical internal combustion engine (typically overhead valve). Rather, what is more important is that the temperatures and pressures encountered during combustion are realistic and comparable to the conditions encountered in a more conventional engine.

With these concerns satisfied, it was decided to use a Briggs and Stratton 92232 engine, with 65mm bore, 44mm stroke, 6:1 compression ratio and 146 cm^3 engine capacity. The engine is modified to operate on either Natural gas or unleaded petrol, and is built into a test cell that allows the user to motor, fire, load and stop the engine from a control panel, as well as choose the fuel supply and engine operating speed required. Each of the connected ancillaries are now discussed.

13.3 Connected Ancillaries

The small engine chosen was built into a user-friendly test cell. This test cell accommodated such requirements as the ability to switch fuel, start, control sparking and load of the engine as well as being safe. Below each of the ancillaries attached to the engine are discussed.

13.3.1 Generator

A Clarke power electrical generator rated at 1.5 KVA is used to apply a load to the engine. It is important as one seeks to test and develop instrumentation, to be able to test at temperatures and pressures higher than that of an idling engine; this is achieved with the load applied with the generator.

13.3.2 Starter Motor

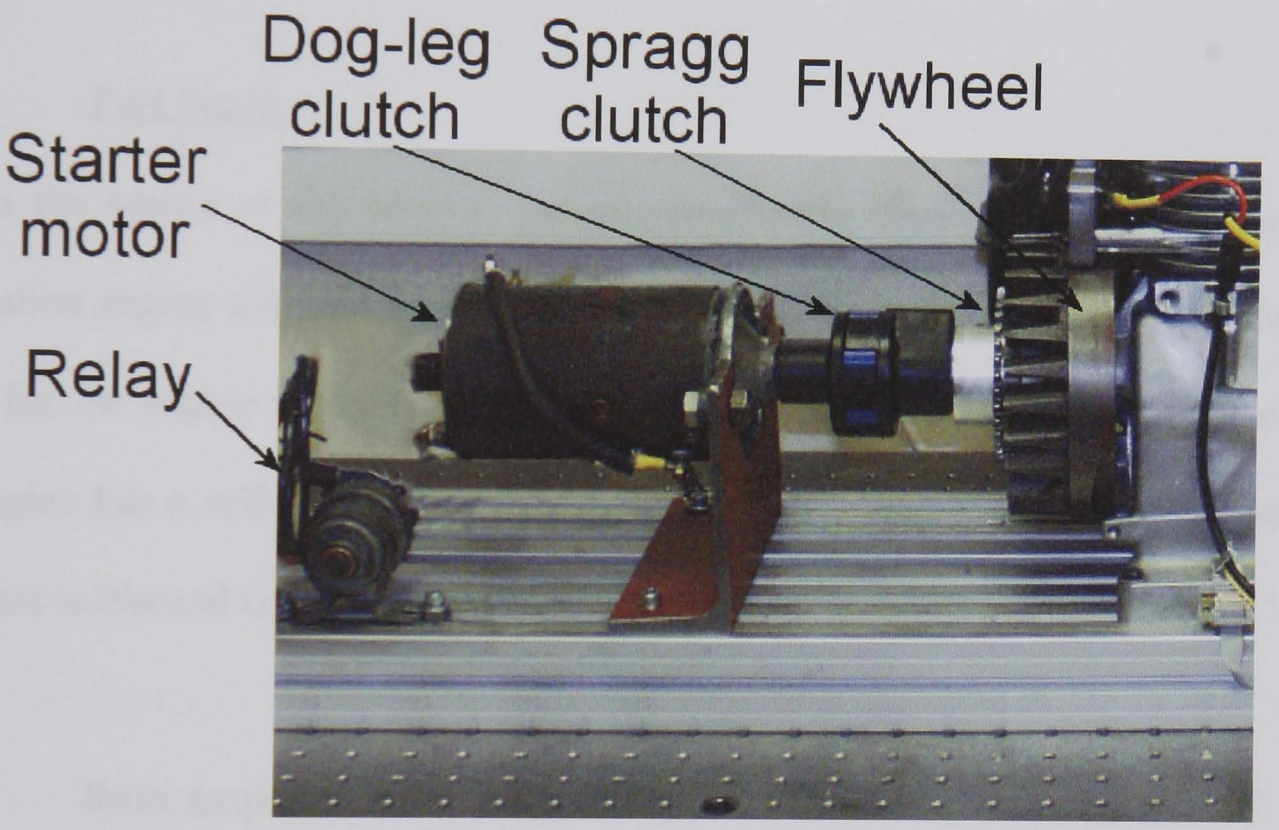

Figure 13.1, Photo of rig starting system.

The Briggs and Stratton engine used comes as standard with a pull cord starter. This is an unacceptable method for regularly and consistently starting an engine. In addition leaves no possibility for investigating flows and sensor evaluation during a motored phase. For this reason the engine was modified to accept a motorcycle (spragg) clutch, a dog-leg clutch, followed by a commercially available Rover starter motor, as shown in Figure 13.1. The starter motor operates with power supplied from a high current 12

volt battery in order to be isolated from the mains power supply, and is triggered through a heavy duty 12 volt relay.

13.3.3 Exhaust

A safe, adequate and reliable exhaust extraction system is an essential requirement for operating an internal combustion engine indoors. PlymoVent fitted such a system that extracts the exhaust gases after they had gone through a silencer and length of copper pipe designed to allow some cooling of the gas before extraction.

13.3.4 Fuel Supply

Due to the nature of the project, the instrumentation developed using the internal combustion engine will find application in the gas turbine market. For this reason the ability for the engine to operate on either Natural Gas or unleaded fuel is essential. The engine has a self-contained 1-litre liquid fuel tank, plus a low pressure gas line that pipes in Natural Gas. It is possible to select the use of either source.

13.4 Data Acquisition

A DT eight channel (expandable to 32 channels), BEDO analogue to digital converter (A2D) with a maximum sapling freq of 1.25MHz was used for data capture. The A2D card was installed in a Dale 333Mhz PC running Windows NT 4.0 operating system, the PC was expanded to 450Mbytes of RAM. The user interface was programmed in Labview, a graphical programming language purchased from National Instruments, which facilitated each of the data acquisition requirements. An electronic 50kHz anti-aliasing filter was employed when sampling.

13.5 Thin Film Gauges

Internal combustion engine measurements are a novel application of the direct-heat-flux gauges (DHFG) [108,109,119-122,125,127,138] described. Developed at Oxford University for the measurement of surface temperature and the determination of heat transfer on gas turbine nozzle guide vanes tested in the Oxford Cold Heat Transfer Tunnel, they are here used to make similar measurements within the combustion zone of an internal combustion engine. They comprise of thin platinum resistance thermometers mounted on an insulating layer bonded to the metal of the piston or cylinder head. The temperature of the metal is measured from sparsely fitted thermocouples mounted close to the surface. Since the metal is of high conductivity and there exists a low spatial variation, few thermocouples are required to accurately determine the metal temperature.

13.5.1 Principals of Thin Film Gauges

The gauge measures the heat flux across an insulating layer by measuring the top surface temperature employing a sputtered thin-film gauge (TFG) and the metal temperature below, using a thermocouple. The TFGs are platinum temperature sensors with a physical thickness less than 0.1μm, width 100μm and length around 2mm. The electrical resistance of the TFG metal sensor changes linerally with temperature within a given temperature range. The gauge is operated in constant currant mode, where a small constant sensing current is passed through the TFG in order to generate a change in voltage proportional to the change in sensor resistance and temperature. The thermal mass of the thin-film gauge is usually negligible, however may be taken into account if required [138], and so the surface temperature history is determined from the resistance-temperature relationship.

The thermal properties of the DHFG and the ratio of the thickness over the thermal conductivity of the insulating layer have been calibrated, in order that from the temperature traces from above and below the insulating layer, it is possible to determine the heat flux. For further information on the process calibration and analysing the temperature traces see Chapter 5, Heat Flux Theory.

13.5.2 Construction and Application

The platinum TFG is sputtered onto the top side of a flexible 50μm polymide insulating layer (Uplilex-s) and a thermocouple is located as near as possible to the metal surface on the bottom side of this insulating layer. Owing to the high thermal conductivity of the metal, the thermocouple provides an accurate measurement of the metal surface temperature. The TFG is adhesively bonded to the test model using a glue layer (3M VHB 9460) of 20μm thickness on top of the thermocouple.

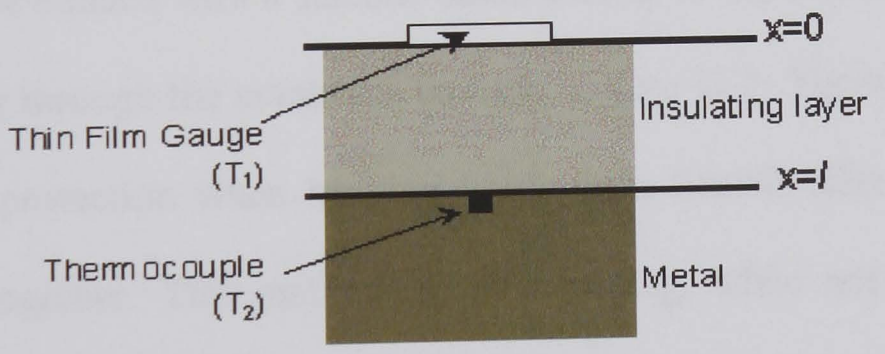

Figure 13.2, Schematic diagram of the DHFG.

Figure 13.2 shows the cross section of the DHFG with the layer ($0 < x < l$). The combined Upilex-plus-glue layer is treated as one homogeneous layer because the thermal properties are very similar. Instrumentation is applied to the insulating layer.

Low resistance flexible wire is soldered to the sputtered platinum on the exposed thin film surface, before passing though the surface to be routed below the metal.

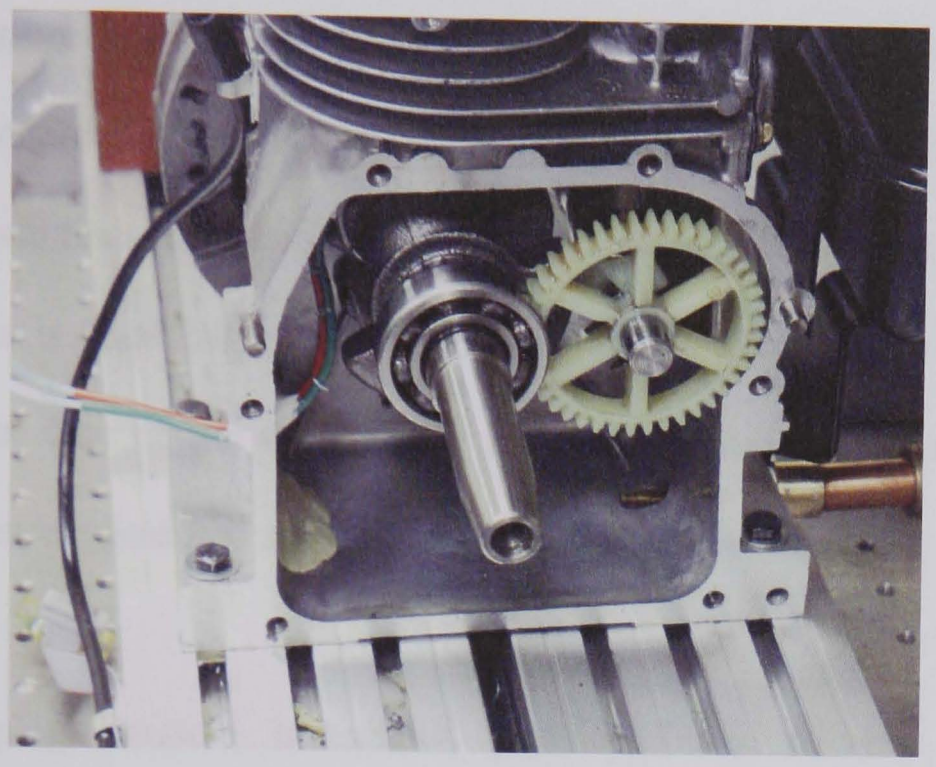

Figure 13.3, Photo showing DHFG wire routing.

Wires for the gauges mounted on the cylinder head simply pass though access holes machined through the head, later sealed with epoxy resin, however wiring on the piston proved trickier. Gauges were mounted on the piston surface in the normal manner, then were bonded with a silicone based sealant to the conrod, before hanging freely and passing through the crankcase housing, Figure 13.3. The wires were offered some degree of protection when hanging freely from flexible silicone tubing which held the wires together. This method of wire routing, while not robust and long lasting, was preferred to using slip rings or similar due to the increased simplicity of instrumentation and the reduced possibility of noise being picked up.

13.6 Other Measuring Devices

An important aspect of engine testing is the ability to accurately measure and record standard engine data, eg. Cylinder pressure and crank angle in order to compare

results between runs and validate with known values and results from other researchers.

13.6.1 Pressure

One of two standard Kistler piezo pressure transducers, models 6117A46 or 6052A1 is used at any one time to record the gas pressure within the cylinder. A Kistler 5001 charge amplifier is used before the signals are sampled with the DT BEDO A2D described above. One of the channels on the A2D is always kept available for the pressure so it can be measured simultaneously to the data of interest.

Kistler spark plug pressure transducer, part 6117A46, contains a small piezo transducer mounted within the spark plug. This arrangement facilitated convenient pressure measurement within any of small engines with no modification to either cylinder or head. The sensitivity (4 ρC/bar) and natural frequency (120 kHz) are both sufficiently high to provide accurate pressure measurements with no lost information. Unfortunately this arrangement caused a small amount of noise from the spark to affect some results so an alternative pressure transducer was used for some tests.

Kistler pressure transducer 6052A1, is a small screw thread pressure transducer calibrated with a dead weight and used to measure the pressure of combustion during the heat flux runs. This transducer gave similar measurements to the spark plug transducer, with the advantage of not introducing noise to the measurements. The sensor has a sensitivity of 19 ρC/bar and a natural frequency of 130 kHz.

13.6.2 Crank Index

The encoder is an essential item of instrumentation as it effectively provides a time signal, recording at which part of the engine cycle the measurements are taken. Either one of two engine crank encoders can be used at any time on the engine. Initial engine tests utilised a HP part number HEDS-5640C06 encoder, however this was later replaced with an industrial EOS 58AA-B18AC1DA1 N2400 encoder that provides higher resolution, increased accuracy and greater life expectancy. Two outputs from the Hengstler gauge can be used. First a once per revolution TTL signal, or alternatively a 2400 pulses per revolution TTL signal. Using the second signal enables triggering the A2D at 0.15° CA intervals, this allows sampling relative to CA, as opposed to time. Each sampling method has advantages depending on circumstances.

13.7 Testing Sequence

The configuration of the engine and its ancillaries provides the operator the ability to make measurements on a motored or fired engine. By activating the starter motor the engine is brought up to a speed of approximately 1300 RPM with or without the spark operating, and with or without the fuel supply. Once both fuel and spark are activated, the engine will start and begin fired operation.

During firing the operator can select if an engine load is required, if so, a variable electrical load may be applied. Application of a load on the engine will reduce the engine speed for a given throttle position, increase in-cylinder pressure, and increase the light emission of the flame.

The A2D may be configured to either start sampling at the first top dead centre (TDC) piston position when the operator first starts to motor the engine, and will record for a predetermined number of samples at a given sampling rate; alternatively the A2D can sample at a predefined crank angle interval.

13.8 Problems Encountered

Most aspects of the engine and its operation functioned correctly with no problems, however the DHFGs were troublesome in two regards.

Firstly, the soldered junctions failed after only a few engine runs, this was due to the low melting point solder used to attach the low resistance wire. This was corrected when the piston was re-instrumented with new gauges by protecting the soldered joints with an additional adhesive layer of Upilex. After this simple modification no further problems were noted.

Secondly, the wires running between the piston gauges and the exterior of the engine would fail after approximately 50 engine runs, equating to around one hour of constant use. Although an inconvenience, this was acceptable since not only is this sufficient time to record all the data required at any one engine build, but also problems with alternative wire routing methods were avoided

APPENDIX D

MATLAB DE-WARPING ALGORITHM

(Author: Richard Marsh [76])

Method

1. Load in the image (all images must be square, i.e. have the same number of vertical and horizontal raster lines.)
2. Convert the image into an n ´ n matrix; where n is the number of pixels per raster line.
3. Start at the first grey level co-ordinate (1,1).
4. Calculate the distance from the centre of the image to this pixel. The centre of the image is located at (n/2, n/2). A simple Pythagorean calculation.
5. Look up the amount of shift required from the 'shift vector'. Calculate the new values of x and y for this pixel.
6. Assign the grey level at this point to its new co-ordinates.
7. Repeat steps 4, 5 and 6 for the whole matrix.
8. When finished, output the matrix as an image.

```
phi=imread('chess.tif','tiff');
load rad3.out;
rad=rad3;
n=1340;                          %size of image (must be square!!!)

%-----------------------------------------------------------------
cx=-670;
for i=1:669;
      cx=cx+1;
      cy=-670;
      for j = 1:1340;
            cy=cy+1;
            r=round((((i-670)^2)+(j-670)^2)^0.5);
            if r<=670
            phin(i,j)=phi(ceil(cx/rad(r))+500,ceil(cy/rad(r))+500);
            end;
      end;
end;
for i=671:1339;
      cx=cx+1;
      cy=-670;
      for j = 1:1340;
            cy=cy+1;
            r=round((((i-670)^2)+(j-670)^2)^0.5);
            if r<=670;
            phin(i,j)=phi(ceil(cx/rad(r))+500,ceil(cy/rad(r))+500);
            end;
      end;
end;
%-----------------------------------------------------------------
%imshow(phi)
%figure(2);
%imshow(phin)
imwrite(phin,'chessout.jpg','jpg');
```

APPENDIX E

'OH' (308 NM) FILTER CALIBRATION

Shown below is the calibration chart of the filter used for measuring the 'OH' emission of the flame front. The 'OH' radical is known to emit at 308 nm, the calibration below shows this filter is centred on 307.6 nm and has a bandpass of 10.8 nm at 50% transmission.

APPENDIX E
'OH' (308 nm) FILTER CALIBRATION

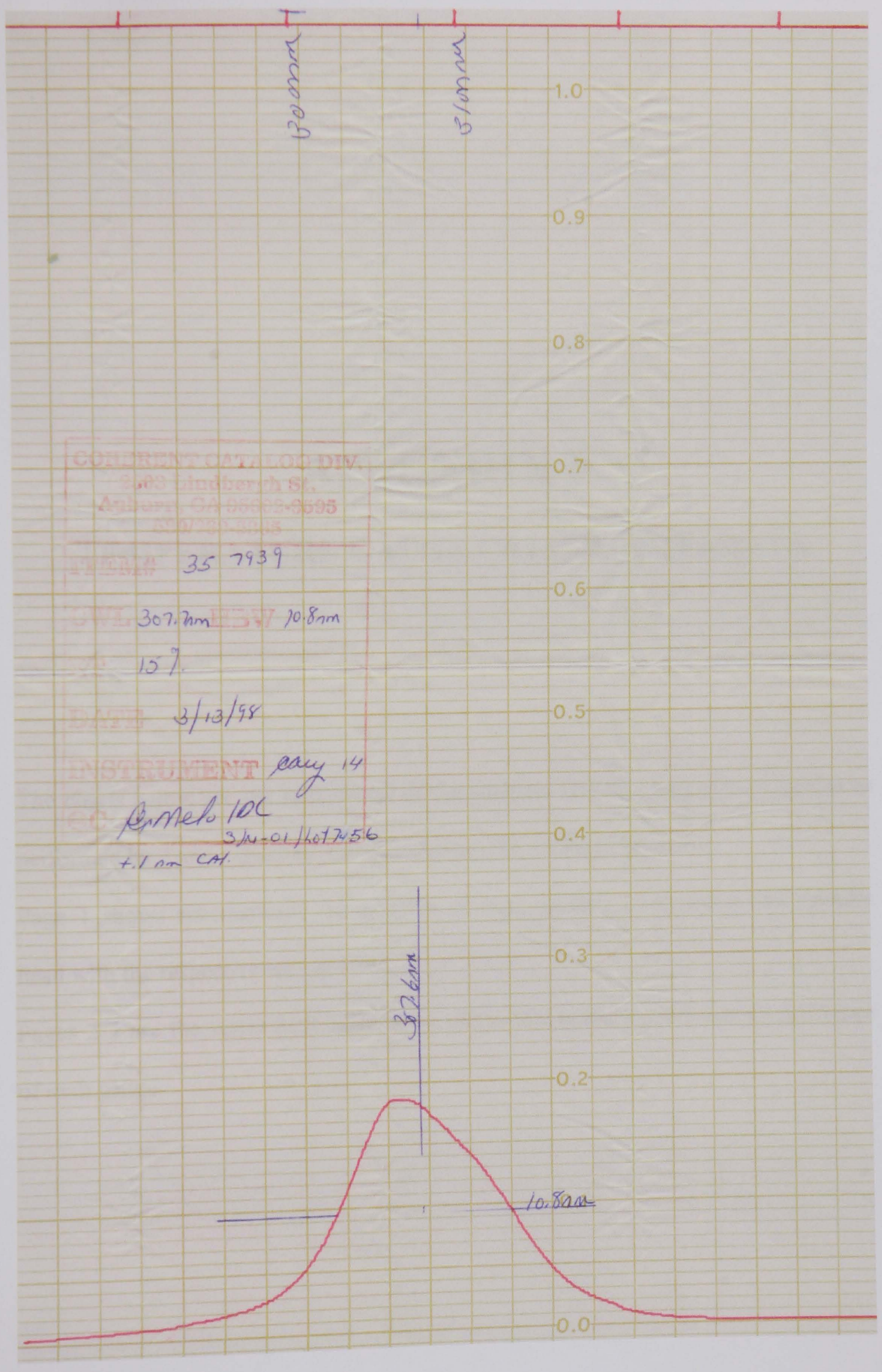

APPENDIX F

TEMPERATURE GAUGE CALIBRATION DATA

The charts below are the calibrations of the platinum thin film temperature gauges as performed by Trevor Godfrey, Osney Laboratories, Oxford University.

Page 1 shows schematically the position of each gauge on the piston and cylinder head with the respective wire colours.

Pages 2-4 are the water bath calibrations of the temperature coefficient of resistance of each gauge.

WARWICK UNI
PISTON + HEAD

OCT 2000

PISTON

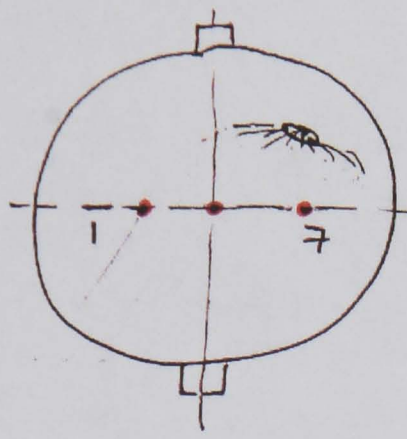

	1	21 Ω	Blue.
T/C •	2	20	Yellow/Brown
	3	20	Red/Black.
T/C •	4	19	L. Blue.
	5	18	Red/WHITE
T/C •	6	18	Yellow
	7	18	Green/Red

THERMOCOUPLE UNDER GAUGE.

(- GOOD CALIB -)

HEAD

THERMOCPL UNDER GAUGE.

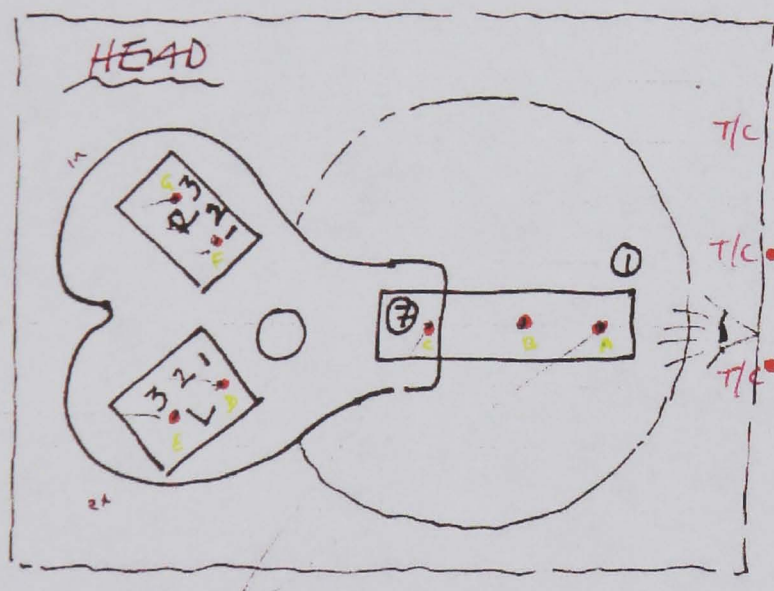

T/C •	1	Yellow	37 Ω
	2	Green/Red	39
T/C •	3	Red/White	41
	4	Brown/Yellow	45
T/C •	5	L. Blue.	48
	6	Red/Black	67
	7	Brown/White.	66

THERMOCOUPLE UNDER

LEFT

T/C •	1	Blue	31
	2	Maroon	24
T/C •	3	BLACK	24

RIGHT

T/C •	1	Green	50
	2	Red	47
T/C •	3	GREEN/Orange	43

SET-UP FILE S.111000

MAIN INFORMATION

SET-UP FILE DATE	: 11:10:00
SET-UP FILE TIME	: 3:00
LOGGED-DATA FILE DATE	: 11:10:00
LOGGED-DATA FILE TIME	: 4:00
RUN NUMBER (Filename)	: 111000
MODEL NUMBER	: :
NUMBER OF FILMS	: 13
MAXIMUM TEMP. (Deg. C.)	: 55
SETTLE TIME (seconds)	: 180
SETTLE TOL. (Deg. C.)	: .9
NUMBER OF TEMP. POINTS	: 12
PROBE 0 RES. AT 20 DEG.C.	: 108.545
PROBE 0 TEMP. COEFFICIENT	: 0.3882
PROBE 24 RES. AT 20 DEG.C.	: 108.545
PROBE 24 TEMP. COEFFICIENT	: 0.3882
REFERENCE PROBE NUMBER	: 0

TEMPERATURE POINTS

1 = 30	2 = 35	3 = 40	4 = 45	5 = 50
6 = 55	7 = 53	8 = 47	9 = 42	10 = 37
11 = 32	12 = 27			

THIN FILM GAUGE INFORMATION

FILM	MODEL NUMBER	COLOUR CODE
CH0	Reserved for thermometer probe	
CH1	1	YELLOW
CH2	2	GREE/RED
CH3	3	RED/WHI
CH4	4	BRO/YELL
CH5	5	L.BLUE
CH6	6	RED/BLA
CH7	7	BRO/WHI
CH8	8	BLUE
CH9	9	MAUVE
CH10	10	BLACK
CH11	11	GREEN
CH12	12	RED
CH13	13	GREE/ORAN

COMMENTS
None.

HEAD

PROCESSED DATA FILE P.111000

Channel Index	Regression coefficient	Resistance at 20 deg.C.	Proportional change / deg.C.
0	1.00000024	108.544999	3.57639713E-3
1	0.997903516	38.5833948	1.30718873E-3
2	0.99808119	39.6273107	1.32753987E-3
3	0.998765176	41.2877157	1.37269946E-3
4	0.999190493	45.4356911	1.34195228E-3
5	0.997812087	48.7327651	1.32040745E-3
6	0.997577377	57.900566	1.29358096E-3
7	0.997778086	66.6323223	1.28257288E-3
8	0.985010756	31.2236752	1.28637667E-3
9	0.994678608	24.3701302	1.31625296E-3
10	0.988726521	24.3093915	1.32570679E-3
11	0.997074385	50.4969887	1.30706057E-3
12	0.997223184	48.055678	1.30731888E-3
13	0.997568997	43.2314145	1.30613137E-3
24	0.17517036	-59.1157968	-0.310175122

HEAD

APPENDIX F
TEMPERATURE GAUGE CALIBRATION DATA

SET-UP FILE S.61000

MAIN INFORMATION

SET-UP FILE DATE	: 6:10:00
SET-UP FILE TIME	: 3:00
LOGGED-DATA FILE DATE	: 6:10:00
LOGGED-DATA FILE TIME	: 9:00
RUN NUMBER (Filename)	: 61000
MODEL NUMBER	: :
NUMBER OF FILMS	: 7
MAXIMUM TEMP.(Deg. C.)	: 55
SETTLE TIME (seconds)	: 180
SETTLE TOL. (Deg. C.)	: .9
NUMBER OF TEMP. POINTS	: 12
PROBE 0 RES. AT 20 DEG.C.	: 108.545
PROBE 0 TEMP. COEFFICIENT	: 0.3882
PROBE 24 RES. AT 20 DEG.C.	: 108.545
PROBE 24 TEMP. COEFFICIENT	: 0.3882
REFERENCE PROBE NUMBER	: 0

TEMPERATURE POINTS

1 = 30	2 = 35	3 = 40	4 = 45	5 = 50
6 = 55	7 = 53	8 = 47	9 = 42	10 = 37
11 = 32	12 = 27			

THIN FILM GAUGE INFORMATION

FILM	MODEL NUMBER	COLOUR CODE
CH0	Reserved for thermometer probe	
CH1	1	BLUE
CH2	2	YELLOW/BROWN
CH3	3	RED/BLACK
CH4	4	L.BLUE
CH5	5	RED/WHITE
CH6	6	YELLOW
CH7	7	GREEN/RED

PISTON

COMMENTS

None.

PROCESSED DATA FILE P.61000

Channel Index	Regression coefficient	Resistance at 20 deg.C.	Proportional change / deg.C.
0	1.00000007	108.545	3.576397E-3
1	0.99897082	22.108455	1.78384964E-3
2	0.999609817	19.5561722	1.80216504E-3
3	0.999103104	19.4830763	1.80040498E-3
4	0.99908325	18.659033	1.8069301E-3
5	0.998811067	18.2970162	1.81392407E-3
6	0.99791199	18.9880287	1.87602873E-3
7	0.999106345	19.2030763	1.82665653E-3
24	9.41207217E-2	47.3857784	0.284436425